Defense Nuclear Agency
Alexandria, VA 22310-3398

DNA-TR-95-26

Optical Stress Gauge Development for Very High Stresses
Piezoraman Measurements and Analysis

Yogendra M. Gupta
Washington State University
Physics Dept
Pullman, WA 99164

November 1995

Technical Report

DTIC
SELECTED
NOV 2 0 1995
G

19951115 145

CONTRACT No. DNA 001-90-C-0074

DESTRUCTION NOTICE:

REPORT DOCUMENTATION PAGE

Public reporting burden for this collection of information is estimated to average 1 hour per response including the time for reviewing instructions, searching existing data sources, gathering and maintaining the data needed, and completing and reviewing the collection of information. Send comments regarding this burden estimate or any other aspect of this collection of information, including suggestions for reducing this burden, to Washington Headquarters Services Directorate for information Operations and Reports, 1215 Jefferson Davis Highway, Suite 1204, Arlington, VA 22202-4302, and to the Office of Management and Budget, Paperwork Reduction Project (0704-0188), Washington, DC 20503.

1. AGENCY USE ONLY (Leave blank)	2. REPORT DATE 951101	3. REPORT TYPE AND DATES COVERED Technical 900612 – 940731

4. TITLE AND SUBTITLE
Optical Stress Gauge Development for Very High Stresses
Piezoraman Measurements and Analysis

5. FUNDING NUMBERS
C   - DNA 001-90-C-0074
PE - 62715H
PR - RJ
TA - RI
WU- DH303820

6. AUTHOR(S)

Yogendra M. Gupta

7. PERFORMING ORGANIZATION NAME(S) AND ADDRESS(ES)
Washington State University
Physics Dept
Pullman, WA 99164

8. PERFORMING ORGANIZATION REPORT NUMBER

SDC-165-FTR

9. SPONSORING/MONITORING AGENCY NAME(S) AND ADDRESS(ES)
Defense Nuclear Agency
6801 Telegraph Road
Alexandria, VA 22310-3398
TDTR/Flohr

10. SPONSORING/MONITORING AGENCY REPORT NUMBER

DNA-TR-95-26

11. SUPPLEMENTARY NOTES

12a. DISTRIBUTION/AVAILABILITY STATEMENT

Approved for public release; distribution is unlimited.

12b. DISTRIBUTION CODE

13. ABSTRACT (Maximum 200 words)

Experiments and analyses were carried out to demonstrate the use of diamond crystals as very high stress, optical transducers under shock loading. Experimental methods were developed to routinely permit time-resolved measurements (10 ns resolution) of stress induced frequency shifts of the Raman line in shocked diamonds. Plate impact experiments were conducted to achieve peak stresses to 500 kbar for uniaxial strain compression along the [110] and [100] orientations. Over the stress range examined, the Raman shifts in the shocked diamonds were completely reversible. The triple degeneracy of the diamond Raman line was completely lifted for the [110] orientation and partially lifted for the [100] orientation. A nonlinear elastic equation of state was developed for diamond. A theoretical model is described for relating the Raman shifts to an arbitrary deformation of the diamond crystals. All of the tensor coefficients in the model can be obtained from the [110] data. The [100] data provide an independent check of the predictive capability of the theoretical model. Good agreement was also observed with available hydrostatic data and uniaxial stress data at low stresses. The present work provides a firm basis for the development of an optical transducer for use at very high stresses.

14. SUBJECT TERMS

Stress Gauge	Diamond	
Optical Sensor	Shock Wave	
Fiber Optic Probe	Raman Measurements	Very High Pressure

15. NUMBER OF PAGES
234

16. PRICE CODE

17. SECURITY CLASSIFICATION OF REPORT UNCLASSIFIED	18. SECURITY CLASSIFICATION OF THIS PAGE UNCLASSIFIED	19. SECURITY CLASSIFICATION OF ABSTRACT UNCLASSIFIED	20. LIMITATION OF ABSTRACT SAR

CLASSIFIED BY:

N/A since Unclassified.

DECLASSIFY ON:

N/A since Unclassified.

SUMMARY

The overall goal of the present work was to develop an optical stress transducer that can be used at very high stresses (several hundred kbar and higher) under dynamic loading. Such a transducer in conjunction with the ruby gauge can provide optical stress gauges which will permit time resolved stress measurements (with ns resolution) over a broad range of stresses (5-10 kbar to several hundred kbar and perhaps a Mbar and higher). An additional advantage of such gauges is that they can be used in conjunction with optical fibers to monitor stresses remotely.

The scientific basis for the proposed development was the use of stress induced frequency shift and splitting of the diamond Raman line (1333 cm^{-1}). A major component of the present effort was the development of experimental methods to routinely permit time resolved measurements of stress induced frequency shifts of the Raman line in diamonds shocked to very high stresses. Optical fibers were used to transmit the excitation laser light to the sample and the scattered Raman signal from the sample to the detection equipment. The latter consisted of a spectrograph, streak camera, and a two-dimensional detector. The sensor output consists of intensity vs wavelength vs time data. The small size of the diamond samples required special care in sample assembly and optical alignment.

Well characterized plate impact experiments were carried out to a peak stress of approximately 500 kbar and for uniaxial strain compression along the [110] and [100] orientations. Good quality data were obtained in this work. Over the stress range examined, the Raman shifts in diamond were completely reversible. This is an important result for stress measurement applications. Uniaxial strain compression completely lifts the triple degeneracy along the [110] orientation and partially lifts the degeneracy along the [100] orientation. Thus, the sensor output provides a good measure of the nonhydrostaticity experienced by the sensor. A nonlinear elastic equation of state was constructed for diamond using a finite strain formalism similar to that used in our earlier work on shocked ruby. Use of second and third order elastic constants provides the Hugoniot relations for the different orientations. Using impedance matching methods, the peak stresses were determined in the diamond samples.

A piezoraman tensor model, based on a lattice dynamics approach, was used to relate the measured Raman shifts and splitting to the stresses in the diamond. Because diamond is a cubic crystal, three piezoraman coefficients are sufficient to determine Raman shifts for any arbitrary deformation. Data from uniaxial strain compression along the [110] orientation provide a unique determination of the three coefficients. The data over the entire stress range can be fitted by a constant value of these coefficients, that is -- no nonlinearity

iii

of the coefficients could be discerned. *The predictive capability of the theoretical model and the relevant parameters was demonstrated by the good agreement between the theoretical predictions and the experimental measurements along the [100] orientation.* Additionally, available hydrostatic data and uniaxial stress data at low stresses were in agreement with the model predictions.

Thus, all of the objectives for the present work were completed successfully and the present results provide a good basis for using the diamond gauge for high stress measurement applications. Since the completion of the experimental work reported here, we have improved our detection system so that improved signal to noise can be obtained with 1-2 ns resolution.

PREFACE

This report describes a research effort sponsored by the Defense Nuclear Agency under contract DNA001-90-C-0074. The project monitor, Mr. M. Flohr, is sincerely thanked for his support of this effort.

The principal investigator gratefully acknowledges the hard work and outstanding contributions of Dr. J.M. Boteler who carried out this work for his Ph. D dissertation. His dedication was central to the success of this project. Discussions with Dr. S.M. Sharma regarding lattice dynamics theories were most helpful. Paul Bellamy and Dave Savage assisted with the experimental effort and Tammany Joy assisted with various project matters.

Accesion For		
NTIS CRA&I	☒	
DTIC TAB	☐	
Unannounced	☐	
Justification		
By		
Distribution /		
Availability Codes		
Dist	Avail and / or Special	
A-1		

CONVERSION TABLE

Conversion factors for U.S. Customary to metric (SI) units of measurement.

MULTIPLY ——————————————→ BY ——————————————→ TO GET
TO GET ◄—————————————— BY ◄—————————————— DIVIDE

angstrom	$1.000\ 000\ \times\ E\ -10$	meters (m)
atmosphere (normal)	$1.013\ 25\ \times\ E\ +2$	kilo pascal (kPa)
bar	$1.000\ 000\ \times\ E\ +2$	kilo pascal (kPa)
barn	$1.000\ 000\ \times\ E\ -28$	meter^2 (m^2)
British thermal unit (thermochemical)	$1.054\ 350\ \times\ E\ +3$	joule (J)
calorie (thermochemical)	$4.184\ 000$	joule (J)
cal (thermochemical/cm^2)	$4.184\ 000\ \times\ E\ -2$	mega joule/m^2 (MJ/m^2)
curie	$3.700\ 000\ \times\ E\ +1$	*giga becquerel (GBq)
degree (angle)	$1.745\ 329\ \times\ E\ -2$	radian (rad)
degree Fahrenheit	$t_k = (t°F + 459.67)/1.8$	degree kelvin (K)
electron volt	$1.602\ 19\ \times\ E\ -19$	joule (J)
erg	$1.000\ 000\ \times\ E\ -7$	joule (J)
erg/second	$1.000\ 000\ \times\ E\ -7$	watt (W)
foot	$3.048\ 000\ \times\ E\ -1$	meter (m)
foot-pound-force	$1.355\ 818$	joule (J)
gallon (U.S. liquid)	$3.785\ 412\ \times\ E\ -3$	meter^3 (m^3)
inch	$2.540\ 000\ \times\ E\ -2$	meter (m)
jerk	$1.000\ 000\ \times\ E\ +9$	joule (J)
Joule/kilogram (J/kg) radiation dose absorbed	$1.000\ 000$	Gray (Gy)
kilotons	4.183	terajoules
kip (1000 lbf)	$4.448\ 222\ \times\ E\ +3$	newton (N)
kip/inch^2 (ksi)	$6.894\ 757\ \times\ E\ +3$	kilo pascal (kPa)
ktap	$1.000\ 000\ \times\ E\ +2$	newton-second/m^2 (N-s/m^2)
micron	$1.000\ 000\ \times\ E\ -6$	meter (m)
mil	$2.540\ 000\ \times\ E\ -5$	meter (m)
mile (international)	$1.609\ 344\ \times\ E\ +3$	meter (m)
ounce	$2.834\ 952\ \times\ E\ -2$	kilogram (kg)
pound-force (lbs avoirdupois)	$4.448\ 222$	newton (N)
pound-force inch	$1.129\ 848\ \times\ E\ -1$	newton-meter (N·m)
pound-force/inch	$1.751\ 268\ \times\ E\ +2$	newton/meter (N/m)
pound-force/foot^2	$4.788\ 026\ \times\ E\ -2$	kilo pascal (kPa)
pound-force/inch^2 (psi)	$6.894\ 757$	kilo pascal (kPa)
pound-mass (lbm avoirdupois)	$4.535\ 924\ \times\ E\ -1$	kilogram (kg)
pound-mass-foot^2 (moment of inertia)	$4.214\ 011\ \times\ E\ -2$	kilogram-meter^2 (kg·m^2)
pound-mass/foot^3	$1.601\ 846\ \times\ E\ +1$	kilogram/meter^3 (kg/m^3)
rad (radiation dose absorbed)	$1.000\ 000\ \times\ E\ -2$	**Gray (Gy)
roentgen	$2.579\ 760\ \times\ E\ -4$	coulomb/kilogram (C/kg)
shake	$1.000\ 000\ \times\ E\ -8$	second (s)
slug	$1.459\ 390\ \times\ E\ +1$	kilogram (kg)
torr (mm Hg, 0° C)	$1.333\ 22\ \times\ E\ -1$	kilo pascal (kPa)

*The becquerel (Bq) is the SI unit of radioactivity; 1 Bq = 1 event/s.
**The Gray (GY) is the SI unit of absorbed radiation.

TABLE OF CONTENTS

Section   **Page**

SECTION 1

INTRODUCTION

In 1984 a research effort was initiated at Washington State University to examine the feasibility of developing optical stress transducers for use under dynamic loading.[1] This preliminary investigation suggested that such a development was indeed feasible and subsequent efforts have resulted in the successful development of the ruby gauge for use under shock loading.[2,3] The ruby gauge provides an optical stress transducer with nanosecond time resolution and an upper stress limit of approximately 175 kbar. More importantly, this development was based on an in-depth examination of the piezoluminescence problem so that the optical response of the ruby can be related to any arbitrary deformation. As indicated later, this attribute is important for DNA applications.

The work described in this report was motivated by the interest in developing an optical stress transducer that would permit time-resolved stress measurements at very high stresses (several hundred kbar). Since these stresses are much higher than the upper limit of the ruby gauge, the new development was intended to complement the ruby gauge. The successful development of a very high stress optical transducer coupled with our ruby and rhodamine work would provide optical stress transducers over a very wide stress range (2-3 kbar to several hundred kbar). As before, an in-depth understanding of the sensor response to arbitrary loading was deemed as an important objective. *Time-resolved, frequency shift of the first order Raman line of diamond ($\omega_o = 1333\ cm^{-1}$) was the basis for the proposed development.* Similar to the 1984 study in ruby,[1] the feasibility of undertaking Raman measurements in shocked diamonds was demonstrated by conducting some preliminary experiments.[4] These results, though quite crude when compared to our current achievements, were important in establishing the conceptual basis for the subsequent work described here. The specific objectives of the present work were as follows:

1. Development of an experimental method to routinely permit time-resolved measurements of stress induced frequency shifts of the Raman line in shocked diamonds. Because diamond sensors can only be used in very small sizes, precise experimental measurements are non-trivial.

2. Measure the frequency shift as a function of the longitudinal stress to several hundred kbar. This task was somewhat open ended since the upper stress limit for diamond crystals was not known. It was important that frequency shifts be obtained for precisely defined uniaxial strain conditions in the diamond crystals.

3.   Conduct experiments on at least two orientations to establish the optimal orientation and to obtain sufficient data to carry out a complete piezoraman analysis.

4.   Develop a nonlinear elastic equation of state for diamond to determine the stresses in the optical experiments. If possible, check the predicted response against continuum measurements.

5.   Develop an analytic model for relating the Raman shifts to an arbitrary deformation of diamond crystals. Determine the model parameters from the shock data and, if possible, evaluate the predictive capabilities of such a model.

The above list of objectives was designed to develop a detailed understanding of the relationship between the optical output and an arbitrary mechanical state of the diamond gauge, that is, a tensor relationship for the piezoraman measurements. This development is in a conceptual sense similar to the electro-mechanical model used in analyzing piezoresistance gauge data (ytterbium and manganin gauges) and the opto-mechanical model used for the ruby gauge.

Generally speaking, the problem of stress measurements in materials can be divided into two parts: (i) the transduction problem (electro-mechanical or opto-mechanical relationship), that is, relating the electrical or optical output of the gauge to the mechanical state of the gauge, and (ii) the inclusion problem, that is, relating the mechanical state of the gauge to the free-field mechanical state of the material. Because stress is a tensor quantity, the transduction problem needs to be properly formulated and the gauge output has to be examined for a variety of well defined, loading conditions. Essentially, the transduction or opto-mechanical problem needs to be solved in such a manner that the gauge or sensor output can be related to any arbitrary deformation of the sensor. *This requirement is important for field applications where the loading conditions may deviate significantly from the laboratory experiments.*

The work described in this report addresses the transduction problem. Our approach consisted of conducting well characterized shock wave, uniaxial strain experiments on precisely oriented diamond crystals. By carefully measuring the stress induced frequency shifts of the diamond Raman line and using an appropriate theoretical framework, we developed the tensor relationship between frequency shifts and stresses in the diamond. Knowledge of all the piezoraman constants can permit a quantitative determination of the changes in the diamond Raman spectrum for any arbitrary deformation.

2

SECTION 2

SYNOPSIS OF EXPERIMENTS AND ANALYSES

The work carried out in this DNA contract constituted the Ph.D thesis of J. Michael Boteler under the guidance of the principal investigator. This thesis is reproduced as an appendix to this final technical report. In the interest of optimizing time and resources, this section provides a synopsis of the results obtained in Boteler's work and a road map to the contents in Boteler's thesis for the readers interested in further details.

Although Boteler's thesis constituted a fundamental scientific investigation typical of a Ph. D dissertation in Physics, it contains all the elements required to address the objectives outlines in Section 1. Before discussing the research accomplishments, a few remarks are in order. The selection of diamond as a sensor, by the principal investigator, was not arbitrary. We wanted a material that had a higher elastic limit than ruby, was mechanically stable and easy to handle, had good optical properties, had measurable stress induced changes, and the signal quality was sufficiently good to permit high time-resolution (~10ns) measurements. The major and most obvious disadvantage of using diamond crystals is the high cost. This necessitates small samples.

Chapter 2 of Boteler's thesis presents a good background on the crystal structure and the Raman spectrum of diamond. Past experimental work on Raman shifts under static high pressure has been tabulated. Theoretical studies relating to polarization selection rules and Raman intensities are also summarized. A good discussion of strain induced frequency shifts based on both group theoretical methods (qualitative discussion) and lattice dynamics approach (quantitative calculations) is presented. The lattice dynamics approach can be easily simplified to a phenomenological tensor model. We will return to this issue later in our discussion.

An important element of the current project was the development of experimental methods to routinely permit time-resolved measurements of stress induced frequency shifts in diamond (objective 1). A detailed account of this development is presented in Chapter 3 of Boteler's thesis. Some of the important achievements of this development were: attainment of time-resolution down to 10 ns; use of optical fibers to transmit the light to and from the sample; target fabrication and alignment for small samples (3 mm in diameter x 0.75 mm in thickness); and attainment of 500 kbar impact stresses. *Since the completion of this work*

3

in 1993, we have made improvements to our recording system that will now permit a time resolution of 1-2 ns and a significant improvement in the signal to noise ratio.

At present, there are no precise Hugoniot data on well oriented diamond crystals. Because continuum measurements in shocked diamonds were outside the scope of the present work, a nonlinear elastic equation of state was developed for diamond.* Using a finite strain formalism, similar to that used in our ruby work, values of the second and third order elastic constants were used to generate a Hugoniot for the diamond (objective 4). Existing data on second order pressure derivatives were used to determine the third order constants. The theoretical formalism permits the calculation of the Hugoniot for various crystallographic orientations. Details of the theoretical development can be seen in Chapter 2 of Boteler's thesis.

By using impactors with well characterized shock response, impedance matching methods were used to calculate the longitudinal stress in the diamond samples. The results of these calculations are presented in Chapter 4. This chapter also describes all of the experimental results in the present work. Experiments were carried out on diamond samples oriented along the [110] and [100] orientations (objectives 2 and 3). The maximum longitudinal stress attained in our experiments was approximately 500 kbar. Uniaxial strain experiments along the [110] orientation are particularly valuable because the triple degeneracy of the diamond Raman line is completely lifted for shock compression along this orientation. Not only does this provide a novel example of shock induced symmetry lowering[5], it has the practical benefit that all of the tensor coefficients can be obtained from data along this orientation. Experimental data along the [100] orientation are also presented in Chapter 4. For shock compression along the [100] orientation, the triple degeneracy is only partially lifted, and a singlet and a doublet are observed in the experimental data. The [100] results can be used to make an independent evaluation of the predictive capability of the piezoraman tensor coefficients. *A very important result for stress transducer applications is that the diamond Raman shift is completely reversible for the maximum stress (500 kbar) examined in this work. Thus, the diamond gauge will display no hysteresis over the range examined.*

---

* Modeling diamond as an elastic solid is appropriate because our Raman data showed that the diamond response was completely reversible to 500 kbar.

Because the maximum stress in our current work was 500 kbar, we can safely say that diamond can be used as a stress gauge to this stress level. We conjecture that diamond should perform well as a stress gauge up to 1 Mbar and higher. However, higher stress experiments are needed to confirm this conjecture. It is interesting to point out that in our current work, the diamond samples sustained a stress difference of over 400 kbar without undergoing any inelastic deformation.

The theoretical analysis to meet objective 5 is presented in Chapter 2 and the analytic expressions for data analysis are presented in the first part of Chapter 5. All of the piezoraman tensor coefficients were determined from the [110] data and they are listed in Table 5.1 of Chapter 5. Over the stress range examined, the tensor coefficients did not show any stress-dependence (or nonlinear behavior). Precision of the linear coefficients can be ascertained by noting the good agreement between the theoretical predictions and the experimental data over the entire stress range examined in our work.

The predictive capability of the piezoraman model derived from the [110] data can be seen by noting the good agreement between the predicted and measured results for the [100] orientation. Good agreement between our model predictions and the low stress data (uniaxial stress loading), and the hydrostatic data can also be seen in Chapter 5.

In conclusion, all of the objectives for this project were successfully completed. Based on the work reported here, the development of a very high stress optical transducer (500 kbar and likely higher) has been demonstrated in laboratory shock wave experiments. Although the use of this capability for DNA applications will require further work (to adapt the gauge to a particular application), the experimental and analytic developments presented here provide a sound basis for undertaking such an effort.

Finally, we point out that the transduction problem (the focus of the present work) for the diamond gauge was completed in much shorter time than the ruby work because of two main reasons: the vibrational spectra are easier to analyze and there were theoretical developments in the literature that could be utilized; the experimental experience gained in the ruby gauge development directly benefited the present work.

SECTION 3

REFERENCES

1. P. Horn, Y.M. Gupta, and G.E. Duvall, "Feasibility of Measuring Ruby Luminescence Wavelength Shift Under Shock Loading", Defense Nuclear Agency Report DNA-TR-85-392 (1985), (UNCLASSIFIED).

2. Y.M. Gupta, P.D. Horn, and J.A. Burt, "Ruby Luminescence Wavelength Shift to Measure Stress in Shock Wave Experiments", Defense Nuclear Agency Report DNA-TR-89-136 (1989), (UNCLASSIFIED).

3. Y.M. Gupta, "Optical Stress Gauge Development: Piezoluminescence Measurements and Analysis", Defense Nuclear Agency Technical Report, DNA-TR-93-128 (1994), (UNCLASSIFIED).

4. Y.M. Gupta, P.D. Horn, and C.S. Yoo, Appl. Phys. Lett. **55**, 33 (1989), (UNCLASSIFIED).

5. J.M. Boteler and Y.M. Gupta, Phys. Rev. Lett. **71**, 3497 (1993), (UNCLASSIFIED).

APPENDIX

TIME RESOLVED RAMAN SPECTROSCOPY IN DIAMONDS SHOCK COMPRESSED ALONG [110] AND [100] ORIENTATIONS

Abstract

by John Michael Boteler, Ph.D.
Washington State University
May 1993

Chairman: Yogendra M. Gupta

Strain-induced symmetry changes in diamond were examined by measuring the first order Raman spectrum of single crystals shocked along the [110] and [100] directions. Uniaxial strain along these directions is predicted to completely or partially lift the triple degeneracy of the ambient Raman line.

Peak longitudinal stresses ranging from 12 to 45 GPa (1% to 3.5% density compression) were achieved in plate impact, uniaxial strain loading experiments. Time-resolved Raman spectra with 10ns resolution were obtained during shock compression to determine the shifted frequencies. The degenerate Raman line was observed to split due to the presence of large nonhydrostatic stresses. This is the first reported observation of such splittings during shock experiments. Data collected for the [110] orientation indicate that the observed spectra are accurately described by three singlets, suggesting a complete lifting of the degeneracy. Raman spectra collected for the [100] orientation were consistent with singlet and doublet lines, suggesting a partial removal of the degeneracy. All frequency-shifts were observed to increase with density compression.

A three parameter, perturbation model was used to analyze the results. The data for the [110] orientation provided a unique determination of the three parameters. The data for the [100] orientation was in good agreement with the predictions based on these parameters, providing and independent check. Unlike the previous parameter values determined from uniaxial stress measurements, the present values demonstrate a good fit to the observed frequency shifts over the entire stress range considered. The centroids of

the shifted frequencies for each orientation were compared with static high pressure measurements of the degenerate Raman line. Good agreement was demonstrated for compression to 3.5%, suggesting that the centroid location is not influenced by the nonhydrostaticity. The static high-pressure measurements are also in good agreement with the predictions based on the present work.

The present results show that the three perturbation parameters determined in this work may be used to predict the Raman frequency shifts and splittings for other loading conditions.

TABLE OF CONTENTS

Chapter 1

INTRODUCTION

Diamond has long been known for its remarkable strength and chemical inertness in harsh environments.[1] Numerous industrial applications of diamond take advantage of these unique properties. For many technical applications, it is the optical and thermal characteristics of diamond which are of greatest interest. Diamond has the widest range of spectral transmission as well as the largest thermal conductivity of all known solids. These attributes make it ideal for optical windows and a myriad of laser applications. Because of these unique properties and its simple structure, diamond has been (and continues to be) a subject of numerous scientific investigations.

Infrared absorption and Raman scattering techniques may be performed on diamond to determine its impurity content and local symmetry. Indeed, the infrared absorption of diamond is the accepted method for classifying diamonds.[2] The Raman spectrum at ambient conditions is well known to be triply degenerate.[3] The large Raman scattering cross-section[4] and high mechanical strength of diamond make it an ideal candidate for high pressure studies. The Raman spectrum of diamond has been examined at large compressions in recent Diamond Anvil Cell (DAC) measurements.[5, 6] The Raman frequency shifts and line splittings[7] have also been examined for small compression due to applied uniaxial stress.[8] The present work extends these studies to uniaxial strain loading along particular crystallographic directions.

1.1 MOTIVATION

Shock wave, uniaxial strain experiments provide a unique method for examining the response of materials to large compression and strongly nonhydrostatic conditions. The continuum measurements performed during shock compression typically measure the

shock velocity, particle velocity, and longitudinal stress in the material. Collectively these measurements provide insight into the stress-volume relationship for the material.

The passage of a shock front through a material can produce changes in many of the solid state properties of the material. Many of these changes are transient and must be examined during the shock compression process. Structural and/or symmetry changes immediately behind the shock front are of particular interest. Thus, time-resolved spectroscopy measurements performed during shock compression compliment the continuum measurements by providing a better understanding of shock induced changes at the atomic/molecular level.

Time-resolved Raman spectroscopy is a promising experimental technique for determining structural changes during shock compression experiments.[9, 10] The symmetry changes behind the shock front may be identified by the corresponding changes in the vibrational Raman spectrum. The purpose of the present work is to investigate the strain-induced symmetry changes in diamond using time-resolved Raman spectroscopy.

Gupta et. al.[11] first demonstrated the feasibility of performing time-resolved Raman spectroscopy on diamond during shock loading. However, their data did not show the expected splitting of the degenerate Raman line. The present work addresses the strain-induced symmetry changes with improved time and wavelength resolution. It was hoped that the improvement in resolution would reveal structure not observed in the previous investigation of Gupta et. al.[11]

1.2 OBJECTIVE AND APPROACH

The overall goal of this work was to use time-resolved Raman spectroscopy during shock compression of diamond to investigate strain-induced symmetry changes.

The specific objectives to meet this goal were to :

(1)   Develop the capability to perform Raman spectroscopy under shock-loading with a time-resolution of 10 ns or better. Due to the small sample size, a very fast time resolution was necessary to ensure adequate recording time.

(2)   Measure changes in the Raman spectrum of diamonds subjected to uniaxial strain to examine symmetry changes due to large nonhydrostatic stresses.

(3)   Analyze the results in terms of the first order perturbation to the frequency shift due to applied strain.

(4)   Develop a consistent picture of strain induced effects in order to compare present results with other diamond studies and to provide a predictive capability for strain induced changes.

The approach taken to achieve the desired time-resolution was to build upon earlier developments wherever possible to take advantage of proven designs and to maximize efficiency. The design goal of 10 nanosecond time-resolution was based upon the estimated number of spectra that could be recorded for a shock wave traveling through a 0.75 mm thick sample. The optical collection system used by Gustavsen and Gupta[12] in their Raman study on α-quartz served as the starting point for the present work. To obtain the desired time-resolution, the collection system was modified to improve the signal throughput and to accommodate a much faster recording time. The small size of the diamond samples posed problems in mounting and optical alignment that were not encountered in earlier work, and a complete redesign of the Raman target cell was necessary. The approach taken in the new target design was to develop a more flexible sample holder that could accommodate small samples and permit a precise placement of the optics for alignment purposes.

For the purpose of analysis and experimental design, the effect of strain on the Raman spectrum in diamond was modeled as a first-order perturbation. This model,

developed by Ganesan et al.,[13] is based on the quasi-harmonic approximation to the crystal potential. The model may be used to predict frequency shifts and degeneracy of the strained Raman spectrum. The applied strain may also be modeled as a finite deformation of the diamond lattice and the predicted degeneracy checked using the correlation method in group theory. Because the Raman spectrum is polarization sensitive, calculations were made to determine the selection rules that governed the presence and intensity of the splittings for ambient and uniaxial strain conditions.

Raman measurements of diamond were obtained for uniaxial strain compression along the [110] and [100] crystallographic directions. The uniaxial strain condition was generated using plate-impact experiments in a light-gas gun. The approach taken in these experiments was to perform the majority of the experiments along the [110] orientation and perform a few experiments along the [100] orientation. The maximum density compression of 4 percent in these experiments was a result of the projectile velocity attainable and the choice of impactor materials.

Most of the experiments were performed on the [110] orientation because the perturbation model indicates that the degeneracy is completely removed for strain along this direction and that three distinct frequencies are possible. For strain along [100], two frequencies are possible, one of which is doubly degenerate. The quasi-harmonic theory indicates that these frequency locations may be predicted with information obtained solely from the [110] data. Thus, the [100] experiments provide an independent check of the parameters derived from the [110] experiments. The results of the present study were compared to previous uniaxial stress results[8] and static high-pressure studies.[5, 6, 14-17]

Specifically, the following tasks were carried out in the present work:

(1)   Modify the existing Raman collection system to achieve 10 nanoseconds time-resolution.

(2)   Design the Raman target cell to accommodate the small sample size. The design
needs to address sample mounting and optical alignment.

(3)   Apply the quasi-harmonic model for strain-induced Raman frequency shifts to
predict the results for uniaxial strain along the [110] and [100] directions to aid in
experimental design.

(4)   Determine changes in the Raman spectrum of diamonds for shock compression
along the [110] and [100] crystallographic directions.

(5)   Use the quasi-harmonic model and polarization calculations to analyze the
experimental results.

(6)   Compare results from the present study to previous work under static loading
conditions.

1.3 ORGANIZATION OF THE THESIS

Chapter 2 reviews previous high-pressure studies of the Raman line in diamond
and provides general background information on the theory used in this study. Details of
the quasi-harmonic model used to examine deformation induced changes in the Raman
spectrum are described. The theoretical formulation used to model the nonlinear elastic
response in diamond is also presented.

Chapter 3 presents the experimental methods used in the present study. The
overall experimental configuration is discussed, and the individual components are
described. Details of the target and projectile construction are provided. The calibration
procedures and experimental diagnostics are discussed, followed by a summary of the
impact configurations and operating conditions for all of the experiments.

Chapter 4 presents the Raman frequency measurements for the [110] and [100]
uniaxial strain experiments. The procedure used to fit the experimental peak locations is
discussed. An example is given to demonstrate the impedance matching technique used to

determine the longitudinal stress in the diamond. This chapter concludes with a discussion of the experimental precision and uncertainties.

Chapter 5 presents the analysis and discussion of the experimental results obtained in this work. The strain-induced frequency shifts of the Raman spectrum are examined and correlated to parameters in the quasi-harmonic model. Expressions for these parameters are provided as functions of the observed shifts and the applied uniaxial strain. The experimental results are compared to the model predictions based on the new anharmonic parameters. Present results are compared to Raman shifts in diamond for previous static loading measurements.

Chapter 6 summarizes the important findings of this study. Conclusions based on the findings are presented, and suggestions for future experimental work are indicated.

The Appendices provide details that support or otherwise elaborate the discussion contained in the various chapters. Appendix A gives the technical details for target and projectile construction. Appendix B provides an example of a time synchronization design for a typical experiment. Appendix C contains all of the raw data plots from the experimental records. Appendix D provides the details for the calculation of the elastic constants for uniaxial strain along the [110] direction. Appendix E presents the bond-stretching and bond-bending parameters for diamond, silicon, and germanium.

Chapter 2

EXPERIMENTAL AND THEORETICAL BACKGROUND

This chapter presents background material on the lattice structure of diamond and the lattice vibrations that produce the Raman spectrum. Previous high-pressure investigations of the diamond Raman spectrum, relevant to the present study, are summarized. Results from these prior studies will be compared in Chapter 5 with the experimental results found in the present investigation.

The quasi-harmonic model[13] and the polarization selection rules, central to this work, are discussed in this chapter. Use of the quasi-harmonic model to predict frequency shifts, is demonstrated for several strain configurations. Polarization selection rules are developed in this chapter for the simple backscatter geometry only. Modification of these rules to reflect the quasi-backscatter geometry is addressed in Chapter 5.

The shock Hugoniot for diamond has not been measured and the nonlinear elastic material response of diamond is not accurately known. Details are given for the approach taken in this work to overcome these deficiencies.

2.1 DIAMOND STRUCTURE AND THE RAMAN SPECTRUM

2.1.1 Crystal Structure and Symmetry

Diamond is a crystalline form of carbon and is the hardest material known. Its structure consists of carbon atoms that lie on two interpenetrating face-centered cubic sub-lattices[18] as shown in Figure 2.1. In this figure, the open and shaded circles represent carbon atoms on the two constituent sub-lattices, one cornered at point 1 and the other at $\bar{1}$ located 1/4 the distance along the cubic body diagonal away from 1. The lattice spacing is shown as $2a$ in this figure. Each primitive unit cell contains two atoms, each of which have four nearest neighbors and twelve next-nearest neighbors. The nearest neighbors are arranged in a covalently bonded tetrahedron with each atom of one sub-
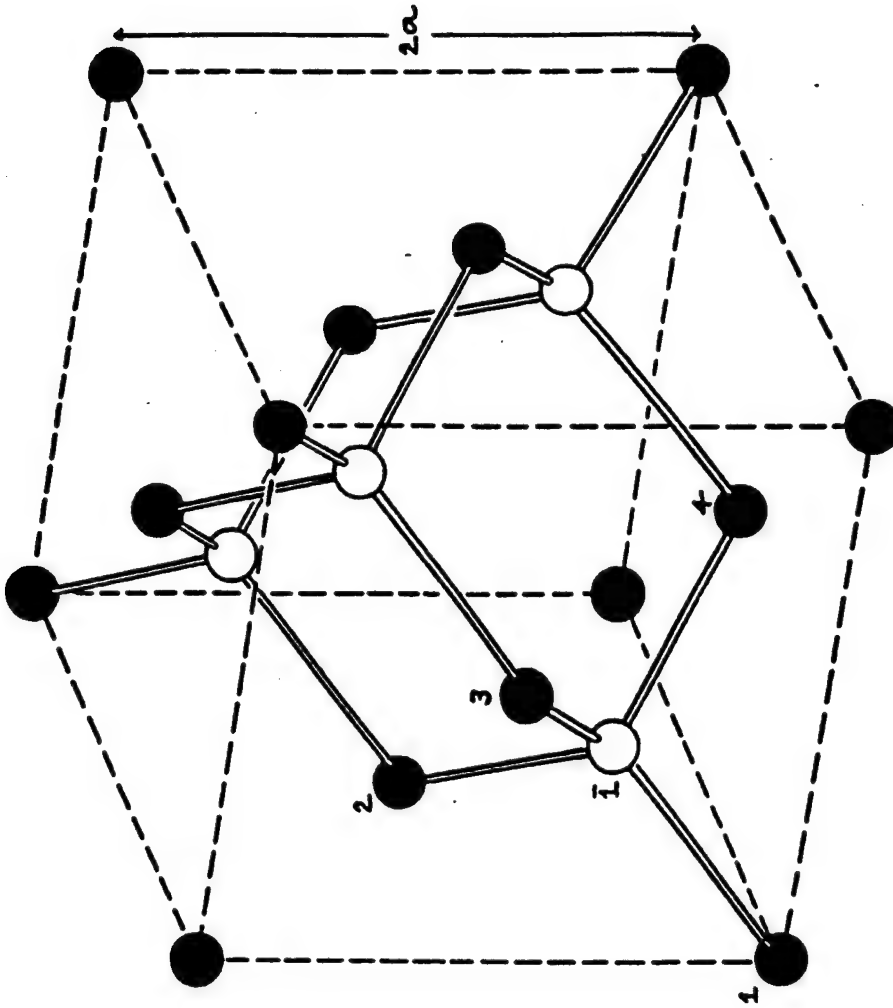
Figure 2.1   Diamond Lattice (Adapted from Ref. 19). The open and filled circles represent the atoms on the two different sublattices.

lattice located at the center of the tetrahedron formed by its four nearest neighbors of the other sub-lattice. One such tetrahedron is shown in the Figure 2.1 for the four nearest neighbors of the atom located at $\bar{1}$, designated as: **1,2,3,4**.

The atomic coordinates for two adjacent primitive cells are given[19] in Figure 2.2. In both figures the lattice constant is **2a**. Hence, the two sub-lattices are displaced by $(\sqrt{3}/2)a$ along the body diagonal. The barred numbers in Figure 2.2 distinguish the atoms of one sub-lattice from the corresponding atoms of the other sub-lattice with the same number designation. Thus, there are eight atoms in a unit cell composed of the two atoms in the primitive cell, forming the lattice basis, and their four nearest-neighbors.

2.1.2 Raman Spectrum

The Raman effect[20] in diamond was first observed by Ramaswamy[21] in 1930. Due to the extremely small intensity of the Raman line[22] ($I_{Raman\ line} \approx 10^{-8}\ I_{Source}$) and the necessity for a coherent light source, the technique did not become popular until the invention of the laser. Beginning with the work of Smith,[19] several studies of the Raman line in diamond have been reported.[3, 14-17] Solin and Ramdas[3] investigated the first- and second-order Raman Spectra of diamond between room and liquid helium temperature. At room temperature, they observed the first-order line position to be 1332.5(5) cm^{-1} shifted from the laser line at 5145 Å and having a linewidth of 1.65(2) cm^{-1}. The number in parenthesis indicates the uncertainty in the last decimal place.

The lattice vibrations in diamond that are Raman-active, correspond to the relative motion between the two face-centered-cubic (fcc) sub-lattices. As shown in Figure 2.3, there are three identical vibrations normal to the faces of the cube inscribing the tetrahedron.[19] The tetrahedron shown here has the same number designation as Figure 2.1. In crystallographic terminology, the $\{x_1, x_2, x_3\}$ system is designated as $\{[100],[010],[001]\}$. The carbon-carbon bond length is[23] 1.5445 Å, so that the lattice spacing (**2a**) is 3.567 Å and the angle between any two C-C bonds in the tetrahedron is given by $\cos^{-1}(-1/3) \cong 109.5°$.
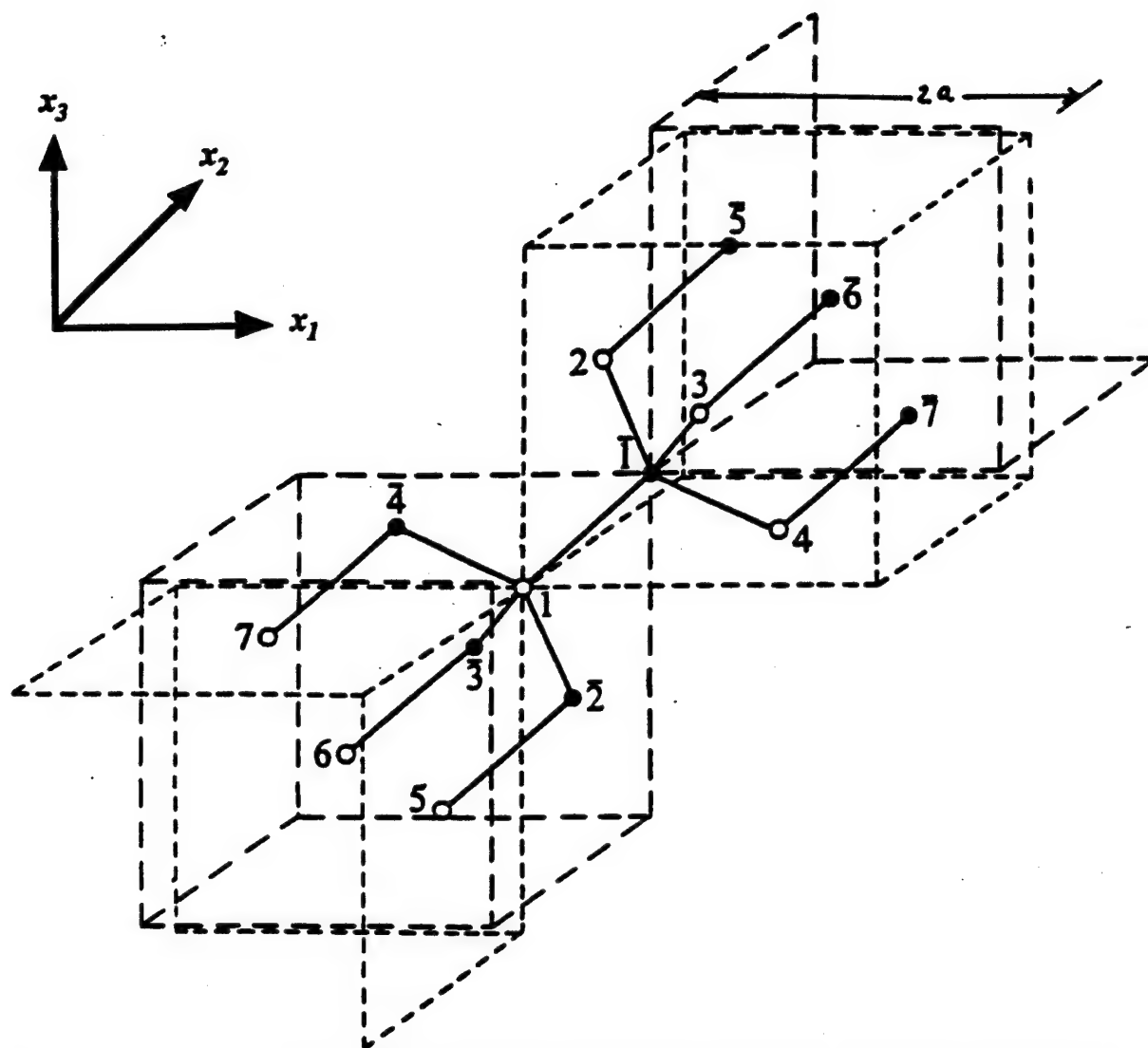
n	x_1	x_2	x_3
1	0	0	0
2	0	a	a
3	a	0	a
4	a	a	0
$\bar{1}$	a/2	a/2	a/2
$\bar{2}$	a/2	-a/2	-a/2
$\bar{3}$	-a/2	a/2	-a/2
$\bar{4}$	-a/2	-a/2	a/2

Figure 2.2 Atomic Coordinates for Diamond (Adapted from Ref. 19).
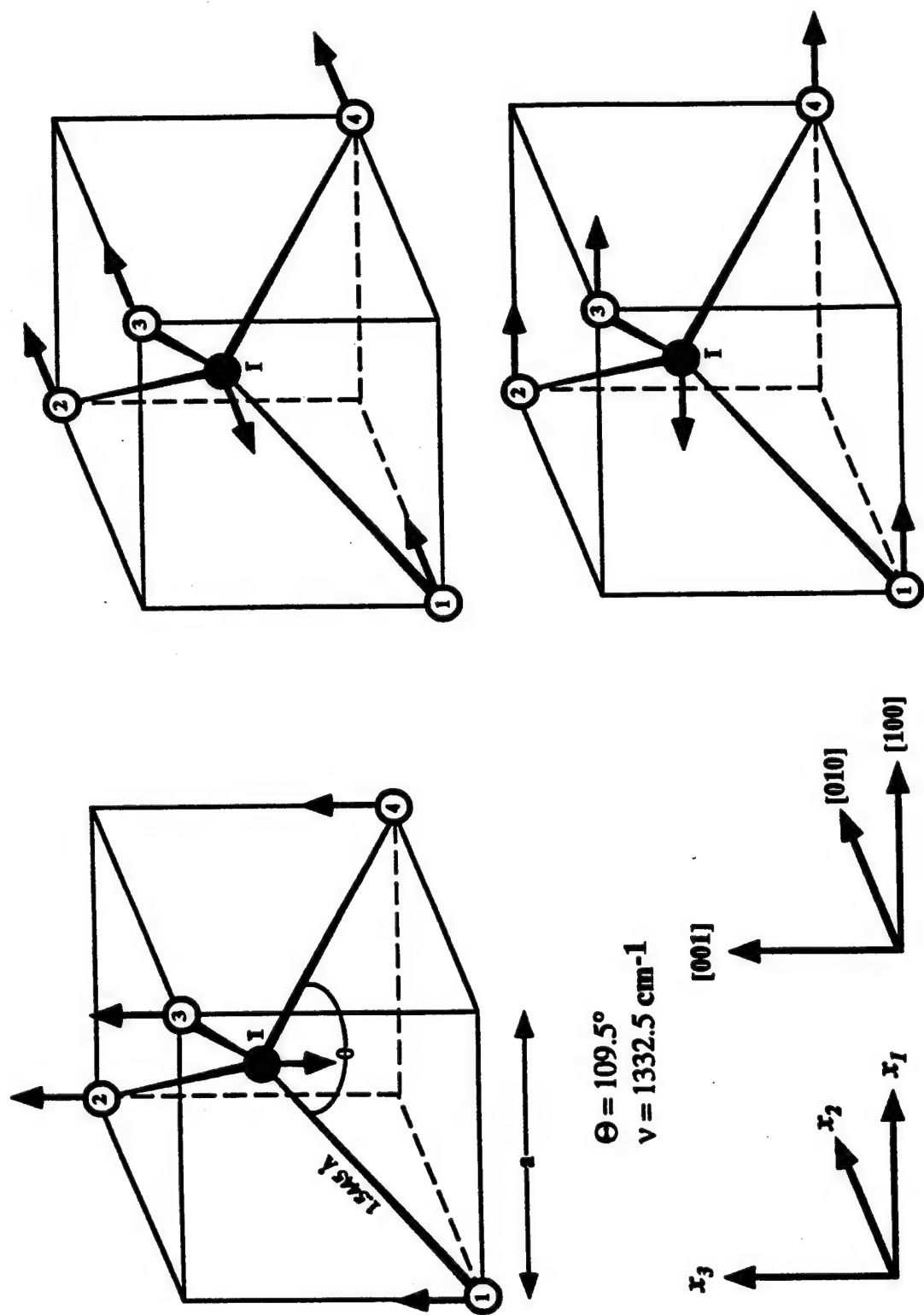
Figure 2.3 Tetrahedral Arrangement and Atomic Vibrations.

$\Theta = 109.5°$

$\nu = 1332.5$ cm^{-1}

The Raman effect in diamond may be regarded as inelastic scattering of the incident photons from the three vibrations just described. The measured shift in frequencies corresponds to the vibrational frequencies of the lattice and under ambient conditions there would only be a single Raman line (triply degenerate) at 1332.5 cm^{-1}.

An alternative approach for showing the vibrations is illustrated in Figure 2.4. In this figure, the projection of the two sub-lattices is shown for the three crystallographic directions indicated to the right of the figure. This method of projection can be particularly useful when considering lattice deformations.

By perturbing the cubic symmetry, the vibrational degeneracy may be partly, or completely, lifted. The simplest case is depicted in Figure 2.5, where a compression along the [100] direction deforms the cube to a tetragonal Bravais lattice. In this system, two of the vibrations are the same (forming a doublet) and the third vibrational mode forms a singlet along the direction of compression. Note that no assumptions may be made, *a priori*, regarding the magnitude of the resultant vibrations. For example, the singlet frequency is greater than the doublet for the case of diamond, whereas the converse is true for Germanium.[24] Discussion of compression along [110] and [111] directions is deferred to Section 2.3, where it will be seen that the phonon polarization directions associated with the predicted splittings, reflect the direction of the resultant vibrational modes.

The lifting of the degenerate vibrational modes through symmetry deformation may also be predicted using group theory. This will also be addressed briefly in Sect. 2.3.

2.2 PAST EXPERIMENTAL WORK ON STRESS INDUCED SHIFTS

Understanding how a covalently bonded material (such as diamond) responds to deformation gives important insight into the short-range interatomic forces that form the lattice structure. The effects of applied stress on diamond may be manifested by frequency shifts, and/or splitting of the triply degenerate normal vibrational modes. In the
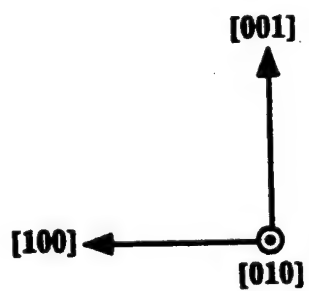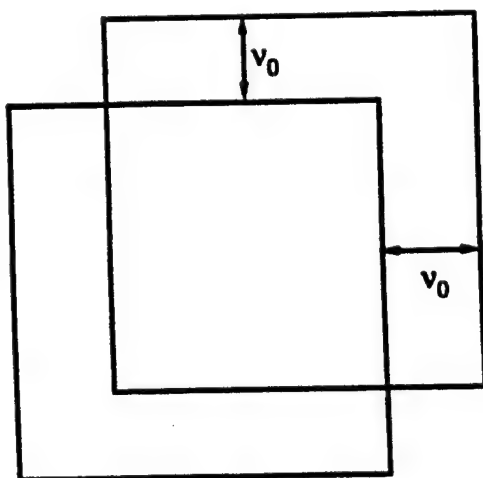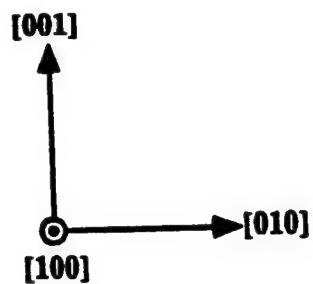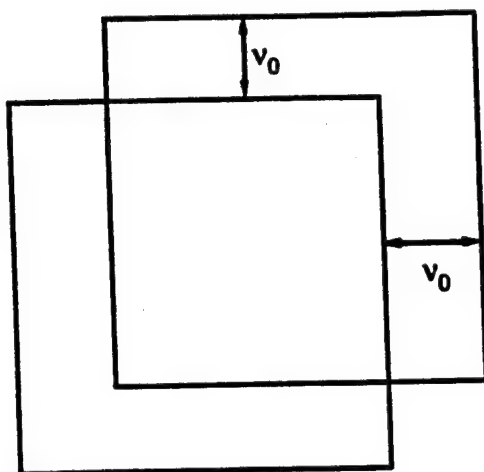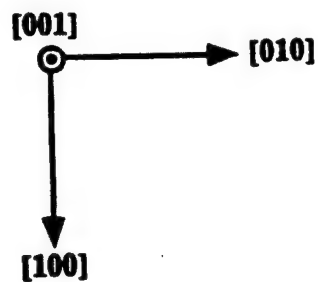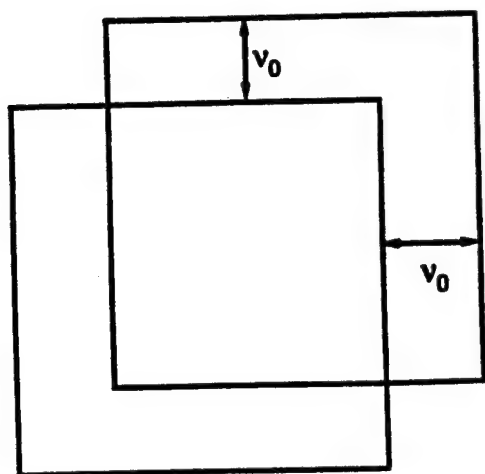
Figure 2.4 Projection of Sub-Lattices and Vibrations.
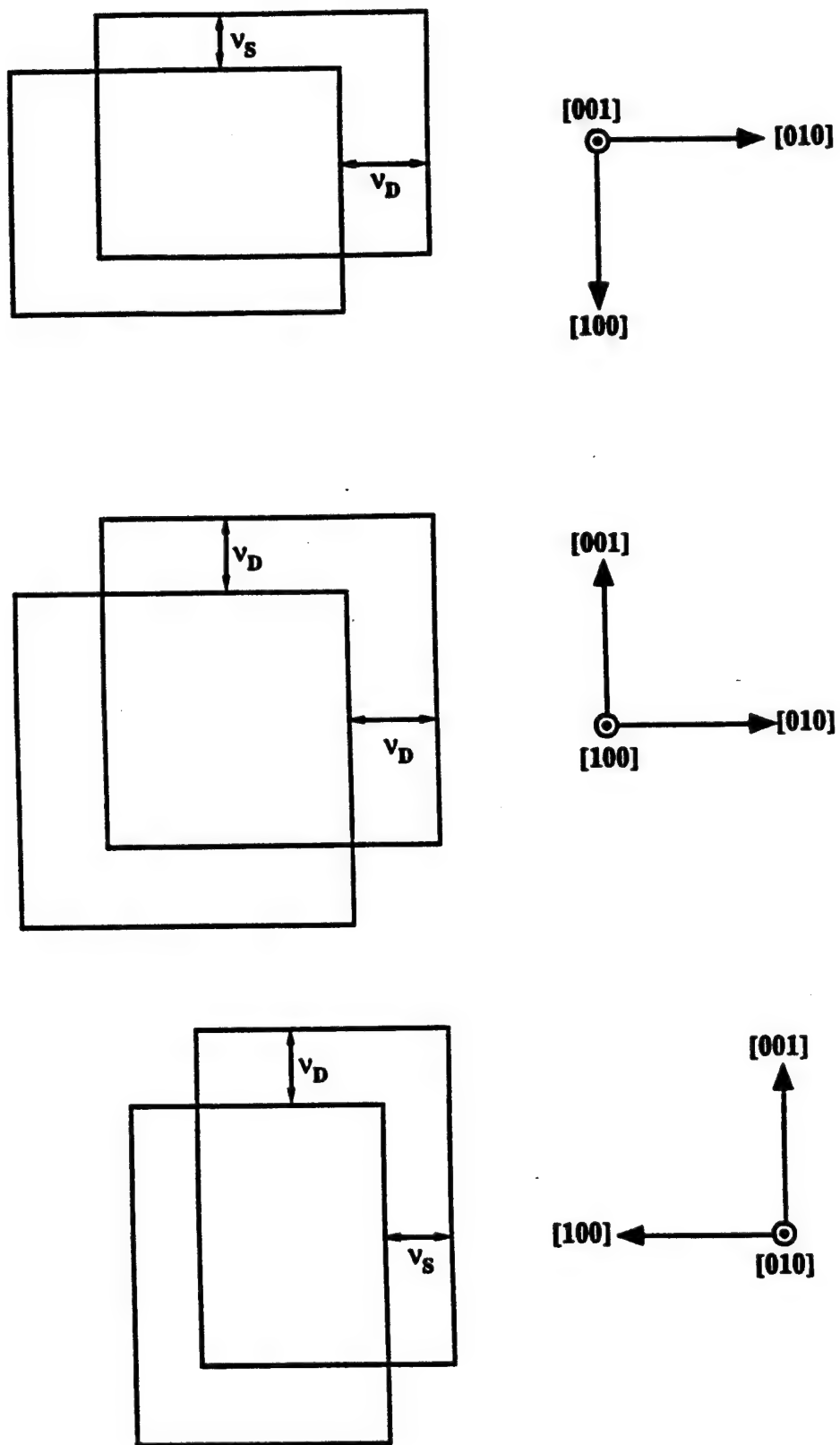
Figure 2.5 Projection of Sub-Lattices and Vibrations for Compression Along [100].

microscopic theory presented in Section 2.3.2, it will be seen that these effects display the directional nature of the binding forces.

The experimental conditions that yield an isotropic deformation of the lattice are commonly referred to as *hydrostatic*.[25] The symmetry-conserving nature of true hydrostatic deformation is illustrated in Figure 2.6. In this figure, a uniform, isotropic strain has been applied to the diamond lattice of Figure 2.4. The resulting symmetry is identical to the zero-strain symmetry, and the vibration mode remains triply degenerate. However, the frequency of the vibration has been shifted by an amount Δv resulting in a new vibrational frequency of v', where

$$v' = v_0 + \Delta v \qquad (2.1)$$

Modern hydrostatic measurements are typically performed in a gasketed Diamond Anvil Cell[26,27] . The sample is placed between two opposing diamond anvils, that apply the pressure. The gasket allows the sample to be encapsulated in a pressure-transmitting medium. Nonhydrostacity arises in the Diamond Anvil Cell for high pressures because of the nonuniform behavior of the pressure medium. Ferraro[28] has stated that pressure transmitting fluids are applicable to only about 100 kbar, beyond which the measured pressure must be considered as an average pressure. Solid media such as frozen xenon may be able to further extend the hydrostatic pressure range, but the point of departure from hydrostatic to nonhydrostatic compression is not well defined. This uncertainty poses questions regarding the nature of the stress state and whether inferred pressure effects are due to hydrostatic conditions, shear stress, or a combination of both. Any splitting of the degenerate phonon spectrum in a cubic crystal, such as diamond, indicates a symmetry-breaking caused by a nonhydrostatic stress state.

In the following discussion, experiments performed on the Raman spectrum of diamond in the Diamond Anvil Cell and similar experiments will be grouped under the heading Pressure Effects to distinguish them from experiments designed to examine
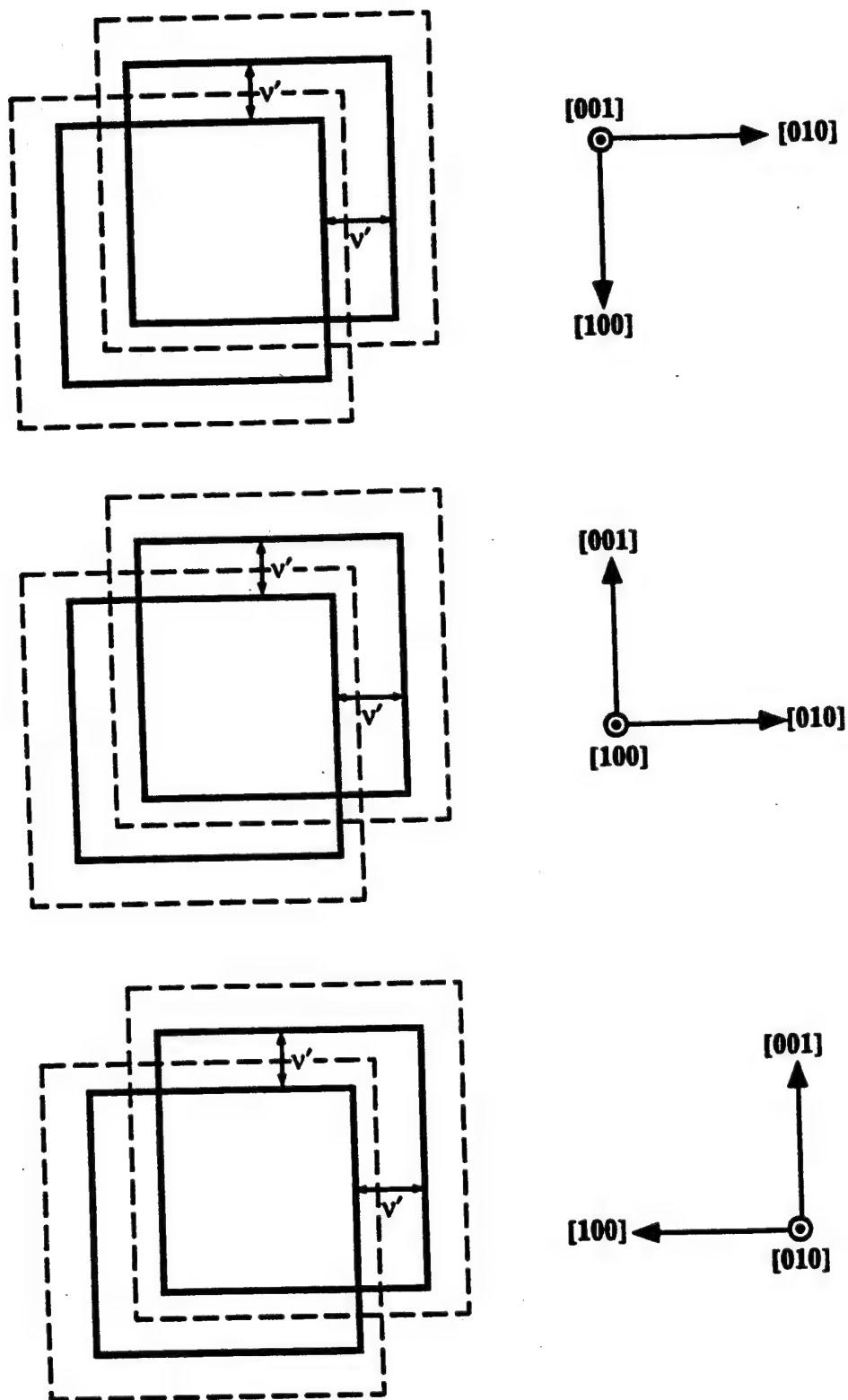
Figure 2.6 Projection of Sub-Lattices and Vibrations For Isotropic Strain.

nonhydrostatic effects. Experiments designed to examine nonhydrostatic effects are discussed separately.

2.2.1 Pressure Effects

The first investigation of the pressure-induced phonon frequency shifts in diamond was performed by Mitra et al.[16] They reported on frequency shifts $\Delta\omega_H$ for pressure approaching 10 kbar. Here $\Delta\omega_H$ indicates the pressure-induced frequency shift from the ambient value of 1332.5 cm^{-1}. In their experiments, the hydrostatic pressure was produced hydraulically inside an oil-filled optical cell using a reciprocating hand pump. The pressure was measured by a Manganin pressure gauge accurate to within 1 % over the 10 kbar range. Their results indicated a value of $\frac{d\omega_H}{dP} = 2.83(3)$ cm^{-1}/GPa. Where the number indicated in parenthesis indicates the uncertainty in the last significant figure.

Parsons[14] used a modified version of a tetrahedral anvil device to study the pressure effects on the Raman spectrum of diamond to 24 kbar. In this device the anvils were made of tungsten carbide and the pressure medium was powdered potassium chloride, which was packed around the sample. The pressure was delivered by two sets of opposing tungsten carbide anvils. The pressure was measured by recording the shift in the absorption band of nickel dimethylglyoxime[29] doped into a pellet of sodium chloride. The pressure scale was corroborated by the observed phase transition of potassium chloride from face-centered-cubic to body-centered-cubic at 19.4 kbar. For the pressure range considered in this study, he found $\frac{d\omega_H}{dP} = 3.6(3)$ cm^{-1}/GPa.

Tardieu et al.[6] performed experiments designed to study the pressure and temperature dependence of the first-order Raman spectrum in diamond. Their apparatus was a Diamond Anvil Cell that was enclosed in a steel membrane. Pressure to the Diamond Anvil Cell was supplied by inflating the steel membrane. The pressure medium was a methanol-ethanol mixture (4:1) and the pressure was determined by measuring the

ruby R_1 line shift[30]. They reported a pressure derivative of $\frac{d\omega_H}{dP} = 2.64(10)\,{}^{cm^{-1}}\!/_{GPa}$ over a pressure range 0-150 kbar.

Boppart et al.[5], measured the Raman spectra of diamond to 270 kbar using a Diamond Anvil Cell and a variety of pressure transmitting media. The purpose of their study was to investigate the use of the diamond Raman frequency shift as a possible alternative to the ruby scale. The experiments were performed at room temperature using hydrogen, argon, and xenon as pressure transmitting media. Due to difficulties with the first two media, only solid xenon was used at pressures beyond 150 kbar. The ruby R_1 line shift was used to determine the experimental pressures . Their results indicated a value of $\frac{d\omega_H}{dP} = 2.87(10)\,{}^{cm^{-1}}\!/_{GPa}$ for the shifted peaks.

Similar to the work of Boppart et al.[5], the study by Hanfland et al.[17] used solid xenon in a Diamond Anvil Cell to 400 kbar. They measured a value of $\frac{d\omega_H}{dP} = 2.90(5)\,{}^{cm^{-1}}\!/_{GPa}$ using the ruby scale as a calibration.

At the extreme range of reported 'hydrostatic' pressures is the work of Goncharov et al.[15] They reported Raman scattering from diamond up to pressures of 720 kbar using a Diamond Anvil Cell with solid xenon as a pressure medium. The pressure was determined from the ruby R_1 line shift. The pressure dependence was found to be $\frac{d\omega_H}{dP} = 3.01(1)\,{}^{cm^{-1}}\!/_{GPa}$. These workers found that their data were best fit by a Pressure-Frequency relation that was quadratic in the frequency shifts.

In all of these experiments, the measured hydrostatic pressure shift of the optical phonon at constant temperature was used to calculate the isothermal mode Grüneisen parameter[25] γ_i. This parameter is a measure of the anharmonicity of the crystal lattice and its value provides insight into the interatomic forces acting within the crystal.[25] Within the limits of the quasi-harmonic model γ_i is expected to be a constant. For the ith normal mode it may be written as

$$\gamma_i = -\left(\frac{\partial \ln \omega_i}{\partial \ln V}\right)_T \qquad (2.2)$$

where ω_i is the mode frequency and V is the crystal volume.

In essence, γ_i is an exponent that describes how the mode frequency scales with a change in volume. It may be determined from the pressure dependent frequency shift if the isothermal compressibility κ_T, or bulk modulus B, is known,

$$\gamma_i = -\frac{V}{\omega_i}\left(\frac{\partial \omega_i}{\partial P}\frac{\partial P}{\partial V}\right)_T = \frac{1}{\kappa_T \omega_i}\left(\frac{\partial \omega_i}{\partial P}\right)_T \qquad (2.3)$$

Furthermore, if it is assumed that γ_i is independent of temperature, Grüneisen's approximation[31], $\bar{\gamma} = \gamma_i$, is justified.

The experimental values for the pressure dependence of the frequency shift and mode Grüneisen constant for static pressures up to 72 GPa are summarized in Table 2.1.

Table 2.1 Summary of Pressure Induced Shifts.

$\frac{d\omega_H}{dP}$ (cm^{-1}/GPa)	$\bar{\gamma}$	P (kbar)	Reference
2.83 ± 0.03	0.94 ± 0.1	10	Mitra et al.[16]
3.2 ± 0.2	1.06 ± 0.08	10	Grimsditch et al[15]
3.6 ± 0.3	1.19 ± 0.09	24	Parsons[14]
2.64 ± 0.01	0.90 ± 0.05	150	Tardieu et al.[6]
2.87 ± 0.01	0.95 ±0.03	270	Boppart et al.[5]
2.90 ± 0.05	0.96 ± 0.02	400	Hanfland et al.[17]
3.01 ± 0.01	1.00 ± 0.03	720	Goncharov et al.[15]
3.0 ± 0.3	1.00 ± 0.09	Mean Values and Standard Deviation	

For the experimental values given in Table 2.1, the mean values for the pressure derivative and the mode Grüneisen constant are 3.0 ± 0.3 cm^{-1}/GPa and 1.00 ± 0.09, respectively. Some comments are appropriate regarding the nature of the stress state for the experimental data given in this table.

The investigation performed by Parsons[14] used a solid pressure-transmitting medium. As a rule solids are capable of sustaining shear stress, and even though one may apply isotropic pressure to the medium, it is not clear that the resulting pressure at the sample will be isotropic. At best the pressure measured in this work should be considered an average.

The methanol-ethanol (4:1) mixture used in the study of Tardieu et al.[6] freezes at 104 kbar and the onset of nonhydrostatic conditions has been found to be as low as 50 kbar.[28] Thus, the pressure measured in this study is almost certainly an average value for pressures approaching 150 kbar .

The use of solid xenon as a pressure medium has been recommended for hydrostatic pressures up to 300 kbar.[28] However, Boppart et al.[5] suggested that the observed deviations in their data from expected hydrostatic results at pressures beyond 200 kbar were probably due to nonhydrostaticity in the xenon. This observation casts some doubt on the validity of the measurements of Hanfland et al.[17] and Goncharov et al.,[15] who used solid xenon well beyond 300 kbar. Hanfland et al.[17] states that the uniaxial stress that can be sustained by solid xenon at an average pressure of 400 kbar is less than 10 kbar, but cites no data that would support this claim.

2.2.2 Nonhydrostatic Effects

Studies that have used uniaxial stress or uniaxial strain to investigate the Raman spectrum in diamond are discussed here. Along with the mode Grüneisen constant, these techniques yield additional anharmonic constants that give a direct measure of the deformation potentials,[32] or spring constants,[7] acting within the crystal. The stress state

is well defined for experiments of this type, and hydrostatic behavior may be inferred through the quasi-harmonic model to be presented in Section 2.4.2.

The only uniaxial stress experiments in diamond are those by Grimsditch, Anastassakis and Cardona.[8] They investigated the effect of uniaxial stress loading along [001] and [111] directions on the Raman frequency of diamond to a stress of 10 kbar. Their results for the frequency dependence on pressure and the Grüneisen constant are given in Table 2.1 for comparison with pressure measurements. Compression applied along the [100] and [111] directions in cubic crystals is predicted[13] to partially remove the threefold degeneracy resulting in singlet and doublet lines. Grimsditch et al.,[8] used polarization techniques to identify these lines that otherwise would have been difficult to resolve at such low stresses.

The uniaxial stress study of Grimsditch et al.,[8] yielded measurements for very low stresses. In contrast, shock compression experiments provide a convenient method to examine the response at very large nonhydrostatic stresses. This experimental technique has the added advantage of simplifying the analysis because of the uniaxial strain conditions as shown in Section 2.4.2.

Prior to the results reported in the present study, the only uniaxial strain experiments performed on diamond were those of Gupta et al.[11] Their work was intended primarily to demonstrate the feasibility of performing time-resolved Raman measurements during shock loading. They examined the [110] orientation subjected to a uniaxial strain generated by a 121 kbar longitudinal stress wave. Theoretical predictions suggest that the threefold degeneracy is completely lifted for these conditions. Unfortunately, the temporal and spatial resolution were not sufficient to resolve the individual phonon frequencies, and they detected only a single shifted line with considerable width. Hence, these data do not permit a quantitative analysis.

2.3. POLARIZATION SELECTION RULES AND RAMAN INTENSITIES

The ability to predict the strain-induced frequency response of the Raman spectrum of diamond is accomplished in two stages: First, the selection rules are determined which permit experimental observation of the Raman-active vibrational modes, and second, the frequency response due to the applied strain is determined. The selection rules that address the experimental observability of the Raman lines are discussed here. Emphasis is placed on simple backscatter geometry. Generalization to the quasi-backscatter geometry is deferred until Chapter 5. The microscopic theory that accomplishes the second task is discussed in Section 2.4.2.

The polarization selection rules for Raman scattering have been addressed in the work of Loudon,[33] Herzberg,[34] and many others. Raman scatter may manifest itself through electronic and rotational transitions in addition to pure vibrational transitions. For single crystal first-order Raman studies in diamond, it is the vibrational transitions that are of interest.

When monochromatic laser light is incident on a crystal, the electric field component of the radiation, $\bar{E}$, may induce an electric dipole moment $\bar{\mu}$ in the material. If the net effect is small, the Hamiltonian may be written as

$$H = H_0 + H' \tag{2.4}$$

where H_0 contains terms that describe the crystal energy and the radiation field separately, and $H' = -\sum_i \mu_i \cdot \bar{E}$ is treated as a perturbation to the total energy. The problem of finding transition probabilities, intensities, and crossections is reduced to the problem of finding matrix elements of the induced electric dipole

$$\langle \Psi(r,R) | \bar{\mu} | \Psi'(r,R) \rangle \tag{2.5}$$

where 'r' is the electron position coordinate, and 'R' is the nuclear position coordinate, and $\Psi(r,R)$ is the wavefunction of the combined electronic and nuclear system. In general, the wavefunction $\Psi(r,R)$ is complicated but may be simplified by several assumptions.

Because the nuclei are much heavier than the electrons, they move more slowly. Application of the Born-Oppenheimer approximation[35] allows separate treatment of the electrons and the nuclei in the crystal. A snapshot of the lattice vibration would show the nuclei essentially at rest, surrounded by the electron clouds, in a position that may be removed from the equilibrium position. In this picture, the electrons adjust their configuration to the instantaneous positions of the nuclei, and the effect of the kinetic energy of the nuclei on the electron energies is neglected; this is called the *adiabatic approximation*.[39] Hence, the wavefunction is separable $\Psi(r,R) \Rightarrow \psi_e(r,R)\psi_n(R)$, where $\psi_e(r,R)$ is the electronic wavefunction and $\psi_n(R)$ is the nuclear wavefunction.

Further, if the incident energy is insufficient to cause electronic transitions the wavefunction becomes $\Psi(r,R) \Rightarrow \psi_v(R)$ where $\psi_v(R)$ is the wavefunction for the pure vibrational modes. This is a reasonable assumption for diamond because the band gap is ≈ 6 eV.

Loudon[36] has presented a quantum mechanical treatment of the first-order Raman effect in crystals. He follows the approach of Born and Huang[25] in describing the scattered Raman intensity in terms of the polarizability tensor α_{ij}. This tensor relates the dipole moment and the electric field vectors (first rank tensors). If E_x, E_y, and E_z are the components of the electric vector relative to the cubic axes, the components of $\bar{\mu}$ may be written as

$$\begin{pmatrix} \mu_x \\ \mu_y \\ \mu_z \end{pmatrix} = \begin{bmatrix} \alpha_{xx} & \alpha_{xy} & \alpha_{xz} \\ \alpha_{yx} & \alpha_{yy} & \alpha_{yz} \\ \alpha_{zx} & \alpha_{zy} & \alpha_{zz} \end{bmatrix} \begin{pmatrix} E_x \\ E_y \\ E_z \end{pmatrix} \qquad (2.6)$$

The polarizability is a symmetric tensor so that $\alpha_{xy}=\alpha_{yx}$, $\alpha_{yz}=\alpha_{zy}$, and $\alpha_{xz}=\alpha_{zx}$. Because the polarizability is dependent upon the vibrational motion, it is a function of the position coordinates of the constituent atoms (x_i). If the relative displacements from equilibrium of the two diamond sub-lattices are sufficiently small, the polarizability may be expanded in a Taylor series about the displaced positions[37]

$$\alpha_{ij} = \alpha_{ij}^0 + \sum_k \left(\frac{\partial \alpha_{ij}}{\partial x_k} \right) x_k + \sum_{k,l} \left(\frac{\partial^2 \alpha_{ij}}{\partial x_k \partial x_l} \right) x_k x_l + O(x^3) \qquad (2.7)$$

Thus, determining the nonzero matrix elements in Eq. (2.5) becomes a matter of calculating the polarizability moment

$$\langle \psi_v | \alpha_{ij} | \psi_{v'} \rangle = \alpha_{ij}^0 \delta_{vv'} + \sum_k \left(\frac{\partial \alpha_{ij}}{\partial x_k} \right) \langle \psi_v | x_k | \psi_{v'} \rangle + ... \qquad (2.8)$$

The first term corresponds to Rayleigh or elastic scattering and the second term gives rise to first-order Raman scattering. The expression given by Eq. (2.8) has been truncated to give the harmonic approximation. First-order Raman scattering occurs if $v_k = v_{k'} \pm 1$ <u>and</u> if there is a change in the electronic polarizability[38] given by $\left(\partial \alpha_{ij} / \partial x_k \right)$. The expression for the change in polarizability is commonly called the Raman tensor[33] and is denoted by $R_{ij}(k)$. In practice, it is the nonzero elements of the Raman tensor which are used to calculate the intensity.

The elements of $R_{ij}(k)$ have been tabulated for all 32 crystallographic point groups.[33] Provided in Table 2.2 are the tensor components corresponding to the Raman active vibrations for the cubic crystallographic point groups.[39] The tensors in this table are given with respect to the principal cubic axes {xyz} chosen to be parallel to the [100], [010], [001] crystallographic directions, respectively. For the triply degenerate diamond vibration, the tensors of interest correspond to the F_{2g} representation.

Cubic

$$\begin{vmatrix} a & . & . \\ . & a & . \\ . & . & a \end{vmatrix} \quad \begin{Vmatrix} b+3^{1/2}c & . & . \\ . & b-3^{1/2}c & . \\ . & . & -2b \end{Vmatrix} \begin{vmatrix} c-3^{1/2}b & . & . \\ . & c+3^{1/2}b & . \\ . & . & -2c \end{vmatrix} \quad \begin{Vmatrix} . & . & . \\ . & . & d \\ . & d & . \end{Vmatrix} \begin{Vmatrix} . & . & d \\ . & . & . \\ d & . & . \end{Vmatrix} \begin{Vmatrix} . & d & . \\ d & . & . \\ . & . & . \end{Vmatrix}$$

$Ox, Oy, Oz \parallel$ C_2^x, C_2^y, C_2^z		A	$E,1$	$E,2$	F,x	F,y	F,z
23	$\mathcal{T}$	A	$E,1$	$E,2$	F,x	F,y	F,z
m3	$\mathcal{T}_h$	A_g	$E_g,1$	$E_g,2$	$F_g,1$	$F_g,2$	$F_g,3$

$$\begin{vmatrix} b & . & . \\ . & b & . \\ . & . & -2b \end{vmatrix} \quad \begin{vmatrix} -3^{1/2}b & . & . \\ . & 3^{1/2}b & . \\ . & . & 0 \end{vmatrix}$$

Ox, Oy, Oz or S_4		A_1	$E,1$	$E,2$	F_2,x	F_2,y	F_2,z
432	O	A_1	$E,1$	$E,2$	$F_2,1$	$F_2,2$	$F_2,3$
$\bar{4}3m$	$\mathcal{T}_d$	A_1	$E,1$	$E,2$	F_2,x	F_2,y	F_2,z
m3m	O_h	A_{1g}	$E_g,1$	$E_g,2$	$F_{2g},1$	$F_{2g},2$	$F_{2g},3$

Table 2.3 Raman Tensors for the Cubic Crystallographic Point Groups.

The intensity of a Raman line is proportional to the square of the product of the incident and scattered polarizations with the Raman tensor[33]

$$I = A \sum_n \left| \sum_{\rho,\sigma} e_\rho^i R_{\rho\sigma}(n) e_\sigma^s \right|^2 \qquad (2.9)$$

where e_ρ^i is the incident polarization, e_σ^s is the scattered polarization, $R_{\rho\sigma}(n)$ is the $\rho\sigma$ component of the nth Raman scattering tensor, and A is a constant of proportionality. The importance of polarization for Raman scattering experiments is implicit in Eq. (2.9). By altering the incident and scattered polarization, the experimenter may select different Raman tensor components. This selection process may be exploited to suppress certain vibrations and enhance others to facilitate experimental observations.

2.3.1 Calculation of Ambient Intensities: Backscattering

To demonstrate the use of Eq. (2.9), the relative intensities for the ambient spectrum of diamond will be calculated for the backscattering geometry along the [100] and [110] directions. The calculations that follow are applications of the method outlined by Loudon.[33] The present experiments deviated from the pure backscatter geometry and these deviations will be addressed in Chapter 5.

Note that the material properties for cubic materials, such as the elastic constants, are defined for the principal cubic axes {[100],[010],[001]}. To be consistent with the developments in Section 2.4.2, where all shifted frequency results are formulated with respect to the principal cubic axes, it is important that the relationship between the principal crystallographic and laboratory axes be known. For the case of [100] backscatter this is straight forward but for [110] backscatter care needs to be exercised.

Raman Intensity for [100] Backscatter Geometry

The laboratory coordinate system denoted by upper-case (X,Y,Z) is shown in Figure 2.7 (a). This coordinate system has been defined so that the positive X direction points down the barrel of the gas gun. During an actual experiment, the projectile travels up the barrel in the -X direction. In Figure 2.7 (a), the diamond crystal is represented by a cube with its principal crystallographic directions {[100],[010],[001]} oriented in such a manner that the crystallographic system is coincident with the laboratory axes {X,Y,Z}.

The backscatter geometry is pictured below in Figure 2.7 (a). In a pure backscatter configuration, the incident radiation with wave vector $\mathbf{k}^i$ propagates along the positive X direction, and the scattered radiation with wave vector $\mathbf{k}^s$ is detected along the -X direction. For scattering parallel to the XZ plane, Eq. (2.9) gives:

$$I_{\parallel} = A\sum_n \left| e_Y^i R_{YZ}(n)e_Z^s + e_Z^i R_{ZZ}(n)e_Z^s \right|^2 \tag{2.10}$$

and for scattering perpendicular to the XZ plane

$$I_{\perp} = A\sum_n \left| e_Y^i R_{YY}(n)e_Y^s + e_Z^i R_{ZY}(n)e_Y^s \right|^2 \tag{2.11}$$

Note that all parameters are to be interpreted in the laboratory frame in which the measurements are made.

As will be discussed in Section 2.4.1, the F_{2g} irreducible representation of O_h is the only Raman-active phonon mode and is triply degenerate under ambient conditions (no external forces). Inspection of Table 2.2 gives the Raman tensors for the representation

$$\begin{bmatrix} 0 & 0 & 0 \\ 0 & 0 & d \\ 0 & d & 0 \end{bmatrix} , \begin{bmatrix} 0 & 0 & d \\ 0 & 0 & 0 \\ d & 0 & 0 \end{bmatrix} , \begin{bmatrix} 0 & d & 0 \\ d & 0 & 0 \\ 0 & 0 & 0 \end{bmatrix} \tag{2.12}$$

$$F_{2g}(1) \qquad\qquad F_{2g}(2) \qquad\qquad F_{2g}(3)$$
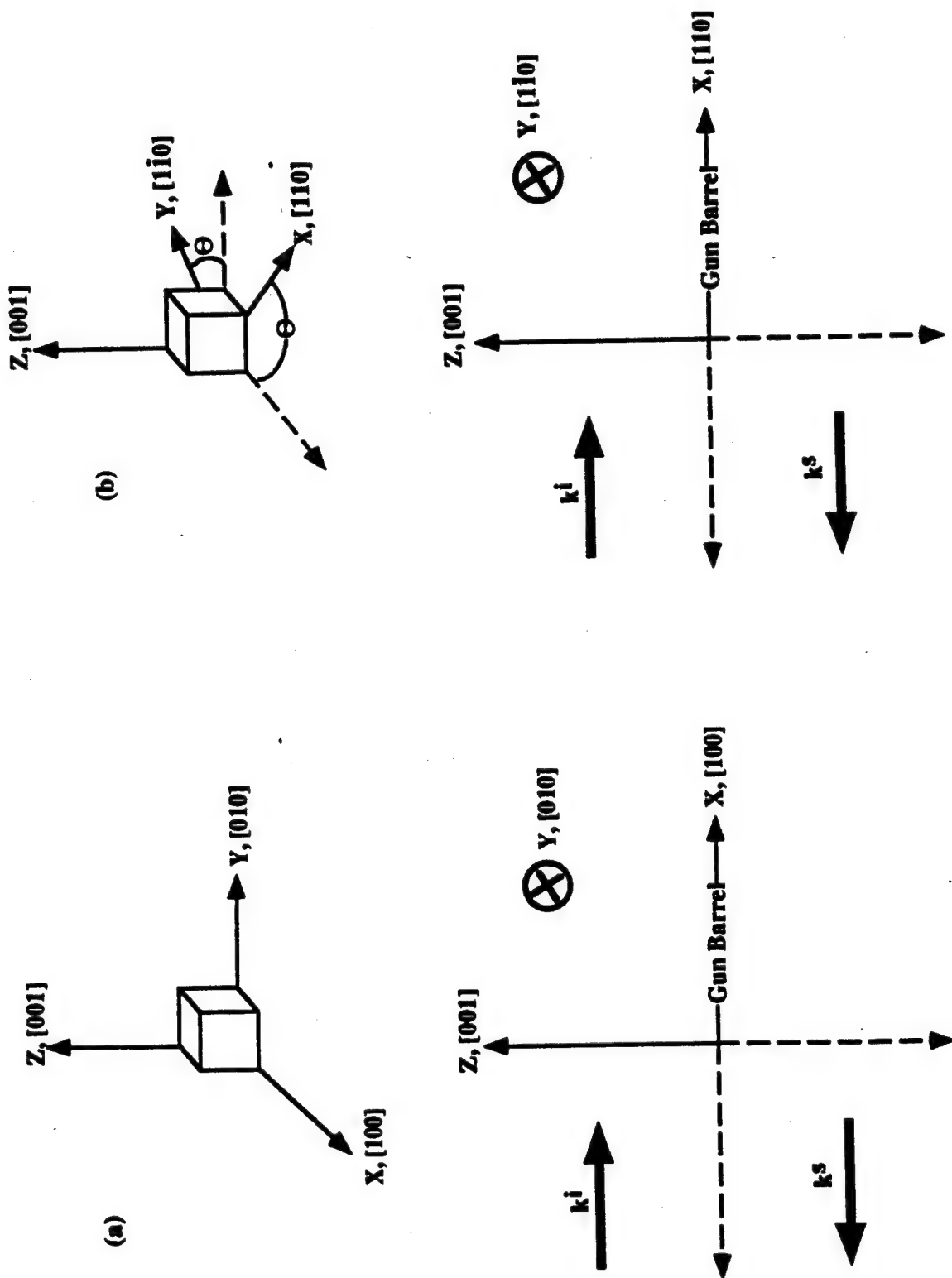
Figure 2.7 (a) [100] Backscatter Geometry, (b) [110] Backscatter Geometry.

By inspection the only nonvanishing components of the Raman tensor are

$$R_{YZ}(1) = R_{ZY}(1) = R_{XZ}(2) = R_{ZX}(2) = R_{XY}(3) = R_{YX}(3) = d$$

Substituting into Eq. (2.10) and Eq. (2.11), and noting that for incident light that is natural (unpolarized) the total scattered intensity is the sum of the parallel and perpendicular components,[40] gives

$$I_{total} = I_{\parallel} + I_{\perp} = 2Ad^2 \tag{2.13}$$

Raman Intensity for [110] Backscatter Geometry

The relative orientation of the laboratory system {XYZ} with respect to the orthogonal crystallographic system {[110],[1$\bar{1}$0],[001]} is shown in Figure 2.7 (b). The discussion of backscatter for the [110] geometry is complicated by the fact that the Raman tensors given in Table 2.2 for the F_{2g} representation are defined with respect to the principal crystallographic directions.

In the following discussion, the principal crystallographic directions {[100],[010],[001]} are designated by lower case {xyz}, respectively. For [110] backscatter, the crystallographic system {[110],[1$\bar{1}$0],[001]} corresponds to {x'y'z'}, respectively. The transformation matrix between these two systems is given by

$$\begin{pmatrix} x' \\ y' \\ z' \end{pmatrix} = \begin{pmatrix} \cos\theta & \sin\theta & 0 \\ -\sin\theta & \cos\theta & 0 \\ 0 & 0 & 1 \end{pmatrix} \begin{pmatrix} x \\ y \\ z \end{pmatrix} \tag{2.14}$$

In tensor notation, Eq. (2.14) takes on a compact form

$$x_i' = a_{ij} x_j \tag{2.15}$$

where a_{ij} is the ij[th] element of the transformation matrix a and

$$a = \frac{1}{\sqrt{2}} \begin{pmatrix} 1 & 1 & 0 \\ -1 & 1 & 0 \\ 0 & 0 & \sqrt{2} \end{pmatrix} \qquad (2.16)$$

The Raman tensors given in Table 2.2 are given with respect to the {xyz} directions; it is first necessary to find the polarizability tensor along the new directions {x'y'z'}. Because the polarizability is a second rank tensor, the transformation is

$$\alpha'_{ij}(n) = a_{ik} a_{jl} \alpha_{kl}(n) \qquad (2.17)$$

Expanding Eq. (2.17) and evaluating the resulting transformation matrix elements yields the following set of relationships between the old and new polarizability tensors,

$$\left. \begin{aligned} \alpha'_{xx}(n) &= \frac{1}{2}\alpha_{xx}(n) + \alpha_{xy}(n) + \frac{1}{2}\alpha_{yy}(n) \\ \alpha'_{yy}(n) &= \frac{1}{2}\alpha_{xx}(n) - \alpha_{xy}(n) + \frac{1}{2}\alpha_{yy}(n) \\ \alpha'_{zz}(n) &= \alpha_{zz}(n) \\ \alpha'_{xy}(n) &= \alpha'_{yx}(n) = -\frac{1}{2}\alpha_{xx}(n) + \frac{1}{2}\alpha_{yy}(n) \\ \alpha'_{xz}(n) &= \alpha'_{zx}(n) = \frac{1}{\sqrt{2}}\alpha_{xz}(n) + \frac{1}{\sqrt{2}}\alpha_{yz}(n) \\ \alpha'_{yz}(n) &= \alpha'_{zy}(n) = -\frac{1}{\sqrt{2}}\alpha_{xz}(n) + \frac{1}{\sqrt{2}}\alpha_{yz}(n) \end{aligned} \right\} \qquad (2.18)$$

The Raman tensor in the primed frame is the change in the polarizability with respect to the displacement of the diamond sublattices. The phonon polarizations in the primed frame are given by

$$\frac{1}{\sqrt{2}}\begin{bmatrix} 1 \\ 1 \\ 0 \end{bmatrix} , \quad \frac{1}{\sqrt{2}}\begin{bmatrix} 1 \\ \bar{1} \\ 0 \end{bmatrix} , \quad \begin{bmatrix} 0 \\ 0 \\ 1 \end{bmatrix} \qquad (2.19a)$$

A–36

When uniaxial strain is applied along the [110] direction we will be interested in calculating the intensity for the phonon polarizations given by Eq. (2.19a). The three Raman tensors are found to be

$$
\begin{bmatrix} 0 & 0 & d \\ 0 & 0 & 0 \\ d & 0 & 0 \end{bmatrix} \, , \quad \begin{bmatrix} 0 & 0 & 0 \\ 0 & 0 & -d \\ 0 & -d & 0 \end{bmatrix} \, , \quad \begin{bmatrix} d & 0 & 0 \\ 0 & -d & 0 \\ 0 & 0 & 0 \end{bmatrix} \qquad (2.19b)
$$

$$
F_{2g}(1) \qquad\qquad F_{2g}(2) \qquad\qquad F_{2g}(3)
$$

By examination, the only nonvanishing tensor elements are:

$$
R'_{XZ}(1) = R'_{ZX}(1) = d
$$
$$
R'_{YZ}(2) = R'_{ZY}(2) = -d
$$
$$
R'_{XX}(3) = d, \quad R'_{YY}(3) = -d
$$

Substitution of these tensor elements into Eqs. (2.10) and (2.11) yields the total intensity for this scattering geometry

$$
I_{total} = I_{\parallel} + I_{\perp} = Ad^2 + 2Ad^2 = 3Ad^2 \qquad (2.20)
$$

Comparison of Eqs. (2.13) and (2.20) reveals that Raman scattering is anisotropic in diamond; in fact, Raman scattering is anisotropic in all cubic materials.[41]

The tensors of Eq. (2.19b) are identical with those found by Anastassakis[43] for the same orientation. It may be noted that the tensors found for this scattering geometry may be reached in a less circuitous manner by using the zeroth-order eigenfunctions (found in Section 2.4.2) to determine their form.

2.3.2 Strain Effects on Intensity

The foregoing discussion is applicable to the unstrained case only. In addition to the splitting of the degenerate F_{2g} representation, the application of uniaxial strain can cause intensity changes and may allow some previous vanishing matrix elements to have nonzero values. To first-order in the applied strain, the Raman tensor becomes:[42,43]

$$R_{\alpha\beta} = R_{\alpha\beta}^0 + R_{\alpha\beta,\delta\gamma}\eta_{\delta\gamma} \tag{2.21}$$

where $R_{\alpha\beta}^0$ is the zeroth-order Raman tensor and

$$R_{\alpha\beta,\delta\gamma} = \frac{1}{2}\left(\frac{dR_{\alpha\beta}}{d\eta_{\delta\gamma}}\right) \tag{2.22}$$

Thus, the strain induced changes in the Raman scattering tensor are approximately linear in the strain and for small strain, $R_{\alpha\beta,\delta\gamma}\eta_{\delta\gamma} \ll R_{\alpha\beta}^0$, the effect is vanishingly small.

Anastassakis and Burstein[43] have derived the tensor contributions corresponding to Eq. (2.22). They show that the action of an external strain may be described by five independent components (b,c,d,e,f). These components essentially describe the admixture of irreducible representations caused by the strain. To avoid confusion with notation already developed here, these components are replaced by (e,f,g,h,i). For uniaxial strain along the [100] direction, the resultant Raman tensors are:

$$\begin{pmatrix} 0 & 0 & 0 \\ 0 & 0 & d+\eta_{xx}e \\ 0 & d+\eta_{xx}e & 0 \end{pmatrix}, \quad \begin{pmatrix} 0 & 0 & d+\eta_{xx}g \\ 0 & 0 & 0 \\ d+\eta_{xx}g & 0 & 0 \end{pmatrix}, \quad \begin{pmatrix} 0 & d+\eta_{xx}g & 0 \\ d+\eta_{xx}g & 0 & 0 \\ 0 & 0 & 0 \end{pmatrix} \tag{2.23a}$$

$$(B_{2g}) \qquad\qquad\qquad (E_g) \qquad\qquad\qquad (E_g)$$

Comparison with Eq. (2.12) indicates that the polarization selection rules do not change because these tensors have nonzero values in the same locations as the unstrained tensors.[43] The observed intensity may change, however, due to the additional strain dependent term.

For uniaxial strain along the [110] direction, the situation is more complicated. For this strain $\eta_{xx} = \eta_{yy} = \eta_{xy} = \eta_{yx} = \eta/2$ and Eq. (2.21) yields

$$
\left.
\begin{array}{ll}
B_{2s} & \begin{pmatrix} 0 & 0 & \left[d+\dfrac{\eta}{2}(e+g+i)\right] \\ 0 & 0 & 0 \\ \left[d+\dfrac{\eta}{2}(e+g+i)\right] & 0 & 0 \end{pmatrix} \\[4em]
B_{3s} & \begin{pmatrix} 0 & 0 & 0 \\ 0 & 0 & -\left[d+\dfrac{\eta}{2}(e+g-i)\right] \\ 0 & -\left[d+\dfrac{\eta}{2}(e+g-i)\right] & 0 \end{pmatrix} \\[4em]
A_{1s} & \begin{pmatrix} d+\dfrac{\eta}{2}(2g+h) & 0 & 0 \\ 0 & -\left[d+\dfrac{\eta}{2}(2g-h)\right] & 0 \\ 0 & 0 & \dfrac{\eta}{2}f \end{pmatrix}
\end{array}
\right\}
\qquad (2.23b)
$$

Eq. (2.23b) may be compared to the ambient tensors give by Eq. (2.19). As in the previous case of [100] uniaxial strain, the observed intensities may differ somewhat from the ambient values. In addition, there is now a tensor element $\left(\dfrac{\eta}{2}f\right)$ that has a nonzero value. This new element can influence the polarization selection rules allowing additional contributions to the observed mode intensities. In the limit of vanishing strain, Eq. (2.23) reduces to the zero-strain tensors of Eq. (2.19).

From Eq. (2.9) it is seen that the measured intensity is proportional to the square of the Raman tensor element for a given mode:

$$I \propto R_{\alpha\beta}^2 \equiv \left(R_{\alpha\beta}^0\right)^2 + 2R_{\alpha\beta}^0 \cdot R_{\alpha\beta,\delta\gamma}\eta_{\delta\gamma} \qquad (2.24)$$

The observed change in the intensity due to the applied strain is proportional to $\Delta I \propto 2R_{\alpha\beta}^0 \cdot R_{\alpha\beta,\delta\gamma}\eta_{\delta\gamma}$. In principle, by observing the fractional change in intensity, it is possible to assign a value for $R_{\alpha\beta,\delta\gamma}$. Anastassakis and Burstein[43] found this effect to account for roughly 1 part in 10^8 of the intensity.

For the work reported here, intensity fluctuations on the order of 10-15 % were not uncommon in the recorded spectrum, but these were due to fluctuations in the laser intensity and were present even in the ambient spectrum. Thus, any contribution to the intensity due to $R_{\alpha\beta,\delta\gamma}$ was not expected to be observed. To summarize, for the present work the observed intensity is considered to be adequately described by the square of the zero-strain Raman tensor.

2.4 STRAIN INDUCED FREQUENCY SHIFTS

To examine strain-induced frequency shifts, two approaches are considered here. In the first approach, the group-correlation method is applied to the diamond point group to arrive at the new point group symmetry of the strained lattice. This method predicts the resulting irreducible representations of the group and their respective degeneracy. In the second approach, a microscopic theory is described which permits the calculation of the frequency shifts as well as the degeneracy. Note that the second approach presupposes that the vibrational spectrum is Raman-active.

In the analysis presented in Chapter 5, the quasi-harmonic model given in the second approach (Section 2.4.2) is used exclusively.

2.4.1 Qualitative Predictions For Splittings: The Correlation Method

One of the fundamental postulates in crystal physics is Neumann's Principle:[44] *The symmetry elements of any physical property of a crystal must include the symmetry elements of the point group of the crystal.* When the crystal lattice is elastically deformed

by a homogeneous strain, it forms a new symmetry that contains the symmetry elements common to the unstrained crystal and the strain itself.[45] The collection of symmetry elements such as rotation, reflection, etc., which leave the crystal invariant, form the point group of the crystal, and the arrangement of these symmetry elements within a Bravais lattice, form the space group. For diamond, the point group is O_h and the space group is O_h^7.

Diamond possesses ten symmetry operations, which are contained in the full octahedral point group O_h, and each has a specific number of elements. For example, a $\pi/2$ rotation about the normal to a cube face (C_4) will leave the cube unchanged (invariant) and because there are six cube faces, there are six elements for this symmetry operation.

For the O_h point group, there are 48 symmetry elements that comprise the order of the group (h). Corresponding to each symmetry operation, is a set of orthogonal matrices which represent the group operationally. These matrices are of dimension l_i and the dimensionality theorem requires that they obey the relation,[46]

$$\sum_{i=1}^{10} l_i^2 = h$$

There is only one unique solution and it is given by

$$1^2 + 1^2 + 1^2 + 1^2 + 2^2 + 2^2 + 3^2 + 3^2 + 3^2 + 3^2 = 48$$

Hence, there are four 1-dimensional, two 2-dimensional, and four 3-dimensional mutually orthogonal matrices termed the *irreducible representations* of the group.

The symmetry operations and irreducible representations for a point group are conveniently displayed in a compact form called a character table. The entries in the table are *characters* that are normally symbolized by χ and are equal to the sum of the diagonal matrix elements. The character table[47] for O_h is given in Table 2.3. Listed across the top are the symmetry operations and their respective number of elements, and in the leftmost

Table 2.3 Character Table For Cubic O_h (Ref. 49).

Symmetry elements
$I, 8C_3, 6C_2, 6C_4, 3C_4^2, i, 6S_4, 8S_6, 3\sigma_h, 6\sigma_d$

Symmetry types and characters

O_h	I	$8C_3$	$6C_2$	$6C_4$	$3C_4^2$	i	$6S_4$	$8S_6$	$3\sigma_h$	$6\sigma_d$		
A_{1g}	1	1	1	1	1	1	1	1	1	1		$\alpha_{xx}+\alpha_{yy}+\alpha_{zz}$
A_{1u}	1	1	1	1	1	-1	-1	-1	-1	-1		
A_{2g}	1	1	-1	-1	1	1	-1	1	1	-1		
A_{2u}	1	1	-1	-1	1	-1	1	-1	-1	1		
E_g	2	-1	0	0	2	2	0	-1	2	0		$(\alpha_{xx}+\alpha_{yy}-2\alpha_{zz}, \alpha_{xx}-\alpha_{yy})$
E_u	2	-1	0	0	2	-2	0	1	-2	0		
F_{1g}	3	0	-1	1	-1	3	1	0	-1	-1	R_x, R_y, R_z	
F_{1u}	3	0	-1	1	-1	-3	-1	0	1	1	T_x, T_y, T_z	
F_{2g}	3	0	1	-1	-1	3	-1	0	-1	1		$(\alpha_{xy}, \alpha_{yz}, \alpha_{xz})$
F_{2u}	3	0	1	-1	-1	-3	1	0	1	-1		

A-42

column are listed the irreducible representations. In the notation used here, the A, E, and F refer to 1,2, and 3-dimensional representations, respectively. The g and u subscripts indicate even or odd parity, respectively. In the second to last column the Rs and Ts are the normal coordinates for rotations and translations and are placed in the row whose representation they conform to. The last column lists the polarizability tensor components, α_{ij}, in the row corresponding to their irreducible representation.

One can determine the optical transitions using the table because only representations that contain translation elements will be infrared active, and only those representations containing a tensor element of α_{ij} will be Raman active. Thus, only the A_{1g}, E_g, and F_{2g} irreducible representations are Raman active. Of these, only the F_{2g} representation is three dimensional and can, therefore, represent the triply degenerate normal mode vibration.

In general, the application of a uniaxial strain will lower the point group symmetry of the crystal. Uniaxial strain cannot raise the symmetry because its action serves to remove some of the symmetry operations of the original crystal. In the new symmetry, the representation F_{2g} may or may not be irreducible.

The correlation method[48] relates the site symmetry of each atom in the strain-free lattice to the symmetry of the same atom in the strained configuration. The representations may be compared in a group correlation table[48] shown in Table2.4. Here, the factor group is considered to be that of the unstrained lattice (in the present case O_h).

The space group reduction scheme of Peiser et al.[45] shows that for the space group O_h^7, the site symmetry becomes D_{4h} for strain along [100], D_{2h} for strain along [110], and D_{3d} for strain along [111]. Examination of the correlation table in Table 2.4 for these point groups reveals that the F_{2g} irreducible representation splits into a singlet and a doublet for the D_{4h} and D_{3d} point groups, and three singlets for D_{2h}. These results are summarized in Table 2.5..

Table 2.4 Correlation Table For O_h and Its Subgroups (Ref. 48).

O_h	O	T_d	T_h	T	D_{2d}	D_{3d}	$C_{\infty v}$	D_3	$C_{3i}=S_6$
A_{1g}	A_1	A_1	A_g	A	A_{1g}	A_{1g}	A_1	A_1	A_g
A_{2g}	A_2	A_1	A_g	A	A_{2g}	B_{1g}	A_2	A_2	A_g
E_g	E	E	E_g	E	E_g	$A_{1g}+B_{1g}$	A_1+B_1	A_1+E	E_g
F_{1g}	F_1	F_1	F_g	F	$A_{2g}+E_g$	$A_{2g}+E_g$	A_1+E	A_1+E	A_g+E_g
F_{2g}	F_2	F_2	F_g	F	$A_{1g}+E_g$	$B_{2g}+E_g$	A_2+E	A_1+E	A_g+E_g
A_{1u}	A_1	A_1	A_u	A	A_{1u}	A_{1u}	A_1	A_1	A_u
A_{2u}	A_2	A_1	A_u	A	A_{2u}	B_{1u}	A_2	A_2	A_u
E_u	E	E	E_u	E	E_u	$A_{1u}+B_{1u}$	A_1+B_1	A_1+E	E_u
F_{1u}	F_1	F_2	F_u	F	$A_{2u}+E_u$	$A_{2u}+E_u$	A_1+E	A_1+E	A_u+E_u
F_{2u}	F_2	F_1	F_u	F	$A_{1u}+E_u$	$B_{2u}+E_u$	A_2+E	A_1+E	A_u+E_u

O_h	C_3	C_2,σ_d / D_{2d}	C_2,σ_h / D_{2h}	$C_{\infty v}$	D_4	C_{4h}	S_4	C_4
A_{1g}	A	A_1	A_1	A_1	A_1	A_g	A	A
A_{2g}	A	B_1	B_1	B_1	B_1	B_g	B	B
E_g	E	A_1+B_1	A_1+B_2	A_1+B_2	A_1+B_1	A_g+B_g	$A+B$	$A+B$
F_{1g}	$A+E$	A_2+E	A_2+E	A_2+E	A_2+E	A_g+E_g	$A+E$	$A+E$
F_{2g}	$A+E$	B_2+E	B_1+E	B_1+E	B_2+E_g	B_g+E_g	$B+E$	$B+E$
A_{1u}	A	B_1	B_1	A_1	A_1	A_u	B	A
A_{2u}	A	A_1	A_1	B_1	B_1	B_u	A	B
E_u	E	A_1+B_1	A_1+B_1	A_1+B_2	A_1+B_2	A_u+B_u	$A+B$	$A+B$
F_{1u}	$A+E$	B_2+E	B_1+E	A_2+E	A_2+E	A_u+E_u	$B+E$	$B+E$
F_{2u}	$A+E$	A_2+E	A_1+E	B_1+E	B_2+E_u	$A+E$	$B+E$

O_h	$3C_2$ / D_{2h}	$C_2,2C_2'$ / D_{2h}	C_2,σ_h / C_{2v}	C_2,σ_d / C_{2v}	C_2,σ_h / C_{2v}	$3C_2$ / D_2	$C_2,2C_2'$ / D_2
A_{1g}	A_g	A_g	A_1	A_1	B_1	A	A
A_{2g}	A_g	B_{1g}	A_1	A_2	A_1	A	B_1
E_g	$2A_g$	A_g+B_{1g}	$2A_1$	A_1+A_2	A_1+B_1	$2A$	$A+B_1$
F_{1g}	$B_{1g}+B_{2g}+B_{3g}$	$B_{1g}+B_{2g}+B_{3g}$	$A_2+B_1+B_2$	$A_2+B_1+B_2$	$A_2+B_1+B_2$	$B_1+B_2+B_3$	$B_1+B_2+B_3$
F_{2g}	$B_{1g}+B_{2g}+B_{3g}$	$A_g+B_{2g}+B_{3g}$	$A_1+B_1+B_2$	$A_1+B_1+B_2$	$A_1+A_2+B_2$	$B_1+B_2+B_3$	$A+B_2+B_3$
A_{1u}	A_u	A_u	A_2	A_2	B_2	A	A
A_{2u}	A_u	B_{1u}	A_2	A_1	A_2	A	B_1
E_u	$2A_u$	A_u+B_{1u}	$2A_2$	A_1+A_2	A_2+B_2	$2A$	$A+B_1$
F_{1u}	$B_{1u}+B_{2u}+B_{3u}$	$B_{1u}+B_{2u}+B_{3u}$	$A_1+B_1+B_2$	$A_1+B_1+B_2$	$A_1+B_1+B_2$	$B_1+B_2+B_3$	$B_1+B_2+B_3$
F_{2u}	$B_{1u}+B_{2u}+B_{3u}$	$A_u+B_{2u}+B_{3u}$	$A_1+B_1+B_2$	$A_1+B_1+B_2$	$A_1+A_2+B_2$	$B_1+B_2+B_3$	$A+B_2+B_3$

O_h	C_2,σ_h / C_{2h}	C_2',σ_h / C_{2h}	σ_h / C_s	σ_d / C_s	C_2 / C_2	C_2' / C_2	C_i	C_1
A_{1g}	A_g	A_g	A'	A'	A	A	A_g	A
A_{2g}	A_g	B_g	A'	A''	A	B	A_g	A
E_g	$2A_g$	A_g+B_g	$2A'$	$A'+A''$	$2A$	$A+B$	$2A_g$	$2A$
F_{1g}	A_g+2B_g	A_g+2B_g	$A'+2A''$	$A'+2A''$	$A+2B$	$2A+B$	$3A_g$	$3A$
F_{2g}	A_g+2B_g	$2A_g+B_g$	$A'+2A''$	$2A'+A''$	$A+2B$	$2A+B$	$3A_g$	$3A$
A_{1u}	A_u	A_u	A''	A''	A	A	A_u	A
A_{2u}	A_u	B_u	A''	A'	A	B	A_u	A
E_u	$2A_u$	A_u+B_u	$2A''$	$A'+A''$	$2A$	$A+B$	$2A_u$	$2A$
F_{1u}	A_u+2B_u	A_u+2B_u	$2A'+A''$	$2A'+A''$	$A+2B$	$2A+B$	$3A_u$	$3A$
F_{2u}	A_u+2B_u	$2A_u+B_u$	$2A'+A''$	$A'+2A''$	$A+2B$	$2A+B$	$3A_u$	$3A$

Table 2.5 Strain Induced Point Groups.

Direction of compression	New point group symmetry	$\vec{F} = 0$	$\vec{F} \neq 0$
[100]	D_{4h}	$F_{2g}(3)$	$B_{2g}(1)$ $E_g(2)$
[111]	D_{3d}	$F_{2g}(3)$	$A_{1g}(1)$ $E_g(2)$
[110]	D_{2h}	$F_{2g}(3)$	$A_{1g}(1)$ $B_{2g}(1)$ $B_{3g}(1)$

In Section 2.1.2 it was found that compression along [100] lowered the symmetry to tetragonal and partially removed the degeneracy. Table 2.5 shows that the specific point group within the tetragonal system is D_{4h}, and the irreducible representations for the singlet and doublet are $B_{2g}(1)$ and $E_g(2)$, respectively. Similar statements may be made for [110] and [111] compressions. Although only qualitative information has been gained by the application of group theory, it is gratifying that the results confirm the earlier more intuitive observations.

2.4.2 Calculation of the Strain Induced Frequency Shifts

The group correlation method considered in the previous section provides purely qualitative information. To determine the cause and magnitude of the strain-induced frequency shifts, a microscopic approach is taken.

The diamond lattice dynamics will first be discussed for the unstrained (ambient) condition.

Expansion for the Crystal Potential [25]

As discussed in Section 2.1.1, the primitive basis for the diamond structure is composed of two atoms that are repeated throughout the crystal. In general, the position vector that identifies a particular atom in a lattice composed of l unit cells with k atoms in each cell is given by

$$x(lk) = x(l) + x(k) \qquad (2.24)$$

where $x(l)$ is the distance to the lth cell and $x(k)$ is the position of the kth atom in this cell. Each atom in the crystal possesses a kinetic energy due to its vibration about its mean position. The collective sum of all such energies gives the total kinetic energy of the crystal

$$T = \sum_{lk\alpha} \frac{p_\alpha^2(lk)}{2M_k} \qquad (2.25)$$

where p_α is the α component of the momentum of the kth atom in the lth cell; the kth atom has a mass M_k.

The crystal potential energy may be considered as a function of the positions of the constituent atoms as they oscillate about their rest positions. Choosing $u_\alpha(lk)$ to be the α component of one such atomic displacement from its equilibrium position $X_\alpha(lk)$, the crystal potential may be expanded in a Taylor series summed over all such displacements

$$\Phi = \Phi_0 + \sum_{lk\alpha} \Phi_\alpha(lk) u_\alpha(lk) + \frac{1}{2} \sum_{lk\alpha} \sum_{l'k'\beta} \Phi_{\alpha\beta}(lk; l'k') u_\alpha(lk) u_\beta(l'k')$$
$$+ \frac{1}{6} \sum_{lk\alpha} \sum_{l'k'\beta} \sum_{l''k''\gamma} \Phi_{\alpha\beta\gamma}(lk; l'k'; l''k'') u_\alpha(lk) u_\beta(l'k') u_\gamma(l''k'') + \dots \qquad (2.26)$$

Where Φ_0 is the crystal potential when all atoms are at their rest positions and

$$\left.\begin{aligned}
\Phi_\alpha(lk) &= \frac{\partial \Phi}{\partial u_\alpha(lk)}\bigg|_0 \\[2mm]
\Phi_{\alpha\beta}(lk;l'k') &= \frac{\partial^2 \Phi}{\partial u_\alpha(lk)\partial u_\beta(l'k')}\bigg|_0 \\[2mm]
\Phi_{\alpha\beta\gamma}(lk;l'k';l''k'') &= \frac{\partial^3 \Phi}{\partial u_\alpha(lk)\partial u_\beta(l'k')\partial u_\gamma(l''k'')}\bigg|_0
\end{aligned}\right\} \qquad (2.27)$$

The derivatives are evaluated at the atomic rest positions. $\Phi_\alpha, \Phi_{\alpha\beta},$ and $\Phi_{\alpha\beta\gamma}$ represent the interactions between individual atoms and are often called the *atomic force constants*. For example, $\Phi_{\alpha\beta}(lk;l'k')$ represents a negative force on atom (lk) in the α direction due to the displacement of atom $(l'k')$ in the β direction.

The Hamiltonian for the crystal system may be partitioned into harmonic and anharmonic contributions, thus

$$H = H_0 + H_{anharmonic} \qquad (2.28)$$

where

$$H_0 = \sum_{lk\alpha} \frac{p_\alpha^2(lk)}{2M_k} + \frac{1}{2}\sum_{lk\alpha}\sum_{l'k'\beta} \Phi_{\alpha\beta}(lk;l'k')u_\alpha(lk)u_\beta(l'k') \qquad (2.29)$$

and

$$H_{anharmonic} = \frac{1}{6}\sum_{lk\alpha}\sum_{l'k'\beta}\sum_{l''k''\gamma} \Phi_{\alpha\beta\gamma}(lk;l'k';l''k'')u_\alpha(lk)u_\beta(l'k')u_\gamma(l''k'') + \dots \qquad (2.30)$$

At this stage, the exact solutions to H_0 are typically calculated, and the perturbation due to $H_{anharmonic}$ is considered.

The expansion of the crystal potential given by Eq. (2.26) is based upon the displacements of the atoms from their equilibrium positions. For the application of strain, the atoms may be considered to be at rest positions removed from the static equilibrium

positions.[13,49] To study the effect of applied strain on the frequency spectrum, the crystal potential is expanded in powers of the differences in these displacements.

Application of Strain to the Crystal Potential

Following Ganesan et al.,[13] the crystal expansion is performed in terms of the new equilibrium positions, $\xi_\alpha(lk)$, resulting from application of the strain. They are defined by

$$\xi_\alpha(lk) = \sum_\beta \eta_{\alpha\beta} X_\beta(lk) + d_\alpha(lk) + u_\alpha(lk) \tag{2.31}$$

where the first term describes the effect of the deformation on the unstrained equilibrium position $X(lk)$, $d_\alpha(lk)$ describes any resulting shift of the sub-lattices, and $u_\alpha(lk)$ is the displacement of the atom from its new equilibrium position. Also, $\eta_{\alpha\beta}$ is the Lagrangian strain defined to be negative in compression.

The expansion is the same as for Eq. (2.26). Designating the new potential as $\hat{\Phi}$, the vibrational Hamiltonian may be written in the harmonic approximation as

$$H_{vib} = \sum_{lk\alpha} \frac{p_\alpha^2(lk)}{2M_k} + \frac{1}{2} \sum_{lk\alpha} \sum_{l'k'\beta} \hat{\Phi}_{\alpha\beta}(lk;l'k') u_\alpha(lk) u_\beta(l'k') \tag{2.32}$$

From Hamilton's equations, the equation of motion for the strained crystal may be determined

$$\dot{u}_\alpha = \frac{\partial H_{vib}}{\partial p_\alpha(lk)}; \quad and, \quad \dot{p}_\alpha = -\frac{\partial H_{vib}}{\partial u_\alpha(lk)} \tag{2.33}$$

$$\therefore \quad M_k \ddot{u}_\alpha = -\sum \hat{\Phi}_{\alpha\beta}(lk;l'k') u_\beta(l'k') \tag{2.34}$$

The normal mode solutions of Eq. (2.34) are assumed to be of the form

$$u_\alpha(lk) = \frac{1}{\sqrt{M_k}} \chi_\alpha(k) \exp[i\mathbf{k} \cdot \mathbf{x}(l) - i\omega t] \tag{2.35}$$

Using Eq. (2.35), the equation of motion becomes

$$\omega^2 \chi_\alpha(k) = \sum_{k'\beta} D_{\alpha\beta}(kk'|\mathbf{k})\chi_\beta(k') \qquad (2.36)$$

where

$$D_{\alpha\beta}(kk'|\mathbf{k}) = \frac{1}{\sqrt{M_k M_{k'}}} \sum_{l'} \hat{\Phi}(lk;l'k')e^{i\mathbf{k}\cdot\{\mathbf{x}(l)-\mathbf{x}(l')\}} \qquad (2.37)$$

defines the *Dynamical Matrix*. The square-root values of the dynamical matrix eigenvalues yield the allowed normal mode frequencies.

Ganesan et al.[13] pointed out that the solutions of (2.36) describe the motion for the displacements of individual atoms. By uncoupling the center of mass motion from the relative displacement between the two atoms comprising a primitive cell, the relative motion of the two sub-lattices for the diamond structure can be determined.

Denoting the new displacement coordinates by $\zeta_\alpha(l)$, Eq. (2.36) takes the form:

$$\omega^2 \zeta_\alpha = \sum_\beta G_{\alpha\beta}\zeta_\beta \qquad (2.38)$$

In Eq. (2.38), $G_{\alpha\beta}$ is a real, symmetric matrix that is related to the atomic force constants by,

$$G_{\alpha\beta} = -\frac{2}{M} \sum_{l'} \hat{\Phi}_{\alpha\beta}(01;l'2) \qquad (2.39)$$

Note that the force constants have been specialized for the diamond lattice where all M_k are of equal mass, and $k = 1,2$, because there are only two atoms per unit cell. Note also that the elements of $G_{\alpha\beta}$ are identical to the $K_{\alpha\beta}$ of Anastassakis and Burstein,[50] which they refer to as the effective spring constants.

The elements of $G_{\alpha\beta}$ describe solutions to the total vibrational Hamiltonian in the harmonic approximation. To determine the perturbation to the eigenfrequencies due to the applied strain, $G_{\alpha\beta}$ is expanded in a power series to first-order in the strain:

$$G_{\alpha\beta} = G_{\alpha\beta}^{(0)} + \sum_{\mu\nu} G_{\mu\nu\alpha\beta}^{(\eta)} \eta_{\mu\nu} \qquad (2.40)$$

The zeroth-order solution to the vibrational Hamiltonian describes the frequency spectrum in the absence of strain. If the triply degenerate Raman frequency (or reference frequency) is given by ω_R, then from Eq. (2.38)

$$\omega_R^2 \zeta_\alpha = \sum_\beta G_{\alpha\beta}^{(0)} \zeta_\beta \qquad (2.41)$$

The $G_{\mu\nu\alpha\beta}$ of Eq. (2.40) are symmetric fourth-rank tensors and are described by Ganesan et al.[13] in terms of the second- and third-order atomic force constants.

The equation of motion for the total vibrational Hamiltonian is now given by

$$\sum_\beta \left\{ G_{\alpha\beta}^{(0)} + \sum_{\mu\nu} G_{\mu\nu\alpha\beta}^{(\eta)} \eta_{\mu\nu} \right\} \zeta_\beta = \omega^2 \zeta_\alpha \qquad (2.42)$$

Using the orthonormal properties of the eigenvectors $\left(\zeta_\alpha \cdot \zeta_\beta = \delta_{\alpha\beta} \right)$, the perturbation to the Raman spectrum is determined from the eigenvalues of the secular equation

$$\left| \sum_{\mu\nu} G_{\mu\nu\alpha\beta}^{(\eta)} \eta_{\mu\nu} - \lambda \delta_{\alpha\beta} \right| = 0 \qquad (2.43)$$

where $\lambda = \omega^2 - \omega_R^2$.

Expanding Eq. (2.43), the matrix assumes the form

$$\begin{bmatrix} \sum_{\mu\nu} G_{\mu\nu11}\eta_{\mu\nu} - \lambda & \sum_{\mu\nu} G_{\mu\nu12}\eta_{\mu\nu} & \sum_{\mu\nu} G_{\mu\nu13}\eta_{\mu\nu} \\ \sum_{\mu\nu} G_{\mu\nu21}\eta_{\mu\nu} & \sum_{\mu\nu} G_{\mu\nu22}\eta_{\mu\nu} - \lambda & \sum_{\mu\nu} G_{\mu\nu23}\eta_{\mu\nu} \\ \sum_{\mu\nu} G_{\mu\nu31}\eta_{\mu\nu} & \sum_{\mu\nu} G_{\mu\nu32}\eta_{\mu\nu} & \sum_{\mu\nu} G_{\mu\nu33}\eta_{\mu\nu} - \lambda \end{bmatrix} = 0 \qquad (2.44)$$

Because the $G_{\mu\nu\alpha\beta}$ represent tensor properties of the crystal, Eq. (2.44) may be greatly simplified by imposing Neumann's Principle. Just as for the elastic constants C_{ijkl}, it may be shown that[51]

$$\begin{aligned} G_{1111} &= G_{2222} = G_{3333} = p \\ G_{1122} &= G_{2211} = G_{2233} = G_{3322} = G_{1133} = G_{3311} = q \\ G_{1212} &= G_{2121} = G_{1221} = G_{2112} = G_{1313} = G_{3131} \\ &= G_{1331} = G_{3113} = G_{2323} = G_{3232} = G_{2332} = G_{3223} = r \end{aligned} \qquad (2.45)$$

Using the relationships in Eq. (2.45), the frequency shifts due to applied strain are given by the solutions to the following determinant:

$$\begin{vmatrix} p\eta_{11} + q(\eta_{22} + \eta_{33}) - \lambda & 2r\eta_{12} & 2r\eta_{13} \\ 2r\eta_{12} & p\eta_{22} + q(\eta_{11} + \eta_{33}) - \lambda & 2r\eta_{23} \\ 2r\eta_{13} & 2r\eta_{23} & p\eta_{33} + q(\eta_{11} + \eta_{22}) - \lambda \end{vmatrix} = 0 \qquad (2.46)$$

Because of the uniaxial strain condition in shock compression experiments, the solutions to Eq. (2.46) are straightforward. However, care must be taken to ensure that the strains are properly defined with respect to the crystal axes.

The determinant given in Eq. (2.46) has also been derived by Anastassakis and Burstein[50] using a phenomenological approach. In their model the experimental results are fit to three parameters K_1, K_2, and K_3 (effective spring constants). This approach is useful in describing the macroscopically observed behavior, but tells us nothing regarding the underlying forces acting at the atomic level. The benefit of the Ganesan et al.[13] quasi-

harmonic model, presented here, is that the connection may be made to the atomic behavior through Eq. (2.39) and may be modeled from force field theories.

Frequency Shifts For Uniaxial [100] Strain

For uniaxial strain along [100] ($\eta_{xx} = \eta$), the secular matrix assumes the simple diagonal form:

$$\begin{vmatrix} p\eta - \lambda & 0 & 0 \\ 0 & q\eta - \lambda & 0 \\ 0 & 0 & q\eta - \lambda \end{vmatrix} = 0 \tag{2.47}$$

The eigenvalue and eigenvector solutions are

$$\lambda_s = p\eta \quad , \quad \rho_s = \begin{pmatrix} 1 \\ 0 \\ 0 \end{pmatrix}$$

$$\lambda_d = q\eta \quad , \quad \rho_d = \begin{pmatrix} 0 \\ 1 \\ 0 \end{pmatrix} , \quad \rho_d = \begin{pmatrix} 0 \\ 0 \\ 1 \end{pmatrix} \tag{2.48}$$

The subscript indicates the degeneracy as singlet (s) or doublet (d) and $\lambda_i = \omega_i^2 - \omega_R^2$, as in Eq. (2.43). The new eigenfrequencies due to the uniaxial strain η_{xx} are found to be

$$\Delta\omega_s = \omega_R \left\{ \left[1 + \frac{p\eta}{\omega_R^2} \right]^{\frac{1}{2}} - 1 \right\}, \; and \; \; \Delta\omega_d = \omega_R \left\{ \left[1 + \frac{q\eta}{\omega_R^2} \right]^{\frac{1}{2}} - 1 \right\} \tag{2.49}$$

Frequency Shifts For [110] Strain

Because the uniaxial strain is defined along the laboratory X-axis and the secular matrix in Eq. (2.46) is written in the crystallographic {xyz} system, the strain along [110] must be transformed to the {xyz} system. The strain is a second rank tensor similar to

polarizability that was previously transformed using Eqs. (2.16) and (2.17). However, in the earlier discussion the transformation was from the crystallographic to the primed system $\{x'y'z'\}$. The relation for the inverse transformation is given by $\eta_{ij} = a_{ki}a_{lj}\eta'_{kl}$.

Following the same procedure as for the polarizability, a set of equations analogous to Eq. (2.18) are found that relate the primed and unprimed strains. In terms of the applied uniaxial strain η'_{11}, the strain matrix in the crystallographic system is given by

$$\underline{\eta} = \frac{1}{2}\begin{pmatrix} \eta' & \eta' & 0 \\ \eta' & \eta' & 0 \\ 0 & 0 & 0 \end{pmatrix} \text{, thus } \eta_{xx} = \eta_{yy} = \eta_{xy} = \eta_{yx} = \frac{\eta'}{2}. \tag{2.50}$$

Substitution into the secular equation yields

$$\begin{vmatrix} \left(\dfrac{p+q}{2}\right)\eta - \lambda & r\eta & 0 \\ r\eta & \left(\dfrac{p+q}{2}\right)\eta - \lambda & 0 \\ 0 & 0 & q\eta - \lambda \end{vmatrix} = 0 \tag{2.51}$$

There are three solutions to Eq. (2.51). The eigenvalues and eigenvectors are

$$\left. \begin{array}{c} \lambda_1 = q\eta, \quad \lambda_2 = \left(\dfrac{p+q+2r}{2}\right)\eta, \quad \lambda_3 = \left(\dfrac{p+q-2r}{2}\right)\eta \\[2mm] \rho_1 = \begin{pmatrix} 0 \\ 0 \\ 1 \end{pmatrix}, \quad \rho_2 = \dfrac{1}{\sqrt{2}}\begin{pmatrix} 1 \\ 1 \\ 0 \end{pmatrix}, \qquad \rho_3 = \dfrac{1}{\sqrt{2}}\begin{pmatrix} 1 \\ -1 \\ 0 \end{pmatrix} \end{array} \right\} \tag{2.52}$$

and the eigenfrequencies are

$$\Delta\omega_1 = \omega_R\left\{\left[1 + \frac{q\eta}{\omega_R^2}\right]^{\frac{1}{2}} - 1\right\},$$

$$\Delta\omega_2 = \omega_R\left\{\left[1 + \frac{(p+q+2r)\eta}{2\omega_R^2}\right]^{\frac{1}{2}} - 1\right\}, \quad \Delta\omega_3 = \omega_R\left\{\left[1 + \frac{(p+q-2r)\eta}{2\omega_R^2}\right]^{\frac{1}{2}} - 1\right\} \tag{2.53}$$

Thus, as expected, there are three distinct frequencies shifted from the ambient phonon frequency by an amount indicated by Eq. (2.53).

Frequency Shifts For [111] Strain

Although no experimental work is reported for this configuration, the calculated frequency shifts are presented for completeness.

For this geometry, the transformation matrix analogous to Eq. (2.16) is given by:

$$\underline{a} = \begin{pmatrix} \dfrac{1}{\sqrt{3}} & \dfrac{1}{\sqrt{3}} & \dfrac{1}{\sqrt{3}} \\ -\dfrac{1}{\sqrt{6}} & -\dfrac{1}{\sqrt{6}} & \dfrac{2}{\sqrt{6}} \\ \dfrac{1}{\sqrt{2}} & -\dfrac{1}{\sqrt{2}} & 0 \end{pmatrix} \qquad (2.54)$$

Figure 2.8 provides the relationship between the crystallographic axis and the strain axis. Transforming the strains using $\eta_{ij} = a_{ki}a_{lj}\eta'_{kl}$ gives the strain matrix

$$\underline{\eta} = \frac{1}{3}\begin{pmatrix} \eta' & \eta' & \eta' \\ \eta' & \eta' & \eta' \\ \eta' & \eta' & \eta' \end{pmatrix} \qquad (2.55)$$

Hence, the secular equation becomes

$$\begin{vmatrix} \left(\dfrac{p+2q}{3}\right)\eta - \lambda & \dfrac{2r\eta}{3} & \dfrac{2r\eta}{3} \\ \dfrac{2r\eta}{3} & \left(\dfrac{p+2q}{3}\right)\eta - \lambda & \dfrac{2r\eta}{3} \\ \dfrac{2r\eta}{3} & \dfrac{2r\eta}{3} & \left(\dfrac{p+2q}{3}\right)\eta - \lambda \end{vmatrix} = 0 \qquad (2.56)$$

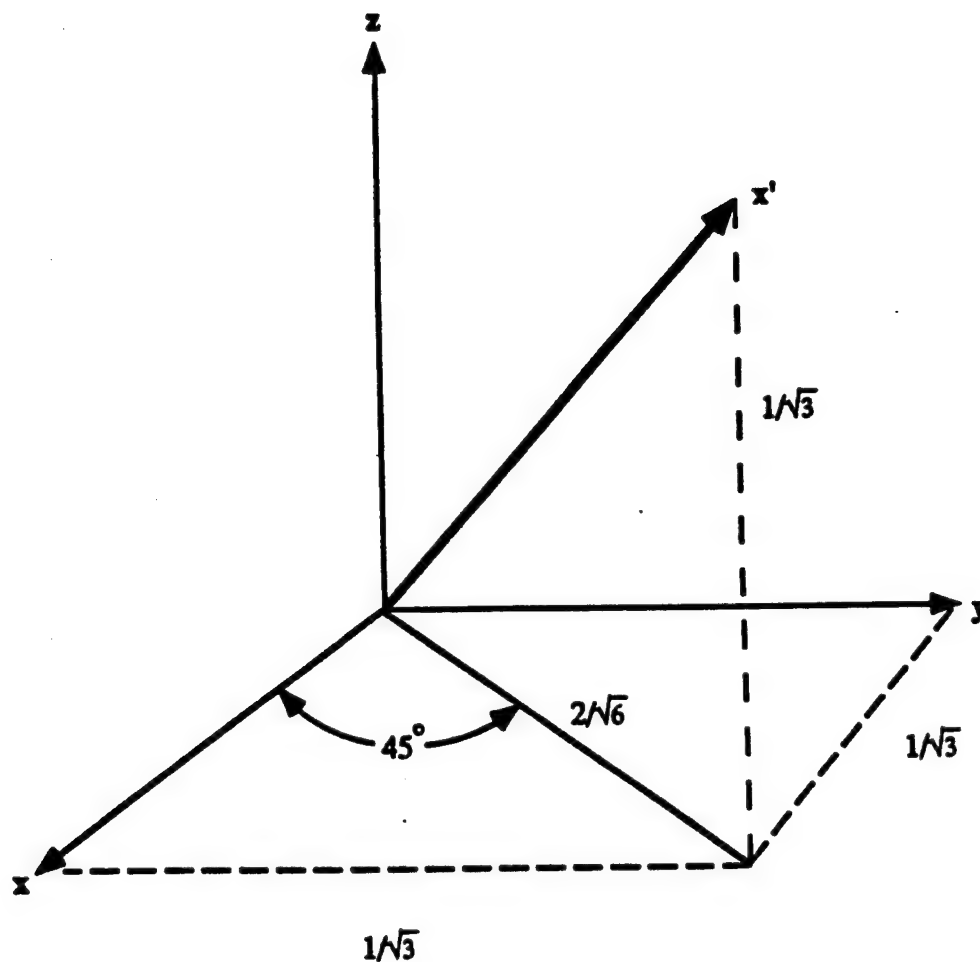with eigenvalues and eigenvectors given by:

Figure 2.8 Relationship between the crystallographic system {xyz} and the primed crystallographic system {x'y'z'} for strain applied along [111].

$$\lambda_d = \left(\frac{p+2q-2r}{3}\right)\eta, \quad \lambda_s = \left(\frac{p+2q+4r}{3}\right)\eta$$

$$\rho_d = \frac{1}{\sqrt{2}}\begin{pmatrix}1\\-1\\0\end{pmatrix} \rho_d = \frac{1}{\sqrt{6}}\begin{pmatrix}1\\1\\-2\end{pmatrix}, \quad \rho_s = \frac{1}{\sqrt{3}}\begin{pmatrix}1\\1\\1\end{pmatrix} \qquad \text{(2.57)}$$

Using the eigenvalues of Eq. (2.57) the corresponding frequency shifts are found to be

$$\Delta\omega_d = \omega_R\left\{\left[1+\frac{(p+2q-2r)\eta}{3\omega_R^2}\right]^{\frac{1}{2}}-1\right\}, \quad \Delta\omega_s = \omega_R\left\{\left[1+\frac{(p+2q+4r)\eta}{3\omega_R^2}\right]^{\frac{1}{2}}-1\right\} \qquad \text{(2.58)}$$

As expected, the degeneracy is only partially lifted.

Calculation of Frequency Shifts For Hydrostatic Strain

Although the experiments performed in this study are for uniaxial strain, the relation calculated for hydrostatic strain is given for use in subsequent analysis.

For hydrostatic strain $\eta_{xx} = \eta_{yy} = \eta_{zz} = \left(\frac{\eta}{3}\right)$. The solutions to Eq. (2.46) for the triply degenerate phonon are

$$\Delta\omega_H = \omega_R\left\{\left[1+\frac{(p+2q)\eta}{3\omega_R^2}\right]^{\frac{1}{2}}-1\right\} = \omega_R\left\{\sqrt{1-2\gamma\eta}-1\right\} \qquad \text{(2.59)}$$

In this expression, γ is the mode Grüneisen constant and, by convention, η is considered negative in compression.[52]

2.5 MECHANICAL RESPONSE OF DIAMOND

As mentioned at the beginning of this chapter, diamond is one of the hardest materials known. More precisely, diamond is known to remain elastic up to very high stresses. By elastic, it is meant that the diamond does not exhibit any sign of yielding or mechanically irreversible behavior.

Diamond has been demonstrated to remain elastic up to pressures exceeding 2.8 Mbar in a Diamond Anvil Cell for long periods of time without manifesting any outward signs of plastic flow.[53] Because the maximum longitudinal stress achieved in the present study was ≈0.5 Mbar, the diamond samples under uniaxial strain were considered to be elastic. This is supported by the results of the present work.

Only two experimental studies that investigate the mechanical properties of diamond using shock compression techniques have been reported in the literature. The work of Pavlovskii[54] on diamond samples oriented along [100] resulted in a linear shock/particle velocity relationship that is inconsistent with the precise measurements of McSkimin and Andreach[55] for the sound velocity for this orientation. Recent work[53] has demonstrated the importance of impurities such as nitrogen on the material strength of diamond and it is not clear as to what diamonds were used in Pavlovskii's work.

Kondo and Ahrens performed two shock experiments on diamonds with an orientation "between the [111] and [110] crystallographic axes."[56] Their study used diamonds that contained cracks and inclusions of unknown origin. They observed a two-wave structure, that they claim suggested a shock-induced transition to a "possibly metallic phase." Because their study generated shock pressures of only ≈630 kbar, it would seem unlikely that the two-wave structure they observed was due to a phase transition. Due to the poor quality of their samples, it is difficult to draw any conclusions from this study.

2.5.1 Linear Elastic Response

The elastic response of diamond has only been measured in the linear regime. In this approximation the stress (σ_{ij}) and strain (η_{kl}) are related through Hooke's Law[44] by

$$\sigma_{ij} = C_{ijkl}\varepsilon_{kl}, \quad for\ i,j,k,l = 1,2,3 \tag{2.60}$$

where C_{ijkl} is a fourth rank tensor called the *stiffness*. For cubic crystals the stiffness constants (or moduli) reduce through symmetry arguments to only three in number. They are given by C_{11}, C_{12}, and C_{44} where the contracted Voigt notation has been used.[44]

The values for the second-order elastic moduli of diamond used in this study are those given by McSkimin and Andreatch.[55] These values at ambient temperature and pressure are given in Table 2.6 in the Voigt notation.

Table 2.6 Elastic Moduli of Diamond.

Modulus	Value ($\times 10^3$ kbar)
C_{11}	10.79 ± 0.05
C_{12}	1.24 ± 0.05
C_{44}	5.78 ± 0.02

Brugger[57] has shown that for cubic crystals, such as diamond, the pure modes for elastic waves propagate along the [100], [110], and [111] directions only. All other propagation directions are considered as nonspecific and result in quasi-longitudinal and quasi-transverse waves[58]. For the work reported here, only pure modes of propagation are considered. The longitudinal and shear wave velocities may be calculated for elastic waves propagating along [100], [110], and [111] in cubic diamond crystals. They are

$$[100] \qquad V_l = \sqrt{\frac{C_{11}}{\rho}}, \qquad V_s = \sqrt{\frac{C_{44}}{\rho}} \qquad\qquad (2.61)$$

$$[110] \qquad V_l = \sqrt{\frac{C_{11}+C_{12}+2C_{44}}{2\rho}}, \quad V_s = \sqrt{\frac{C_{11}-C_{12}}{2\rho}}, \quad V_{s'} = \sqrt{\frac{C_{44}}{\rho}} \qquad (2.62)$$

$$[111] \qquad V_l = \sqrt{\frac{C_{11}+2C_{12}+4C_{44}}{3\rho}}, \qquad V_s = \sqrt{\frac{C_{11}-C_{12}+C_{44}}{3\rho}} \qquad (2.63)$$

In these expressions, $\rho = 3.512$ g/cc is the density of diamond under ambient conditions. Using the values from Table 2.6, the longitudinal and shear wave velocities at ambient conditions are given in Table 2.7 for convenience. It should be noted that the shear wave velocities are doubly degenerate for wave propagation along [100] and [111] whereas, they are nondegenerate for the [110] direction.

Table 2.7 Elastic Wave Velocities in Diamond.

Direction	V_l (mm/μs)	V_s (mm/μs)	$V_{s'}$ (mm/μs)
[100]	17.53	12.83	-
[110]	18.33	11.66	12.83
[111]	18.58	12.06	-

2.5.2 Calculation of the Shock Response of Diamond Using Finite Strain Theory

In the previous section, the stress-strain relation was given by Hooke's law. The degree to which this linear relationship holds depends upon the extent to which the crystal has been elastically deformed. The stress range considered in the present study results in density compression which approaches 4%. The mechanical response of diamond for this compression are better described by the nonlinear elastic stress-strain relations.

Two difficulties arise in determining the nonlinear stress-strain relations for diamond. The first difficulty is that to describe the nonvanishing stresses and strains in the nonlinear regime it is necessary to know the third-order elastic moduli (sixth rank tensors). As will be discussed in Section 2.5.3, these have not been measured for diamond, but values based on Valence Force Field calculations are available. The second difficulty encountered is the lack of shock data on diamond. The approach taken in this study to overcome these difficulties will be discussed after the finite strain formulation is presented.

Before discussing the finite strain formulation, the conservation equations that apply to uniaxial strain shock compression experiments are presented.

Rankine-Hugoniot Jump Conditions

For steady or discontinuous wave propagation in materials subjected to uniaxial strain, the conservation equations can be expressed in a particularly simple form[59]

$$
\left.
\begin{aligned}
\textit{Conservation of mass} \qquad & \rho_0 D = \rho(D - u_P) \\[2ex]
\textit{Conservation of momentum} \qquad & \sigma_{11} = \rho_0 D u_P \\[2ex]
\textit{Conservation of energy} \qquad & E - E_0 = \frac{\sigma_{11}}{\rho_0}\frac{u_P}{D} - \frac{1}{2}u_P^2
\end{aligned}
\right\} \qquad (2.64)
$$

where ρ, E, and σ_{11} describe the density, energy per unit mass, and longitudinal stress in a material behind a shock front moving with velocity D and particle velocity u_P. It is assumed that the material is initially at rest and at zero stress.

Because of the one-dimensional nature of the strain tensor, the stress tensor σ_{ij} will be anisotropic. Measurements made during a shock experiment to determine the

particle velocity u_p and the shock velocity D in a solid can provide only the longitudinal stress. The lateral stress components, needed for the present analysis, cannot be determined directly from the shock data. They need to be determined indirectly from the inferred density compression in the shocked material by using a particular material model. In the present work, the diamond is modeled as a nonlinear elastic solid.

Following the approach used by Horn and Gupta[60] in their work on shock compressed ruby crystals, a finite strain formulation is used to calculate the complete stress state in the shock compressed diamond.

Finite Strain Theory

The finite strain approach of Thurston[52] is used to calculate the nonlinear elastic response of diamond.

A point within a material that moves with the material is called a *particle*. Consider a particle located at position a_i within a crystal. After the crystal has been deformed, the particle is found to be at position x_i. The resulting particle displacement is given by

$$\alpha_i = x_i - a_i \tag{2.65}$$

where α_i is the relative displacement. The particle velocity for this particular point is given by the time derivative[52]

$$u_i = \frac{dx_i}{dt} = \left(\frac{\partial x_i}{\partial t} \right)_{a_1, a_2, a_3} \tag{2.66}$$

A convenient description of the strain existing between two neighboring particles is given by the Green strain[52]

$$\eta_{ij} = \frac{1}{2} \left(\frac{\partial x_m}{\partial a_i} \frac{\partial x_m}{\partial a_j} - \delta_{ij} \right) \tag{2.67}$$

A-61

where ρ_0 is the density. If the displacement in Eq. (2.65) is due to uniaxial strain along the x_1 direction, we can write

$$\left.\begin{array}{l} x_1 = a_1 + \alpha_1 \\ x_2 = a_2 \\ x_3 = a_3 \end{array}\right\} \qquad (2.68)$$

Thus, for uniaxial strain along the x_1 direction Eq. (2.67) becomes

$$\eta_{11} = \frac{\partial \alpha_1}{\partial a_1} + \frac{1}{2}\left(\frac{\partial \alpha_1}{\partial a_1}\right)^2 \qquad (2.69)$$

The internal energy of the crystal may be chosen to be a function of the entropy and strain. Along the Hugoniot, it can be shown that the entropy increase is proportional to the cube of the volume compression.[60] For very stiff materials, such as diamond, the Hugoniot may be approximated by the isentrope of the material to a very good approximation. Horn and Gupta[60] have shown that the error associated with this approximation is less than 1% for a 2.4% compression of ruby.

To obtain the nonlinear stress-strain relationship for diamond the internal energy is expanded in a Taylor series at constant entropy,

$$\rho_0 U(S, \eta_{ij}) = \rho_0 U(S,0) + C_{ij}^S \eta_{ij} + \frac{1}{2} C_{ijkl}^S \eta_{ij} \eta_{kl} + \frac{1}{6} C_{ijklmn}^S \eta_{ij} \eta_{kl} \eta_{mn} + ... \qquad (2.70)$$

where

$$C_{ij}^S = \rho_0 \left(\frac{\partial U}{\partial \eta_{ij}}\right)_S, \qquad C_{ijkl}^S = \rho_0 \left(\frac{\partial^2 U}{\partial \eta_{ij} \partial \eta_{kl}}\right)_S, \qquad C_{ijklmn}^S = \rho_0 \left(\frac{\partial^3 U}{\partial \eta_{ij} \partial \eta_{kl} \partial \eta_{mn}}\right)_S \qquad (2.71)$$

The term linear in strain must vanish in the limit of vanishing stress and the C_{ijkl}^S, C_{ijklmn}^S are the second-, and third-order isentropic elastic constants. The thermodynamic stresses, τ_{ij}, are given by[52]

$$\tau_{ij} = \rho_0 \left(\frac{\partial U}{\partial \eta_{ij}} \right)_S \qquad (2.72)$$

Using the internal energy expansion of Eq. (2.70), the relationship between the thermodynamic stresses and the Green strain is found to be

$$\tau_{ij} = C_{ijkl}^S \eta_{kl} + \frac{1}{2} C_{ijklmn}^S \eta_{kl} \eta_{mn} \qquad (2.73)$$

It is convenient to convert the thermodynamic stresses to the Cauchy stresses defined through the relation[52]

$$\sigma_{kl} = \frac{1}{J} \frac{\partial x_k}{\partial a_j} \frac{\partial x_l}{\partial a_i} \tau_{ij} \qquad (2.74)$$

where J is the Jacobian of the coordinate transformation. For uniaxial strain

$$J = \left| \frac{\partial x_i}{\partial a_j} \right| = \frac{\rho_0}{\rho} \qquad (2.75)$$

From Eq. (2.73)-(2.75) the stress-strain relations may be calculated for any stress state if the second and third-order elastic constants are known. For cubic crystals there are three independent second-order constants[44]

$$\left. \begin{array}{l} C_{11} = C_{22} = C_{33} \\ C_{12} = C_{23} = C_{13} \\ C_{44} = C_{55} = C_{66} \end{array} \right\} \qquad (2.76)$$

and six independent third-order constants

$$
\left.\begin{array}{c}
C_{111} = C_{222} = C_{333} \\
C_{144} = C_{255} = C_{366} \\
C_{112} = C_{223} = C_{133} = C_{113} = C_{122} = C_{233} \\
C_{155} = C_{244} = C_{344} = C_{166} = C_{266} = C_{355} \\
C_{123}, \quad C_{456}
\end{array}\right\} \tag{2.77}
$$

In these expressions the compact Voigt notation[44] has been used here where

$$
(11) \Rightarrow 1, (22) \Rightarrow 2, (33) \Rightarrow 3, (23,32) \Rightarrow 4, (31,13) \Rightarrow 5, (12,21) \Rightarrow 6 \tag{2.78}
$$

We are now prepared to calculate all stresses and strains for uniaxial strain along the two orientations [100] and [110] considered in this study. The finite strain approach thus permits calculation of the lateral as well as the longitudinal stresses. This information will be necessary to analyze the present data and to compare experimental results with previous static measurements.

Shock Propagation Along [100]

For uniaxial strain along [100], the strain matrix takes the simple form:

$$
\eta = \begin{bmatrix} \eta_{11} & 0 & 0 \\ 0 & 0 & 0 \\ 0 & 0 & 0 \end{bmatrix} \tag{2.79}
$$

and as a consequence there is only one non-vanishing strain component that is the same in both the crystallographic and laboratory frame

$$
\eta_{11} = \eta \tag{2.80}
$$

From Eq. (2.73), the thermodynamic stresses are

$$
\tau_{ij} = C_{ij11}\eta + \frac{1}{2}C_{ij1111}\eta^2 \tag{2.81}
$$

and using the relationships (2.76) and (2.77), it is found that

$$\tau_{11} = C_{11}\eta + \frac{1}{2}C_{111}\eta^2, \quad \tau_{22} = \tau_{33} = C_{12}\eta + \frac{1}{2}C_{112}\eta^2, \quad \tau_{ij} = 0, \, for \, i \neq j \qquad (2.82)$$

Combining Eqs. (2.74), (2.75), and (2.81) gives the non-vanishing Cauchy stresses

$$\left.\begin{array}{l} \sigma_{11} = \dfrac{\rho_0}{\rho}\tau_{11} = \dfrac{\rho_0}{\rho}\left[C_{11}\eta + \dfrac{1}{2}C_{111}\eta^2\right] \\[3mm] \sigma_{22} = \dfrac{\rho}{\rho_0}\tau_{22} = \dfrac{\rho}{\rho_0}\left[C_{12}\eta + \dfrac{1}{2}C_{112}\eta^2\right] \\[3mm] \sigma_{33} = \dfrac{\rho}{\rho_0}\tau_{22} = \sigma_{22} \end{array}\right\} \qquad (2.83)$$

Hence, for uniaxial strain along [100] we now have expressions that allow computation of all stresses. Note that in Eq. (2.83) the two lateral stresses are degenerate.

Shock Propagation Along [110]

We need to know the longitudinal and lateral stresses in the wave propagation system {x'y'z'} where x' is parallel to the [110] direction, y' is parallel to [1$\bar{1}$0] , and z' is along [001]. The thermodynamic stresses for uniaxial strain along [110] are given by

$$\tau'_{ij} = C'_{ij11}\eta'_{11} + \frac{1}{2}C'_{ij1111}\eta'^2_{11} \qquad (2.84)$$

The Cauchy stresses in the primed system are defined by

$$\sigma'_{kl} = \frac{1}{J'}\frac{\partial x'_k}{\partial a'_j}\frac{\partial x'_l}{\partial a'_i}\tau'_{ij} \qquad (2.85)$$

Where J' is the Jacobian for the coordinate transformations and is invariant

$$J' = \begin{vmatrix} \dfrac{\partial x_1'}{\partial a_1'} & 0 & 0 \\ 0 & 1 & 0 \\ 0 & 0 & 1 \end{vmatrix} = \dfrac{\rho_0}{\rho} \tag{2.86}$$

The Cauchy stress components of Eq. (2.85) are then

$$\left. \begin{aligned} \sigma_{11}' &= \frac{\rho_0}{\rho} \tau_{11}' \\ \sigma_{22}' &= \frac{\rho}{\rho_0} \tau_{22}' \\ \sigma_{33}' &= \frac{\rho}{\rho_0} \tau_{33}' \\ \sigma_{12}' &= \tau_{21}' \\ \sigma_{13}' &= \tau_{31}' \\ \sigma_{23}' &= \frac{\rho}{\rho_0} \tau_{32}' \end{aligned} \right\} \tag{2.87}$$

in the primed frame.

To evaluate the stresses defined in Eq. (2.87), the values of the primed thermodynamic stresses must be determined in terms of the unprimed constants which are known. These are calculated in Appendix D and are found to be

$$\left. \begin{aligned} \tau_{11}' &= \frac{1}{2}\tau_{11} + \tau_{12} + \frac{1}{2}\tau_{22} \\ \tau_{22}' &= \frac{1}{2}\tau_{11} - \tau_{12} + \frac{1}{2}\tau_{22} \\ \tau_{33}' &= \tau_{33} \\ \tau_{12}' &= \tau_{21}' = 0 \\ \tau_{13}' &= \tau_{31}' = 0 \\ \tau_{23}' &= \tau_{32}' = 0 \end{aligned} \right\} \tag{2.88}$$

The relation between the primed and unprimed elastic constants are also determined in Appendix D. The relations are given in Eq. (D.15) as

$$C'_{11} = \frac{1}{2}(C_{11} + C_{12} + 2C_{44}), \quad C'_{111} = \frac{1}{4}(C_{111} + 3C_{112} + 12C_{166})$$

$$C'_{12} = \frac{1}{2}(C_{11} + C_{12} - 2C_{44}), \quad C'_{112} = \frac{1}{4}(C_{111} + 3C_{112} - 4C_{166})$$

$$C'_{13} = C_{12}, \quad\quad\quad\quad\quad\quad C'_{113} = \frac{1}{2}(C_{112} + C_{123} + 2C_{144})$$

(2.89)

Using Eq. (2.89), Eq. (2.84), and Eq. (2.87), the stress-strain relations are found to be

$$\sigma'_{11} = \frac{1}{2}\frac{\rho_0}{\rho}\left[(C_{11} + C_{12} + 2C_{44})\eta' + \frac{1}{4}(C_{111} + 3C_{112} + 12C_{166})\eta'^2\right]$$

$$\sigma'_{22} = \frac{1}{2}\frac{\rho}{\rho_0}\left[(C_{11} + C_{12} - 2C_{44})\eta' + \frac{1}{4}(C_{111} + 3C_{112} - 4C_{166})\eta'^2\right]$$

$$\sigma'_{33} = \frac{1}{2}\frac{\rho}{\rho_0}\left[2C_{12}\eta' + \frac{1}{2}(C_{112} + C_{123} + 2C_{144})\eta'^2\right]$$

(2.90)

We now have expressions for the nonvanishing stresses for the two uniaxial strain directions considered in this study. Eq. (2.83) provides the nonzero stresses for the [100] strain and Eq. (2.90) for the [110] strain. For a given volume compression $(V/V_0) = (\rho_0/\rho)$, the strain is determined through Eq. (2.67). With this strain value and density compression, the stress components are determined from Eqs.(2.83) or (2.90) depending on the axis of compression. These two sets of expressions are important for the present work because:

(1)　They provide the means necessary to compare the present results with the results of other studies.

(2)　They provide expressions for the longitudinal stress resulting from the application of [100] and [110] uniaxial strain. These stresses may be combined with the Rankine- Hugoniot jump conditions of Eq. (2.64) to calculate the $D - u_p$ relations

for diamond. No shock data for the $D - u_p$ relation are available for any crystallographic orientation of diamond. This relationship is important for calculating the peak stress in the present work using impedance matching techniques for the diamond, and the buffer and impactor materials.

It is reiterated that the strain in Eq. (2.67) is defined as negative in compression. From the positive values given in Table 2.6 for the second-order elastic moduli, it is seen that in general the expressions for stress σ_{ij} are also negative. It is convenient to define a different notation for stress P_{ij}, where

$$P_{ij} = -\sigma_{ij} \qquad (2.91)$$

Using this expression for stress, the jump conditions of Eq. (2.64) may be rearranged to yield expressions for shock velocity and particle velocity as functions of stress and density compression,

$$D = \sqrt{\frac{P_{11}}{\rho_0\left(1 - \dfrac{\rho_0}{\rho}\right)}} \qquad (2.92)$$

and,

$$u_P = \frac{P_{11}}{\rho_0 D} = \sqrt{\frac{P_{11}}{\rho_0}\left(1 - \dfrac{\rho_0}{\rho}\right)} \qquad (2.93)$$

Thus, for a given density compression, the strain, stress, shock velocity, and particle velocity may be determined. The uncertainty in the latter three parameters is directly proportional to the precision with which the higher order elastic constants are known, because they contribute to the longitudinal stress value P_{11}. This is the topic of the following section.

The stress-density expressions for the [100] and [110] strains will be examined in more detail after the following section where values of the third-order elastic constants for diamond are given.

2.5.3 Determination of Third Order Constants

Thurston and Brugger[51] have given exact relationships between combinations of third order elastic constants and the pressure derivatives of second order constants for small amplitude elastic waves. Because the third-order elastic constants of diamond have not been measured experimentally, the only values available have been determined using this method. The expressions given by Thurston and Brugger[51] are:

$$
\left.\begin{aligned}
\frac{1}{2}\left(\frac{d(C_{11}-C_{12})}{dP}\right) &= -1 - \frac{1}{3B}\left(C_{11}-C_{12}+\tfrac{1}{2}C_{111}-\tfrac{1}{2}C_{123}\right) \\
\frac{1}{2}\left(\frac{d(C_{11}+C_{12}+2C_{44})}{dP}\right) &= -1 - \frac{1}{3B}\left(\begin{aligned} C_{11}+C_{12}+2C_{44}+\tfrac{1}{2}C_{111}+2C_{112} \\ +C_{144}+2C_{166}+\tfrac{1}{2}C_{123} \end{aligned}\right) \\
\frac{dC_{44}}{dP} &= -1 - \frac{1}{3B}\left(2C_{44}+C_{144}+2C_{166}\right) \\
\frac{dC_{11}}{dP} &= -1 - \frac{1}{3B}\left(2C_{11}+C_{111}+2C_{112}\right)
\end{aligned}\right\}
\tag{2.94}
$$

where $B = \tfrac{1}{3}\left(C_{11}+2C_{12}\right)$ is the bulk modulus.

Using the second order elastic constants and their pressure derivatives given by McSkimin and Andreach,[55] the third order constants have been estimated using Valence-Force-Field (VFF) models.[8,61] In these models, the third-order constants are written in terms of anharmonic bond-bending and bond-stretching parameters. Grimsditch et al.[8] base their work on a three parameter model developed by Keating[62,63] whereas Anastassakis et al.[61] use a five parameter variation of the same model.

The anharmonic bond parameters are also used to describe the mode Gruneisen parameter and anharmonic parameters {pqr} described in Section 2.4.2. The experimentally determined values for {pqr} thus determine the relationships among the

anharmonic bond parameters. Using these relationships and the second order elastic data, the third order elastic constants may be fit using an iterative procedure.[8, 61] The results for the models by Grimsditch et al.,[8] and Anastassakis et al.[61] are given in Table 2.8, along with the second order pressure derivatives determined by McSkimin and Andreatch.[55]

Because the pressure derivatives of the second order elastic constants are central to the determination of the third-order elastic constants, it is worthwhile to point out that the pressure derivatives were obtained by McSkimin and Andreatch[55] for a pressure range from ambient to 20,000 psi ($\approx$ 1.4 kbar). The experimental uncertainty in using these values for pressures that are two orders of magnitude larger is unknown.

Table 2.8 Values For the Elastic Constants and Their Pressure Derivatives.

$\dfrac{dC_{11}}{dP}$	$\dfrac{dC_{12}}{dP}$	$\dfrac{dC_{44}}{dP}$	C_{111} $10^3\,kbar$	C_{112} $10^3\,kbar$	C_{123} $10^3\,kbar$	C_{144} $10^3\,kbar$	C_{166} $10^3\,kbar$	C_{456} $10^3\,kbar$	Ref.
5.98	3.06	2.98	-	-	-	-	-	-	55
-	-	-	-62.6	-22.6	+1.12	-6.74	-28.6	-8.23	8
-	-	-	-73.67	-21.36	+10.40	+1.86	-32.92	+0.76	61

To determine which set of third-order constants should be used for the present study, it was desirable that some method be used to assess which set provided more reliable values. One simple way of doing this is to rearrange the expressions in Eq. (2.94) to give:

$$\left.\begin{aligned}
C_{111} + 2C_{112} &= -3B\left(\frac{dC_{11}}{dP} + 1\right) - 2C_{11} \\[6pt]
C_{144} + 2C_{166} &= -3B\left(\frac{dC_{44}}{dP} + 1\right) - 2C_{44} \\[6pt]
C_{111} - C_{123} &= -3B\left(\frac{d(C_{11} - C_{12})}{dP} + 2\right) + 2C_{12} - 2C_{11}
\end{aligned}\right\} \quad (2.95)$$

We now have relations among the third order constants in terms of measure second-order constants and their derivatives. Table 2.9 gives the comparison of the available third-order constants to the relationships in Eq. (2.95). Because the values of Anastassakis et al.[61] give closer agreement to the values obtained from Eq. (2.95), their values were selected for use in the present study.

Table 2.9 Comparison of Third-Order Constants.

Parameters	Equation (2.95) (10³ kbar)	Grimsditch et al.[8] (10³ kbar)	Anastassakis et al.[61] (10³ kbar)
$C_{111} + 2C_{112}$	-114.20	-107.8	-116.39
$C_{144} + 2C_{166}$	-64.37	-63.94	-63.98
$C_{111} - C_{123}$	-84.34	-63.72	-84.07

Figures 2.9 and 2.10 are plots of the nonzero stresses P_{ij} and P'_{ij} as functions of the density compression for uniaxial strain along the [100] and [110] directions These plots were calculated from Eqs. (2.83) and (2.90) with the second order elastic constants of McSkimin[55] and the third order values listed in Table 2.8 for a volume compression up to 4 % . The contributions due to the higher order elastic constants are most noticeable for the longitudinal stress. In Figure 2.9, the third order contributions are roughly 50 kbar (@ 4% compression) for P_{11} and in Figure 2.12(a) about 100 kbar (@ 4% compression) for P'_{11}. Note that the lateral stresses are degenerate for [100] strain. It may also be seen in this figure that it makes very little difference which third-order constants are used for uniaxial strain along [100]. In Figure 2.10 the difference between the two third-order constants becomes more pronounced. From Table 2.8 and Eq. (2.90) it may be seen that the difference in values for C_{123}, C_{144}, and C_{166} are responsible. The C_{123} value of

Anastassakis et al.[61] is an order of magnitude larger than that of Grimsditch et al.[8] and they have opposite signs for the C_{144} constant.

In summary, relationships have been established for the nonlinear elastic stress and strain and a set of third-order elastic constants has been selected for the present work. The third-order constants were calculated from the Valence Force Theory by Anastassakis et al.[61] These relationships were used repeatedly during the course of this investigation to calculate longitudinal stress, through impedance-matching, and to compare experimental data in Chapter 5.
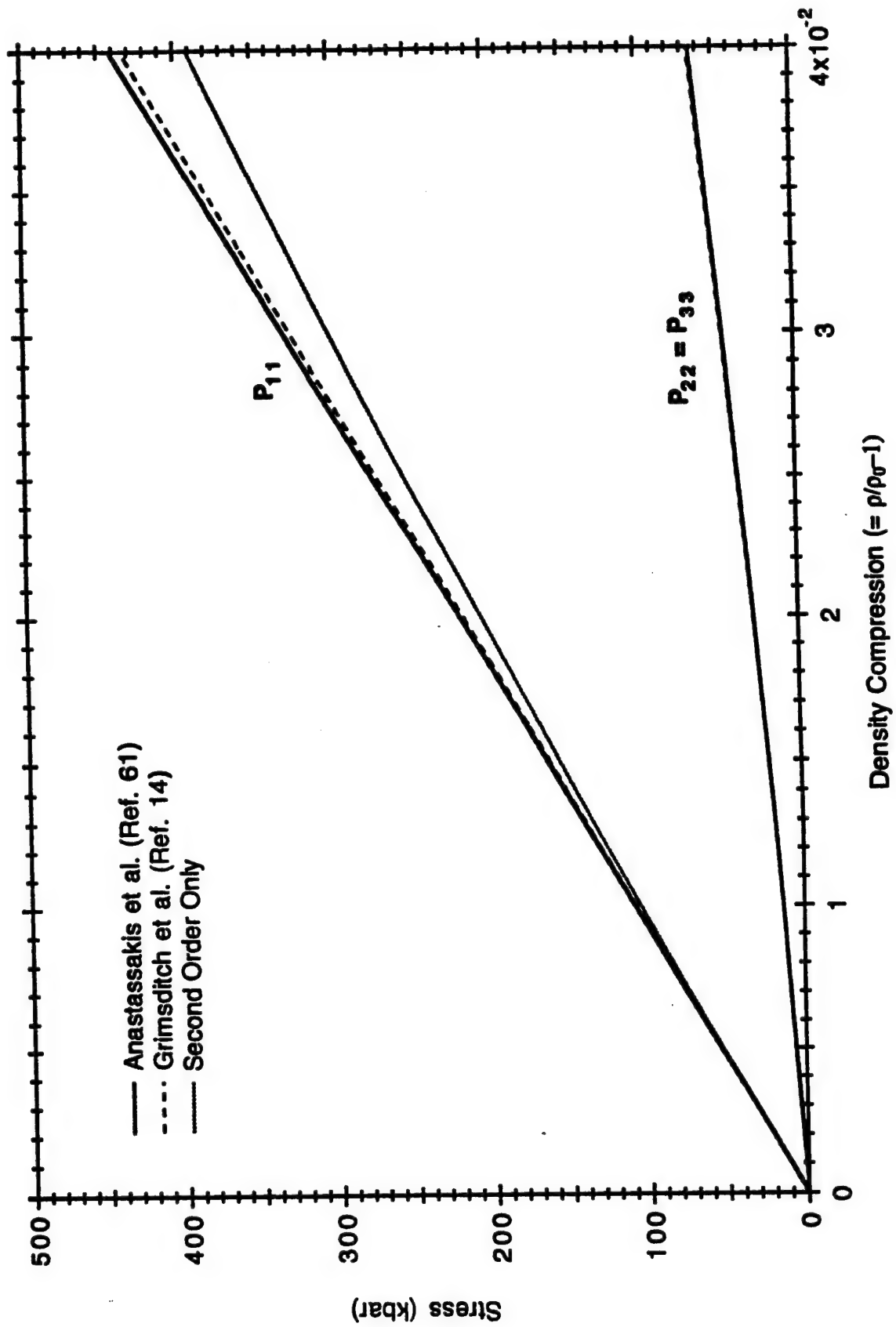
Figure 2.9   Stress versus Density Compression for [100] Strain.
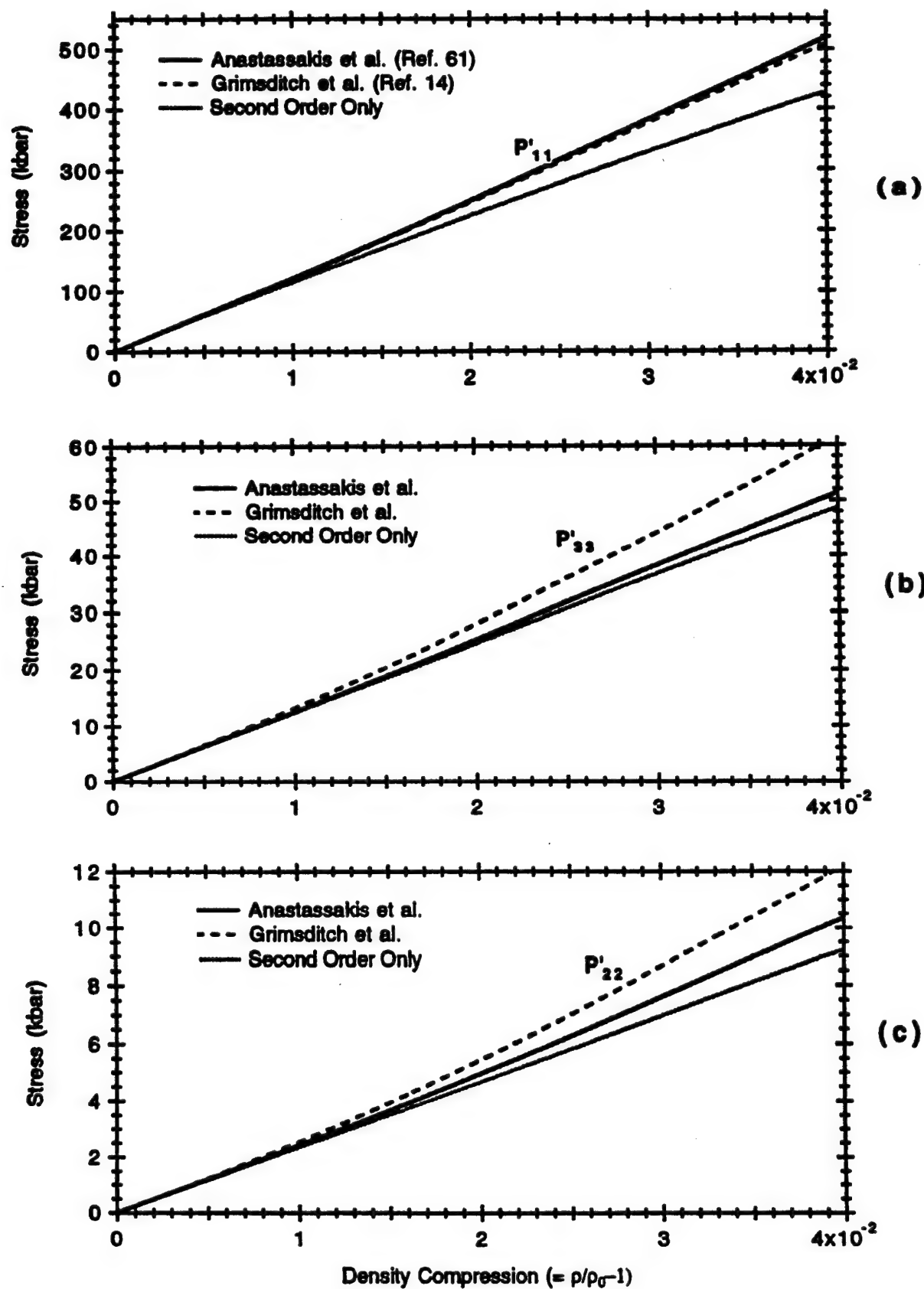
Figure 2.10 Stress versus Density Compression for [110] Strain.

Chapter 3

EXPERIMENTAL METHODS

Information pertaining to the design, construction, and performance of the shock wave experiments is presented in this chapter. Material characteristics are given for diamond samples, and the impactor materials (copper, tantalum, and platinum). The overall experimental design is discussed. Details of the target and projectile construction are given with technical drawings provided in the appendix. The optical components and recording devices for the Raman system are discussed and details of the time and spatial calibration procedures are described. Lastly, the impact arrangements are listed for experiments performed in this work. Some of the optical techniques presented here builds upon earlier developments.[12,64,65]

3.1 MATERIAL CHARACTERIZATION

Diamond

Diamonds may be classified as Ia, Ib, IIa, and IIb depending upon the nitrogen content measured by their infra-red absorption spectrum and whether they manifest semiconducting properties.[66] All samples used in this study were of type IIa. Diamonds of this category have low nitrogen content, an average density[67] of 3.515 g/cc, and possess the highest known thermal conductivity of all materials (~20 W/cmK).

All of the diamond samples were obtained from the Dubbeldee Harris Diamond Corporation. They were provided by the supplier in the shape of round windows approximately 2.5-3 mm in diameter and between 0.5-1.0 mm thick. The sample faces were provided with an optical finish with flatness better than $\lambda/5$, surface roughness < 400 Å, and were parallel to within 5 minutes of arc.

The two crystallographic orientations used in this work were [100] and [110] with tolerances of ± 3°. Each sample was checked for the correct orientation using Laue back-

reflection x-ray photography. The two orientations are easily distinguished because the [100] orientation possesses four mirror planes 45° apart and the [110] orientation has only two mirror planes 90° apart.

Impactor Materials

An impedance matching method was used to achieve the desired longitudinal stress in the diamond samples. Three types of metal impactors were chosen depending on the stress of interest: Oxygen Free High Conductivity (OFHC) Copper, Tantalum, and Platinum. The purity of these materials was 99.95%, 99.9%, and 99.9% respectively. To ensure uniform behavior, all impactors were fabricated from the same material batch. All of these materials have a linear $D - u_p$ relation of the form:[68,69]

$$D = A + Bu_p \qquad (3.1)$$

where D is the shock velocity in the material and u_p is the particle velocity described in Eq. (2.64). A and B are experimentally determined constants. Table 3.1 gives the ambient density, coefficients A and B, and the thermal conductivity λ as obtained from References 68, 69, and 70. The numbers in parenthesis represent the uncertainty in the last two significant figures.

Table 3.1 Selected Material Properties for Cu, Ta, and Pt.

	OFHC Copper	Tantalum	Platinum
ρ_0(g/cc)	8.93	16.656	21.41
A(mm/μs)	3.933(42)	3.293(49)	3.641(49)
B	1.500(25)	1.307(25)	1.541(27)
λ(W/cmK)	4.01	0.575	0.716

Figure 3.1 shows linear $D - u_p$ relationships for the three metals using the tabulated values. Using these experimentally determined $D - u_p$ relationships, the $P - u_p$
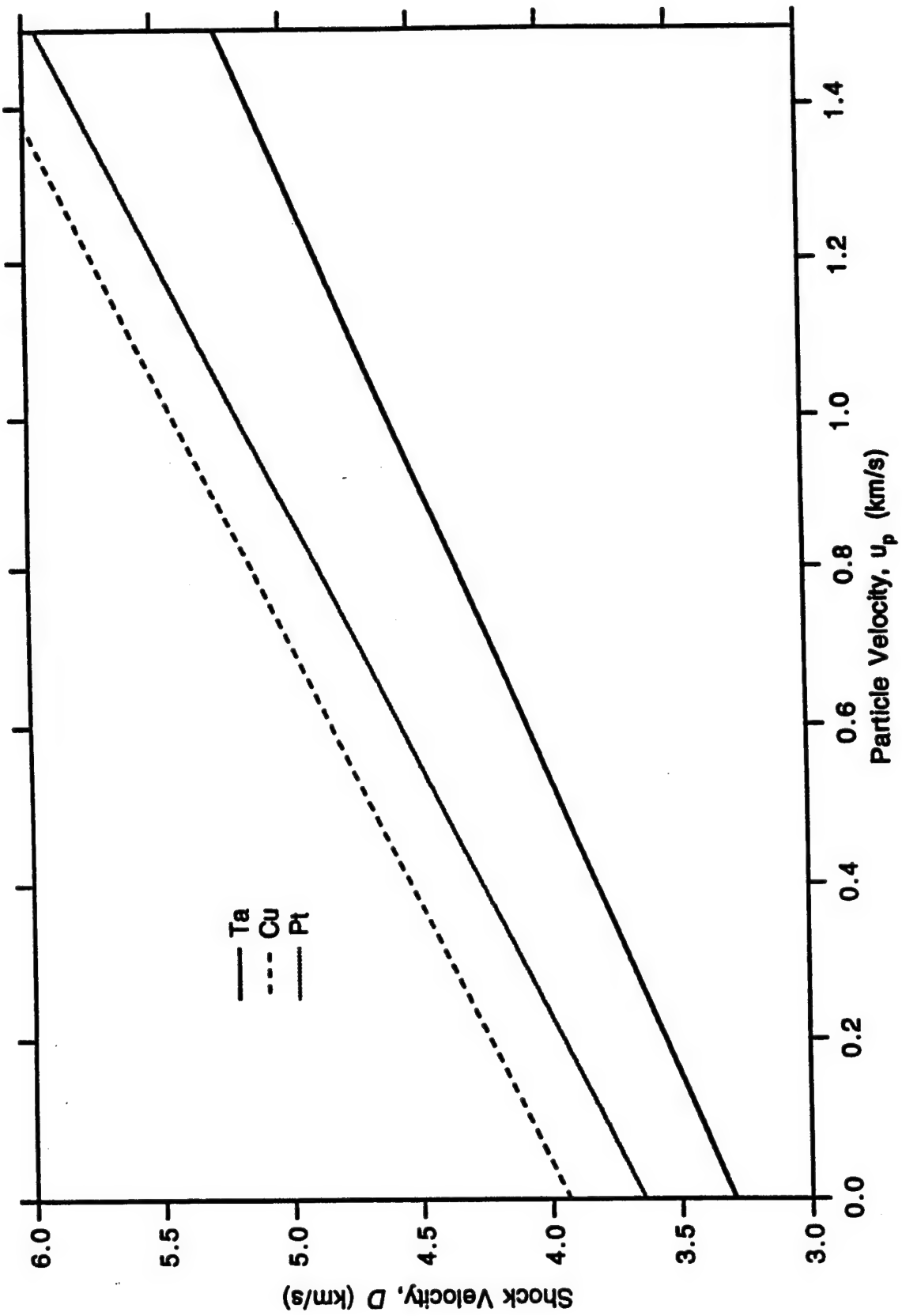
Figure 3.1 Shock Velocity-Particle Velocity For Ta, Cu, and Pt (Ref. 68 and 69).

Hugoniot curves may be determined from the Rankine-Hugoniot jump conditions in Eq. (2.64). These curves are shown in Figure 3.2 for pressures up to 1Mbar.

The Cu, Ta, and Pt impactors used in this study were roughly 6.25 mm in diameter and 2 mm thick. These dimensions helped to keep the projectile mass (as well as the Platinum cost) to a minimum. All OFHC Copper used in this work was from one batch purchased from the Alaskan Copper and Brass Company as alloy C10200 and tested by the supplier for purity per ASTM B152 and found to be 99.95% pure.

3.2 OVERALL EXPERIMENTAL ARRANGEMENT

Figure 3.3 gives an overview of the experimental arrangement. Incident light is provided by a flashlamp-pumped dye laser operating in the visible region at 514.5 nm. The energy delivered to the sample is regulated by an aperture stop which blocks a portion of the laser light exiting the laser head. The light is coupled into an optical fiber and delivered to the sample.

The scattered signal is delivered by another fiber to the spectrometer where it is spatially dispersed. The Raman portion of the signal is then separated from the elastic component (Rayleigh scattered light) by a Raman Holographic Edge Filter that transmits the Raman portion and reflects the remainder. The Raman signal then enters an image converting streak camera that temporally disperses the Raman signal.

The microchannel-plate image intensifier provides the signal gain necessary for detection. Lastly, the intensifier output is lens coupled to a two-dimensional detector array (intensified Vidicon or CCD) and the digitized image is displayed as intensity vs. channel vs. track using an Optical Multichannel Analyzer (OMA) . Post processing routines convert channel to wavenumber and track height to time increments.
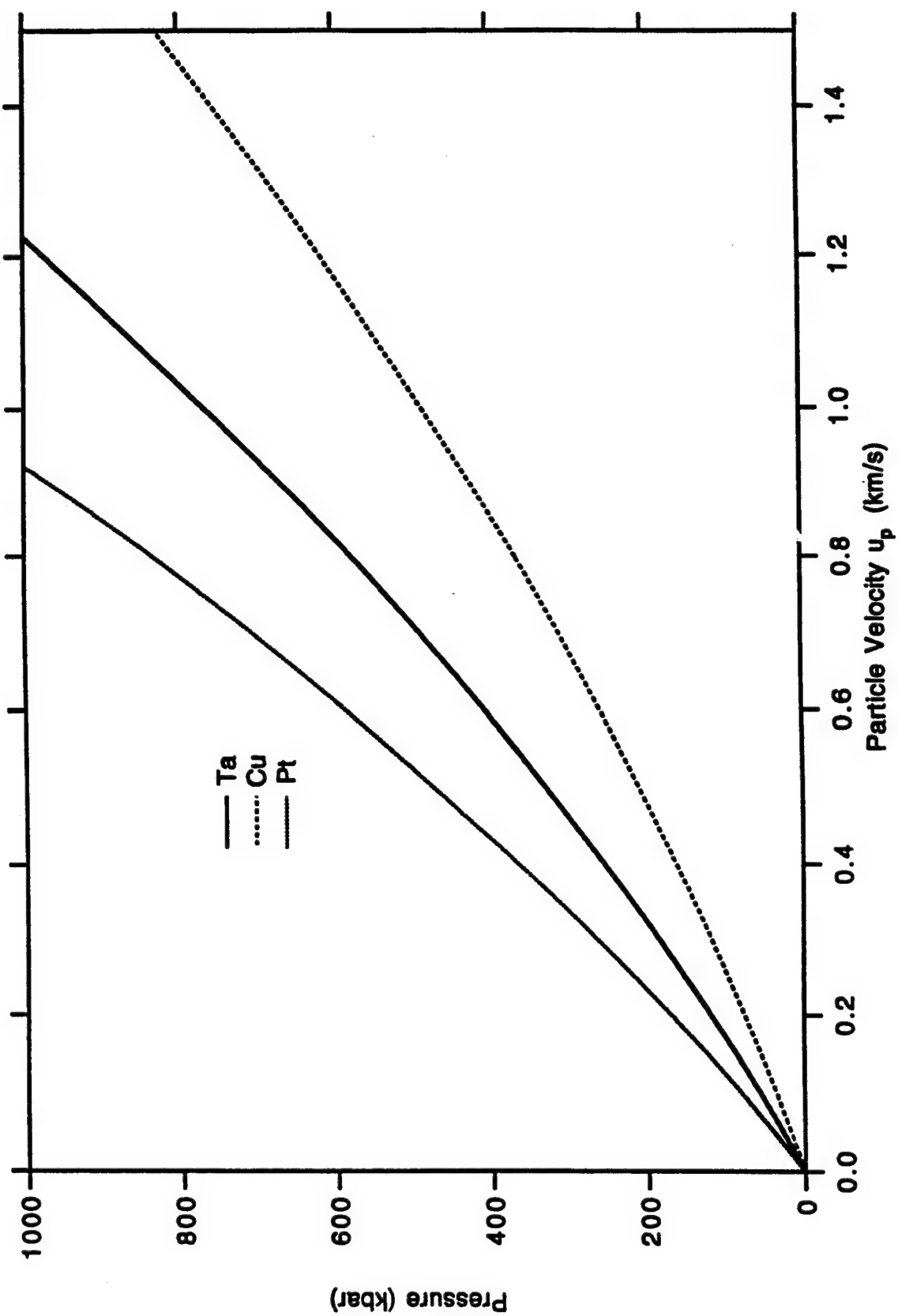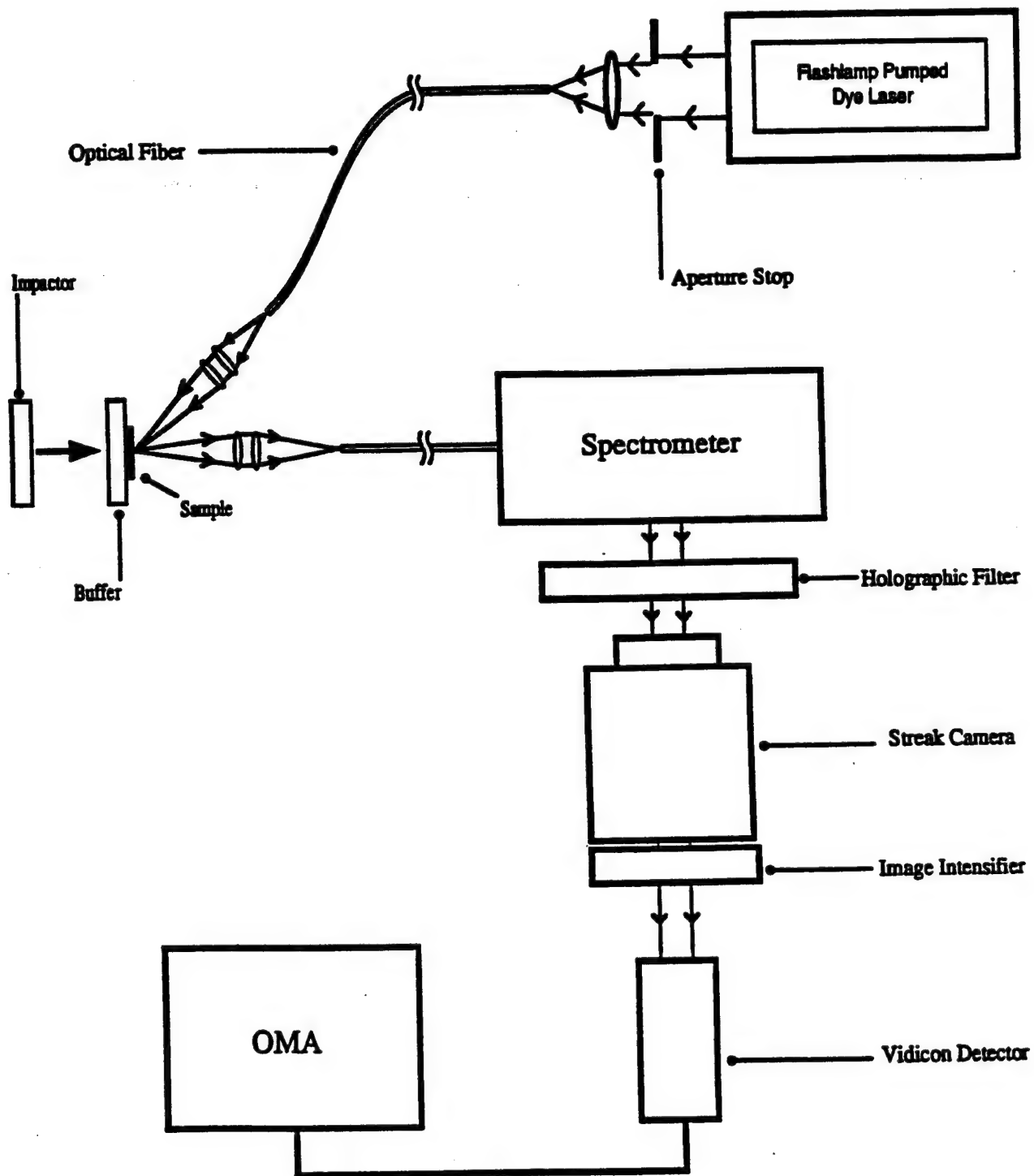
Figure 3.2 Hugoniot Curves for Ta, Cu, Pt.

Fig. 3.3 Overall Experimental Configuration.

3.3 TARGET CONSTRUCTION

Figure 3.4 gives an overall schematic view of the Raman target cell. It consists of four principle components: a) lens assemblies , b) lateral positioner, c) collection optics mount, and d) sample holder. In this figure, the fiber transmitting the laser light enters from the right and is collimated and focused by a lens assembly positioned 45° from the sample normal. A second lens assembly collects the portion of scattered light normal to the sample, collimates it, and focuses it onto the fiber that delivers it to the spectrometer.

The target cell was designed to hold the collimating and focusing optics in place and to allow for precise adjustments of the focus and its position relative to the sample surface. The crossection formed by the optical paths of the two lens assemblies must be positioned as close to the sample center as possible to maximize recording time prior to the arrival of relief waves from the sample edges.

The two lens assemblies are mounted in the lateral positioner that slides on grooves machined into the collection optics mount. The lens assemblies may be rotated and moved in and out to give the desired depth of focus in the sample. The collection optics mount is threaded onto the sample holder to provide an additional focus capability. Set screws are used to prevent the lens assemblies and lateral positioner from moving once the alignment has been performed and a threaded lock-ring is also seated between the optics mount and sample holder to prevent movement. To minimize stray reflections, the interior of the sample holder, collection optics mount, and lateral positioner are painted flat-black. The technical drawings providing further details of the target cell may be seen in Appendix A.

3.3.1 Sample Mounting

Buffer Preparation

The buffer material is used to attach the diamond to the target cell. The small diameter (~ 3 mm) made it difficult to hold the sample in any other manner without
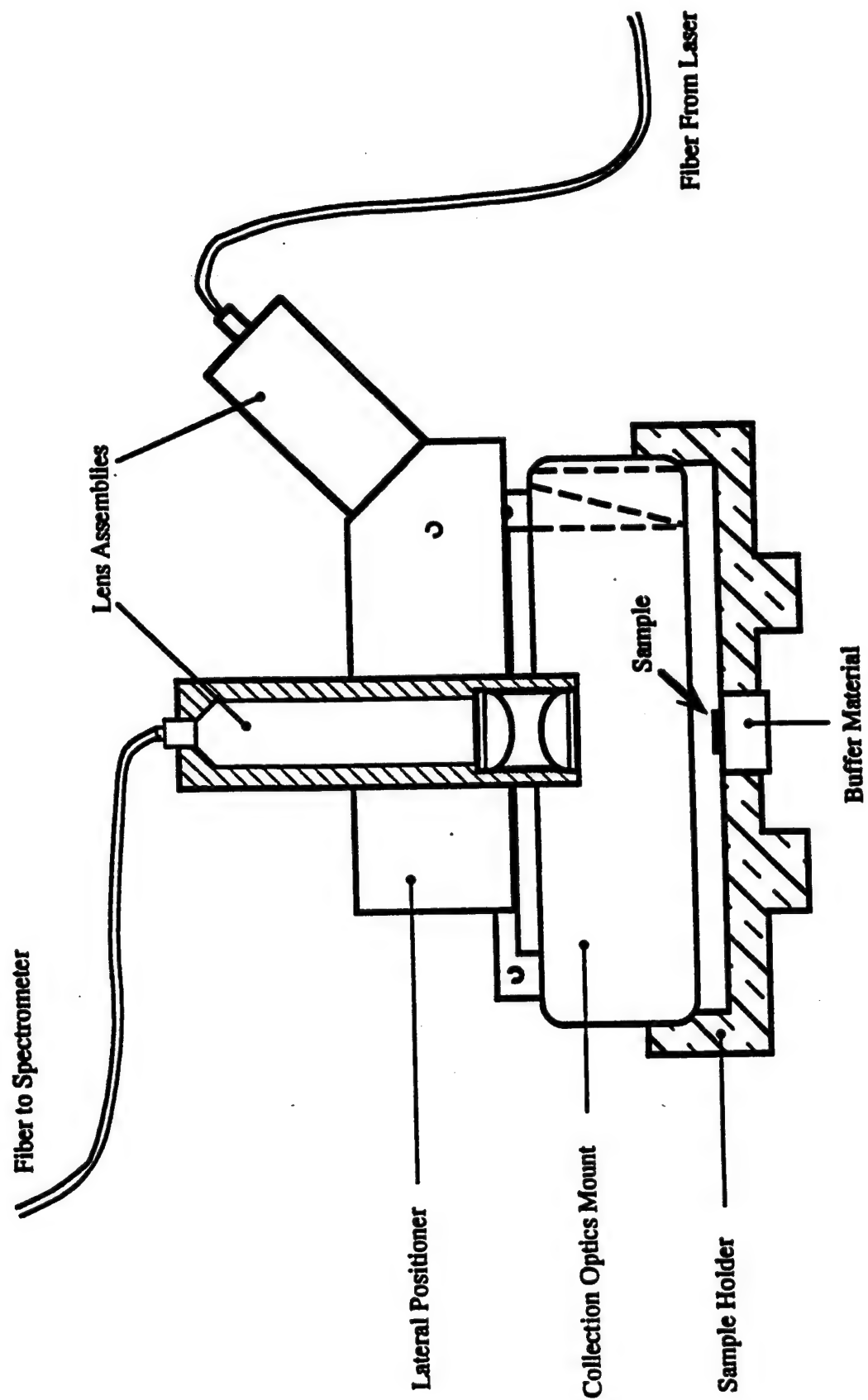
Figure 3.4 Target Cell Schematic.

Fiber From Laser

Fiber to Spectrometer

Lens Assemblies

Sample

Buffer Material

Lateral Positioner

Collection Optics Mount

Sample Holder

A-82

interfering with the laser input or Raman collection paths. After initial experimentation on OFHC Copper, Tantalum, and Platinum buffers, it was found that only the OFHC Copper had adequate thermal conductivity to avoid hot spots and surface damage from the focused laser beam (see Table 3.1). The buffer was highly polished to reflect some of the incident laser light away from the buffer-diamond interface and to improve the overall signal collection.

Each copper buffer was hand lapped in a specially designed jig that held three such pieces. One side was then placed on a polishing wheel and successively polished with 8 μm, 3 μm, and finally 1 μm diamond impregnated paste[71]. Each step in the polishing procedure used a separate nylon cloth on the polishing wheel to avoid cross contamination from the previous grit. After polishing, the surface was examined under a microscope to ensure that the polished surface was free of particles and scratches. If necessary the buffer piece was placed in an ultrasonic cleaner to remove any loose particles. The piece was then measured for thickness and the value recorded for later timing calculations.

Diamond Placement

The bonding of the diamond sample to the buffer, and all subsequent sample assembly, were performed in a laminar flow clean hood to minimize dust and aerosol contamination.

The sample was first centered on the polished buffer surface and held firmly in place in a hand vise using a small amount of pressure; it is important that the diamond not be pressed too tightly against the buffer. Once in place, the diamond was affixed to the buffer using a small bead of 5 minute epoxy placed between the sample edge and buffer and allowed to set for 24 hours. The epoxy must be viscous enough to avoid creeping into the diamond-buffer interface. After 24 hours, the diamond-buffer assembly was removed and examined under a microscope for contaminants.

The quality of the diamond-buffer interface was judged by looking under a Sodium light $\left(\lambda_{Na} = 589.3\,nm\right)$ to examine the interference fringes each of which corresponds to $\lambda/2$. All targets assembled in the manner described here exhibited two fringes at most, with the majority showing only one fringe. The Optical Path Difference (OPD) between the high and low portions of the interface is given by,

$$OPD = \frac{\lambda_{Na}}{2} \times (\# of\ Fringes) \tag{3.2}$$

Because the typical free-surface velocity is $\approx 1\ mm/\mu s$, this path difference results in a 0.6 nanosecond rise time for a two fringe pattern. Since the best resolution attained in this work was ~10ns/track, the wavefront appears for all practical purposes to propagate as a perfect plane wave.

Lastly, the buffer-diamond assembly was fastened onto the sample holder shown in Figure 3.4 with epoxy. Once the buffer-diamond assembly was attached to the sample holder, the holder was then fastened onto the target plate (not shown).

The target plate provides a convenient method for positioning the target cell at the end of the gun barrel. It is a 6 inch round aluminum plate, 3/16 inch thick, with holes appropriately spaced for attaching the target cell and trigger pins used during the shock experiment. The technical drawing for the target plate is given in Appendix A (Figure A.5).

The target plate side mounted onto the end of the gun barrel should be very flat. The plate is first rough sanded on a flat surface and subsequently machine lapped to achieve a flatness to within 1/1000 inch. Subsequently, the sample holder was attached to the target plate. Because working of the material can result in a slight warping, all machining, including drilling and tapping the trigger pin holes, was performed prior to the lapping process.

A-84

3.3.2 Cell Assembly

Transmission and Collection Optics

Figure 3.5 shows the optics assembly used for light transmission and collection. The optical delivery and collection lens systems are identical in construction. Each assembly is composed of two plano-convex lenses 12.5 mm in diameter and a 24 mm focal length that are positioned in the lens holder and separated by a spacer ring. The off-axis design (shown in Figure A.1 of Appendix A) allows for fine adjustment of the focal point by simultaneously moving the fixture up and down while rotating it azimuthally.

A small vent hole ($\approx$ 0.090 inch) is first drilled in the fixture next to the tapped fiber connector hole to allow for air evacuation. The first lens is mounted with the convex side toward the open end of the fixture and is held in place with 5 minute epoxy and the spacer ring.

Before the second lens is installed, the fiber optic connector must be positioned to give a collimated beam. A fiber optic connector (OFTI #300-4SMA-2211) is threaded into the fixture and connected to a laser source used for alignment (HeNe or Ar-ion). The connector may be threaded in and out until a sharp image of the fiber tip is seen. A small drop of epoxy placed between the connector and the lens fixture prevents further movement.

A second vent hole is drilled through the fixture and spacer ring to allow for air evacuation between the lenses. Lastly, the second lens is installed with the convex side facing the first lens as in Figure 3.5.

During assembly care must be taken to keep the lenses free from epoxy, dust, and metal shavings. The laser will burn these materials, possibly fracturing the lens and resulting in experimental failure. It is also important that the fiber fit snugly into its connector because any play in the fiber tip placement may drastically reduce signal collection.
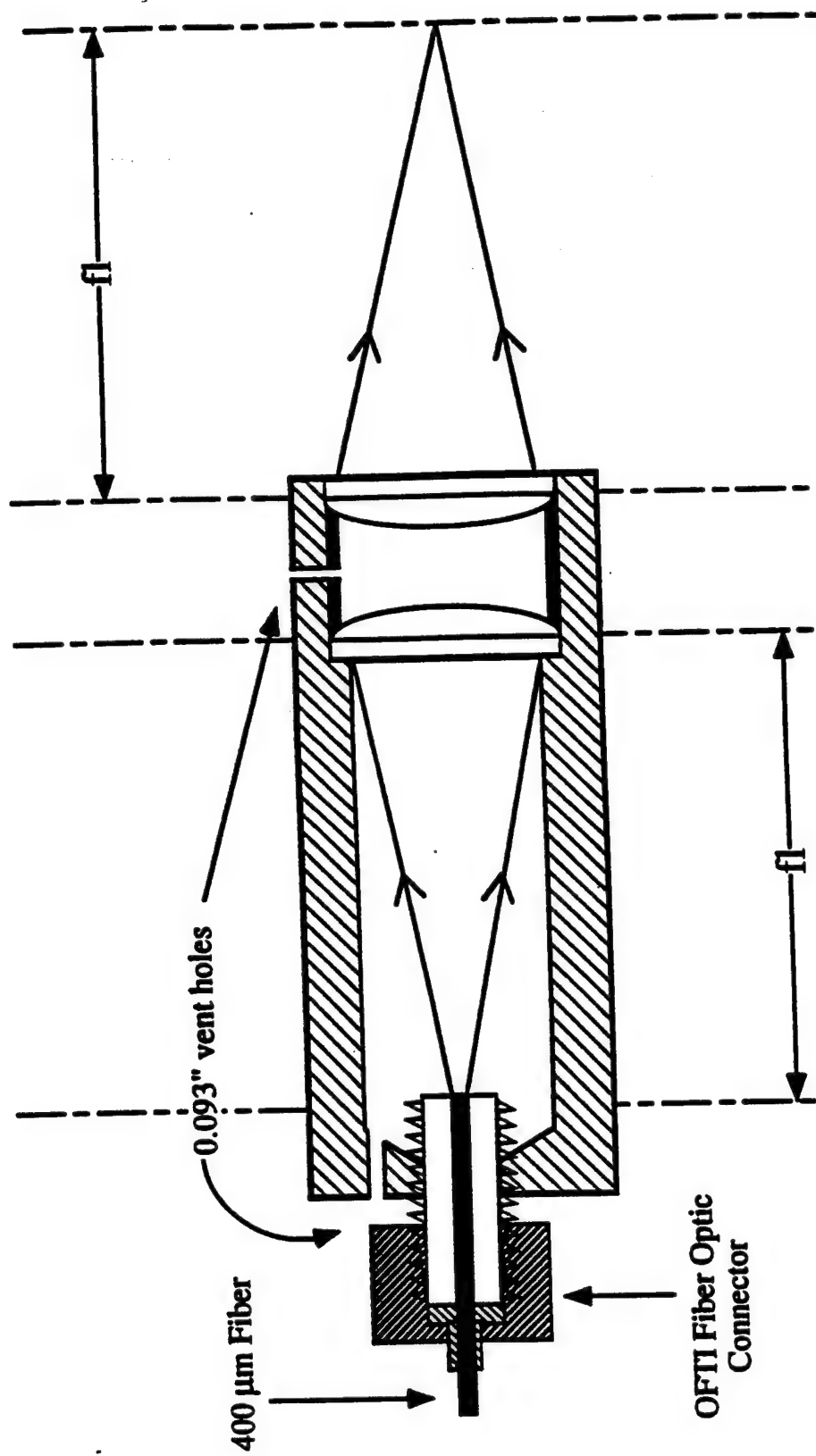
Fig. 3.5   Lens Fixture Details.

0.093" vent holes

400 μm Fiber

OFTI Fiber Optic Connector

fl

fl

Final Assembly

The lateral positioner slides onto the collection optics mount as in Figure 3.4 and is held in place by two #4-40 set screws. Next, the two lens assemblies are inserted into the lateral positioner and secured with #3-48 set screws. This forms the upper half of the target cell.

The sample holder with the attached diamond-buffer piece was fastened to the target plate with three #6-32x1/2" allen head steel screws and six spring loaded Belleville washers. The washers are stacked atop each other as shown in Figure 3.6. This arrangement permits adequate space to make the autocollimation adjustments, discussed in the following paragraph. This formed the lower half of the target cell.

The lower half of the target cell was placed on an alignment bench and viewed through an autocollimating telescope. By adjusting the allen screws, the target plate and the sample were made parallel to within 0.2 miliradian. A drop of epoxy placed on the washers prevented further movement. The top and bottom halves were then threaded together and held fixed by a knurled stop-ring (not pictured). With the target cell thus assembled the optical alignment is performed.

3.3.3 Target Cell Optical Alignment

For the alignment procedure, one end of a dual fiber was connected to a cw laser source (HeNe or Ar-ion) and the two free ends were threaded into the lens assemblies of the target cell. A small piece of semi-opaque packing tape was placed on the diamond surface to provide a screen upon which the beams were focused and positioned. The 45° and 0° beams were first adjusted to a point of intersection in the sample plane defined by the tape. This was most easily accomplished by rotating the threaded top and bottom parts of the target assembly until a satisfactory location was found.

Once the two beams were in rough alignment, fine adjustments were made that moved the focus spot to the center of the sample. The lateral positioner allows
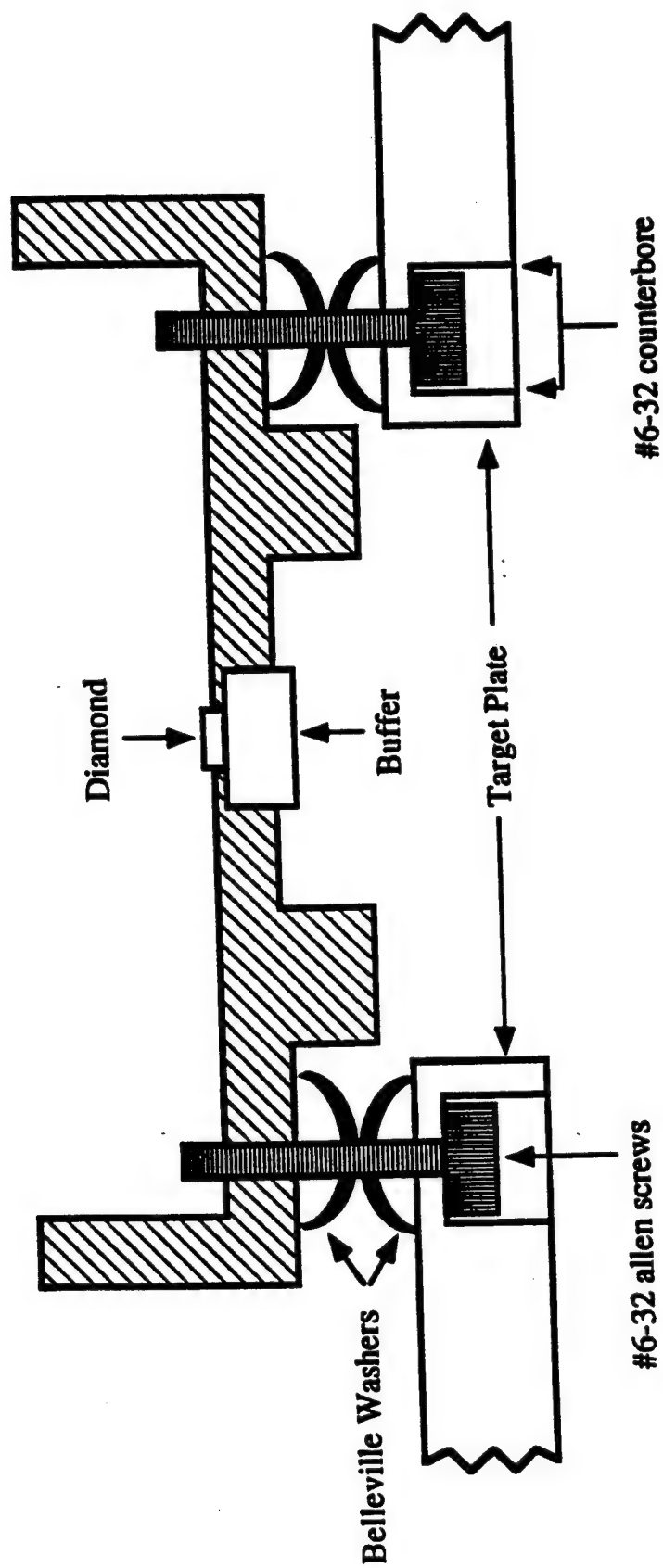
Fig. 3.6 Target Plate -Sample Holder Attachment.

#6-32 counterbore

Diamond

Buffer

Target Plate

#6-32 allen screws

Belleville Washers

movement parallel to the diamond face, and the azimuthal rotation of the lens assemblies permits the focus spot to rotate in the plane. The combination of both of these movements gives an x-y positional capability.

After the two beams were centered and focused onto the diamond, the 45° laser lens assembly was slightly defocused to help avoid laser damage at the diamond-buffer interface. After the alignment procedure, all set screws and the stop-ring were tightened. The tape was carefully removed and the diamond surface cleaned with ethyl alcohol and lens paper.

The small sample size makes the optical alignment exceedingly important in order to avoid edge effects. The laser spot size on the diamond was roughly 0.5 mm and the most common diamond was 2.50 mm in diameter × 0.75 mm thick. For a shock wave traveling at 18 mm/μs, this corresponds to about 40 ns of transit time through the sample thickness. A rough calculation indicates that to reach peak stress before arrival of edge waves, the laser spot cannot stray more than 150 μm from the center of the diamond, or roughly a third of the spot size. A spot that is off center by this much is readily observable to the unaided eye.

3.4 PROJECTILE CONSTRUCTION

In general the projectiles are hollow aluminum (6061-T6) cylinders that are 4" in diameter and vary in length (6-8 inches) depending on the desired velocity. Figure 3.7 is a sketch of a typical projectile with impactor. On one end is mounted the impactor or flyer plate that is fabricated from a material determined by the desired peak stress, and on the other end is a threaded cap also made of aluminum. During a shock experiment the projectile and impactor are accelerated in the gun barrel by using compressed light gas such as Nitrogen or Helium.[72] The impactor strikes the target material launching a stress wave into it and leaving the material behind the wave in a state of uniaxial strain.
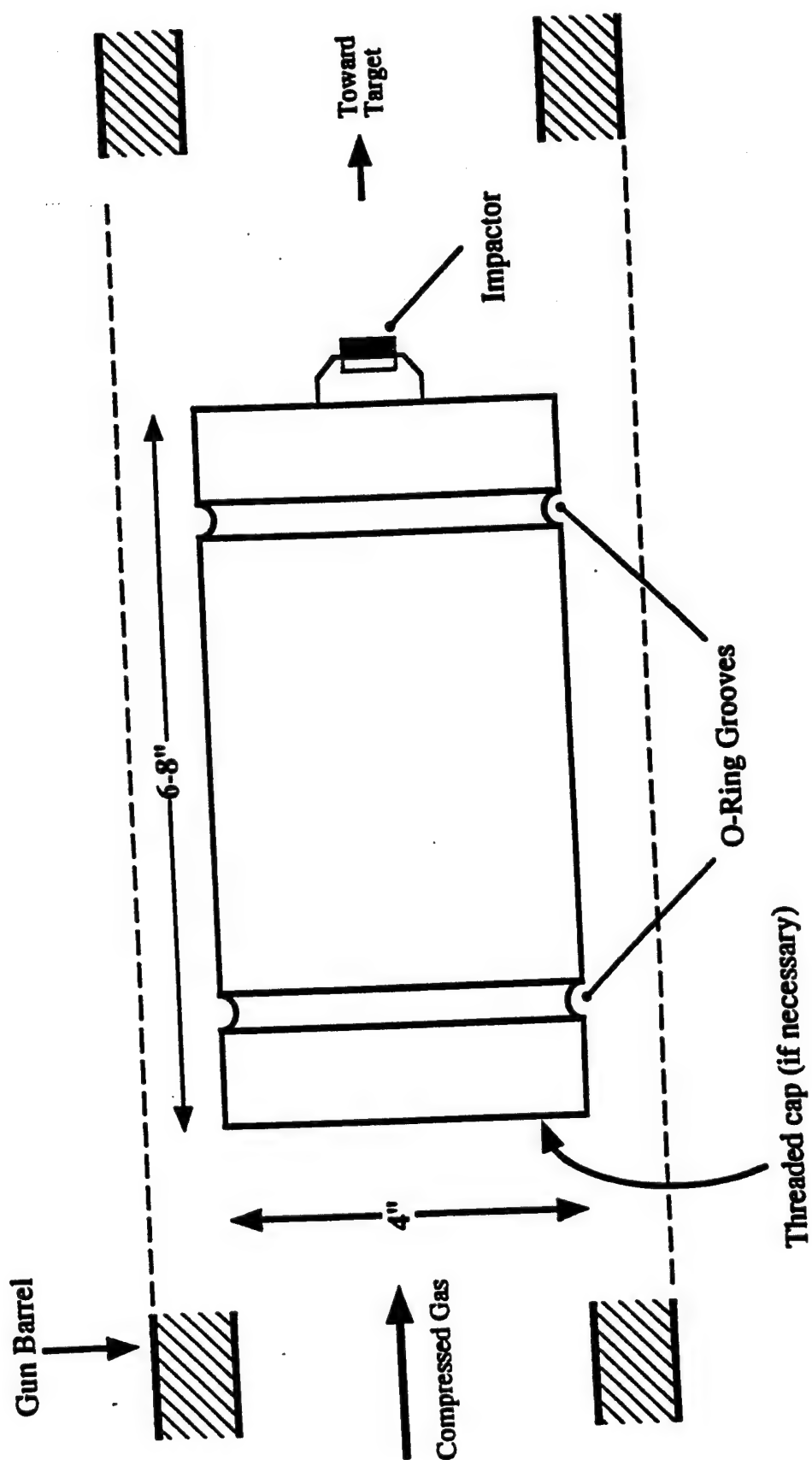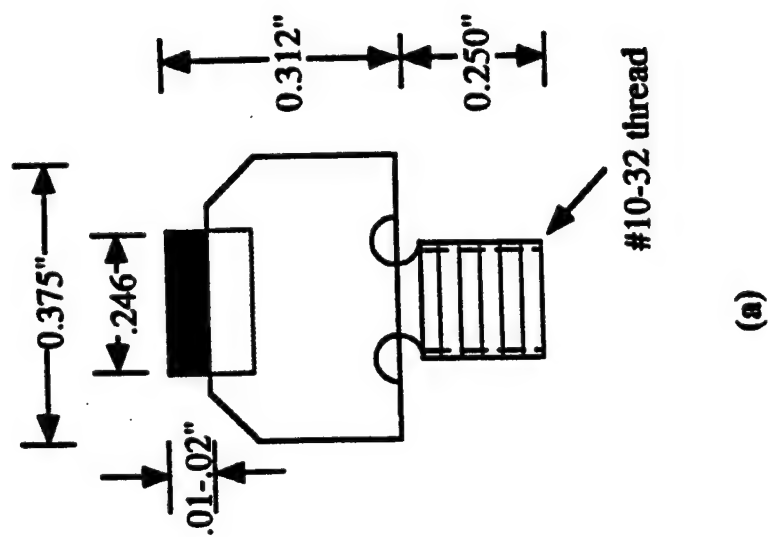
Figure 3.7 Projectile.

The projectiles used in the experiments reported here were of two basic designs: those used for projectile velocities less than 1.0 mm/μs, designated as standard (STD), and those used for velocities greater than 1.0 mm/μs, designated as high velocity (HV). While there are major differences in the two types of projectiles, they perform the same function.

All projectiles used in this work were fabricated by the Technical Services machine shop at Washington State University (WSU). The technical drawings are given in Appendix A. Figure A.6 is a drawing of the STD projectile used in the wrap-around breech for the slower velocities and Figure A.7 shows the HV projectile used in the double-diaphragm breech experiments. Details of these breech configurations as well as other details regarding the light gas gun facility is given in the paper by Fowles et al.[72]
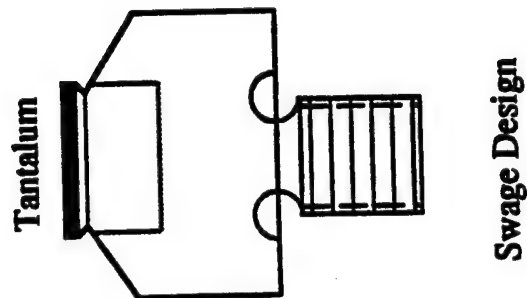
The HV projectile design of Figure A.7 was made by P. Bellamy of the Shock Dynamics Center at WSU. The fastest velocity achieved using this design, with a platinum impactor, was 1.21 mm/μs for this work. However, the same design reached 1.28 mm/μs without an impactor during the testing phase. Velocities of 1.3 mm/μs are attainable with the light gas gun and more advanced projectile designs currently being considered may exceed this figure.
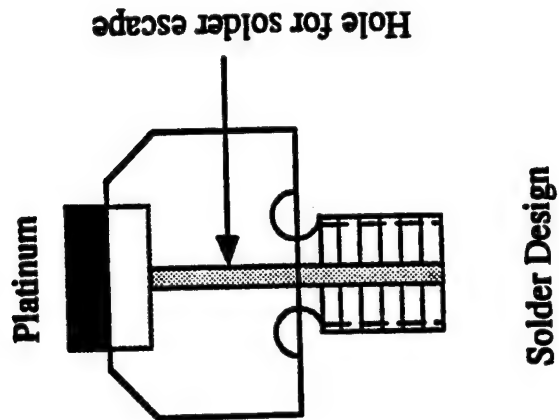
3.4.1 Impactor Design

The impactor materials used were OFHC Copper, Tantalum, Platinum, and Sapphire. Aside from the Sapphire impactor, all impactor assemblies were of the same basic design as shown in Figure 3.8. The only difference was in the manner in which the impactors were held in place. Figure 3.8 (a) gives the overall dimensions for all impactor assemblies; this impactor assembly was made out of a single piece of OFHC copper. Figure 3.8 (b) shows the swage technique for holding the Ta material in place. This material resisted the solder that was used to hold the Platinum material in place. Figure 3.8 (c) shows the Platinum impactor and the small canal through which the excess solder

Hole for solder escape

Platinum

Solder Design

(c)

Tantalum

Swage Design

(b)

0.312"

0.250"

0.375"

.246

#10-32 thread

.01-.02"

(a)

Fig. 3.8   Impactor designs : (a) Copper; (b) Tantalum; (c) Platinum.

was allowed to flow. All of these impactors were slightly undercut to allow better seating against the projectile face.

The actual mounting of the impactor assembly to the projectile was accomplished in the following way. First, a small amount of 815 epoxy was placed on the threads on the back side and the impactor assembly threaded into the projectile face until properly seated. This was allowed to cure for 24 hours. Once cured, the projectile was placed in a lathe and machined such that the projectile face and the impactor face were parallel to within 1/1000 inch. Lastly, any tooling marks were hand lapped from the impactor surface.

For the sapphire impact experiments performed in this study, a different style impactor was used. This impactor design is described in the previous work of Gustavsen and Gupta.[12]

3.5 OPTICAL INSTRUMENTATION

3.5.1 Flashlamp-Pumped Dye Laser

The unusually short recording time for shock experiments ($\approx 1\mu s$) places stringent constraints on the laser source used for Raman experiments. For a satisfactory signal-to-noise ratio, there must be a large number of photons delivered to the sample in a relatively short time span. Most continuously operated lasers lack the necessary energy flux for fast event recording, while the majority of the pulsed lasers provide adequate power but have pulse widths that are too narrow (<100ns). In addition, Q-switched lasers can sometimes display multiple output pulses if the Q-switch opens too slowly.[73] These secondary pulses introduce timing uncertainties which are unacceptable for shock experiments

The flash-lamp pumped dye laser used in this work was the Cynosure (Candela) model SLL-5000 coaxial flashlamp dye laser capable of providing high energy per pulse

at low repetition rates. In the single-shot mode, the SLL-5000 is capable of delivering 20 Joules into a 3.5 μs FWHM pulse, yielding roughly 6 MW.

Using a three prism tuner, this laser is continuously tunable over the entire spectrum from 390-950 nm using commercially available dyes. The dye used for the present experiments was Coumarin 504 supplied by Exciton. This dye has good energy efficiency, an acceptable lifetime, and may be easily tuned to the Argon-Ion laser line at 514.5 nm.

The dye circulator that accompanies the laser head is a closed cycle system with a 20 liter capacity for solvent and dye. The large capacity allows for lengthy use (typically 100 shots) before dye replenishment. The dye is initially dissolved into 200 ml Ethyl Alcohol and then poured into the solvent tank containing 20 liters of Ethylene Glycol. A mixture of 50/50 methanol and distilled water is recommended by the manufacturer as the dye solvent, however, the Ethylene Glycol gives adequate performance without the fire hazard.

The beam uniformity is somewhat affected by thermal distortions at high energy output but can be minimized by using low dye concentrations. To further improve beam quality, a Schotland Triax[74] dye cell is also used. This dye cell is essentially a triple lumen tube made of fused quartz. The dye is circulated in the center tube and a vacuum is maintained between the inner and outer quartz tubes. This feature supposedly has better thermal characteristics when the laser is used at a higher repetition rate. Because the laser was only used in the single shot mode, any improvement due to the Triax configuration was not readily apparent. Table 3.2 summarizes the main features of the dye laser.

Maxwell Trigger

The model 40295 Maxwell trigger generator supplies a 100 kv pulse for triggering high voltage equipment such as the Candela SLL-5000 dye laser. This unit bypasses the built-in trigger source of the dye laser which manifested unacceptable jitter problems (on

Table 3.2 Dye Laser Operating Parameters.

Energy Storage	5000 J
Maximum Rep. Rate	0.1 Hz
Output With Triax	20 J
Pulse Width FWHM	3.5 μs
Tunability	390-950 nm
Linewidth	0.2 nm ($\sim$ 8 cm^{-1})
Beam Divergence	1.5 mR
Flashlamp	Coaxial
Beam Diameter	2.0 cm
Solvent	Ethylene Glycol
Dye	Coumarin 504
Concentration	2.7×10^{-5}

tne order of several hundred nanoseconds) for the present work. The advertised jitter of the Maxwell trigger generator is ~ 10ns. While this unit did indeed solve the jitter problem, it became evident that careful electrical shielding was necessary to minimize the enormous electromagnetic pulse generated at the trigger source.

3.5.2 Optical Fibers and Lenses

The use of optical fibers to transmit the laser light greatly simplifies the experimental design and eliminates most of the tedious alignment problems. Fibers also act to homogenize the laser beam resulting in fewer hot spots and, in general, a more uniform beam profile.

The fibers used for this work were Mitsubishi ST-U400E-SY fused silica optical fiber. This fiber features a high purity 400 μm silica core, a 500 μm fiber diameter and a Nylon jacketed outer diameter of 1.3 mm. It is a step index, multi-mode fiber possessing a wide range of spectral transmission (500-2100nm) and a numerical aperture of 0.2.

To collimate and focus the laser light at the fiber end, two simple plano-convex lenses provided by Rolyn Optics Co. (Stock # 10.0035) were used. They were 12.5 mm in diameter, made from B-270 Crown glass, with a 24 mm focal length.

3.5.3 Spectrometer

The scattered signal from the sample was transmitted to the triple spectrometer (SPEX Model 1877 Triplemate) where it was spatially dispersed. The SPEX is a two stage spectrometer specifically designed for use with CCD's or Vidicon detectors. The first stage is a double monochromator that acts as a selectable bandpass filter feeding the entrance slit of the second stage. The entrance slit is continuously adjustable from 25 μm to 2000 μm in 1 μm increments. The second stage is a 0.6 m single monochromator spectrograph consisting of two concave mirrors and a plano diffraction grating in a

Czerny-Turner configuration. The experimenter may select one of three diffraction gratings (64 mm x 64 mm) mounted on a manually operated turret.

The performance characteristics of the spectrometer depend upon which grating is used. To calculate the dispersion behavior for diffraction gratings, the starting point is the grating equation given by[75]

$$d \sin \alpha + d \sin \beta = m\lambda \qquad (3.3)$$

where d is the groove spacing, α is the angle of incidence, β is the diffracted angle, m is the diffraction order, and λ is the wavelength of the incident light. For a constant angle of incidence, differentiating Eq. (3.3) with respect to λ gives information on how the angle of diffraction depends on wavelength. This is called the angular dispersion for the spectrometer and is given by the expression:

$$\frac{d\beta}{d\lambda} = \frac{m\rho_G}{\cos\beta} \text{ rad/nm} \qquad (3.4)$$

where $\rho_G = d^{-1}$ is the grating groove density in grooves/nm. For the geometry considered here $\cos\beta \approx 1$; hence, the angular dispersion is equivalent to the groove density in nanometers for first-order diffraction.

The linear dispersion is given by the product of the focal length of the spectrometer and the angular dispersion[76]

$$\frac{dx}{d\lambda} = f \times \frac{d\beta}{d\lambda} = f \times m\rho_G \text{ (mm/nm)} \qquad (3.5)$$

Thus, the linear dispersion describes the change in wavelength corresponding to a given distance in the focal plane of the spectrum. For two peaks with wavelengths that differ by an amount $\Delta\lambda$, the separation in the focal plane Δx would be

$$\Delta x = \left(\frac{dx}{d\lambda} \right) \Delta\lambda \qquad (3.6)$$

The ability of a spectrometer to distinguish between adjacent spectral lines is given by the Rayleigh criterion which states that two peaks may be considered resolved if the distance between them is such that the maximum of one falls on the first minimum of the other. This criterion may be written as[77],

$$\Delta x = \frac{f\lambda}{W} \qquad (3.7)$$

where W is the width of the grating. Combining Eqs. (3.5) - (3.7) yields the resolving power of the spectrometer R,

$$R = \frac{\lambda}{\Delta\lambda} = m \cdot N \qquad (3.8)$$

where N is the total number of grooves on the grating obtained by multiplying the groove density ρ_G by the grating width W. The resolving power may be improved by increasing the number of total grooves on the grating or considering higher diffraction orders.

The spectrometer bandpass at FWHM is defined as the product of the slit width and the linear dispersion[77],

$$Bandpass = \left(\frac{d\lambda}{dx} \right) \times slit\ width \qquad (3.9)$$

Thus, Eq. (3.9) sets the minimum slit width necessary to observe a desired bandpass for a fixed linear dispersion.

An image of the entrance slit is formed at the spectrometer output as illustrated in Figure 3.9. In the absence of a time slit, the 400 μm fiber is imaged as a rectangle with a

Slit Width

Fiber →

400 μm

(a) Input at Entrance Slit
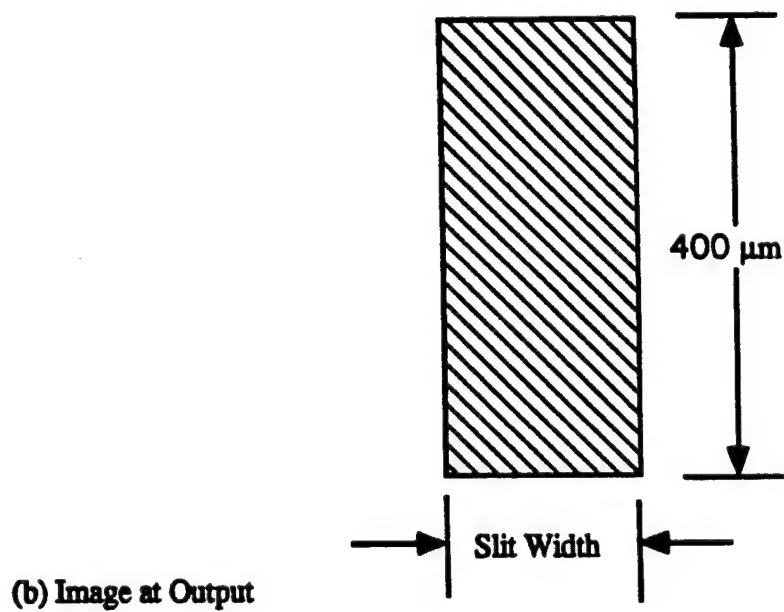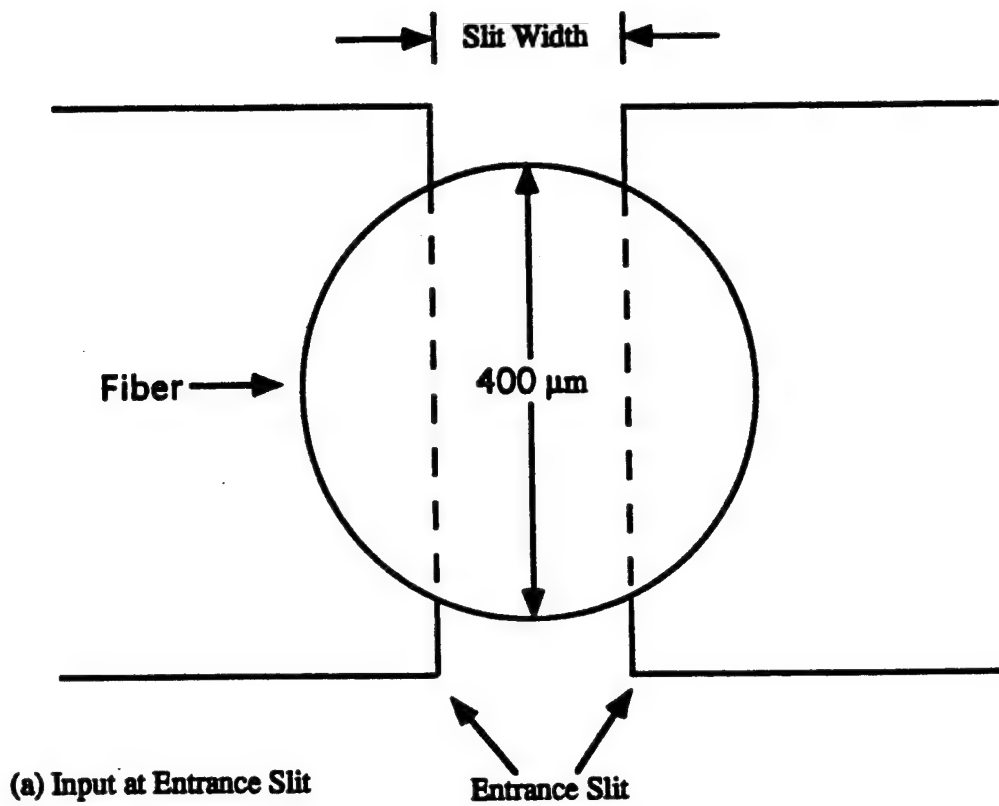
Entrance Slit

400 μm

Slit Width

(b) Image at Output

Figure 3.9 Spectrometer Entrance and Output Images.

width corresponding to the selected entrance slit width and a height given by the diameter of the fiber.

Two gratings were used in the present work, one with a groove density of 1200 groove/mm and one with 1800 groove/mm. Also, the bandpass was effectively set by the linewidth of the dye laser given in Table 3.2 as 0.2 nm (8 cm^{-1}). Table 3.3 summarizes the performance characteristics of the spectrometer for the two gratings used in this study.

Table 3.3 Spectrometer Performance Characteristics.

Grating Density	1200 gr/mm	1800 gr/mm
Linear Dispersion	1.39 nm/mm	0.93 nm/mm
Slit Width	250µm	200µm
Bandpass	0.35 nm (13 cm^{-1})	0.19 nm (7.5 cm^{-1})
Resolution @ 514.5 nm	0.007 nm	0.004 nm
Spectral Coverage	34.8 nm (1316 cm^{-1})	23.3 nm (880 cm^{-1})

Note that for the 1200 groove/mm grating, the minimum slit width established by Eq. (3.9) is 144 µm for a 0.2 nm bandpass; however, to obtain an adequate signal-to-noise it was necessary to open the entrance slit to 250 µm, resulting in a somewhat larger bandpass.

3.5.4 Raman Filter

Under normal operation, the filter stage of the SPEX Triplemate is used to eliminate the Rayleigh component from the Raman signal. However, use of the filter stage results in serious throughput problems and leads to poor signal-to-noise ratios.

The recent development of Raman Holographic Edge (RHE) filters[78] has improved signal collection and Rayleigh rejection considerably . These filters offer high optical

density and angular tunability. They are specifically designed for use in Raman spectroscopy to reject the Rayleigh line and to transmit the spectrally shifted Raman signal. The system throughput as well as the signal-to-noise, is markedly improved with this filter. For the present work the filter stage of the SPEX was bypassed by using a Raman Holographic Edge (RHE) filter.

Holographic edge and notch filters are fabricated by recording interference patterns formed by coherent laser beams in an organic substrate such as dichromated gelatin. Once the emulsion is developed, it is hermetically sealed to protect it from moisture. The high optical density of the filters (over 4.0) provides excellent rejection of the Rayleigh scatter. The spectral width of these filters is typically < 10 nm over the optical density range 0.15 < OD < 4.0, indicating that Raman signals may in principle be detected less than 100 wavenumbers from the laser line. Figure 3.10 (a) and (b) show the OD and transmission as a function of wavelength for a typical notch filter.[79]

The two filters used in this work were: model RHE414.1D fabricated by Physical Optics Corporation (POC) and model HNF-514-1 made by Kaiser Optical Systems.

3.5.5 Streak Camera

Once the spectrometer output image has passed through the Raman Holographic Edge filter, the predominant component of the signal is that due to Raman scattering. The signal then enters an image converting streak camera which records the event and disperses it in time. This allows the experimentalist to correlate each spectrum with a specific time-frame as the event develops.

For the present work, an Imacon Model 790 streak camera was used for temporal dispersion of the spectrometer output. The Imacon 790 incorporates an image converter tube with three pairs of deflection plates in the space between the anode and the screen as illustrated[80] in Figure 3.11. An objective lens forms an image of the spectrometer output which passes through an electrode/anode focusing pair and is converted to an electron
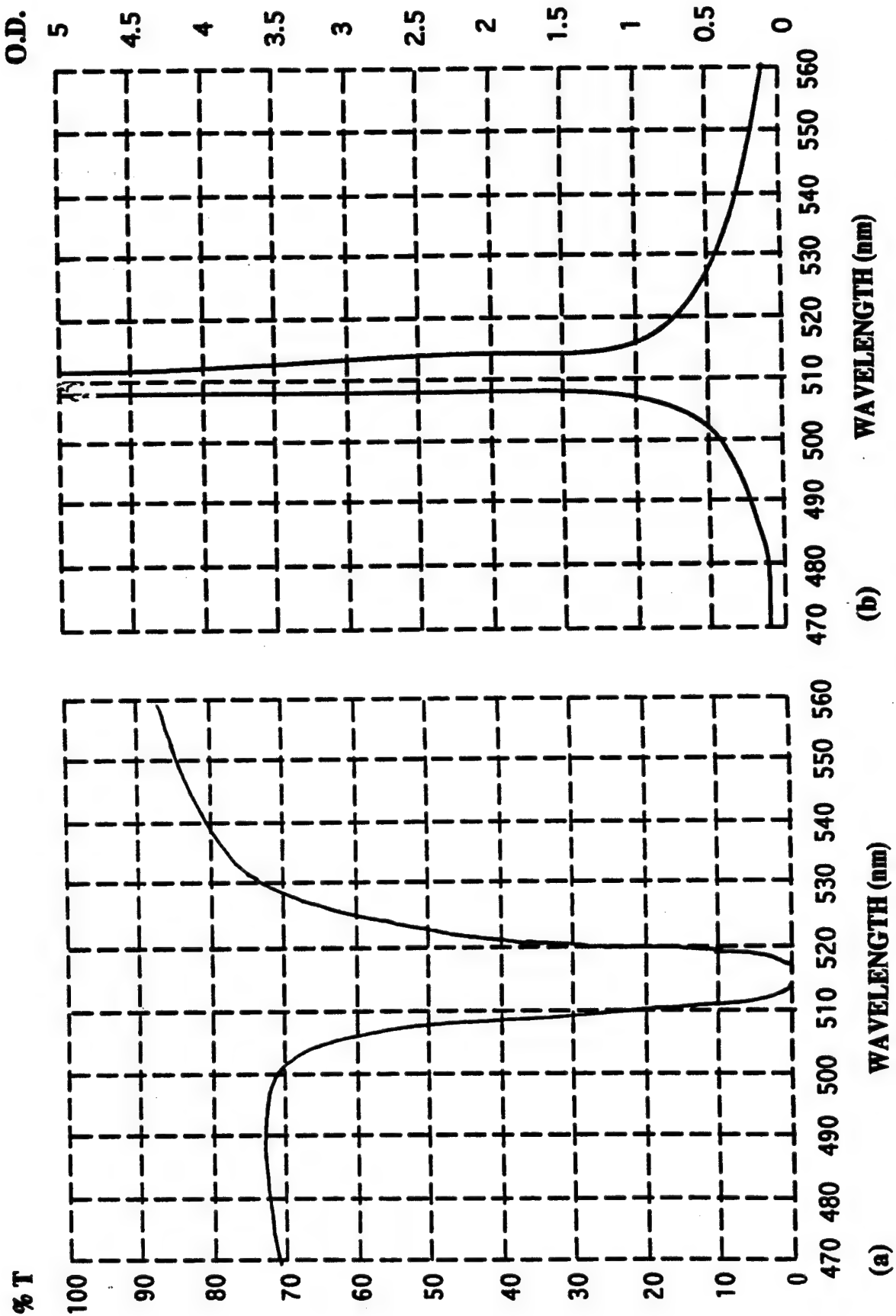
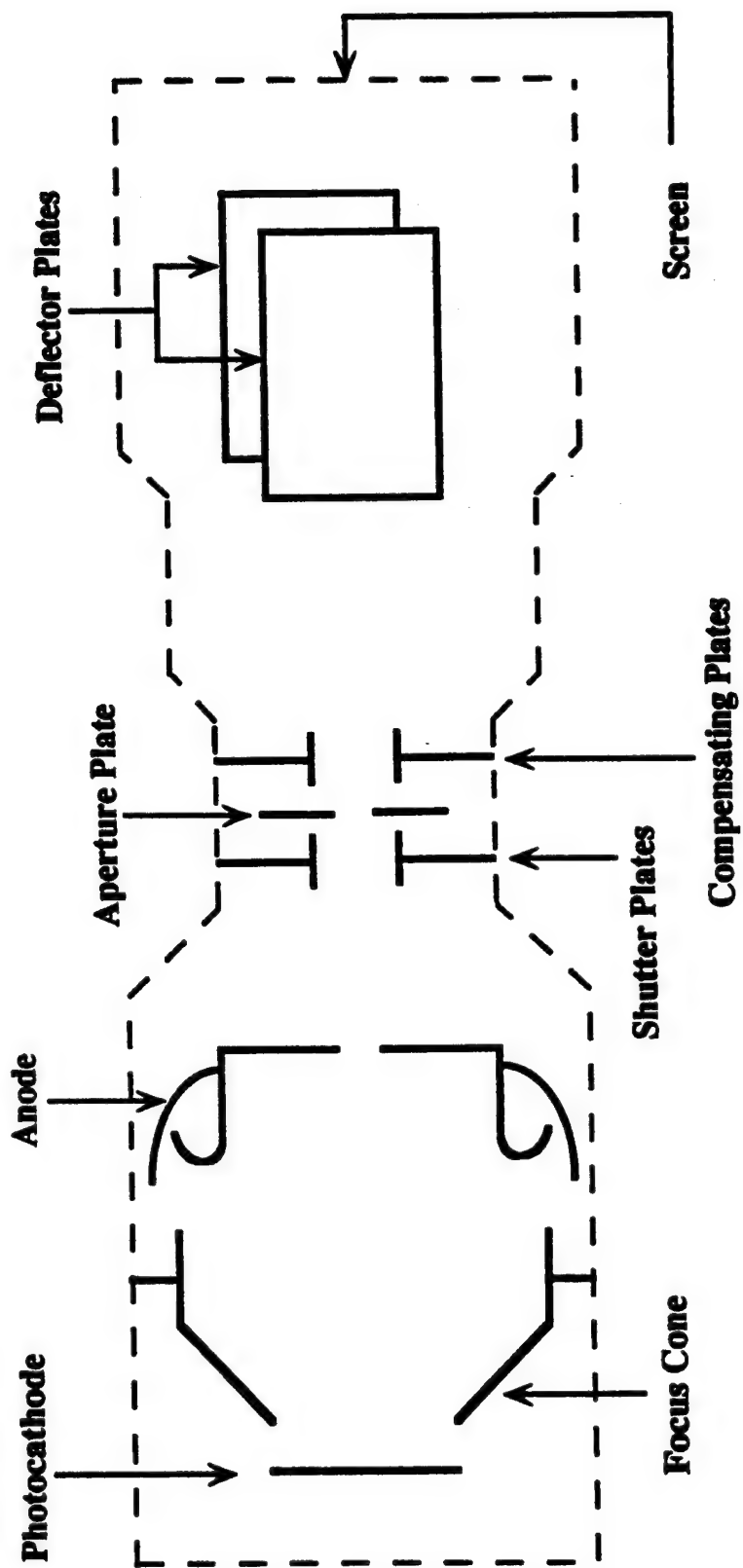Fig. 3.10 (a) Transmission vs. Wavelength, (b) Optical Density vs. Wavelength.

Figure 3.11 Streak Camera Diagram (Adapted from Ref.81).

beam forming a sharp image onto the phosphor screen. Prior to triggering, the electron beam is deflected onto the aperture plate by a constant bias across the shutter plates. When the trigger pulse arrives, the potential across the shutter plates drops to zero allowing the beam to travel to the center of the aperture plate and the streak recording begins. This technique eliminates fogging at the beginning of the streak, thus allowing full use of the available 70 mm streak window.

The temporal resolution ΔT of a streak camera is determined by the streak speed V_s and the image height L on the streak screen,[81] thus

$$\Delta T = \frac{L}{V_s} \qquad\qquad (3.10)$$

The streak camera is capable of streak speeds ranging from 0.01 mm/µs to 300 mm/µs depending on the streak plug-in used. The streak speeds used for the present study were 50 mm/µs and 20 mm/µs. For the 400µm image height, Eq. (3.10) gives a temporal resolution of 8 ns and 20 ns for these streak speeds.

The total recording time for the streak camera may also be determined from the screen dimensions. For the Imacon 790, the phosphor screen has dimensions 70 mm (temporal axis) by 40 mm (spatial axis). Thus, for a streak speed of 50 mm/µs, the total writing time would be 1.4 µs. The usable portion of the total streak recording is limited, however, by the active area of the two-dimensional detector. This is typically on the order of 2-3 cm.

A plug-in is located on the side of the streak camera for calibration purposes. During the temporal calibration procedure (discussed in Section 3.6.1) the operator may apply a constant voltage directly to the deflection plates via this plug-in. When the applied voltage is supplied by a precision time-delay generator, the time resolution of the streak record may be determined. This procedure it treated in detail in Section 3.6.1.

3.5.6 Image Intensifier

An ITT Model F4113 proximity-focused microchannel plate image intensifier was directly coupled to the streak camera active screen. To reduce the background noise, the intensifier was operated in the gated mode. The intensifier has a 40 mm diameter active area and is powered by a 5 volt Dexter Model DS405 power supply. When operated at high gain position, the applied dc voltage across the tube is about 600 volts with a corresponding gain of 5000.

The proximity-focused image intensifier takes the image that is focused onto its photocathode and converts it into electron energies pixel by pixel yielding roughly one electron per incident photon. The electron is confined to a microchannel segment and is accelerated to a positively charged phosphor screen, initiating a cascade of electrons in the process. The electrons are converted back into photons when they strike the phosphor screen. Thus, each pixel has its own image intensifier formed by an individual microchannel in the plate. These devices are capable of producing large signal gain (>5000) while keeping dispersion to a minimum.[82]

3.5.7 Vidicon Detector and OMA

The image intensifier output was lens-coupled to a two-dimensional detector. For most of the experiments, the coupling was to a EG&G model 1254 intensified Vidicon, while for three of the experiments a EG&G model 1430P CCD detector was used.

For both arrangements, the detector head consists of a $n{\times}m$ pixel array that is oriented such that the horizontal direction corresponds to the wavelength and the vertical to the time. Both detectors are programmed through the OMA (Optical Multichannel Analyzer) in a similar manner with only minor differences. The intensified Vidicon system is described in detail because it was used for the bulk of the experimental work.

The Vidicon consists of a 500 × 500 pixel array that must be partitioned in a manner which preserves the fiber image. The active detector area is 2.5 cm × 2.5 cm which is only about 1/3 the total streak length of 70 mm. To determine where the detector is operating within the streak record, the streak camera calibration plug-in described in Section 3.5.5 is used to provide a fiducial that appears on the digitized output as a wavelength shifted spectrum.

To optimize the use of the detector array, one begins by choosing the number of channels that will adequately represent the spatial extent of the spectrum of interest. Two considerations must be taken into account: first, it must be certain that there are enough channels to allow for the anticipated shifts of the spectral line for the grating in use, and second, one must keep in mind that the reading time increases with more channels and this increases the likelihood that charge will 'leak' off, resulting in decreased signal-to-noise. For these reasons, I selected 200 and 400 channel widths corresponding to the 1200 gr/mm and 1800 gr/mm gratings, respectively.

In the temporal direction, the detector array is divided into tracks consisting of several pixel elements each. Because the pixel size is $\approx 25\mu m$, the 400 μm fiber may be imaged onto a track 16 pixels high yielding a total of 31 tracks for the time axis. Hence, there are $31 \times 200(400) = 6,200(12,400)$ data points per record.

Figure 3.12 shows an OMA record for a single track and for 31 tracks comprising a single streak record; the data shown are for the Raman line of diamond (1332.5 cm^{-1}) at ambient conditions. The number of counts (intensity) fluctuates from track to track due to the high amplification and variations in the incident laser intensity.

Target Cell testing At Ambient Conditions

The target cell was test streaked in the Raman system to check for an adequate signal which was characteristically about 1500-2000 counts. If the number of counts was
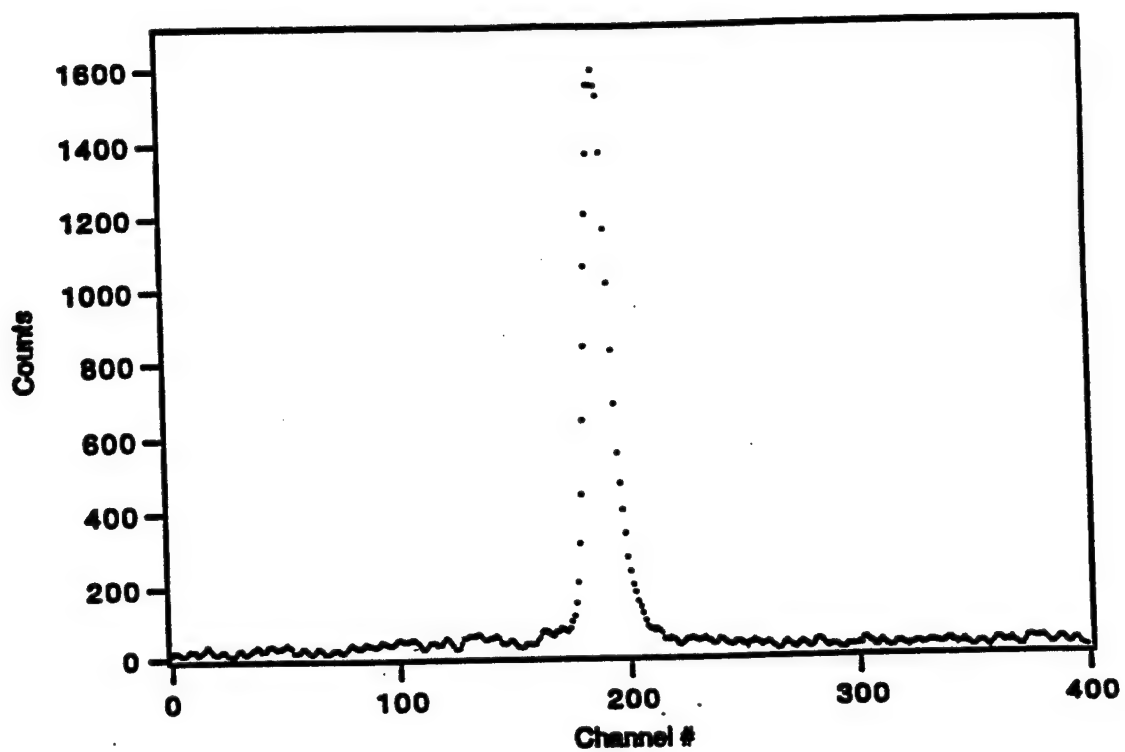
Figure 3.12 (a) Single OMA Track Recording of the 1332.5 cm^{-1} Raman Line in diamond.
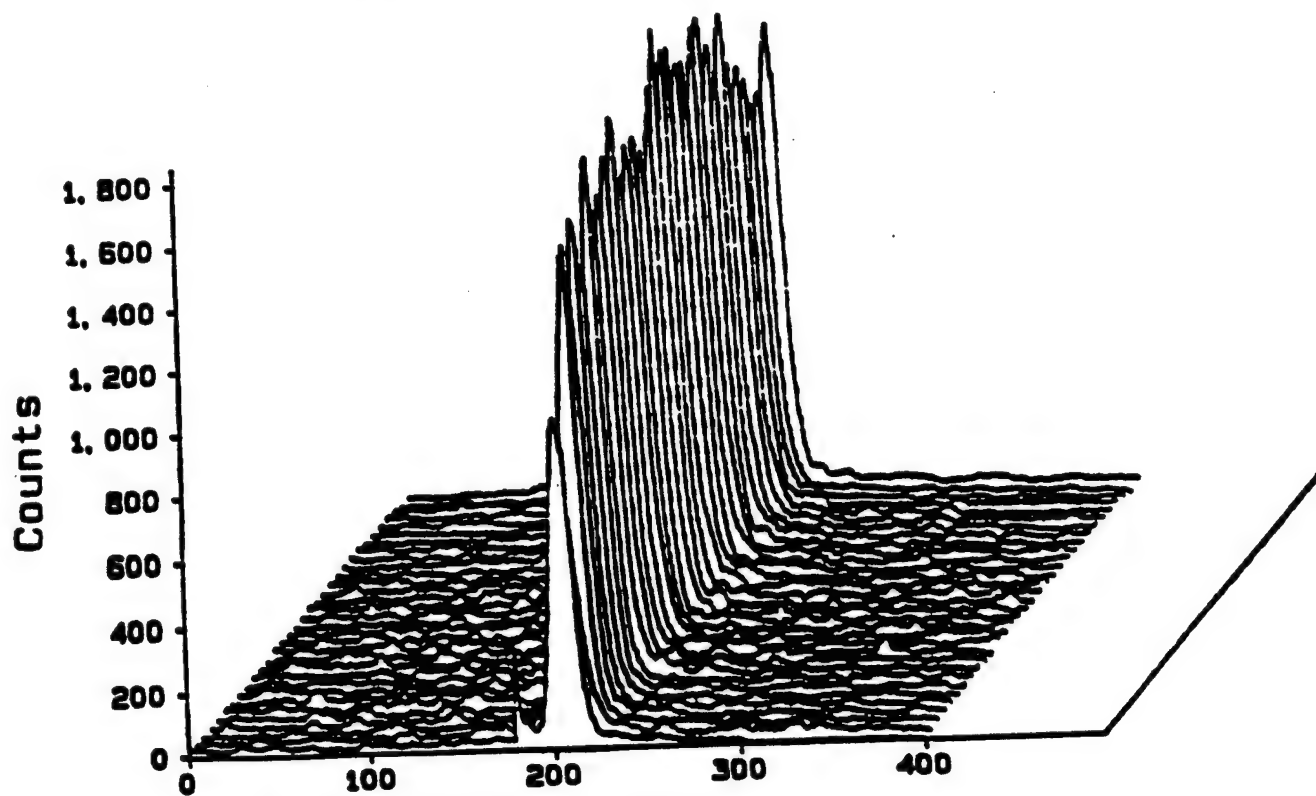

Figure 3.12 (b) Complete OMA Record for 31 Tracks.

A-107

found to be unacceptably low, the laser energy at the fiber output was first checked with a Joulemeter. The Mitsubishi fiber is capable of delivering 100-150 mJ without damage to the core, however, that amount of energy focused onto the sample will cause damage at the Copper surface. It was found that 75 mJ was a tolerable energy level. If necessary, the above alignment procedure was repeated until a sufficient signal was detected.

Setting up the Raman system, locating the phonon, and setting the laser energy should be performed first on a dummy diamond target. The number of laser pulses that strike the real target must be kept to a minimum (three or less) to avoid accumulative laser damage.

Once the target cell has produced an acceptable signal, several dabs of epoxy finalize the cell configuration. The completed target was kept under a clean hood until experiment time.

3.6 CALIBRATION AND DIAGNOSTICS

3.6.1 System Calibration

Before each experiment, the system was calibrated for spatial and temporal resolution. Because the instrumentation was being used for other experimental studies and by other researchers, the calibration procedures were necessary to ensure that the claimed resolution was correct and had not changed from experiment to experiment.

Wavelength Calibration

With the dye laser tuned to the 514.5 nm line of the Argon laser, the diamond Raman line may be observed at ~552 nm (about 1333 cm^{-1} away). Usually, the wavelength calibration is performed by using a spectral line from a well established calibration source such as the 546.1 nm green line of Mercury. However, for the present

study the spectral region of interest is only ~6 nm wide and because there are no adequate sources for calibration in this region the following method was used.

The calibration was performed by mapping the active detector area with the Argon laser line as it was scanned with the SPEX spectrometer. The spectrometer was first calibrated to the 514.5 nm Argon line and then readings were taken at five spectrograph settings spanning the active channel area defined by the OMA (i.e. 400 channels). At each reading the spectrometer setting was recorded and a least squares fit to the channel vs. wavelength was performed. The slope of this fit yielded the wavelength/channel calibration.

For the 1200 groove/mm grating, this calibration was approximately 0.028 nm/channel (1.06 cm^{-1}/channel) and for the 1800 groove/mm grating it was roughly 0.01785 nm/channel (0.67 cm^{-1}/channel). Because lens coupling to the detector introduced a small amount of spherical aberration at the detector edges, this calibration was performed for each track comprising the streak record.

The channel to wavenumber calibration and conversion was given by,

$$\omega(cm^{-1}) = 1332.5\,cm^{-1} - m(x - x_0) \tag{3.11}$$

where m is the slope in units of cm^{-1}/channel, x is the channel number, and x_0 is the least squares fit to the channel number of the unshifted phonon peak for all tracks prior to impact. The excursion of the ambient Raman peak from channel x_0 gives rise to the uncertainty in the frequency shift shown in the next chapter.

Temporal Calibration

Figure 3.13 is an illustration describing the temporal calibration. To begin the calibration, the streak camera is configured to scan the 514.5 nm line of the Argon laser at the streak speed to be used during the experiment. An external trigger pulse is manually
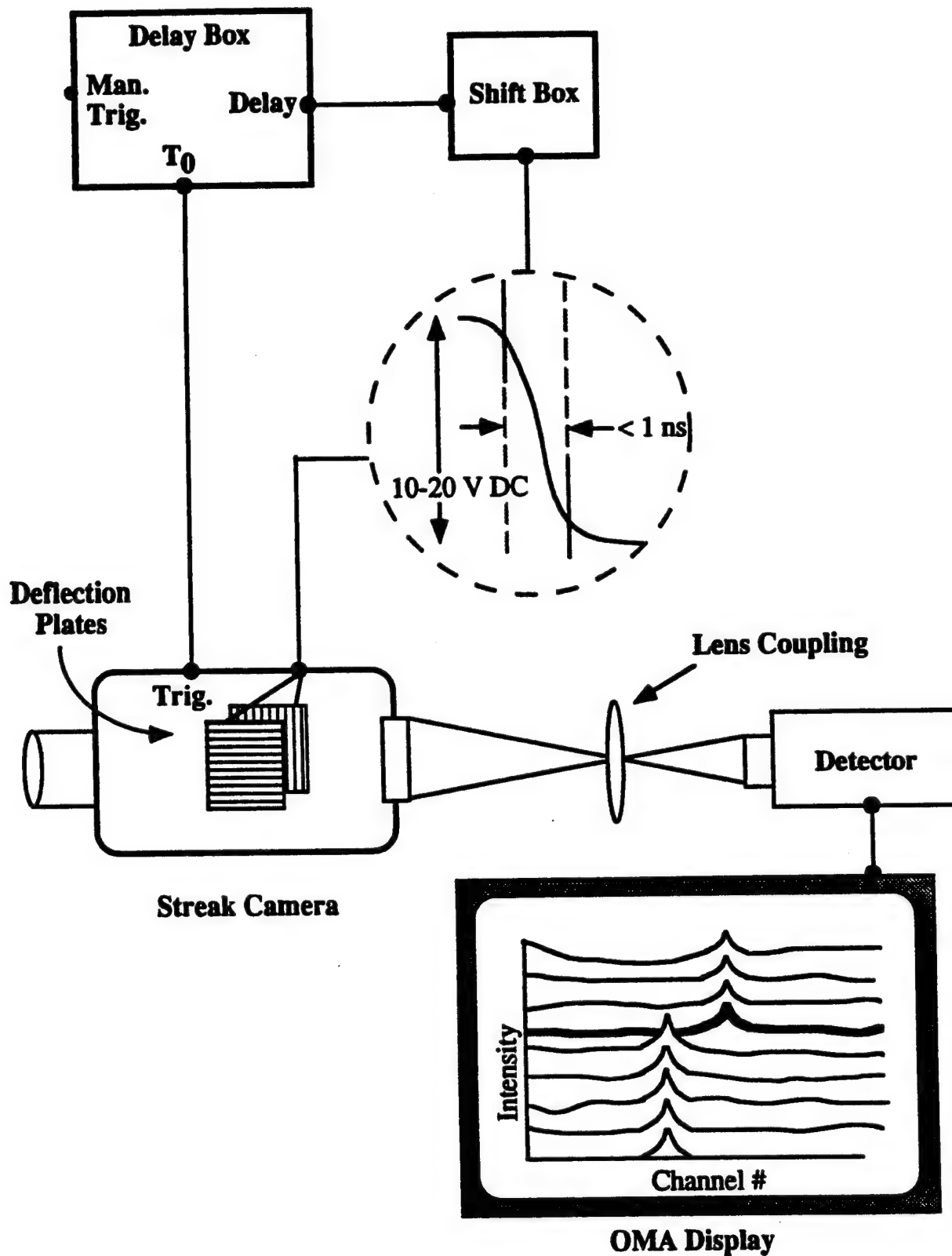
Fig. 3.13   Time Calibration .

supplied to the delay box indicated in the figure. The streak camera is triggered directly from the T_0 output of the delay box and at a time T ($T=T_0$+delay) later, a pulse is sent to the Shift Box. The Shift Box delivers a fast-rise (<1 ns), 10-20 v DC pulse to the deflection plates of the streak camera. In the figure, the highlighted track on the OMA display shows where the shift might occur. The remaining tracks show a constant shift proportional to the applied external voltage. By adjusting the delay output, one may move the shift point forward or backward in the streak window.

A typical experiment might indicate a 1.14 μs delay to track #30 and a 0.86 μs delay to track #1, yielding a time resolution of 9.6 ns /track. The temporal calibration was performed in this manner for all experiments for the streak speed used and resulted in temporal resolutions which clustered around the value of 10 ns/track, ranging from 9.5 to 10.3 ns/track.

Once the resolution per track is known, it is straightforward to determine the delay to a given track within the Vidicon window. The experimenter then designs the timing sequence around a particular OMA track where the impact should occur. In the example just given if it was desired for impact to occur on track #15, then once the streak camera was triggered it would take (860 + 14×9.6)= 0.994 μs to reach track #15.

In an actual experiment, the delay to the impact track must be synchronized with the laser pulse and the impact event to within 100-120 ns. This task must be performed flawlessly for a successful experiment. Appendix B demonstrates how the various timing delays are built into a typical experiment.

3.6.2 Diagnostic Checks

By their nature, shock experiments are difficult to perform and time-resolved shock experiments compound the degree of difficulty. Hence, diagnostic checks are very important. A diagnostic check was used to monitor the streak camera operation by recording its output pulse during the experiment. The laser was checked by recording the

response of a photodiode to the laser pulse. The diagnostic recording was made using a Digitizing Signal Analyzer (DSA). The signals generated by the trigger pins located in the target cell were also displayed on the DSA, thus permitting a record of the synchronization between instrument performance and events occurring during the experiment. As indicated in the example given in Appendix B, the Digitizing Signal Analyzer (DSA) begins recording 500 ns before any critical timing events occur. The diagnostic recording thus proceeds in the background, not interfering with the experiment, ending 10 μs after recording begins.

An additional use of the DSA diagnostic recording is to check that the timing plan, such as that described in Appendix B, is correct. By comparing the streak output on the recording to that predicted in the diagram, one may fine-tune the laser and streak timing to increase the signal or change its position in the streak window.

Figure 3.14 is an example of a typical diagnostic recording. This figure displays the streak monitor pulse from the streak camera, the photo diode response from the laser pulse, and two trigger pin markers. The presence of these diagnostics on the DSA recording indicates that the respective piece of equipment functioned correctly during the experiment and their relative position in time is used to check the synchronization.

As an example of how the diagnostic record may be used *ex post facto*, the absence of the laser pulse on the recording might indicate that the laser didn't lase or perhaps the photo diode malfunctioned, whereas, a diminished signal might be indicative of fiber damage or coaxial flash lamp trouble. Similarly, a missing streak pulse might indicate a problem with the streak camera. If both signals were missing then the delay box, which triggered both instruments, might be the problem or perhaps the trigger pin did not work, etc.
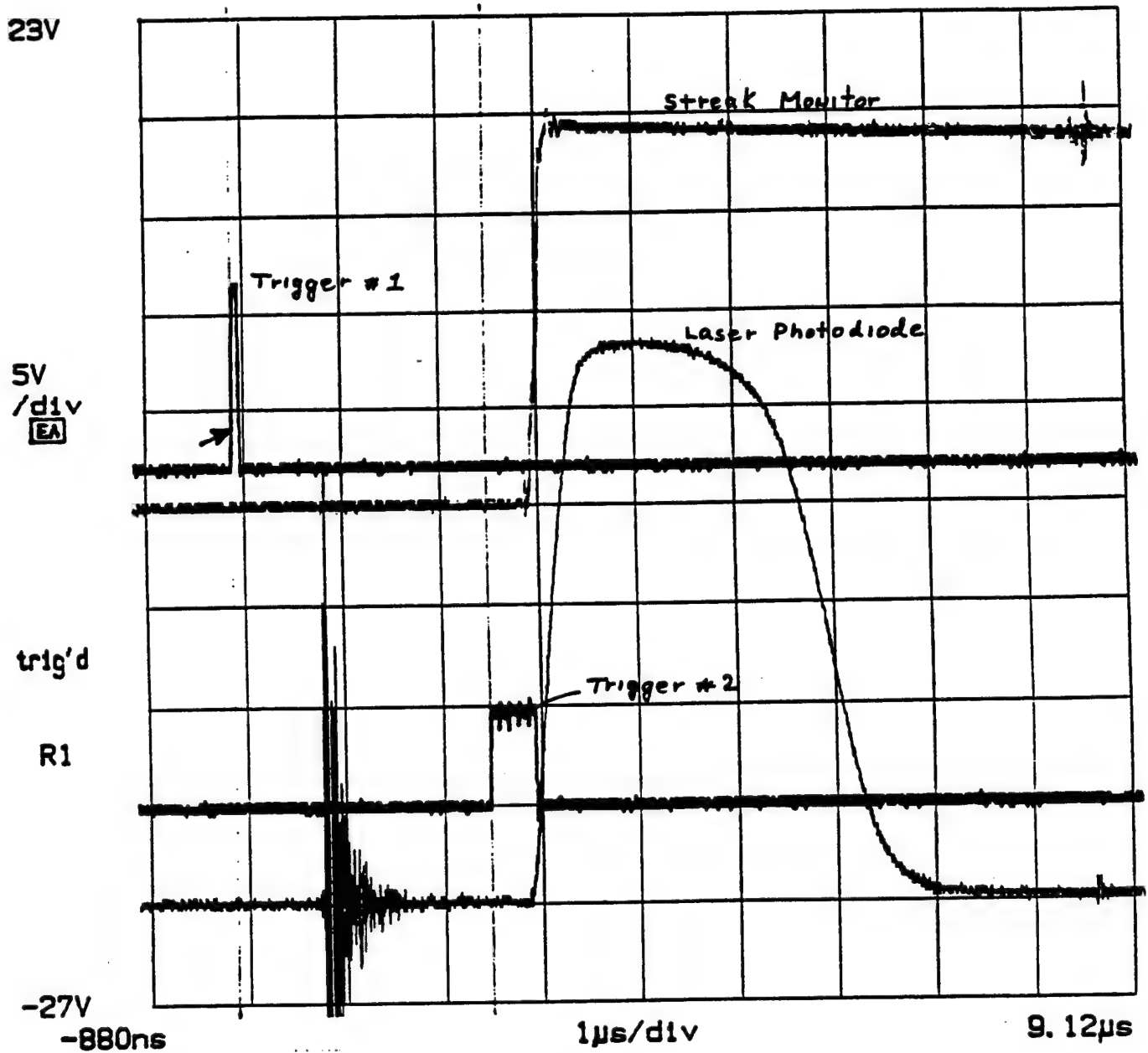
Fig. 3.14   Typical DSA Diagnostic Recording .

3.7 IMPACT EXPERIMENTS

A total of twelve experiments were performed on two diamond orientations to examine shock-induced changes in the Raman spectrum under shock compression. The impact arrangements and recording system settings for these experiments are listed in Table 3.4.

The experiments are numbered 1-12 in order of increasing applied stress. The shot number is also listed in parenthesis in the first column. The shot number is used for record keeping purposes but may also be used to determine the chronological order if desired. For example, Experiment #4 (91-052) was the 52nd experiment performed on the 4-inch gas gun in 1991.

The next two columns list the impactor and buffer materials and their respective thicknesses. The remaining columns list the actual projectile velocity, laser energy incident on the sample, the grating used, and the streak speed. The temporal resolution is given in the last column using the fiber image height of 400 μm and Eq. (3.10).

3.7.1 Individual Experiments

Experiment #1

The previous work of Gupta et al.[11] demonstrated the feasibility of performing time-resolved spectroscopy on diamond under shock loading. The purpose of Experiment #1 was to repeat their study at 120 kbar using the improvements in resolution made for the present study.

The overall target and projectile design used was adapted from Gustavsen's work.[12] The sample was a 3 mm square type IIa diamond 0.25 mm thick and was sandwiched between two discs of z-cut sapphire (0.125" thick x1.0" in diameter). The sample assembly was impacted by an identical piece of z-cut sapphire. Experiment #1 was the only experiment in this study that utilized the filter stage of the SPEX Triplemate spectrometer. The time resolution was 20 ns/track with 25 tracks of recording time.

Table 3.4 Impact Configurations and Experimental Parameters.

Experiment Number (shot #)	Impactor Material (Thk mm)	Buffer Material (Thk mm)	Projectile Velocity (mm/μs)	Laser Energy (mJ)	Grating (gr/mm)	Streak Speed (mm/μs)	Track Resolution (ns/track)
1 (91-006)	Al_2O_3 (3.2)	Al_2O_3 (3.2)	0.538	*	1200	20	20
2 (92-044)	Al_2O_3 (2)	Al_2O_3 (1)	0.562	82	1800	50	10
3 (92-015)	OFHC Copper (2.01)	OFHC Copper (1.988)	0.665	50	1800	50	10
4 (91-052)	OFHC Copper (6.35)	OFHC Copper (6.223)	0.795	75	1200	50	10
5 (92-038)	Platinum (1.998)	OFHC Copper (1.845)	0.758	103	1800	50	10
6 (92-003)	OFHC Copper (3.140)	OFHC Copper (3.137)	1.19	74	1800	50	10
7 (92-030)	Tantalum (2.00)	OFHC Copper (1.980)	1.14	90	1800	50	10
8 (92- 062)	Platinum (1.897)	OFHC Copper (1.962)	1.15	74	1800	20	20
9 (92-032)	Platinum (1.920)	OFHC Copper (1.857)	1.21	84	1800	50	10
10 (92-042)	Platinum (1.971)	OFHC Copper (1.834)	0.802	85	1800	50	10
11 (92-061)	Platinum (1.972)	OFHC Copper (1.948)	0.96	105	1800	20	20
12 (92-060)	Platinum (1.991)	OFHC Copper (1.949)	1.16	103	1800	50	10

* Not observed

Experiment #2

This experiment was a symmetric a-cut sapphire impact, designed to yield 150 kbar in the diamond. The diamond sample was 3.0 mm in diameter and 1.0 mm thick. A thicker diamond was selected to provide additional recording time. The impact and buffer sapphire were 25.4 mm in diameter with thicknesses indicated in Table 3.5. The diamond sample was fixed to the sapphire buffer in the manner described for the copper buffer in Section 3.3.1. The purpose of this experiment was to examine the Raman spectrum close to the laser line and to compare with Experiment # 3 which used a copper buffer. The time resolution was 10 ns/track with 31 tracks of total recording time.

Experiment #3

For this experiment, the impact configuration was symmetric: OFHC copper on OFHC copper buffer. The diamond was 3.0 mm in diameter and 0.5 mm thick. The copper impactor and buffer were 6.3 mm in diameter. The projectile velocity was 0.665 mm/µs for a 167 kbar stress in the sample.

The ambient spectrum taken just prior to the shot, saturated the detector at 3000 counts. To avoid this, the gain was reduced to the medium setting and the laser aperture was opened, allowing more energy to be delivered to the sample site. This reduced the number of counts while improving the signal-to-noise ratio. During the experiment, the peak counts were far less than expected. The laser energy was measured after the experiment and was found to be only 50 mJ indicating possible fiber damage. The laser fiber was replaced after a fracture was discovered at the laser coupling.

Experiment #4

This experiment was similar to Experiment #3 with a symmetric copper impact. It was designed to reach 200 kbar in the diamond sample with a projectile velocity of 0.795 mm/µs. The purpose of this experiment was to demonstrate a 10 ns time-resolution. The diamond sample was 3.0 mm in diameter and 1.0 mm thick. This experiment was the first to achieve 10 ns resolution per OMA track for a total of 30 recorded tracks.

Experiment #5

This experiment was designed for an asymmetric platinum/OFHC copper impact. The design projectile velocity was 0.71 mm/μs for a 250 kbar stress in the diamond sample. The diamond dimensions were 2.5 mm diameter by 0.75 mm thick. The time resolution was 10 ns for 30 tracks total recording time.

Experiment #6

This experiment was a symmetric OFHC copper impact. The design projectile velocity was 1.2 mm/μs for a 320 kbar stress in the diamond. The sample dimensions were 3.0 mm in diameter and 1.0 mm thick. This experiment was the first to use the 1800 groove/mm grating which enhanced the spatial resolution. The stress attained in this experiment was near the limit accessible for copper/copper impact. The time resolution was 10 ns/track with 31 tracks of recording time.

Experiment #7

This experiment was designed as a test of the timing configuration. It was also the first asymmetric impact (Ta on Cu) used in these studies. In addition to the diagnostic checks already mentioned in Section 3.6.3, this test also had a small diamond (1.5 mm x 0.25 mm) to indicate impact. The thickness only allowed for a 14 ns transit time through the diamond and one data track was recorded. The test indicated a 60 ns timing error that was attributed to a deviation from the design projectile velocity of 1.2 mm/μs.

Experiment #8

Impact was an asymmetric platinum on copper with a design projectile velocity of 1.15 mm/μs. A stress of 430 kbar in the sample was the design goal. The sample was 2.5 mm in diameter and 0.75 thick. This experiment was one of three that used the CCD detector array. The wavelength resolution was inferior to the intensified Vidicon. This loss of resolution is due to the difference in lens coupling between the two detection systems. In addition to the loss of wavelength resolution, the count rate was lower than

desired. To boost the number of counts, a slower streak speed was used that degraded the time resolution per track; this is reflected in Table 3.4.

Experiment #9

This experiment used the same impact arrangement as Experiments #5 and #8. The design projectile velocity was 1.2 mm/µs to give a 450 kbar stress in diamond. The purpose was to record data for stress approaching 0.5 Mbar. This experiment represents the largest stress achieved in the present study. The sample was 2.5 mm in diameter and 0.75 mm thick. Time resolution was 10 ns per track for 31 recorded tracks.

Experiment #10

This was the first experiment performed on the [100] orientation. The design velocity for the projectile was 0.8 mm/µs to yield a 275 kbar stress in the sample. Sample dimensions were 2.5 mm diameter and 0.75 mm thickness. The impact configuration was platinum on OFHC copper as discussed previously. Time resolution was 10 ns per track for 31 recorded tracks.

Experiment #11

This experiment was performed on a [100] oriented diamond with dimensions 2.5 mm diameter and 0.75 mm thick. The impact arrangement was platinum on OFHC copper as in Experiment #10. The design velocity for the projectile was 1.0 mm/µs for a longitudinal stress 354 kbar. This experiment used the CCD detection system and the comments made for Experiment #8 are applicable here also. Time resolution was 20 ns per track for 32 total tracks.

Experiment #12

This experiment was performed on the [100] diamond orientation. The impact was asymmetric platinum on copper and the design velocity for the projectile was 1.25 mm/µs for a 455 kbar longitudinal stress in the sample. The sample was 2.5 mm in diameter and 0.75 mm thick. This experiment was performed using the CCD detection system. Time resolution was 10 ns per track for 32 total recorded tracks.

The original experimental designs called for symmetric impact experiments such as Experiments #1- #4 and Experiment # 6. However, for the Platinum and Tantalum materials hot spots developed at the metal-diamond interface due to laser heating. Roughly 120 mJ of energy is focused onto the sample in a 3µs period in essence delivering 35kW into a 400 µm spot. The platinum and tantalum materials have thermal conductivities 6-7 times less than that of copper (see Table 3.1) and the incident energy resulted in localized heating and ablation of material at the interface. The asymmetric impact configurations provided a reasonable solution, although the final stress state in the diamond was slightly less than would have resulted from symmetric impact scenarios.

3.7.2 Firing Sequence

Once a test spectrum demonstrated an adequate signal during ambient testing, the laser energy was measured with a Joulemeter. The trigger pins were then checked for continuity and the optical fibers were securely fastened to the lens assemblies. With the target centered at the gun barrel end, the catcher tank was put in place, and the barrel evacuated. When the gun barrel vacuum reached 50 microns, pressurization of the breech commenced. Depending upon the type of breech used (wrap-around or double-diaphragm), pressurization took from 15 minutes to 1 hour and 15 minutes.

Prior to the actual experiment, one last spectrum under ambient conditions was recorded and the Digitizing Signal Analyzer (DSA) diagnostic record saved. At this stage, the voltage regulator to the dye laser was turned off to avoid self-arming problems. After the final test spectrum, the streak camera shutter was left open and the image intensifier left on to eliminate these items from the check list.

When the target pressure was reached, the vacuum pumps were turned off, the voltage regulator to the laser was turned on, the Digitizing Signal Analyzer armed and the OMA scan initiated. At this point the projectile was fired. After impact, the laser was immediately turned off and all diagnostic and OMA records were saved on computer

disks. Following the experiment, the calibration procedure described in section 3.6.1 was performed.

3.8 EXPERIMENTAL IMPROVEMENTS

Several potential improvements to the experimental arrangement are suggested:

1)   Improved triggering to minimize uncertainty in projectile velocity would allow much faster time-resolution. When conventional shorting-pins are used for triggering, any uncertainty in the projectile velocity directly influences the timing built into the experiment. Timing uncertainties of 50-75 ns are typical.

2)   It would be very useful to be able to control the incident and scattered polarizations during time-resolved vibrational experiments. The depolarization ratio may then be determined experimentally, providing a means of distinguishing the symmetry of the vibrational mode. Polarization preserving fibers are available but were not used in this study because the throughput is poor.

3)   A lighter more structurally sound projectile design needs to be developed for high velocity applications. The light gas gun in the Shock Dynamics Center is designed to accelerate a projectile to 1.5 mm/μs using helium gas pressurized to 6000+ psi. However, as indicated in Table 3.4, the maximum projectile velocity attained in this work was 1.21 mm/μs.

Chapter 4

EXPERIMENTAL RESULTS

The experiments performed in this study may be grouped into two categories: nine experiments with shock compression along the [110] orientation and three experiments with shock compression along the [100] orientation. The raw data records for all of the experiments are provided in Appendix C. The data from the twelve experiments and the intensity versus wavelength fits to the data are described in this chapter.

As stated in Chapter 1, the primary objective of this work was to determine the change in symmetry for the Raman frequency shifts due to applied uniaxial strain. It was shown in Chapter 2 that uniaxial strain along the [110] direction in diamond completely lifts the degeneracy thereby allowing determination of {p,q,r}. For this reason the bulk of the experiments were performed on this particular orientation. The [100] experiments served as an independent check on the {p,q} values.
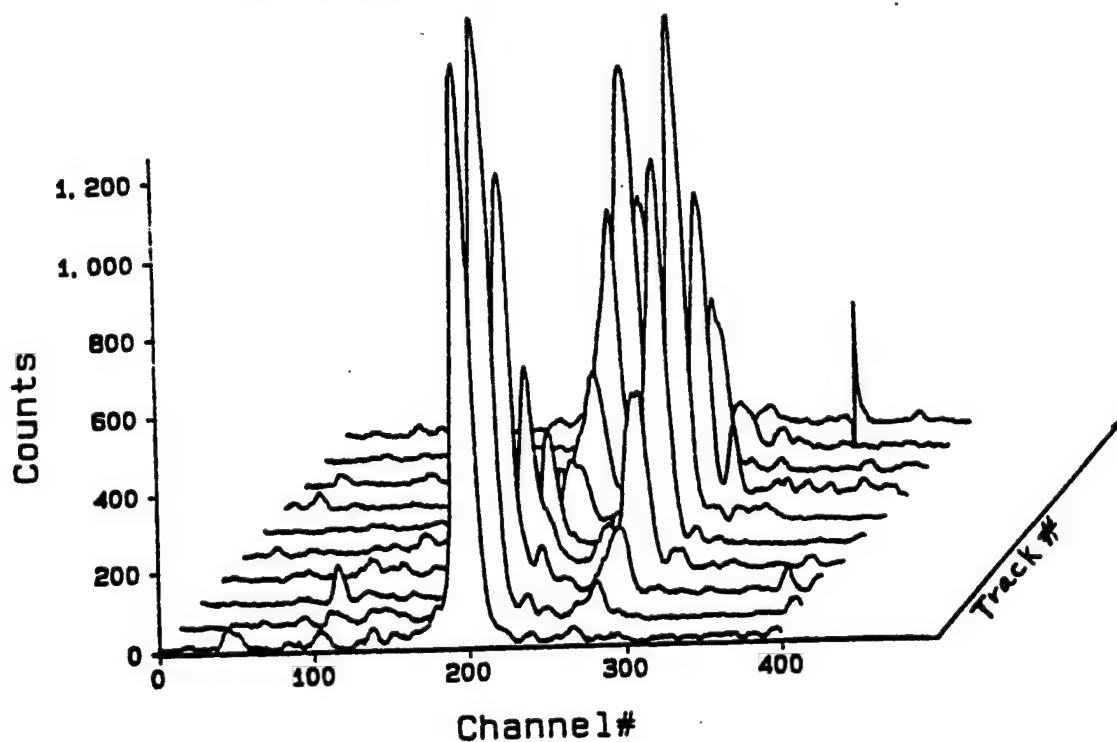
4.1 REPRESENTATIVE OMA RECORDS AND DATA ANALYSIS

Two representative examples of the OMA records are considered here. These examples show data from experiments performed on the [110] and [100] diamond orientations. They are taken from Experiments #9 and #10 (see Table 3.4) and represent the [110] and [100] uniaxial strain data, respectively. The diamond samples for both experiments had the same dimensions (2.5 mm diameter and 0.75 mm thick) and from Table 3.4 it can be seen that the time resolution was 10 ns/track. The peak longitudinal stress was 452 kbar for Experiment #9 and 278 kbar for Experiment #10.

Figure 4.1 show raw OMA data records from these two experiments. To better display the shifted spectrum, only 10 of the 31 tracks are shown, beginning with the track immediately before the arrival of the shock wave. In this figure the Intensity (counts) is plotted as a function of Channel # and Track #.
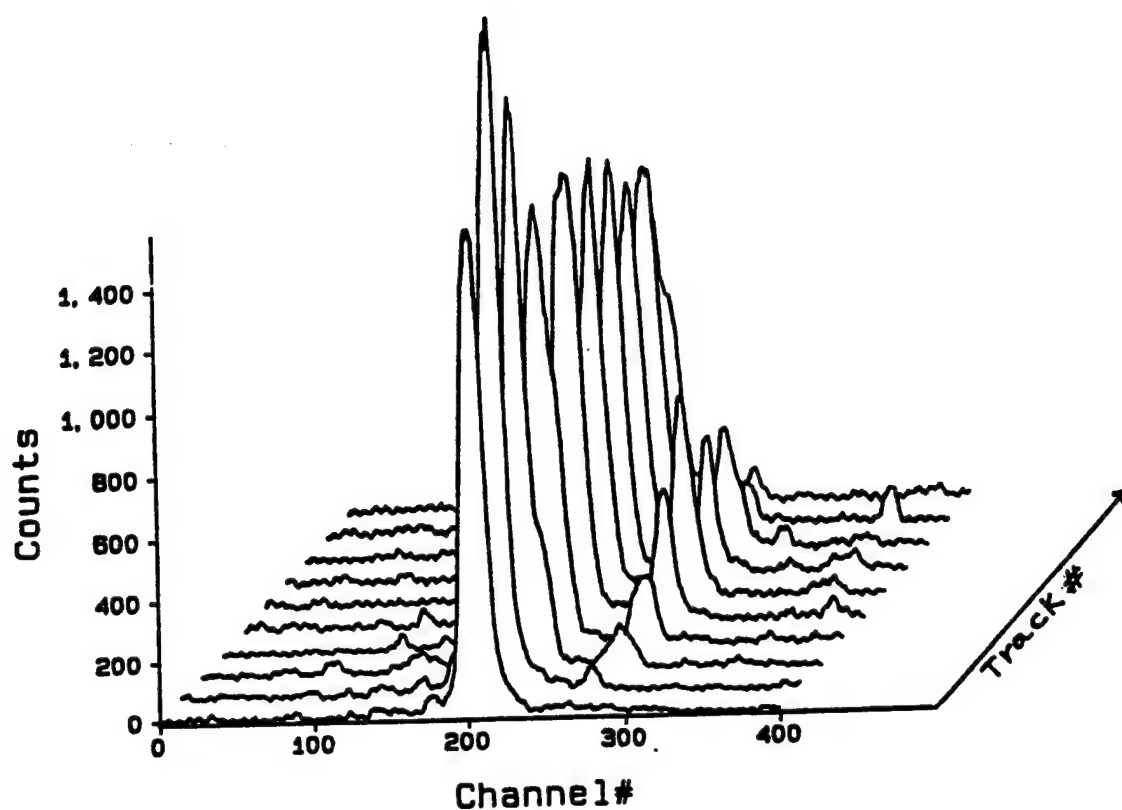
(a)   [110] OMA Record from Experiment #9 (452 kbar).

(b)   [100] OMA Record from Experiment #10 (278 kbar).

Figure 4.1 Representative OMA Records.

Discussion of Representative [110] Spectrum

In Figure 4.1 (a) the ambient Raman line is centered on Channel #200 at Track #1. Between this track and Track #2 (10 ns later) the shock wave has arrived at the sample and a shifted peak is readily seen to the right of the central peak. As the shock wave progresses through the sample and more material is subjected to uniaxial strain, the intensity of the second peak increases accordingly. By Track #6, the shock wave has reached the rear of the diamond and the largest intensity is displayed. The intensity then begins to drop as the release wave arrives from the rear surface. At some point after the seventh track, rarefactions begin to arrive from the sample edges into the observation region and further analysis is not possible. Several comments are appropriate at this point:

1)   The change in intensity for the peak just discussed is sometimes, but not always, accompanied by a corresponding decrease in intensity of the central peak. This is perhaps most noticeable in the raw data for Experiment #4, given by Figure C.1(d) in Appendix C.

2)   After the shock has entered the diamond, the large amplitude peak is not the ambient Raman line, but rather a new line slightly shifted from the ambient Raman line location.

3)   There is a third phonon line, barely discernible in Figure 4.1 (a), located far to the right.

4)   The observed intensities depend, not only upon the polarization rules discussed in Chapter 2, but also on the variations in the intensified vidicon detector response and changes in laser intensity.

Changes in the polarization selection rules due to deviation from the pure backscatter geometry considered in Chapter 2, will be addressed in the following chapter. It will be shown that the actual experimental geometry permits the observation of shifted Raman lines that are not permitted in the pure backscatter geometry.

A-123

Discussion of Representative [100] Spectrum

Figure 4.1 (b) is representative of the [100] experiments. As before, the ambient spectrum is centered on Track #1 at Channel #200. The shock wave has arrived by Track #2, where a small peak may be seen to the right of the ambient peak. As the shock progresses through the sample, the shifted peak intensity continues to rise and peak stress occurs five tracks after impact at Track #6. The simultaneous reduction in intensity (to near zero) of the unshifted central peak, is a feature that was always present in experiments on this orientation. The sharp spike on Track #10 is a detector artifact.

The raw data records from all of the experiments performed in this study are given in Appendix C. Due to image intensifier problems it was necessary to change detection systems for Experiments #8, #11, and #12. These experiments used the EG&G model 1430P CCD detector which used a different lens coupling to the streak camera. This difference resulted in a noticeable loss of wavelength resolution. The scaling for the CCD experiments was roughly 0.95 cm^{-1}/channel. In contrast, the scaling for the intensified Vidicon detector was 0.67 cm^{-1}/channel for the same grating (see Section 3.6.1).

To prevent dark current build-up, the CCD uses an electronic shutter that must be opened immediately before the experiment. As the delay increases between the open shutter command and the fire command, the background noise level also increases. The raw records from these experiments reflect the high background count. However, a subtract mode may be used that effectively eliminates the background. The intensified Vidicon uses a blanking scan that periodically re-initializes the entire detector array automatically, thereby subtracting the background. This feature is built-in to the data acquisition mode so the raw data does not show the background.

4.1.1 Fitting Procedure

For each track of interest, the raw data were calibrated and converted from channel to wavenumber. The wavelength calibration procedure has been described in Section 3.6.1. For convenience Eq. (3.11), which gives the channel to wavenumber conversion, is again given here

$$\omega(cm^{-1}) = 1332.5 cm^{-1} - m(x - x_0) \tag{4.1}$$

where m is the slope in units of cm^{-1}/channel, x is the channel number, and x_0 is the least squares fit to the channel number of the ambient Raman peak for all tracks prior to impact.

The procedure for channel conversion and peak fit is presented here for Track #6 from Experiment #9. Table 4.1 presents the set of slopes that were generated for this experiment by the wavelength calibration procedure described in Section 3.6.1.

Table 4.1 Slopes For Experiment #9.

Track #	Slope (cm^{-1}/channel)	Track #	Slope (cm^{-1}/channel)	Track #	Slope (cm^{-1}/channel)
1	-0.68116	11	-0.66900	21	-0.66703
2	-0.64335	12	-0.66892	22	-0.66407
3	-0.64858	13	-0.66977	23	-0.66381
4	-0.65217	14	-0.67097	24	-0.66283
5	-0.65522	15	-0.67124	25	-0.66144
6	-0.65812	16	-0.67081	26	-0.65781
7	-0.66154	17	-0.67112	27	-0.65566
8	-0.66308	18	-0.67062	28	-0.65315
9	-0.66484	19	-0.66924	29	-0.64984
10	-0.66587	20	-0.66851	30	-0.64570

The least squares fit to the ambient spectrum yielded x_0=205.3. Thus, for Track #6

$$\omega(cm^{-1}) = 1332.5cm^{-1} + 0.65812(x - 205.3)cm^{-1}$$

Figure 4.2 illustrates Track #6 before and after the wavenumber conversion using Eq. (4.1). Each dot in Figure 4.2(a) represents the response of one of the 400 channels which has been converted to wavenumbers in Figure 4.2(b). To determine the peak locations in Figure 4.2 (b), the record was processed by a curve fitting program[83]. The observed spectrum intensity was fit to a three-Gaussian expression of the form,

$$I = I_0 + I_1 \times \exp\left[-\left(\frac{\omega - \omega_1}{FWHM}\right)^2\right] + I_2 \times \exp\left[-\left(\frac{\omega - \omega_2}{FWHM}\right)^2\right] + I_3 \times \exp\left[-\left(\frac{\omega - \omega_3}{FWHM}\right)^2\right] \quad (4.2)$$

where, I_0 is the background intensity level, I_1 is the relative intensity of peak one, ω is the channel number converted to wavenumbers, ω_1 is the peak location in wavenumbers, and $FWHM$ is the Full Width at Half Maximum for the peak. Similar definitions apply to the second peak with fitting parameters (I_2, ω_2) and the third peak with (I_3, ω_3).

To facilitate the curve-fitting process, the initial values of the fitting parameters were seeded with approximate values for peak positions and intensities. Table 4.2 gives the initial seed values, final fitted values, and the standard deviation of these values for this example.

Figure 4.3 illustrates the Gaussian fit of Eq. (4.2) to the 400 data points of Track #6 using the fitting values given in Table 4.2. The figure has been rescaled in (a) to emphasize the area of interest.

It will be seen in Chapter 5 that for the [110] data, one of the predicted peaks (ω_3) lies very close to the ambient peak location at 1332.5 cm^{-1}. Because the observed Raman signal originated from both shocked and unshocked material, it contained both shifted
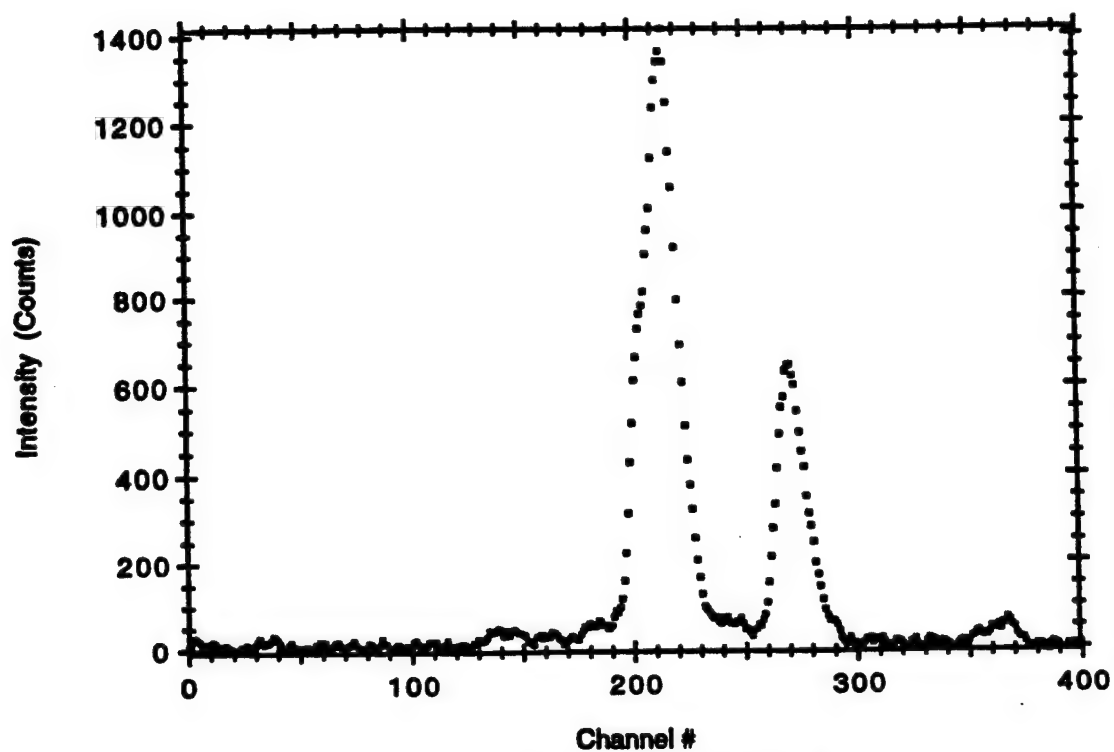
(a) Intensity versus Channel #
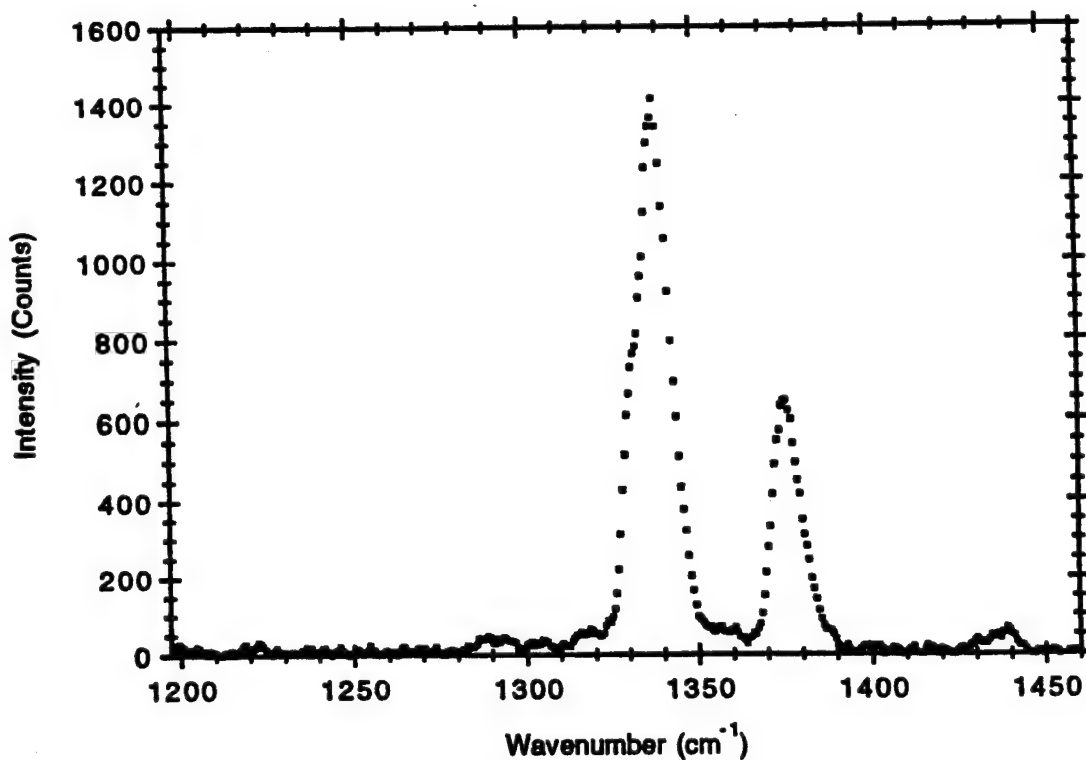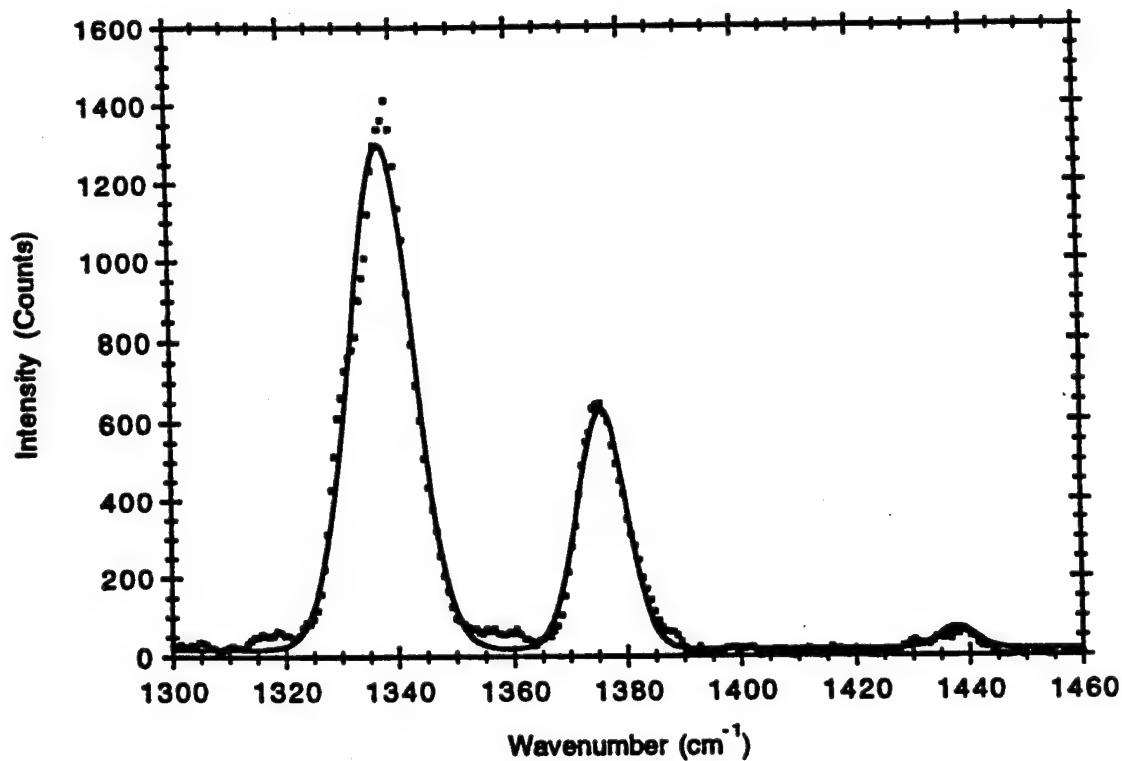

(b) Intensity versus Wavenumber

Figure 4.2 Channel to Wavenumber Conversion.

A-127

Table 4.2 Values of Fitting Parameters For Track #6 of Experiment #9.

Fitting Parameters	Seed Values	Fitted Values	Std. Deviation
I_0	20	17.7	± 1.6
I_1	600	613.4	± 10.2
ω_1 (cm^{-1})	1380	1375.7	± 0.08
FWHM$_1$ (cm^{-1})	8	6	± 0.12
I_2	60	55	± 11.9
ω_2 (cm^{-1})	1440	1438.3	± 1.07
FWHM$_2$ (cm^{-1})	8	5	± 1.5
I_3	1250	1282.7	± 8.9
ω_3 (cm^{-1})	1335	1337.6	± 0.04
FWHM$_3$ (cm^{-1})	8	7.8	± 0.06
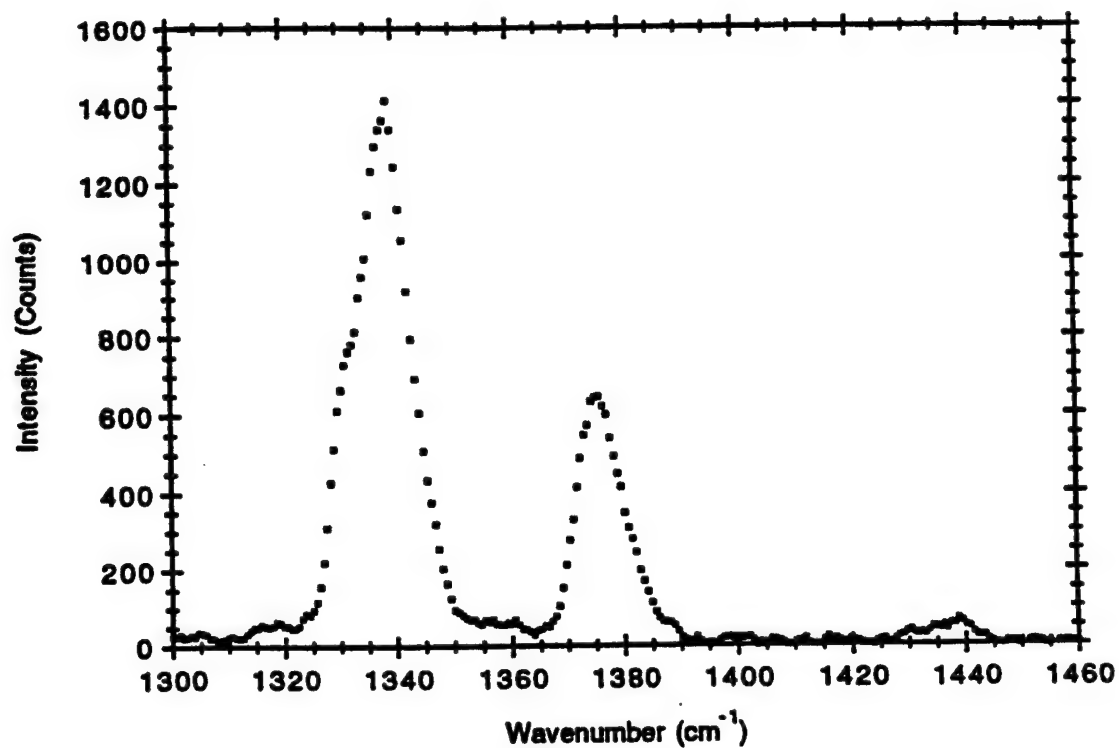
(a) Expanded Scale

(b) Expanded Scale and Fit

Figure 4.3 Rescaling and Intensity vs Wavenumber Fit.

and unshifted Raman peaks. To better resolve the shifted peak location, it was fit to a double Gaussian function similar to Eq. (4.2). During this fitting procedure, the fitting parameters describing the ambient peak were held fixed. All fits to experimental [110] data were performed in this manner. It is emphasized that the purpose of this procedure was to fine-tune the location of the large amplitude peak, not to determine its absolute intensity. Because the peak overlaps the ambient peak, estimates of the intensities are, at best, guesses.

The fitting process for the [100] experiments proceeded in a similar fashion using a double Gaussian function since only two peaks were observed.

## 4.2 Impedance Matching and Calculation of Peak Stress

Each experiment performed in this study was designed to achieve a particular stress in the diamond for either the [100] or the [110] crystallographic orientation. Working backwards from the desired stress, an impedance matching calculation was performed that yielded the necessary projectile velocity.

For experiments where the impactor and buffer are dissimilar materials, such as Experiment #9, the condition for the plates to be in contact requires continuity of stress and particle velocity. The jump conditions given by Eq. (2.64) are used to determine the peak particle velocity. Thus ,for the initial platinum-copper impact, the continuity of stress requires

$$\rho_{Cu} D_{Cu} u_1 = \rho_{Pt} D_{Pt} \left(V_P - u_1 \right) \tag{4.3}$$

where ρ_{Cu} and ρ_{Pt} are the material densities at ambient pressure given in Table 3.1, D_{Cu} and D_{Pt} are the shock velocities in the materials given by Eq. (3.1), V_P is the projectile velocity, and u_1 is the particle velocity on impact.

Figure 4.4 (a) is a plot of relation (4.3) for a projectile velocity of 1.25 mm/µs. At impact, a right-going wave is launched into the copper and a left-going wave into the
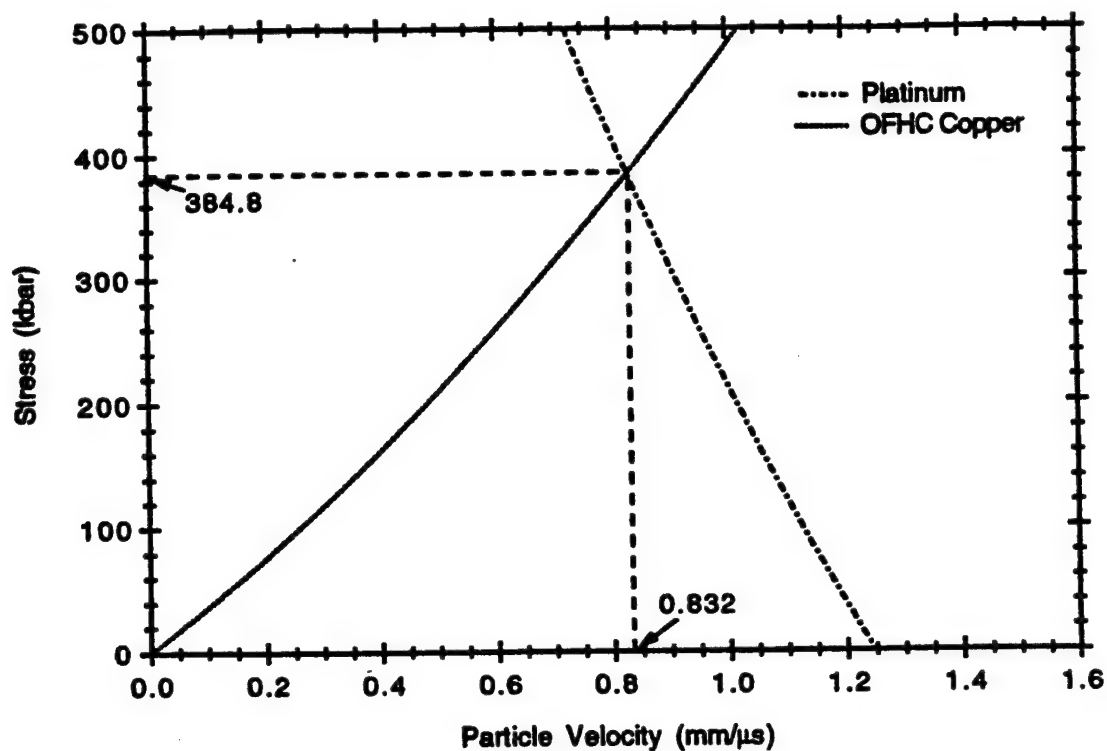
(a) Platinum-OFHC Copper Impact
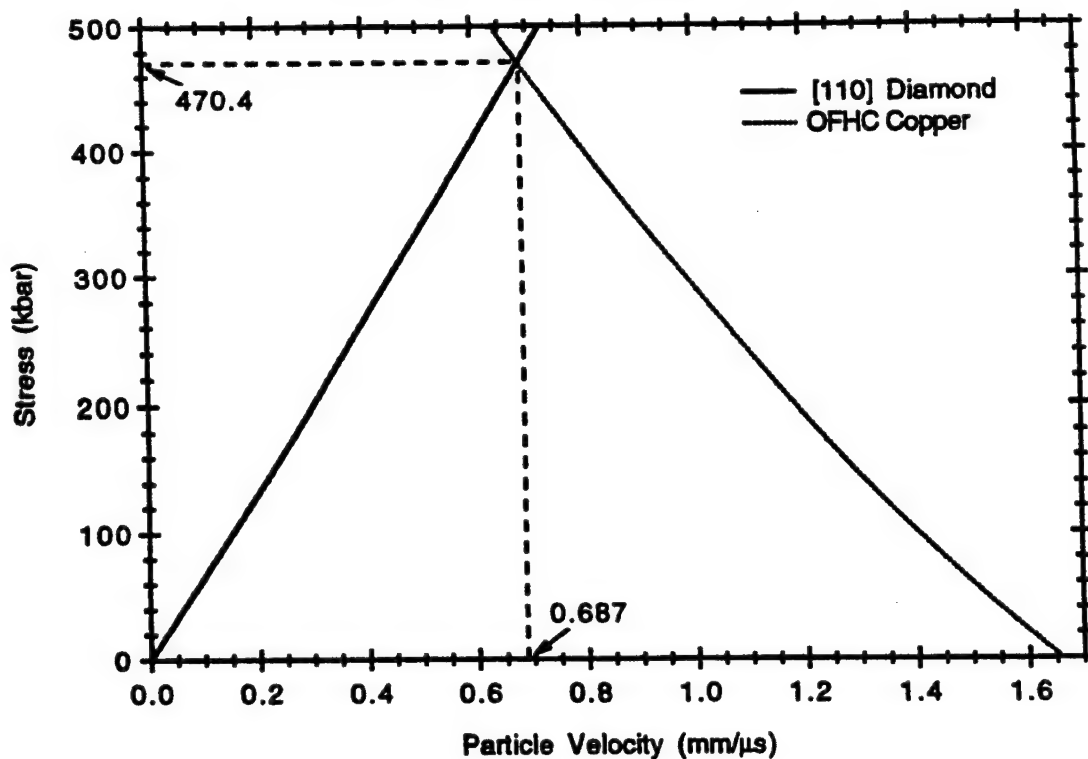
(b) Diamond -Copper Recentered Hugoniot

Figure 4.4 Impedance Matching For Experiment # 9.

platinum; the Hugoniots for these are shown graphically in the figure. The intersection of the two Hugoniots gives the graphical solution to Eq. (4.3) for the particle velocity u_1, this is indicated in the figure along with the impact stress σ_1.

From Table 3.1, Eq. (3.1), and the particle velocity u_1, the shock velocity in the copper buffer material for this impact stress is determined to be

$$D_{Cu} = 3.94 + 1.489u_1 = 5.178 \ mm/\mu s.$$

Using this value for the shock velocity and the buffer thickness given in Table 3.5 (1.857 mm), the shock wave is estimated to take 358.6 ns to reach the diamond-copper interface.

When the shock wave reaches the diamond-copper boundary, a right-going shock wave is launched into the diamond and a left-going shock propagates back into the copper buffer. To illustrate this graphically, an approximation is made in which a mirror image of the original copper Hugoniot is placed at the point (u_1, σ_1) to represent the left-going shock. This is called recentering the Hugoniot and is illustrated in Figure 4.4 (b). This figure is a graphical solution of the expression

$$\rho_C D_{[110]} u_2 = \rho_{Cu} D_{Cu} (2u_1 - u_2) \tag{4.4}$$

where $\rho_C = 3.512 \ g/cc$ is the ambient diamond density, u_2 is the new particle velocity and

$$D_{[110]} = (18.33 + 1.7 \cdot u_2) mm/\mu s \tag{4.5}$$

Eq. (4.5) *is not* an empirical expression. It represents the linear best fit to the $D - u_p$ relation, discussed in Section 2.5.2, for the compression range $0 \le \left(\dfrac{\rho}{\rho_0} - 1 \right) \le 0.04$.

A-132

Table 4.3 (a) summarizes the particle velocities, shock velocities, and peak stress for Experiments #1-#9. The projectile velocity for each experiment is indicated in column 2. Columns 3 and 4 are the particle velocities found from solutions of Eqs. (4.3) and (4.4) and the respective shock velocities are given in the following two columns. The predicted longitudinal stress from the recentered Hugoniot is given in the last column. For Experiments #1-4 and #6 the impactor and buffer were of the same material so that the particle velocity given by Eq. (4.3) is simply half the projectile velocity. Note that the sapphire Hugoniot is described by:[84] $D_{Sapphire} = 11.19 + 1.0u$ $mm/\mu s$.

Similar relationships may be written for the [100] experiments except that the shock velocity for the [100] direction was found to be best fit to the expression

$$D_{[100]} = (17.55 + 0.9 \cdot u_2) mm/\mu s \qquad (4.6)$$

Table 4.3 (b) summarizes the particle velocities, shock velocities, and peak stress for Experiments #10-#12.

4.3 [110] ORIENTATION : EXPERIMENTAL RESULTS

The experiments performed on this orientation exhibited three peaks of varying intensities. The shifted peak location displayed a pronounced dependence on the longitudinal stress. The peak that demonstrated the smallest frequency shift was the most intense, while the peak with the largest frequency shift was the least intense.

Table 4.4 summarizes the principal experimental results for this orientation in the order of increasing compressive stress. The first three columns give the experiment number and impact configuration. Experiments #1 through #4, and Experiment #6 were symmetric Al_2O_3 or OFHC copper impacts. Experiments #5, #8, and #9 were asymmetric platinum on copper impacts and Experiment #7 was as asymmetric tantalum on OFHC copper impact. The respective impactor and buffer thicknesses are given in parenthesis.

A-133

Table 4.3 (a) Particle Velocities and Longitudinal Stress for [110].

Experiment (shot #)	$V_{projectile}$ (mm/μs)	u_1 (mm/μs)	u_2 (mm/μs)	D_{buffer} (mm/μs)	$D_{[110]}$ (mm/μs)	σ (kbar)
1 (91-006)	0.538	0.269	0.186	11.459	18.646	122
2 (92-044)	0.562	0.281	0.231	11.470	18.723	152
3 (92-015)	0.665	0.333	0.254	4.433	18.762	167
4 (91-052)	0.795	0.398	0.307	4.530	18.852	203
5 (92-038)	0.758	0.510	0.402	4.698	19.013	268
6 (92-003)	1.19	0.593	0.473	4.823	19.134	318
7 (92-030)	1.14	0.672	0.550	4.941	19.265	372
8 (92- 062)	1.15	0.768	0.629	5.085	19.399	428.5
9 (92-032)	1.21	0.805	0.662	5.141	19.387	452

(b) Particle Velocities and Longitudinal Stress for [100].

Experiment (shot #)	$V_{projectile}$ (mm/μs)	u_1 (mm/μs)	u_2 (mm/μs)	D_{buffer} (mm/μs)	$D_{[100]}$ (mm/μs)	σ (kbar)
10 (92-042)	0.802	0.539	0.441	4.741	17.947	278
11 (92-061)	0.96	0.642	0.534	4.896	18.031	338.5
12 (92-060)	1.16	0.772	0.655	5.091	18.140	417.5

Table 4.4 Results For [110] Experiments.

Experiment Number (shot #)	Impactor Material (Thick., mm)	Buffer Material (Thick., mm)	Projectile Velocity (mm/μs)	Peak* Stress (kbar)	Frequency Shift (cm⁻¹) from the Ambient Raman line at 1332.5 cm⁻¹		
1 (91-006)	Al_2O_3 (3.2)	Al_2O_3 (3.2)	0.538(2)	122 (113)	$\Delta\omega_1 = 12.1 \pm 1.3$	$\Delta\omega_2 = 29.8 \pm 1.6$	$\Delta\omega_3 = 1.6 \pm 1.3$
2 (92-044)	Al_2O_3 (2)	Al_2O_3 (1)	0.562(5)	152 (141)	$\Delta\omega_1 = 17.2 \pm 1.5$	$\Delta\omega_2 = 35.9 \pm 1.8$	$\Delta\omega_3 = 1.3 \pm 1.5$
3 (92-015)	Copper (2.01)	Copper (1.988)	0.665(1)	167 (155)	$\Delta\omega_1 = 16.3 \pm 1.5$	$\Delta\omega_2 = \dagger$	$\Delta\omega_3 = 2.1 \pm 1.5$
4 (91-052)	Copper (6.35)	Copper (6.223)	0.795(1)	203 (183)	$\Delta\omega_1 = 20.6 \pm 1.2$	$\Delta\omega_2 = 50.5 \pm 1.6$	$\Delta\omega_3 = 2.0 \pm 1.2$
5 (92-038)	Platinum (1.998)	Copper (1.845)	0.758(1)	268 (238)	$\Delta\omega_1 = 24.8 \pm 1.8$	$\Delta\omega_2 = 65.4 \pm 1.9$	$\Delta\omega_3 = 2.8 \pm 1.8$
6 (92-003)	Copper (3.140)	Copper (3.137)	1.190(2)	318 (281)	$\Delta\omega_1 = 32.7 \pm 1.3$	$\Delta\omega_2 = 75.4 \pm 1.6$	$\Delta\omega_3 = 3.7 \pm 1.3$
7 (92-030)	Tantalum (2.00)	Copper (1.980)	1.140(5)	372 (322)	$\Delta\omega_1 = 36.6 \pm 1.0$	$\Delta\omega_2 = \dagger$	$\Delta\omega_3 = 3.5 \pm 1.0$
8 (92-062)	Platinum (1.897)	Copper (1.962)	1.15	428.5 (363)	$\Delta\omega_1 = 44.7 \pm 1.5$	$\Delta\omega_2 = 98.9 \pm 1.9$	$\Delta\omega_3 = 2.9 \pm 1.5$
9 (92-032)	Platinum (1.920)	Copper (1.857)	1.21(1)	452 (386)	$\Delta\omega_1 = 43.3 \pm 1.5$	$\Delta\omega_2 = 105.8 \pm 1.8$	$\Delta\omega_3 = 5.1 \pm 1.5$

* The numbers in parenthesis reflect the stress value by assuming a linear elastic response for diamond.

† Not Observed

The measured projectile velocity is given in column 4. To measure this velocity, three sets of shorting pins connected to digital timers were tripped by the passing projectile just prior to impact. The measured pin spacing and the time interval given by the counters yielded a velocity for each pin set and the mean value was calculated for the three intervals. The deviation from the mean value, which was typically less than 1 %, is shown in parenthesis. For Experiment #8 only one set of pins was shorted.

The values for the peak stress have been determined from Eq. (2.90) which includes the third-order isentropic elastic constants discussed in Section 2.5.2. The uncertainty in the stress calculation is assumed to have a lower bound given by the linear elastic approximation to Eq. (2.90). These stress values are also given in this column in parenthesis for the same density compression.

The remaining columns in Table 4.4 give the fitted peak values for the shifted Raman spectra. The frequency shift refers to the strain-induced shift from the ambient Raman spectrum[3] at 1332.5 cm^{-1}. The fitting procedure was detailed in Section 4.1.1. In each experiment, the track corresponding to the peak stress was used for fitting purposes.

4.3.1 Discussion of Individual [110] Experiments

Uniaxial strain applied along the [110] direction in diamond is predicted to completely lift the triple degeneracy of the ambient Raman line (Section 2.4.2). Experiments performed in this study, for this diamond orientation, confirm this prediction. For seven of the nine experiments performed, the spectrum was fit to three observed peaks, shifted from the ambient peak by the amount indicated in Table 4.4. In the remaining two experiments the third peak was not observed. These nine experiments are discussed individually in this section.

Figures 4.5-4.13 show the recorded spectrum for these experiments at peak longitudinal stress. In each case, the horizontal axis has been calibrated and converted to wavenumbers and the vertical axis reflects the relative intensity in photon counts. Each
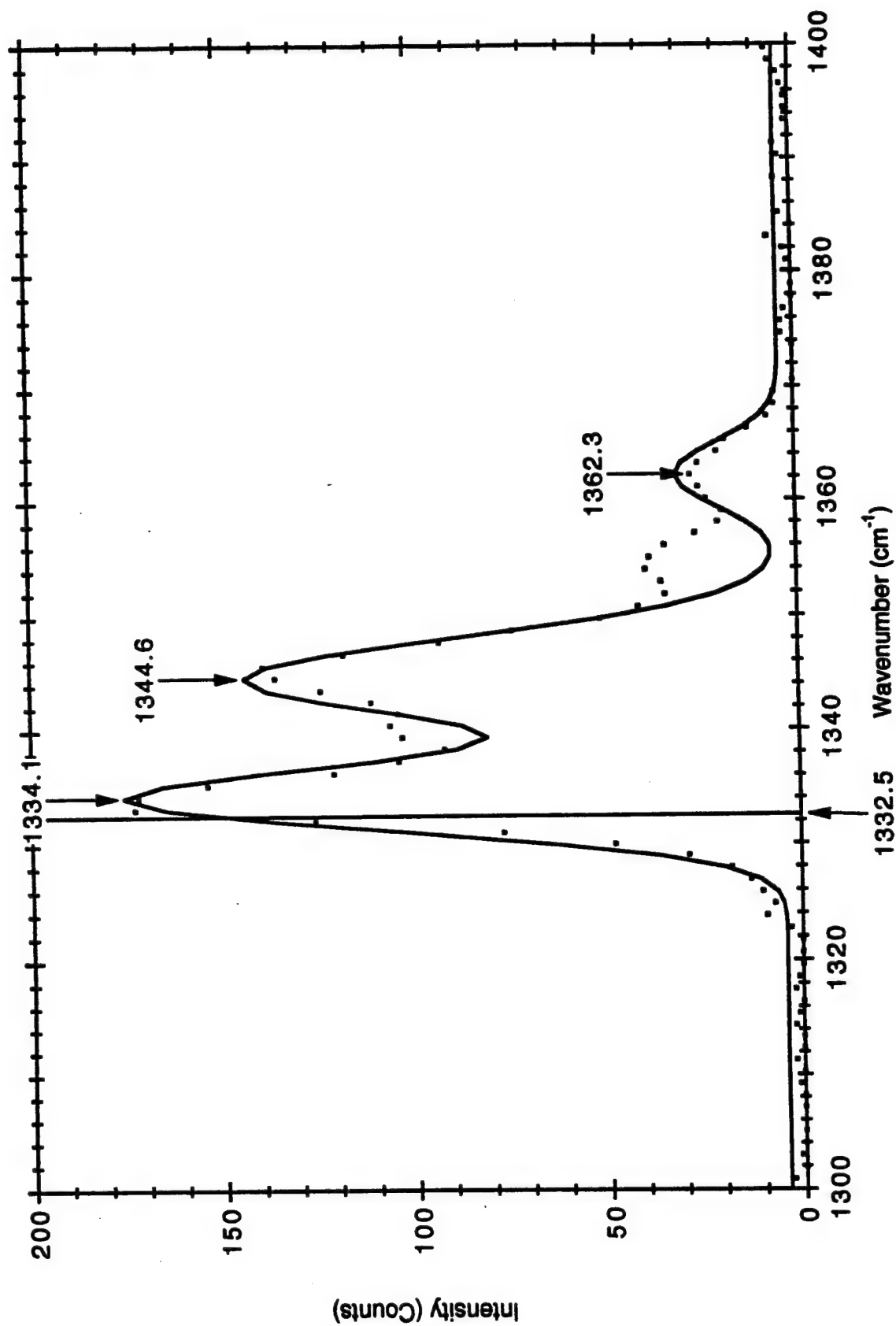
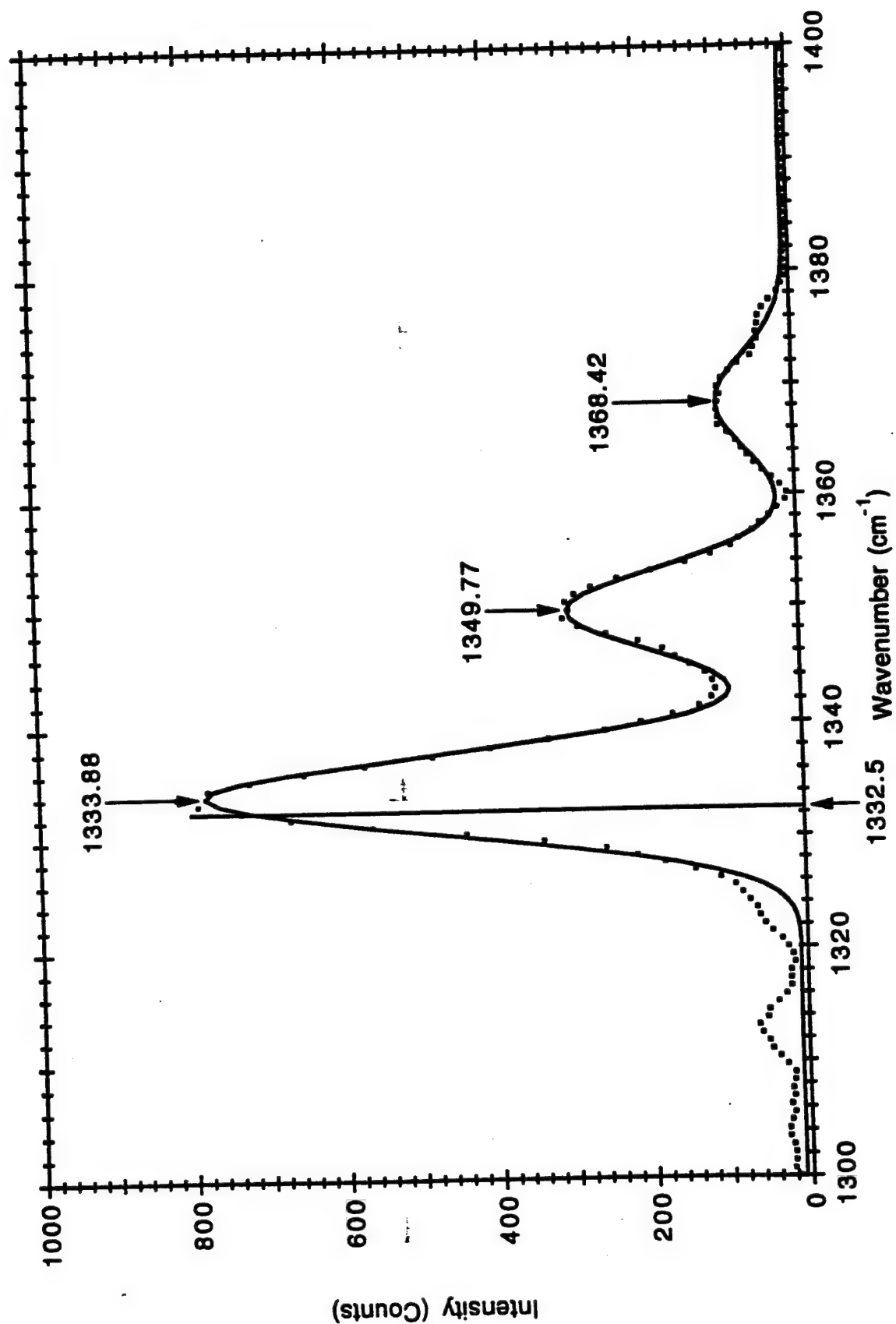Fig. 4.5 Experiment #1 (Shot 91-006), 122 kbar, [110].

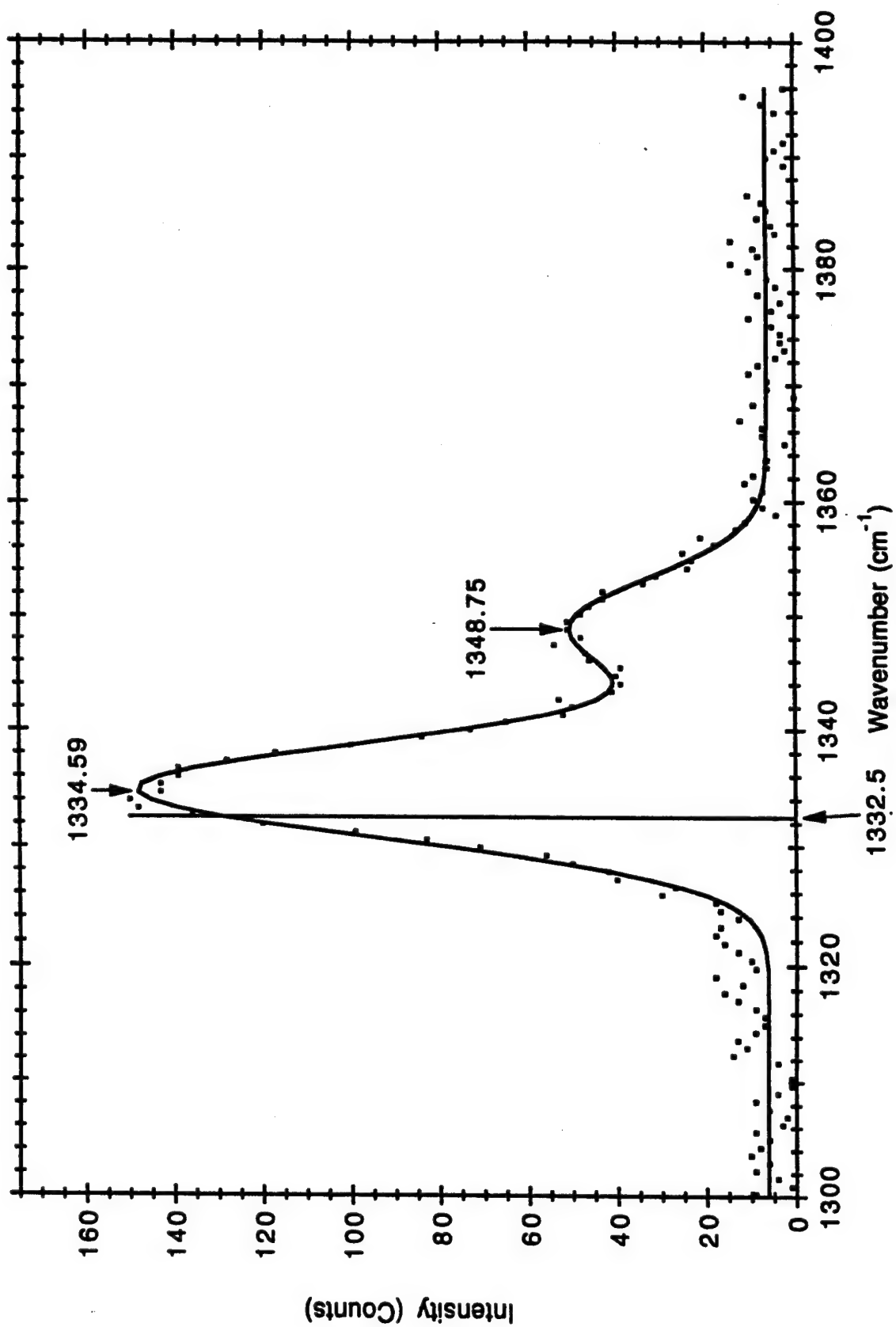Fig. 4.6 Experiment # 2 (Shot 92-044), 152 kbar, [110].

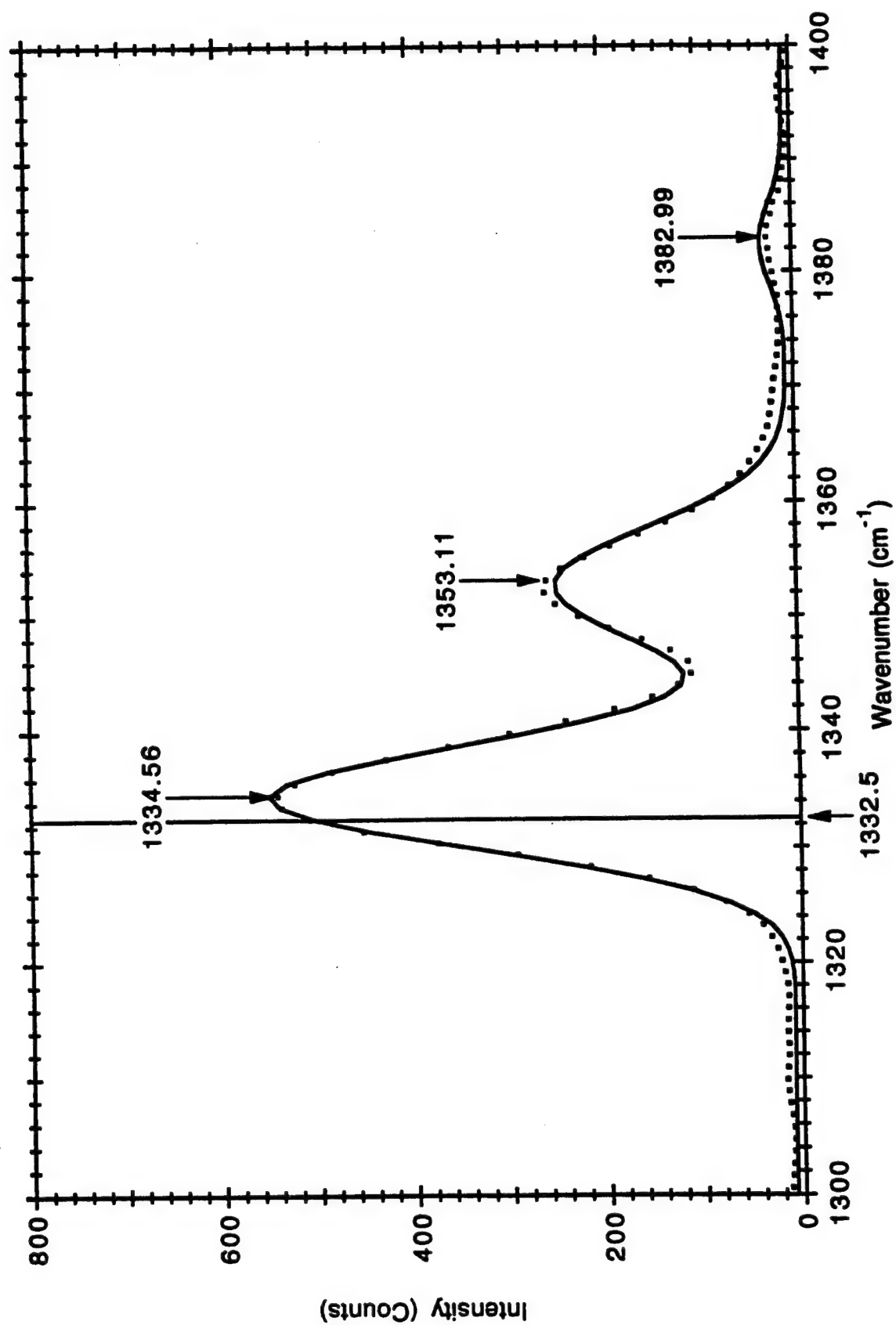Fig. 4.7   Experiment # 3 (Shot 92-015), 167 kbar, [110].

Fig. 4.8   Experiment # 4 (Shot 91-052), 203 kbar, [110].
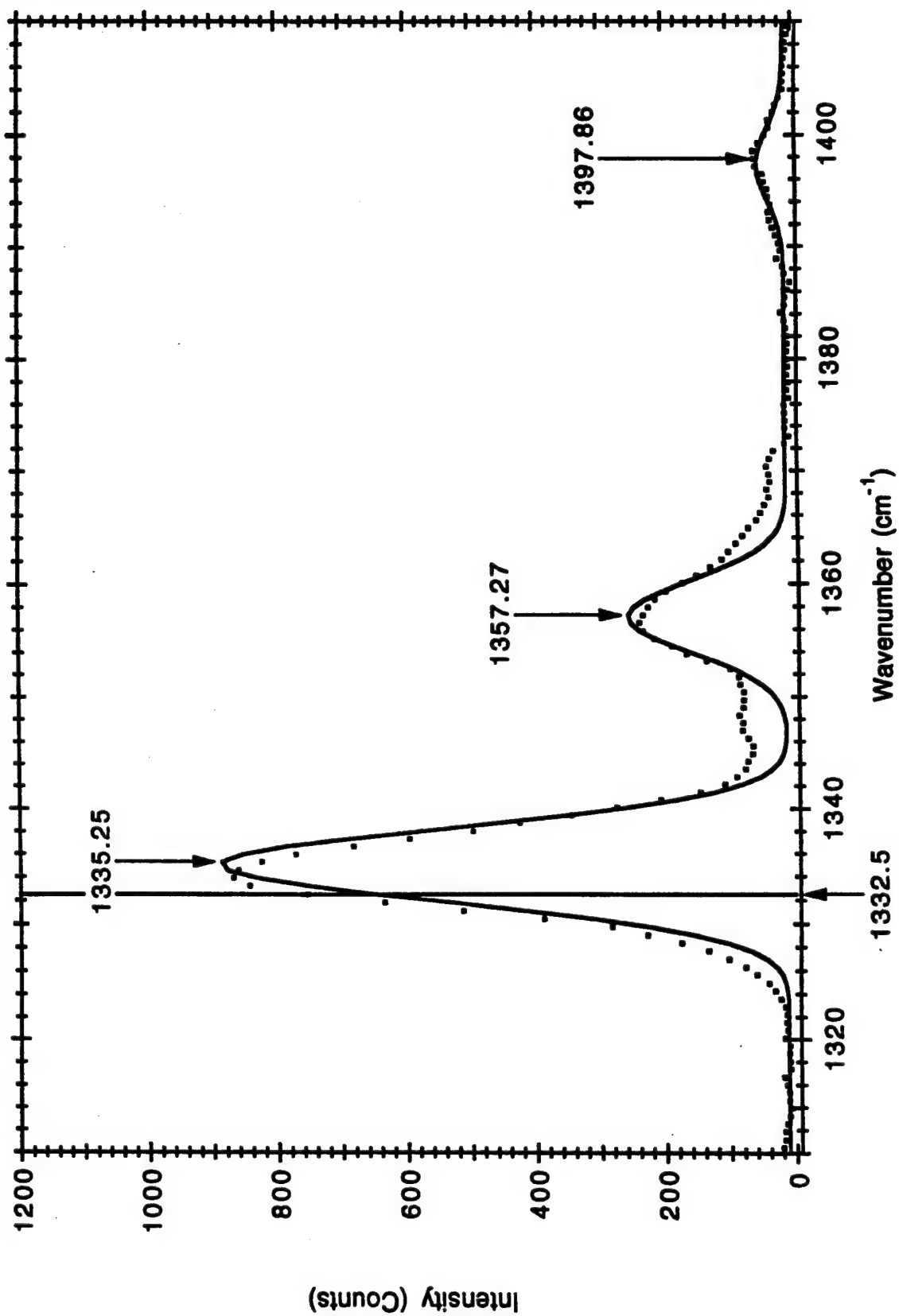
Fig. 4.9 Experiment # 5 (Shot 92-038), 268 kbar, [110].
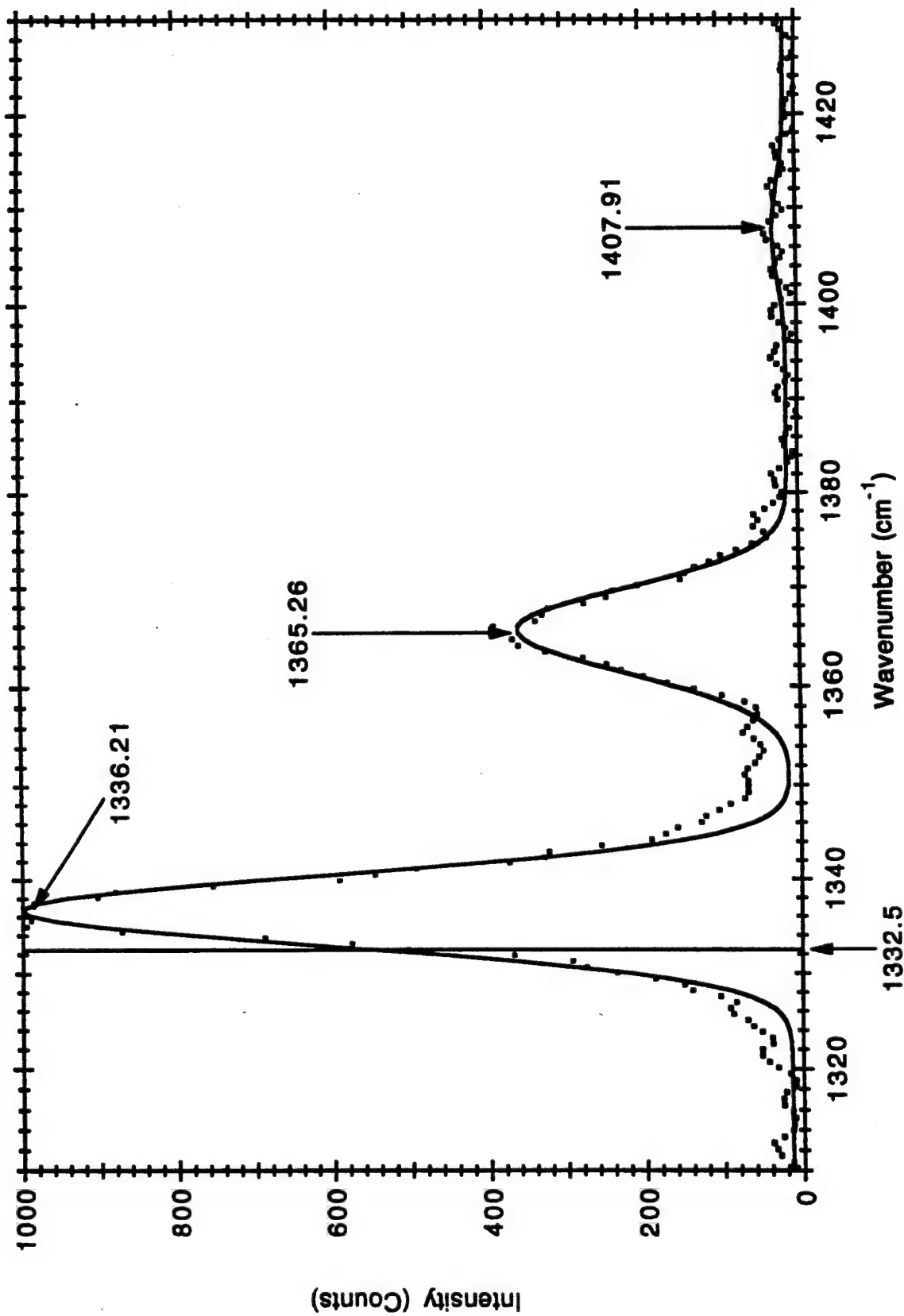
A-141

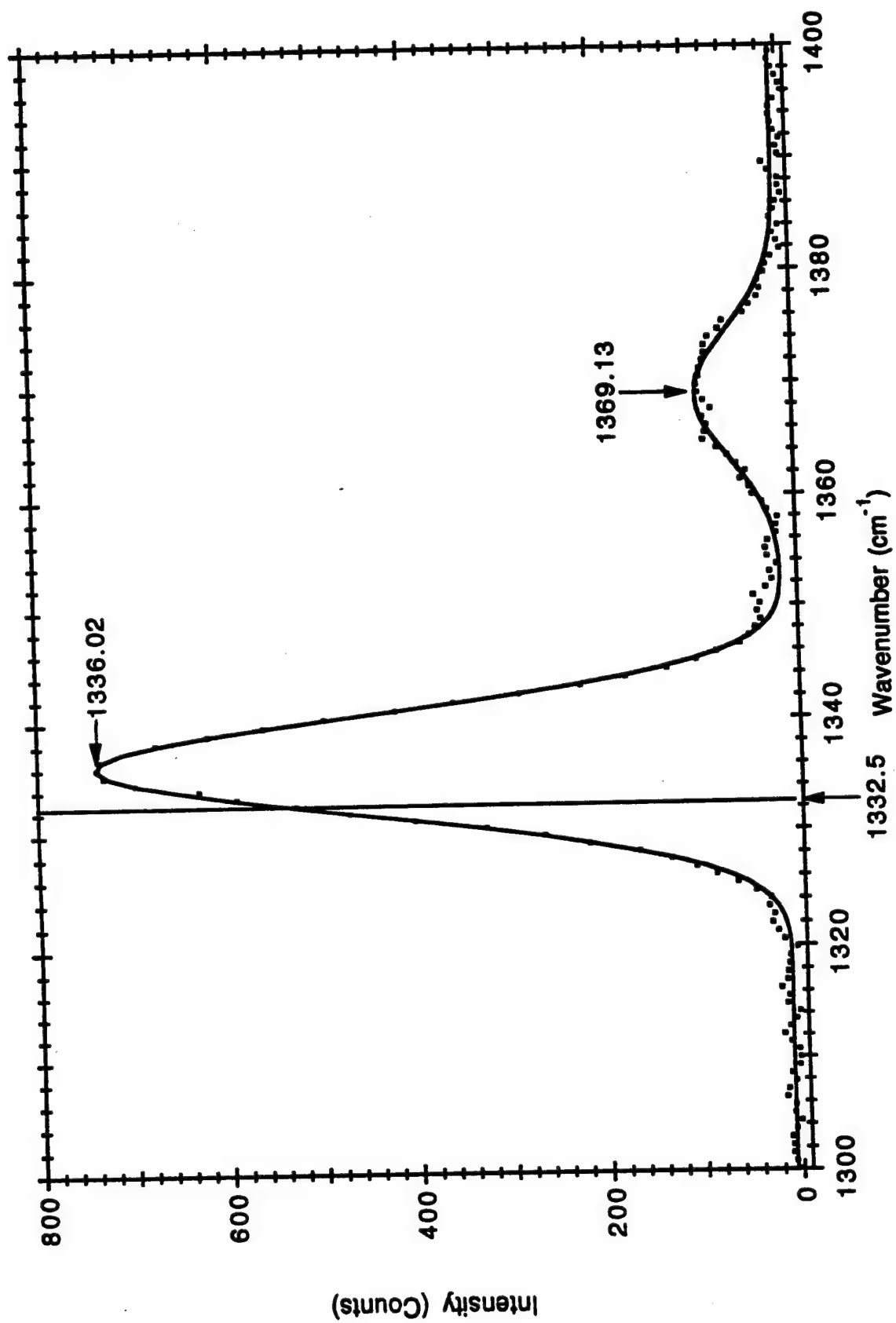Fig. 4.10   Experiment # 6 (Shot 92-003), 318 kbar, [110].

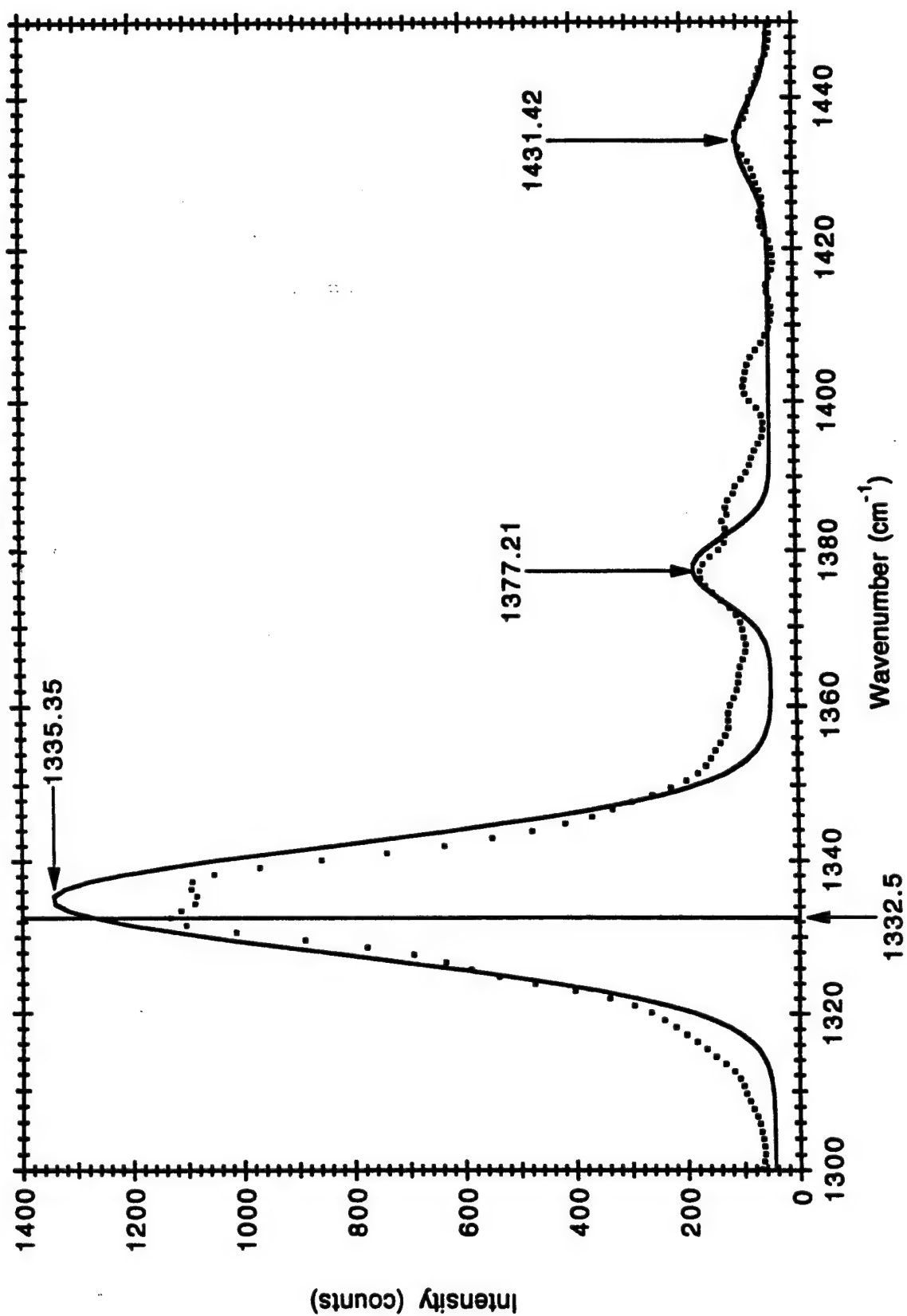Fig. 4.11   Experiment # 7 (Shot 92-030), 372 kbar, [110].

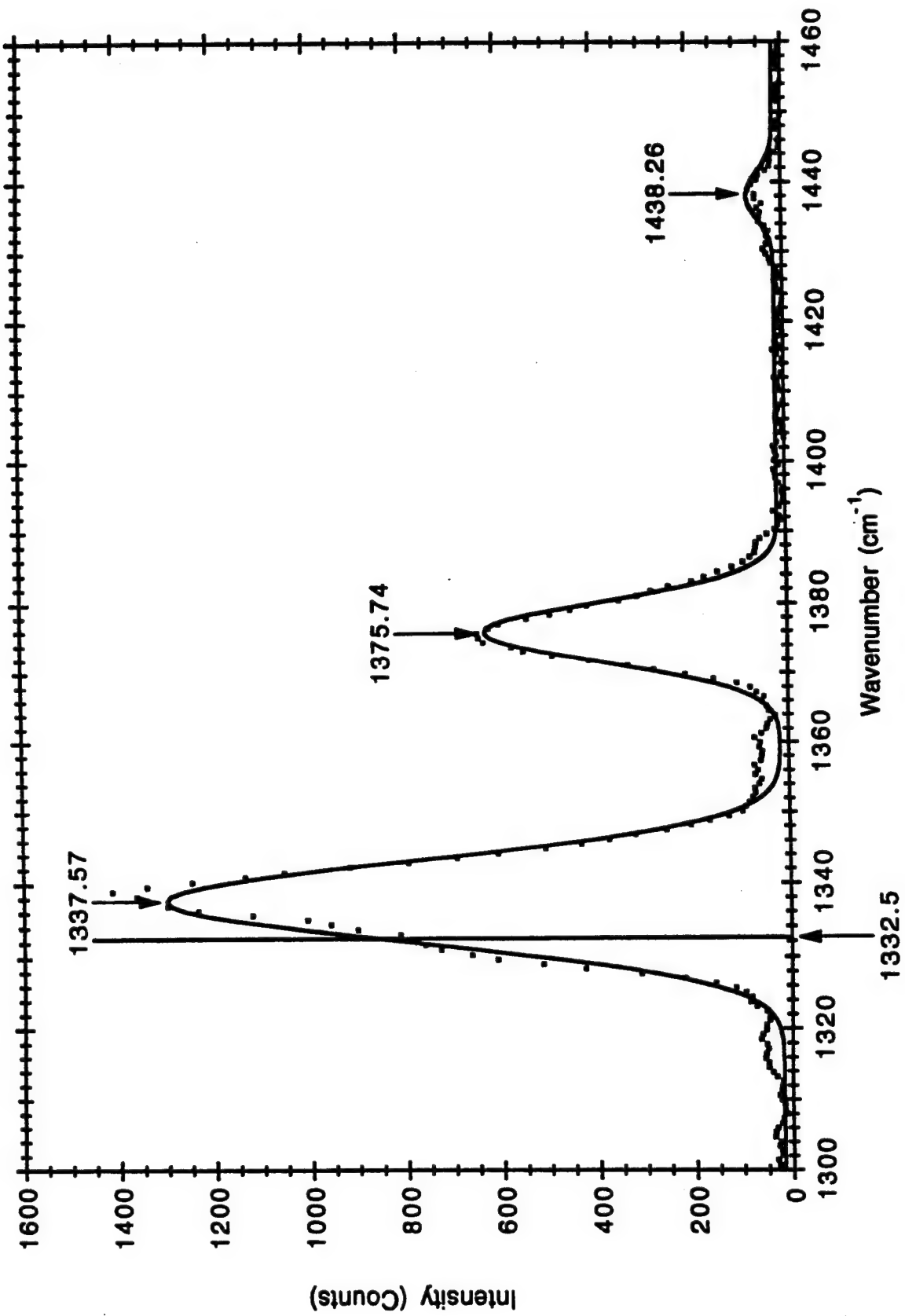Fig. 4.12 Experiment # 8 (shot 92-062), 428.5 kbar, [110].

Fig. 4.13   Experiment # 9 (Shot 92-032), 452 kbar, [110].

plot contains a vertical line representing the ambient 1332.5 cm^{-1} phonon line. The raw data points are represented by square dots on these figures and the solid line is the best fit to the data using a multiple Gaussian curve fitting equation discussed in Section 4.1.1. Annotation is provided above each peak fit for convenience and the longitudinal stress for each experiment is contained in the figure caption.

Experiment #1: The fitted spectrum for this experiment is shown in Figure 4.5. This was the only experiment that used the filter stage of the SPEX spectrometer. The low intensity reflects the reduction in throughput of the spectrometer with the filter stage in use.

The diamond was sandwiched between two sapphire windows to produce a "ring-down" type shock experiment. The difference in shock impedance between the materials results in a stress history in the diamond that initially has a high stress. With each reflection at the boundary, the longitudinal stress is reduced until it matches the stress produced on initial impact at the front sapphire window. After two reflections, the stress in the diamond was nearly equal to the initial impact stress in the sapphire. The fitted frequency peaks are indicated in the figure.

Experiment #2: This experiment was designed to yield a slightly higher stress than Experiment #1 without a back sapphire window. The improved time resolution in this experiment gave ample recording time and the use of a holographic edge filter in lieu of the SPEX filter stage yielded a 4-fold improvement in the signal over that observed in Experiment #1. The three shifted frequency locations are indicated in Figure 4.6.

Experiment #3: Experiment #3 was a symmetric Cu on Cu impact providing 167 kbar longitudinal stress in the diamond. The results from this experiment are shown in Figure 4.7. As stated in Section 3.7.1, the low counts for this experiment was believed to be due

to laser damage to the fiber. Only two shifted peaks were detected and the locations are indicated on the figure; the observed intensity was insufficient to resolve the ω_2 mode.

Experiment #4: As indicated in Table 4.3, this experiment was designed to reach 203 kbar using a symmetric Cu/Cu impact. The fitted spectrum is shown in Figure 4.8. The peak at 1383 cm^{-1} was fitted at a later time after it was realized that this mode could be observed. The fitted peak locations are indicated in the figure.

Experiment #5: Figure 4.9 is a plot of the frequency spectrum for Experiment #5 at the peak stress of 268 kbar. The frequency shifts are indicated on the figure. The complete record is given in Figure C. 1(e) in Appendix C. An interesting feature of this record is the intensity behavior of the central peak. After impact there appears to be an initial drop in intensity, as one would expect, but then the intensity of the peak grows as the shock progresses into the diamond. This is in contrast to the record shown in C.1(d) where the intensity decreases as peak stress in the material is approached.

Experiment #6. The stress attained in this experiment was 318 kbar. The fitted peaks and peak locations are shown in Figure 4.10. Impact occurred 80 nanoseconds later than predicted. The recording time was insufficient to observe the release wave as evident in Figure C.1(f) of Appendix C. Because the uncertainty in the projectile velocity indicate in Table 4.4 does not account for this error, it is suspected that an incorrect measurement of the trigger pin height resulted in the timing error.

Experiment #7: As mentioned in Section 3.7.1, this experiment was intended only as a test of the timing design. The data recorded were a bonus. Unfortunately, the Vidicon was configured to record only 200 channels and the 372 kbar stress placed the $\Delta\omega_2$ frequency

shift off-scale. Figure 4.11 shows the fit to the peak stress spectrum. The third peak should lie at roughly 1420 cm^{-1}.

Experiment #8: Figure 4.12 is the fitted spectrum for this experiment at 429 kbar. The fitted peak locations are indicated on the figure. As already discussed in Section 3.7.1 there was some loss of wavelength and temporal resolution for this experiment. The recorded intensity for the ω_1 shifted frequency is less than that for other experiments on this orientation.

Experiment #9: The 452 kbar stress for this experiment was the largest recorded for the present work. The fitted peak values are given in Figure 4.13. Because the theoretical work lagged somewhat behind the early experiments, it was originally thought that only one shifted peak was being observed. The largest peak was first believed to be the ambient peak, even though it displayed a small shift. This was later clarified and will be discussed in Chapter 5. The peak with the largest shift was not expected to be observed because its relative intensity was predicted to be very small. This peak was identified with certainty in Experiment #9 and subsequent Experiments #5, #2, and #8. Re-examination of earlier records from Experiments #1, #3, and #7 also yielded data for this peak location.

Predictions based on the previous {pqr} best-fit values of Grimsditch et al.[8] did not indicate that there should be any shifted Raman line in the immediate vicinity of the ambient line at 1332.5 cm^{-1}. The observation of the large amplitude peak near the ambient peak location was perplexing. It was thought that, perhaps the thickness of the copper (or the copper itself) was not shocking-up in a uniform manner. Most of the OFHC copper buffer pieces were about 2 mm thick and it was not known what the shock profile looked like as it entered the diamond. To verify that the observed shift of the

central peak was not due to a spreading out of the shock front, two experiments were performed.

The first experiment was designed to shock the [100] diamond orientation using the same impactor/buffer configuration as used for the [110] experiments. The quasi-harmonic model (presented in Chapter 2) predicts two shifted Raman frequencies for strain along [100], a doublet and a singlet. At moderate stress, these two shifted lines are predicted to be many wavenumbers away from the ambient Raman line. Thus, the central (unshifted) Raman line should vanish, or at least diminish, as the uniaxial strain applied along [100] progresses in the material. This experiment was performed at a peak stress of 278 kbar and will be discussed in the following section.

The second experiment was designed to eliminate the copper buffer and replace it with a thin sapphire buffer. The shock response in sapphire has been carefully examined.[84] The thin sapphire buffer should transmit the shock without any spreading. Experiment #2 was a symmetric Al_2O_3/Al_2O_3 impact designed to yield ~150 kbar in a-cut sapphire. Figure 4.6 shows the result at peak stress; it is obvious that the large peak persists. If the copper was not interfering with the shock front, then the question remained; what was the source of this line ?

A re-examination of the Grimsditch et al.[8] paper identified the problem. The best-fit values cited in their work are incorrect. When the correct {pqr} values from their study are used, a peak near the ambient Raman line is predicted. This was confirmed by the [100] experiment discussed in the following section.

4.4 [100] ORIENTATION : EXPERIMENTAL RESULTS

The rationale for conducting experiments on this orientation was to:

1) Check the spectrum at peak stress for traces of the ambient line which is predicted to diminish as the spectrum of the new symmetry manifests itself.

2)   Provide an independent check of the deformation potential values predicted by the [110] data.

Three experiments were performed with uniaxial strain along [100] and longitudinal stress in the 280-420 kbar range. The raw OMA data is given in Figs. C.2(a)-(c) in Appendix C. At peak stress these experiments displayed a large amplitude peak well separated from the ambient line at 1332.5 cm^{-1}. For two of the experiments, a second, much less intense peak, was also observed with a frequency shift slightly less than the large amplitude peak. Both Raman shifted peaks were observed to increase with longitudinal stress. These observations are consistent with the quasi-harmonic model presented in Section 2.4.2 and the polarization selection rules for quasi-backscatter geometry, that are addressed in the next chapter. The shifted line with higher intensity is identified as a singlet Raman-shifted frequency and the less intense line as the doublet Raman-shifted frequency. The triple degeneracy of the ambient Raman frequency is thus observed to be partially lifted for strain along [100].

The results for these experiments are summarized in Table 4.5. In this table, the second and third columns provide the type of material used for the impactor and buffer and their thicknesses. The actual projectile velocity is given in column 4 with the uncertainty shown in parenthesis. The peak nonlinear elastic stress is listed in column 5 and the linear elastic value provided in parenthesis below, this is also indicated at the bottom of the table. The remaining columns in Table 4.5 give the fitted peak values for the two observed frequencies, shifted from the ambient Raman frequency at 1332.5 cm^{-1}. For each experiment, the track corresponding to the peak stress was fit using the procedure described in Section 4.1.1.

4.4.1   Discussion of Individual [100] Shot Results

Figures 4.14-4.16 show the recorded spectrum for these experiments at peak stress. The horizontal axis is calibrated and converted to wavenumbers and the vertical axis

Table 4.5 Results For [100] Experiments

Experiment Number (shot #)	Impactor Material (Thick., mm)	Buffer Material (Thick., mm)	Projectile Velocity (mm/μs)	Peak Stress* (kbar)	Frequency Shift (cm^{-1}) From the Ambient Raman Line at 1332.5 cm^{-1}	
10 (92-042)	Platinum (1.971)	Copper (1.834)	0.802(1)	278 (257)	$\Delta\omega_s = 48.6 \pm 1.8$	$\Delta\omega_D = 32.1 \pm 2.1$
11 (92-061)	Platinum (1.972)	Copper (1.948)	0.963(4)	338.5 (308)	$\Delta\omega_s = 58.8 \pm 1.0$	$\Delta\omega_D = \dagger$
12 (92-060)	Platinum (1.991)	Copper (1.949)	1.160(1)	417.5 (372)	$\Delta\omega_s = 70.1 \pm 1.9$	$\Delta\omega_D = 46.5 \pm 2.2$

* The numbers in parenthesis reflect the stress value by assuming a linear elastic response for diamond.
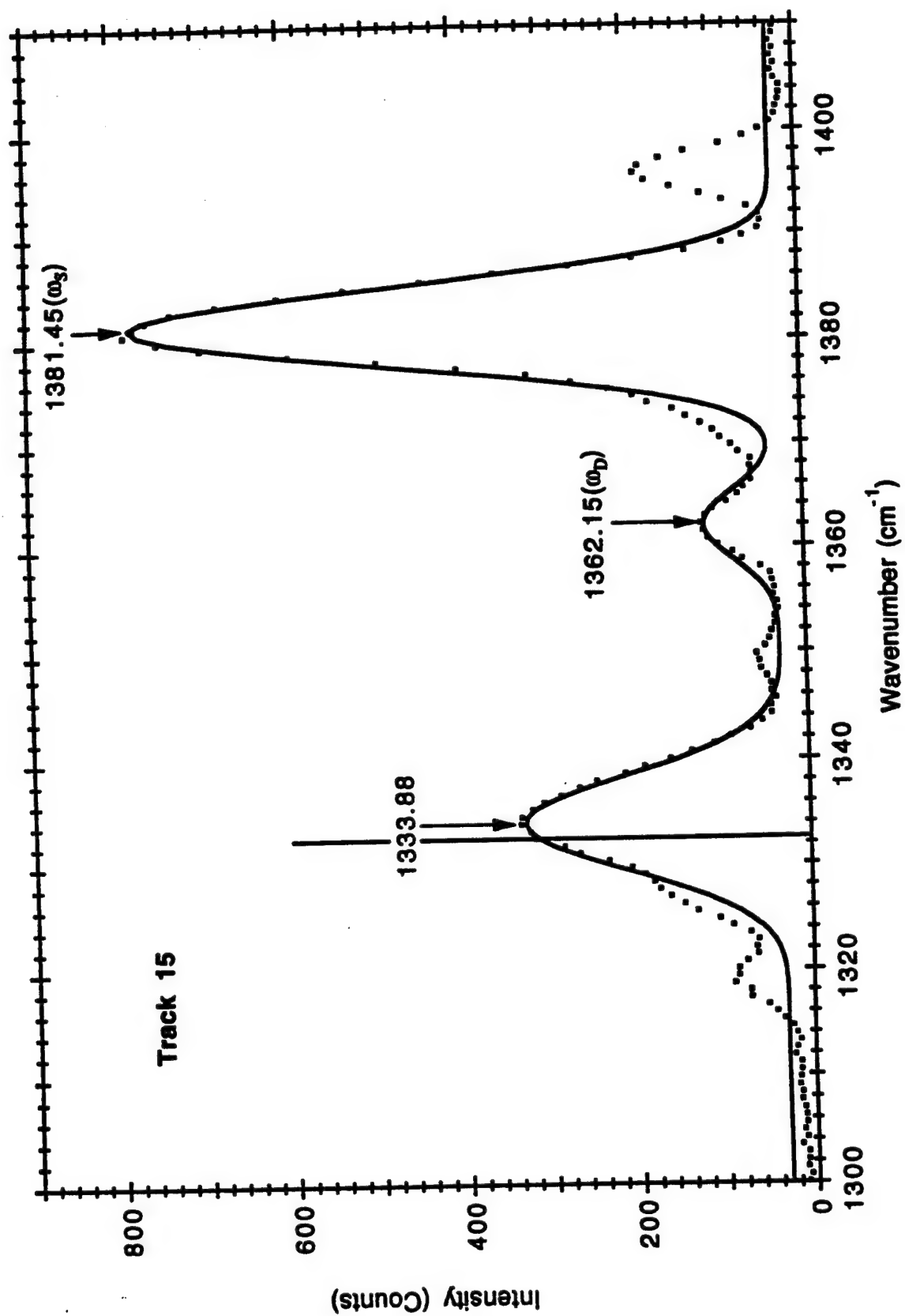
† Not Observed

A-151

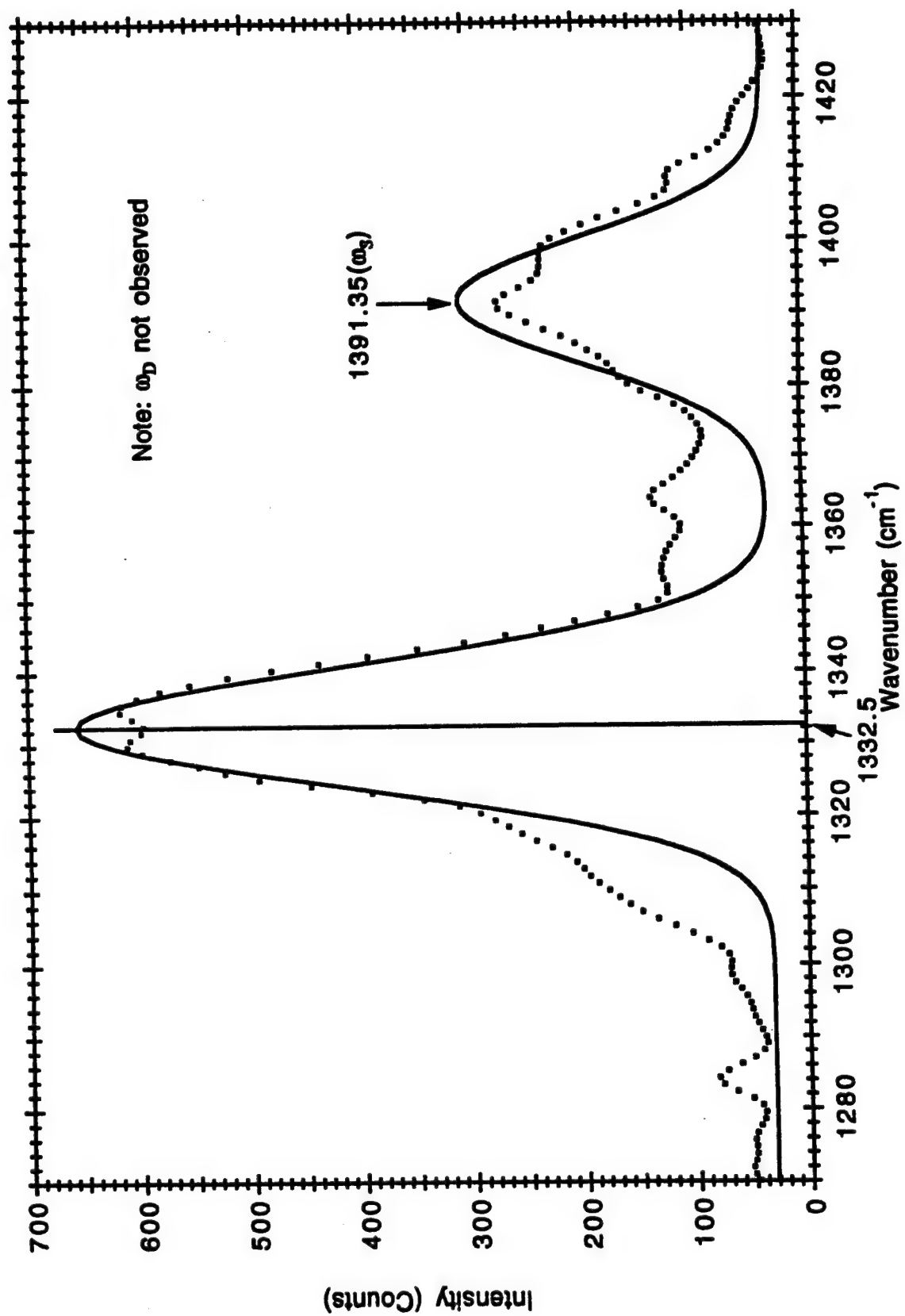Fig. 4.14   Experiment #10 (Shot 92-042), 278 kbar, [100].

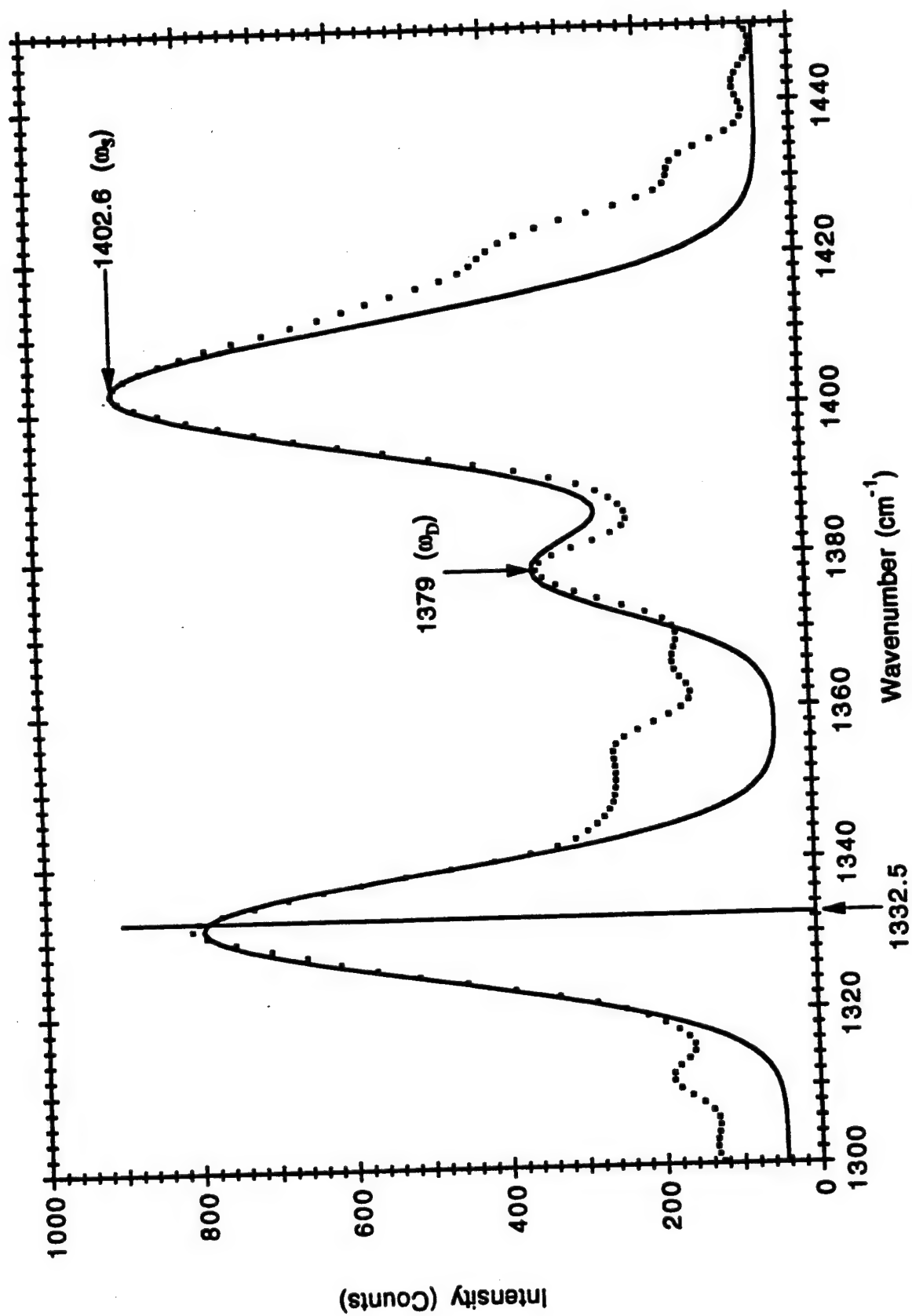Fig. 4.15 Experiment #11 (shot 92-061), 338.5 kbar, [100].

Fig. 4.16 Experiment #12 (shot 92-060), 417.5 kbar, [100].

A-154

reflects the relative intensity in photon counts. The raw data represented by dots and the solid line is the multiple peak Gaussian fit to the raw data. The single vertical line is the ambient Raman frequency at 1332.5 cm^{-1}. As indicated in Table 4.5, all three of these experiments used the platinum on copper impact configuration.

Experiment #10: Experiment #10 was the first experiment performed on the [100] orientation. For this experiment, shock loading produced a longitudinal stress of 278 kbar in the diamond sample. The fitted spectrum is shown in Figure 4.14. The complete OMA recording is provided in Figure C.2(a) of Appendix C.

One striking feature of this spectrum, when compared to all previous OMA records for the [110] experiments, is the reduction in intensity of the ambient line as the shock wave progresses through the material. Figure 4.17 shows details of the fitted track records as the shock wave advances. In this figure, the higher track number occurs earlier in time. Impact occurred on Track #20. Just prior to impact, the ambient intensity averaged ~1200 counts. By Track #18, the shock wave has progressed midway through the diamond sample and the intensity of the ambient peak has dropped by 50% to ~600 counts. By Track #16, the intensity has almost entirely shifted to the higher frequency peaks and subsequently begins to rise again by Track #15. The slight shift of the ambient peak in track # 16 (~3 cm^{-1}) is marginally larger than the uncertainty in the laser position ($\pm 2.5 cm^{-1}$), but is most likely an artifact of the fitting since the position before and after this track are within experimental error. In Figure 4.17, it may also be noted that there appears to be some structure at $\approx$ 1395 cm^{-1}. The occurrence of this structure on three of the tracks suggests that it is real, but its origin is not known.

The marked contrast between these results and the [110] uniaxial strain results suggests that the large ambient peak observed for the latter orientation was not the ambient peak, but rather, a manifestation of strain-induced symmetry reduction.
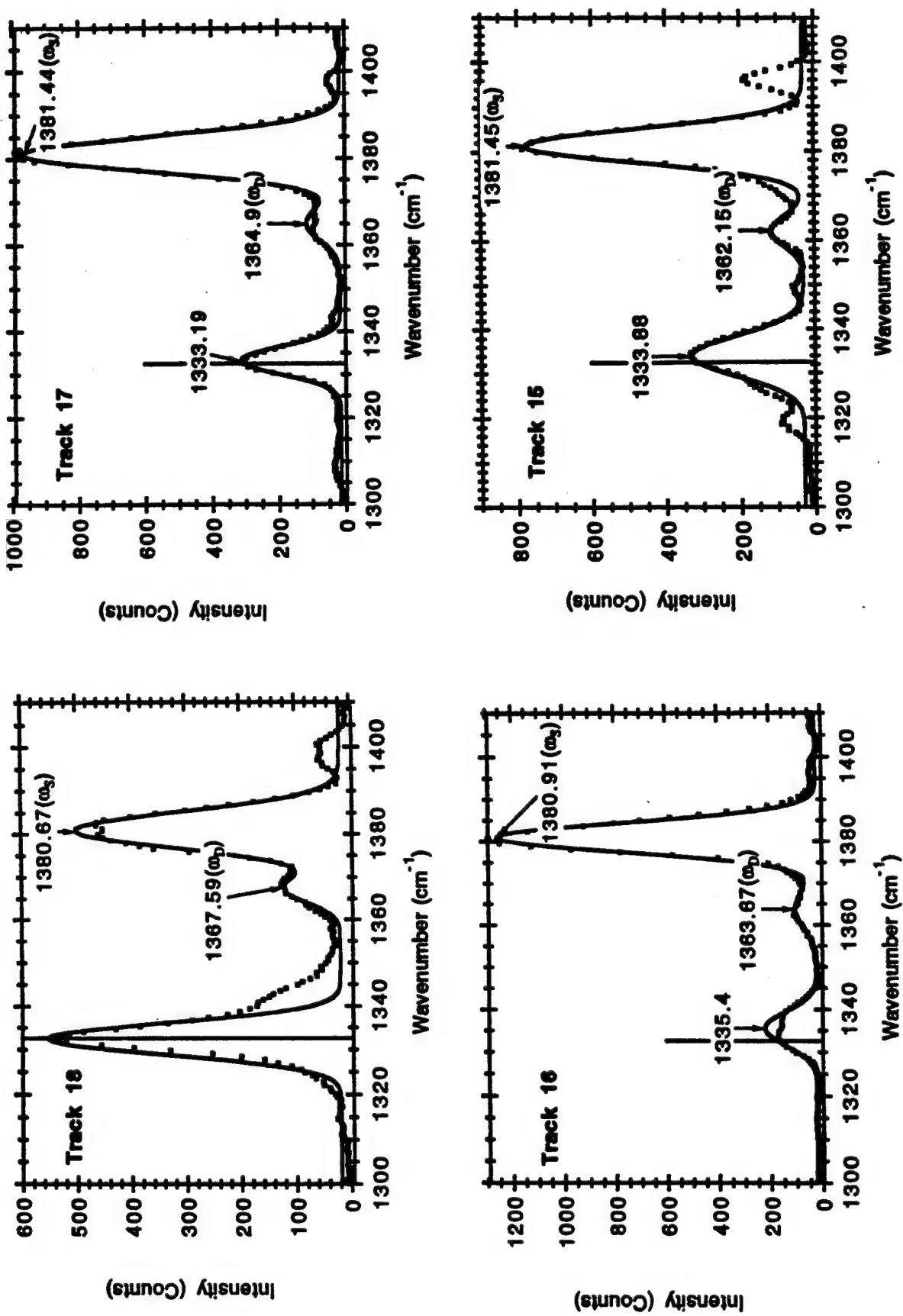
A-155

Figure 4.17 Experiment #10, Tracks #15-#18.

A-156

It is also observed in Figure 4.17, that there remains a finite contribution from the ambient spectrum, even at peak stress. The peak stress is assumed to occur when the shock wave has reached the free surface of the diamond. For time-resolution of 10 ns/track, as much as 1/4 of the sample thickness could still contribute to the ambient signal. This contribution could come from unstressed material, or stressed material which has been relieved from the back surface reflection.

Experiments #11: The longitudinal stress for this experiment was 338 kbar. The results are summarized in Table 4.5. The fitted spectrum is shown in Figure 4.15. This experiment, and Experiment #12 (described next), utilized the CCD detector system described in Section 3.5.7. It has already been mentioned that there was a noticeable loss of wavelength resolution and intensity for experiments performed with this detector. For Experiment #11, the time resolution was only 20 ns/track. The slower time resolution improved the intensity slightly, but made it very difficult to distinguish where peak stress occurred. For 20 ns/track time-resolution, as much as 50% of the stressed material may experience relief from the free surface between the first and second recorded spectrums. Thus, it is not surprising to see such a large contribution from the ambient Raman line as indicated in Figure 4.15. The doublet could not be resolved for the observed spectrum. The complete OMA record is shown in Figure C.11 in Appendix C.

Experiment #12: The results for this experiment are given in Table 4.5 and the fitted spectrum is shown in Figure 4.16. As for Experiment #11 there is an appreciable intensity observed for the ambient spectrum. For this experiment there was sufficient intensity to fit the doublet Raman shifted frequency, located at 1379 cm^{-1} in this figure.

It may be concluded that the observed symmetry changes in diamond shocked along the [100] direction is consistent with the microscopic theory presented in Section

2.4.2 and the polarization selection rules for quasi-backscatter geometry (discussed in the next chapter). The quality of the data for Experiments #11 and #12 is inferior to that of Experiment #10. For the present study, the [100] results are used only as an independent check of the {pqr} values determined from the [110] experiments.

4.5 DISCUSSION OF EXPERIMENTAL ERRORS AND UNCERTAINTIES

The experimental errors and uncertainties discussed in this section are divided into those which affect the measured Raman frequency shift and those which affect the calculated stress values. The errors associated with the shifted Raman frequency values, reported in this study, are treated first.

4.5.1 Error in Frequency Measurement

The measured shifts in the Raman frequencies are used in the following chapter to determine the {pqr} parameters, whose values are critical for the present work. The measured values for the frequency shifts are also used in Chapter 5 to determine the centroid of the splittings, permitting comparison with hydrostatic measurements. Thus, errors in the frequency shift measurement will propagate into the analysis portion of this work.

There are three factors that contribute to the uncertainty in the Raman shifted frequency:

1)   The precision that a wavelength can be determined for the grating-detector combination used to make the measurement, $\delta\lambda_{Detector}$.

2)   Fluctuations in the laser operating frequency, $\delta\omega_L$.

3)   Probable error do to the curve fitting, $\delta\omega_\sigma$.

The first two factors are random errors that affect the precision of the experimental measurements and the third is a statistical uncertainty resulting from the curve-fitting process.

The wavelength resolution at the detector depends on the detector-grating combination used during the experiment. For the intensified Vidicon, the resolution (in cm^{-1}) was found to be 1.06 cm^{-1}/channel for the 1200 groove/mm grating and 0.67 cm^{-1}/channel for the 1800 groove/mm grating. The CCD detector was only used in conjunction with the 1800 groove/mm grating and its resolution was 0.95 cm^{-1}/channel. Thus, for these grating-detector configurations, $\delta\lambda_{Detector} =$ 1.06 cm^{-1}, 0.67 cm^{-1}, and 0.95 cm^{-1}, respectively.

The error due to random fluctuations in the laser line is the major contribution to the uncertainty in the Raman frequency shift. Because the Raman frequency (ω_R) is equal to the laser frequency (ω_L) minus the characteristic Raman shift ($\Delta\omega_{shift}$), any change in the laser frequency necessarily effects the Raman frequency

$$\omega_R = \omega_L - \Delta\omega_{shift}, \Rightarrow (\omega_R \pm \delta\omega_L) = (\omega_L \pm \delta\omega_L) - \Delta\omega_{shift} \tag{4.7}$$

The magnitude of the laser fluctuations may be determined in the following manner. In discussing the wavelength calibration in Section 3.6.1, it was noted that mapping the spectrometer grating (1800) onto the 2-dimensional Vidicon detector array yielded a calibration factor given by $s = 0.01785\, nm/channel$. Hence, prior to impact, if the laser line ω_L that was centered on Channel #200 appeared to fluctuate ± 1 channel, in subsequent tracks (before impact) the 'new' laser line would now be $\omega'_L = (\omega_L \pm \delta\omega_L)$, where $\delta\omega_L = 0.01785\, nm$. This fluctuation corresponds to 1.35 cm^{-1}, in wavenumbers. During the impact event, Eq. (4.7) indicates that if the laser frequency has shifted by 1.35 cm^{-1}, then so too has the observed Raman frequency, because the Raman shift remains constant at $\Delta\omega_{shift} = 1332.5\, cm.^{-1}$

During an actual shock experiment, the splitting of the degenerate Raman line makes identification of the exact laser position difficult to determine. Instead, the laser

line fluctuations are followed for every track leading up to impact, and the mean square deviation from that position is used to determine the uncertainty in the laser line position. In the present work, the laser line fluctuations typically ranged between 1-2 cm.$^{-1}$ If the triply degenerate frequency (ω_R) is partially or completely lifted, the resultant Raman lines are affected in exactly the same manner by any uncertainty in the laser line.

Lastly, the values reported in Tables 4.4 and 4.5 for the frequency shifts are the fitted values. The fitting program is an iterative process that computes values for the Gaussian coefficients and continues with the fitting process until the best fit is attained. Along with the fitted value, the standard deviation from the mean value ($\delta\omega_\sigma$) is also given. Table 4.2 for Experiment #9 is an example of such an output. The error in the final, fitted, Raman frequency shift determined from the Root-Mean-Square of the uncertainties $\delta\lambda_{Detector}$, $\delta\omega_L$, and $\delta\omega_\sigma$. For Experiment #9, the laser frequency was observed to fluctuate by 1.35 cm^{-1}, using this number and the information from Table 4.2, the uncertainty in the three observed Raman shifted frequencies is

$$\delta\omega_1 = \sqrt{\left(1.34cm^{-1}\right)^2 + \left(0.67cm^{-1}\right)^2 + \left(0.08cm^{-1}\right)^2} \cong 1.5cm^{-1}$$

$$\delta\omega_2 = \sqrt{\left(1.34cm^{-1}\right)^2 + \left(0.67cm^{-1}\right)^2 + \left(1.07cm^{-1}\right)^2} \cong 1.8cm^{-1}$$

$$\delta\omega_3 = \sqrt{\left(1.34cm^{-1}\right)^2 + \left(0.67cm^{-1}\right)^2 + \left(0.04cm^{-1}\right)^2} \cong 1.5cm^{-1}$$

The uncertainty in frequency, calculated in this manner, is reflected in Table 4.4 for the [110] experiments and similarly in Table 4.5 for the [100] experiments. Thus, the error in measuring the Raman frequency is dominated by the fluctuation in frequency of the incident laser light. This affects all observed Raman frequencies equally. As remarked earlier, the peak with the largest frequency shift for [110] experiments (ω_2) is also the least intense. The fitted values for this peak indicate slightly larger deviations from the mean than for the more intense peaks, this can be seen in Table 4.2 for Experiment #9.

4.5.2 Uncertainty in Stress Calculations and Measurements

In order to calculate the nonzero stresses for this work the relationships derived in the finite strain formalism presented in Section 2.5.2 were used. Because the third-order constants used in this formalism are calculated (rather than measured) quantities, they contribute a systematic uncertainty in the nonzero stress calculations. The difference between the stress calculations, with and without these constants, will be discussed in the next chapter to convey the magnitude of this effect.

To calculate the longitudinal stress in the diamond an impedance matching calculation was performed (described in Section 4.2 of this chapter). Systematic error is introduced into these calculations due to uncertainties in the Cu, Ta, and Pt Hugoniots used to describe the initial impact. Mitchell and Nellis[68] have carefully examined the uncertainty in longitudinal stress for different impact configurations. For symmetric impact configurations, the uncertainty in longitudinal stress is given by[68]

$$\frac{\delta P}{P} = \left[\left(\frac{\delta \rho_0}{\rho_0} \right)^2 + \left(\frac{\delta D}{D} \right)^2 + \left(\frac{\delta V}{V} \right)^2 \right]^{\frac{1}{2}} \tag{4.8}$$

where $\delta \rho_0$ is the uncertainty in ambient density, δD is the uncertainty in shock velocity, and δV is the uncertainty in projectile velocity. Mitchell and Nellis[68] found that the uncertainty in shock velocity dominated in Eq. (4.8) for these materials, ranging from 0.5 to 1.2 %. The fractional uncertainties for projectile velocity and ambient density were typically $\approx 0.1\%$. For the present work the uncertainty in projectile velocity ranged from 0.4% to $\approx 1.0\%$ (Experiment #2), as indicated in Tables 4.4 and 4.5. Assuming the same uncertainty in density as Mitchell and Nellis[68] and using their maximum uncertainty in shock velocity, we find $(\delta P/P) \approx 1.5\%$ for the symmetric impacts in this study.

For non-symmetric impacts the uncertainty in longitudinal stress may be calculated in the following manner. The total fractional uncertainty in the longitudinal stress may be written as the sum of experimental and systematic contributions[68]

$$\frac{\delta P}{P} = \left(\frac{\delta P}{P}\right)_{experimental} + \left(\frac{\delta P}{P}\right)_{systematic} \qquad (4.9)$$

The systematic error is introduced because the particle velocity is calculated from measured quantities and the impactor Equation Of State, rather than being measured directly as in symmetric impacts. Following the procedure given by Mitchell and Nellis,[68] the uncertainty in the shock velocity for the impacting material is given by a two-standard-deviation (95% confidence level). The 2-σ deviation is least-squares fit to a quadratic expression in particle velocity

$$2\sigma = A_0 + A_1 u_p + A_2 u_p^2 \qquad (4.10)$$

The values for the coefficients in Eq. (4.10) are given in Table 4.6 for the Ta, Cu, and Pt materials as obtained from references 68-69.

Table 4.6 Uncertainty Parameters for Cu, Ta, and Pt Shock Velocities.

Material	$A_0 \ (mm/\mu s)$	A_1	$A_2 \ (\mu s/mm)$
Cu	0.0359	-0.0172	0.0061
Ta	0.0547	-0.03798	0.0102
Pt	0.0478	-0.02773	0.0858

Using $D^+ = D + 2\sigma$, and $D^- = D - 2\sigma$ we may calculate an upper (P^+) and lower (P^-) limit for the shock pressure so that $\delta P = \frac{1}{2}(P^+ - P^-)$. Using the material properties of Table 3.1 and the uncertainty parameters in Table 4.6, an estimate may be made for the systematic contribution. For Experiment #7, the impactor was Ta and the systematic contribution is $\approx 1\%$. Similarly, for Experiment #9 the impacting material was Pt and the

systematic contribution is ≈ 1.1%. Assuming the uncertainty of the projectile velocity (≈ 1%) to be the principal experimental contribution to Eq. (4.9), for non-symmetric impact we find

$$\frac{\delta P}{P} = \left(\frac{\delta P}{P}\right)_{experimental} + \left(\frac{\delta P}{P}\right)_{systematic} \approx 2\% \qquad (4.11)$$

Hence, the uncertainty in longitudinal stress ($P = -\sigma$) is slightly larger than that for symmetric impact.

The discussion thusfar has assumed that the projectile impact has launched a perfect plane wave into the target assembly. In actual practice the impactor will strike the target at some finite angle called the tilt angle. Impact tilt affects the orientation of particle motion in the sample and thus may contribute strain in undesirable directions. The impact tilt was measured twice during the series of experiments reported here, and in both cases was found to be less than 0.5 mrad. To obtain an estimate of what effect the tilt will have in the diamond, the tilt of the induced shock front in the copper buffer is first calculated. Using $D_{Cu} \approx 5\,mm/\mu s$, as the shock velocity in the copper buffer and $V \approx 1\,mm/\mu s$ as a typical projectile velocity, the tilt of the shock front in the copper buffer due to a 0.5 mrad projectile tilt is ≈ 2.5 mrad. This tilt produces a much larger tilt of the induced shock front in the diamond. Using $D_{diamond} \approx 18\,mm/\mu s$ for the shock velocity in diamond, the induced wavefront is tilted by ≈ 9 mrad.

The particle velocity (u_p) for diamond was not measured in the present study. However, because it is measured normal to the sample surface, in the presence of tilt we may write $u_p(\theta_{tilt}) = u_p \cos\theta_{tilt}$. For a tilt of 9 mrad this corresponds to a .004% error in the particle velocity. The longitudinal stress is related to the particle velocity through the jump conditions in Eq (2.64). Thus, a .004% error in the particle velocity yields the same error in the longitudinal stress value.

A very similar error is introduced by the uncertainty of the crystallographic axis orientation. In Section 3.1 it was stated that the diamond samples were supplied with tolerances of $\pm 3°$ for the two diamond orientations used in this study. This corresponds to a ≈ 50 mrad tilt and a 0.1% error in the particle velocity. Thus, it may be concluded that, in the present study, tilt and crystallographic axis mis-alignment do not contribute significantly to the calculated longitudinal stress.

4.6 SUMMARY OF THE MAIN EXPERIMENTAL RESULTS

The principal experimental results presented in this chapter may be briefly summarized as follows:

1) Nine experiments were performed on diamond with uniaxial strain along the [110] direction. The longitudinal stress in the diamond was calculated to be in the 122 kbar to 452 kbar range. In seven of these experiments, three Raman peaks were observed. They displayed shifts in frequency, from the ambient Raman peak, that increased with peak stress. In the remaining two experiments only two peaks were observed because of instrument limitations. These results suggest that the triply degenerate ambient Raman frequency is completely lifted for uniaxial strain along [110], in agreement with the theoretical predictions presented in Chapter 2.

2) Three shock compression experiments were performed with uniaxial strain along the [100] direction in diamond. Two Raman-shifted peaks were identified in these experiments. They are consistent with the singlet and doublet Raman frequency shifts predicted in the theory of Chapter 2 for strain along the [100] direction. This suggests that the degeneracy of the Raman frequency has been partially lifted by application of this strain. The shift of these peaks from the ambient Raman frequency was observed to increase with longitudinal stress over the calculated range 278 kbar to 418 kbar.

Chapter 5

ANALYSIS AND DISCUSSION OF EXPERIMENTAL RESULTS

The results presented in Chapter 4 are analyzed using the theoretical developments presented in Chapter 2. The experimental data yield frequency shifts from which the values for the anharmonic parameters {pqr} values and mode Grüneisen constant γ are determined.

Predictions based on the {pqr} values from the present work are compared with predictions using the previous {pqr} values of Grimsditch et al.[8] for [110] and [100] uniaxial strain in diamond. The mean stress and splitting centroid are determined for each experiment and compared to the static high-pressure studies performed on the Raman spectrum of diamond.

Modifications must be made to the polarization selection rules given in Chapter 2, to reflect the actual experimental geometry (quasi-backscatter). This is discussed in the following section.

5.1 SYNOPSIS OF PREDICTED SPLITTINGS AND FREQUENCY SHIFTS

To aid the discussion in this chapter, the theoretical relationships presented in Chapter 2 are summarized here and adapted, where necessary, to conform to the actual experimental arrangement used in this work.

5.1.1 Quasi-Backscatter Geometry

Intensity measurements made of the ambient Raman spectrum for this study routinely displayed fluctuations as large as 10-15%, from track to track, during a complete recording (see Figure 3.12 (b)). Because the fluctuations were so large, absolute intensity measurements were not attempted in this study. The Raman intensity is proportional to the product of the Raman tensor with the incident and scattered light

polarizations, thus, even if absolute measurements are not possible, qualitative predictions can be made for a specific scattering geometry.

In Section 2.3.2, expressions were developed for describing the relative intensity of back-scattered light from a sample at ambient pressure. The laboratory coordinate system was described by the set of axes { XYZ } denoted by upper case letters, and the $(+)\hat{X}$ direction was defined as parallel to the barrel of the light gas gun. The crystallographic coordinate system was designated by the lower case { xyz }, representing the crystallographic directions {[100],[010],[001]} respectively, and defined in such a manner that $\hat{x}$ was parallel to $\hat{X}$. It was further assumed that the crystal was so oriented that : $\hat{y}//\hat{Y}$, and $\hat{z}//\hat{Z}$. The Raman tensors and polarization components are defined with respect to the laboratory frame, { XYZ }, in which the intensity is measured.

Similarly, for the coordinate system { x'y'z' } corresponding to the directions {[110],[1$\bar{1}$0],[001]} , $\hat{x}'$ was chosen to be parallel to $\hat{X}$, $\hat{y}'//\hat{Y}$, and $\hat{z}'//\hat{Z}$. Because the Raman tensors are defined with respect to the principle crystallographic system, care must be exercised in transfroming to the primed crystallographic system. The polarizability tensors are transformed to the primed system and the changes in polarizability along the directions of the normal mode vibrations (phonon polarization) are taken into account.

The discussion of Section 2.3.2 must be modified somewhat to reflect the actual experimental set-up. The incident laser light was brought in at an angle of 45° to the X-axis of the laboratory frame. This geometry helps to minimize the unscattered laser light, which is $\approx 10^8$ times more intense than Raman scattering.

For an arbitrary scattering center located in the diamond, the direction of propagation of the incident light in the diamond is shown in Figure 5.1 and is given by Snell's law
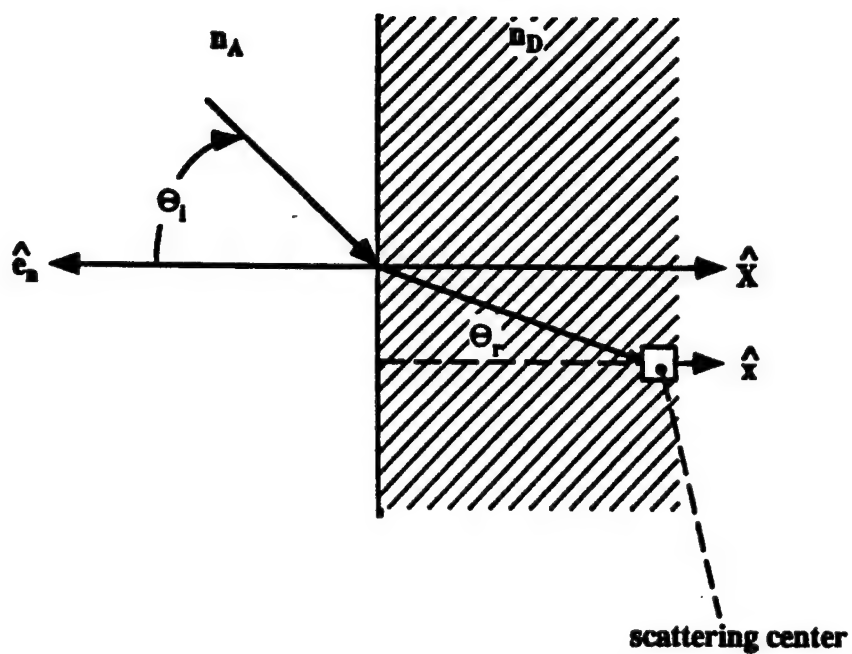
$$n_A \sin \theta_i = n_D \sin \theta_r \qquad (5.1)$$

A-166

Figure 5.1   Refracted Angle of Incident Light In Diamond.

or

$$\therefore \quad \theta_r = \sin^{-1}\left[\left(\frac{n_A}{n_D}\right)\sin\theta_i\right] \qquad (5.2)$$

where n_A is the refractive index of air, n_D is the refractive index of diamond, $\theta_i = 45^0$, θ_r is the refracted angle in the diamond, and $\hat{e}_n$ is the unit normal to the air-diamond interface. Choosing $n_A = 1$, and $n_D = 2.43$ (Edwards[66]), Eq. (5.1) gives $\theta_r = 16.9^\circ$.

Figure 5.2 shows the quasi-backscatter geometry, relative to the laboratory coordinate system. The incident laser light with wave vector k^i propagates in the laboratory frame, making an angle of θ_r to the crystallographic x-axis (recall $\hat{x}//\hat{X}$). The scattered light with wave vector k^s is collected parallel to the X-axis. The incident light has polarization components $\hat{e}^i_X = \sin\theta_r$, $\hat{e}^i_Y$, and $\hat{e}^i_Z = \cos\theta_r$, and the scattered light has polarization components $\hat{e}^s_Y$, and $\hat{e}^s_Z$. The scattered signal, as before for the backscattering geometry, is considered to have contributions parallel and perpendicular to the XZ scattering plane. The total observed intensity is the algebraic sum of these contributions.

The change in scattering geometry shown in Figure 5.2 permits an additional polarization component along the laboratory X-axis, for the incident light. To determine the modification to the intensity of the scattered light we recall Eq. (2.9)

$$I = A\sum_n \left|\sum_{\rho,\sigma} e^i_\rho R_{\rho\sigma}(n) e^s_\sigma\right|^2 \qquad (5.3)$$

where e^i_ρ is the incident polarization, e^s_σ is the scattered polarization, $R_{\rho\sigma}(n)$ is the $\rho\sigma$ component of the nth Raman scattering tensor, and A is a constant of proportionality. The quantum mechanical derivation for the Raman scattering efficiency given by Loudon[33, 36] demonstrates that the constant A, varies as the fourth power of the incident laser frequency. Thus, higher incident frequencies are desirable.
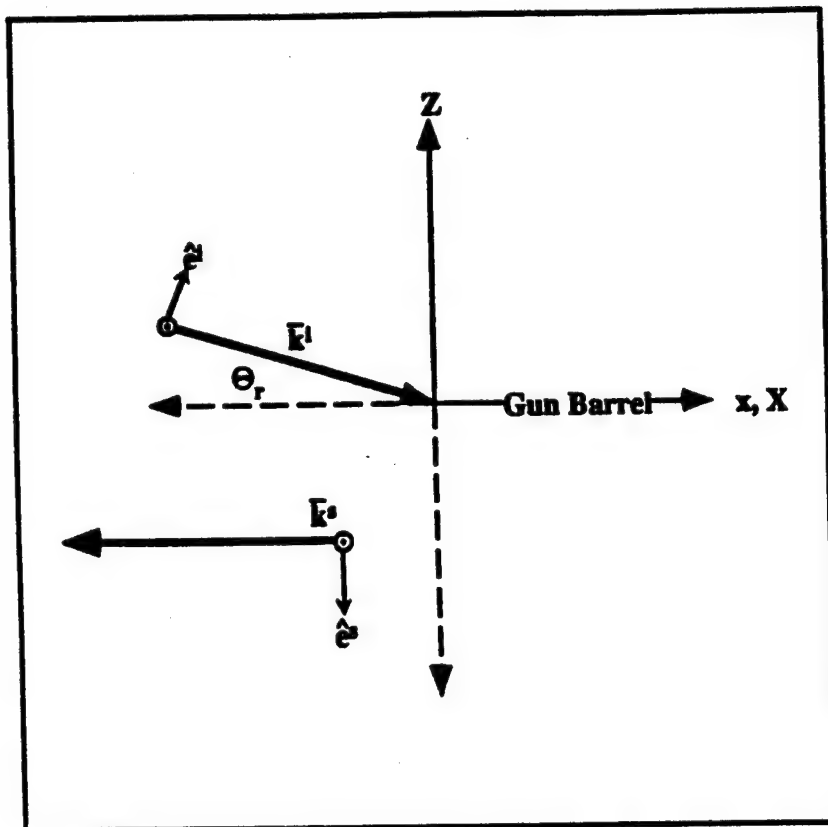
Figure 5.2 Quasi-Backscatter Scattering Geometry.

A-169

In the laboratory frame {XYZ}, scattering parallel to the XZ plane is determined by expanding Eq. (5.3) in terms of the incident and scattered polarizations to yield

$$I_{\shortparallel} = A\sum_{n}\left|e_X^i R_{XZ}(n)e_Z^s + e_Y^i R_{YZ}(n)e_Z^s + e_Z^i R_{ZZ}(n)e_Z^s\right|^2 \tag{5.4}$$

Similarly, for scattering perpendicular to the XZ plane it is found that

$$I_{\perp} = A\sum_{n}\left|e_X^i R_{XY}(n)e_Y^s + e_Y^i R_{YY}(n)e_Y^s + e_Z^i R_{ZY}(n)e_Y^s\right|^2 \tag{5.5}$$

It is important to note that the Raman tensors indicated in Eqs. (5.4) and (5.5) are written with respect to the laboratory frame of reference. For the {xyz} crystallographic system, these tensors are given by Eq. (2.12), and for the primed crystal directions {x'y'z'} the tensors are given by Eq. (2.19b).

5.1.2 Raman Spectrum For [100] Strain

The effect of uniaxial strain on the frequency of the Raman spectrum was presented in Section 2.4.2. It was demonstrated that the potential energy of the strained crystal could be expanded in a Taylor's series about new atomic positions that were different from the unstrained equilibrium positions. Subsequently, the equations of motion for the crystal vibrations were shown to be solutions of the modified dynamical matrix $G_{\alpha\beta}$ that was expressed in a power series in the applied strain.

For uniaxial strain along the [100] direction, two distinct solutions to the secular matrix were found, one corresponding to a singlet frequency shift $\Delta\omega_S$ and one corresponding to a doubly degenerate frequency shift $\Delta\omega_D$. They are given by

A-170

$$\Delta\omega_S = \omega_R \left\{ \left[1 + \frac{p\eta}{\omega_R^2} \right]^{\frac{1}{2}} - 1 \right\}$$

$$\Delta\omega_D = \omega_R \left\{ \left[1 + \frac{q\eta}{\omega_R^2} \right]^{\frac{1}{2}} - 1 \right\}$$

(5.6)

where ω_R is the ambient Raman frequency at $1332.5 cm^{-1}$, and the $\{pq\}$ are two of the three anharmonic parameters described by the fourth rank tensor $G_{\alpha\beta\gamma\delta}$.

Substitution of the eigenvalue solutions $\lambda_i = \omega_i^2 - \omega_R^2$ into the secular equation provides the eigenvectors that characterize the polarization directions for the corresponding phonons. Performing this substitution yields

$$\rho_s = \begin{pmatrix} 1 \\ 0 \\ 0 \end{pmatrix}; \qquad \rho_D = \begin{pmatrix} 0 \\ 1 \\ 0 \end{pmatrix}; \qquad \rho_D = \begin{pmatrix} 0 \\ 0 \\ 1 \end{pmatrix} \qquad (5.7)$$

Thus, the shifted Raman frequency corresponding to the singlet is polarized along the direction of applied strain and the doublet is polarized orthogonal to the applied strain along the crystal directions $\hat{y}$ and $\hat{z}$.

The experimental ability to observe the frequency shifted Raman singlet and/or doublet is dictated by the experimental geometry and the intensity expressions as discussed in the previous sub-section. To apply Eqs. (5.4) and (5.5) we must first recall the form of the Raman tensors for strain along the crystallographic [100] direction. For small strain, these tensors are found from Eq. (2.23a) to be given by

$$\begin{pmatrix} 1 \\ 0 \\ 0 \end{pmatrix} \begin{bmatrix} 0 & 0 & 0 \\ 0 & 0 & d \\ 0 & d & 0 \end{bmatrix}, \quad \begin{pmatrix} 0 \\ 1 \\ 0 \end{pmatrix} \begin{bmatrix} 0 & 0 & d \\ 0 & 0 & 0 \\ d & 0 & 0 \end{bmatrix}, \quad \begin{pmatrix} 0 \\ 0 \\ 1 \end{pmatrix} \begin{bmatrix} 0 & d & 0 \\ d & 0 & 0 \\ 0 & 0 & 0 \end{bmatrix} \qquad (5.8)$$

Singlet (B_{2g}) Doublet (E_g) Doublet (E_g)

To the left of each tensor representation is the corresponding phonon polarization vector as indicated in Eq. (5.7). The Raman tensors are labeled according to whether they contribute to the singlet or the doublet frequency shift. The irreducible representations determined in Section 2.4.1, and listed in Table 2.4 for the strained symmetry, are given in parentheses. For notational convenience, the frequency shifts are referred to as singlet or doublet, with the understanding that the $\Delta\omega_S \Rightarrow \Delta\omega_{B_{2g}}$ and $\Delta\omega_D \Rightarrow \Delta\omega_{E_g}$ assignments have been made.

Inspection of the Raman tensors given in Eq. (5.8) indicates that there are only two nonvanishing components that may contribute to the singlet intensity and four that may contribute to the doublet intensity. These are

$$\left.\begin{aligned} R_{YZ}(S) = R_{ZY}(S) = d(S) \\ R_{XZ}(D) = R_{ZX}(D) = d(D) \\ R_{XY}(D) = R_{YX}(D) = d(D) \end{aligned}\right\} \tag{5.9}$$

The respective degeneracy is written in parenthesis to avoid any possible confusion.

Eq. (5.2) indicates that a nonvanishing Raman tensor component is a necessary requirement for observing a given intensity, provided the appropriate incident and scattered polarizations are present. To better illustrate the importance of polarization in this selection process, Eqs.(5.3) and (5.4) may be rewritten in light of the nonvanishing components indicated in (5.9). This gives

$$I_{\parallel} = A\left\{\left|e_X^i R_{XZ}(D)e_Z^s\right|^2 + \left|+e_Y^i R_{YZ}(S)e_Z^s\right|^2\right\} \tag{5.10}$$

$$I_{\perp} = A\left\{\left|e_X^i R_{XY}(D)e_Y^s\right|^2 + \left|+e_Z^i R_{ZY}(S)e_Y^s\right|^2\right\} \tag{5.11}$$

By choosing the appropriate incident and scattered polarizations, it is thus possible to exclude either the singlet or the doublet line. For the work reported here, the incident

laser light was unpolarized and no attempt was made to restrict the scattered polarization. Hence, the observed intensity is just the algebraic sum of Eqs. (5.10) and (5.11). This arrangement had the advantage of allowing the observation of both lines simultaneously.

Substituting the values for the Raman tensor elements and the polarization vectors described in Section 5.1.1, we arrive at the intensity expression for the [100] strain case

$$I_{total} = I_\parallel + I_\perp = A\{2d^2(D)\sin^2(\theta_r) + d^2(S)[1 + \cos^2\theta_r]\} \tag{5.12}$$

In Section 2.3.2 it was shown that for small strain, it is reasonable to assume that, $d^2(D) \approx d^2(S)$. Based upon this assumption, we can approximate the relative intensities as

$$\frac{I_{single t}}{I_{doublet}} \approx \frac{1}{2}\left(\frac{1 + \cos^2\theta_r}{1 - \cos^2\theta_r}\right) = 11.3, \; for \; \theta_r = 16.9^\circ \tag{5.13}$$

For the two experiments where both the singlet and doublet were observed, the ratio of the singlet intensity to the doublet intensity was roughly 9:1 and 3:1. These ratios are not too surprising when Figures 4.14 and 4.16 are re-examined. In both of these figures the ambient Raman frequency is observed to be present. If all of the ambient intensity had been transferred to the singlet and doublet, Eq. (5.13) should be approximately correct. However, there is no reason to assume that Eq. (5.13) is accurate when the symmetry has not been completely deformed. Intensity fluctuations from the vidicon are also a problem for these measurements, as discussed earlier.

5.1.3 Raman Spectrum For [110] Strain

The basic theory of Section 2.4.2 leading up to the secular equation may be applied to uniaxial strain along [110]. It is emphasized, however, that the secular

equation is written for the principal crystallographic axes {[100], [010], [001]} and care must be taken in defining the applied strain correctly. The correct formulation for uniaxial strain along [110] is given by the strain matrix of Eq. (2.50), where $\eta_{xx} = \eta_{yy} = \eta_{xy} = \eta_{yx} = \eta'/2$. Here, η' is the magnitude of the uniaxial strain along the [110] direction.

For this strain three unique solutions to the secular matrix of Eq. (2.46) were found. The corresponding eigenfrequencies of these solutions are predicted to be shifted from the ambient value, ω_R, by:

$$
\left.
\begin{aligned}
\Delta\omega_1 &= \omega_R \left\{ \left[1 + \frac{q\eta'}{\omega_R^2} \right]^{\frac{1}{2}} - 1 \right\} \\[2mm]
\Delta\omega_2 &= \omega_R \left\{ \left[1 + \frac{(p+q+2r)\eta'}{2\omega_R^2} \right]^{\frac{1}{2}} - 1 \right\} \\[2mm]
\Delta\omega_3 &= \omega_R \left\{ \left[1 + \frac{(p+q-2r)\eta'}{2\omega_R^2} \right]^{\frac{1}{2}} - 1 \right\}
\end{aligned}
\right\}
\tag{5.14}
$$

In these expressions, it is seen that all three of the anharmonic parameters { pqr } are present. It is thus possible to determine values for these parameters from this single diamond orientation provided the polarization selection rules permit their observation. As for the previous case, the eigenvalue solutions are substituted back into the secular matrix to yield the phonon polarizations for these frequencies. The normalized results are,

$$
\rho_1 = \begin{pmatrix} 0 \\ 0 \\ 1 \end{pmatrix}; \qquad \rho_2 = \frac{1}{\sqrt{2}} \begin{pmatrix} 1 \\ 1 \\ 0 \end{pmatrix}; \qquad \rho_3 = \frac{1}{\sqrt{2}} \begin{pmatrix} 1 \\ -1 \\ 0 \end{pmatrix} \tag{5.15}
$$

Hence, the shifted frequency $\Delta\omega_2$ is polarized parallel to the applied strain, and $\Delta\omega_1$ and $\Delta\omega_3$ are polarized along the crystallographic directions $\hat{z}'$ and $\hat{y}'$, respectively (perpendicular to the strain).

It is necessary to apply the intensity expressions summarized by Eqs. (5.4) and (5.5) to ascertain which shifted frequencies may be experimentally observed for the quasi-backscatter geometry. For small strain, the Raman tensors were found to be given by,

$$
\begin{pmatrix} 0 \\ 0 \\ 1 \end{pmatrix} \begin{bmatrix} d & 0 & 0 \\ 0 & -d & 0 \\ 0 & 0 & 0 \end{bmatrix} , \quad \begin{pmatrix} 1 \\ 1 \\ 0 \end{pmatrix} \begin{bmatrix} 0 & 0 & d \\ 0 & 0 & 0 \\ d & 0 & 0 \end{bmatrix} , \quad \begin{pmatrix} 1 \\ \bar{1} \\ 0 \end{pmatrix} \begin{bmatrix} 0 & 0 & 0 \\ 0 & 0 & -d \\ 0 & -d & 0 \end{bmatrix} \qquad (5.16)
$$

$$ 1 \left(A_{1_s} \right) \qquad\qquad 2 \left(B_{2_s} \right) \qquad\qquad 3 \left(B_{3_s} \right) $$

To the left of each tensor representation is the phonon polarization determined from the eigenfunctions of the secular matrix. The tensors are labeled as 1, 2, or 3 according to the mode they correspond to. The irreducible representations determined in Section 2.4.1, and listed in Table 2.4, for the strained symmetry are shown in parentheses. The shifted frequencies will continue to be designated as in Eq. (5.14) with the understanding that $\Delta\omega_1 \Rightarrow \Delta\omega_{A_{1_s}}$, $\Delta\omega_2 \Rightarrow \Delta\omega_{B_{2_s}}$, $\Delta\omega_3 \Rightarrow \Delta\omega_{B_{3_s}}$.

By inspection, the nonvanishing tensor elements are found to be

$$
\left.
\begin{aligned}
R_{XZ}(2) &= R_{ZX}(2) = d(2) \\
R_{YZ}(3) &= R_{ZY}(3) = -d(3) \\
R_{XX}(1) &= d(1), \quad R_{YY}(1) = -d(1)
\end{aligned}
\right\} \qquad (5.17)
$$

It may be noted that some of the tensor elements are negative. Because the intensity, crossection, and transition probability are all proportional to the square of the Raman scattering tensor, the sign of $d(i)$ will not affect the calculations. Estimates of the

magnitude, as well as the sign of the Raman tensor element for diamond at ambient pressure, have been reported in the literature.[85] The most recent measurement given by Grimsditch et al.[85] is $|d| = 4.4\,\mathring{A}^2$.

Using the tensor elements provided in Eq. (5.17), the intensity may be expressed as contributions parallel and perpendicular to the scattering plane. Thus

$$\left.\begin{array}{l} I_{\parallel} = A\left\{d^2(2)\sin^2\theta_r + d^2(3)\right\} \\ I_{\perp} = A\left\{d^2(1) + d^2(3)\cos^2\theta_r\right\} \end{array}\right\} \qquad (5.18)$$

Therefore, the total intensity is given by

$$I_{total} = I_{\parallel} + I_{\perp} = A\left\{d^2(1) + d^2(2)\sin^2\theta_r + d^2(3)\left[1 + \cos^2\theta_r\right]\right\} \qquad (5.19)$$

$$= \quad I_1 \quad + \quad I_2 \quad + \quad I_3$$

For small strain, Eq. (2.23b) indicates that it is reasonable to assume that $d^2(1) \approx d^2(2) \approx d^2(3)$. With this assumption we can approximate the relative intensities as

$$\left.\begin{array}{l} \dfrac{I_1}{I_2} \approx \dfrac{1}{1 - \cos^2\theta_r} \cong 12 \\[4mm] \dfrac{I_3}{I_2} \approx \dfrac{1 + \cos^2\theta_r}{1 - \cos^2\theta_r} \cong 23 \end{array}\right\} \qquad (5.20)$$

The relative intensities for the ratios given by Eq. (5.20) were determined from the present experimental data to be: $(I_1/I_2) \approx 6(3)$, and $(I_3/I_2) \approx 16(8)$. For this study, the polarization selection rules were employed as a means to predict the occurrence of the shifted Raman lines and to provide crude estimates of their relative intensity. The disparity between the predicted relative intensities of Eq. (5.20) and the actual values is

noted. However, because the ambient Raman line lies so close to the $\Delta\omega_3$ mode, it is not known to what extent the ambient line contributes to this intensity .

5.2 DETERMINATION OF ANHARMONIC PARAMETERS FROM SHOCK DATA

In this section, the theoretical developments just summarized are used to determine the values of the anharmonic parameters {pqr}. These parameters are directly linked to the atomic force constants that describe the lattice dynamical behavior. Thus, they represent the link between experimental data and various *ab initio* theoretical calculations.

The analysis of [110] uniaxial strain data will be presented first. As stated earlier, this orientation permits determination of all three anharmonic constants. With the {pqr} values determined solely from the [110] data, the results from the [100] strain experiments may then be used as an independent check of the {pq} values.

The experimentally measured frequency shifts will be compared to the expressions of Eq. (5.14) and Eq. (5.6) for the {pqr} values determined from the present work and those determined previously by Grimsditch et al.[8] from uniaxial stress measurements. Comparison of predictions based on the present work to static high pressure studies and discussion of the mode Grüneisen constant are deferred to Section 5.3.

5.2.1 Analysis of the [110] Data

The relationships provided by Eq. (5.14) for the observed frequency shifts as functions of the anharmonic parameters may be inverted to yield expressions for the {pqr} values. These are given by

$$\frac{p}{\omega_R^2} = \frac{1}{\eta'} \left\{ \left[\left(\frac{\Delta\omega_2}{\omega_R} \right) + 1 \right]^2 + \left[\left(\frac{\Delta\omega_3}{\omega_R} \right) + 1 \right]^2 - \left[\left(\frac{\Delta\omega_1}{\omega_R} \right) + 1 \right]^2 - 1 \right\} \qquad (5.21a)$$

$$\frac{q}{\omega_R^2} = \frac{1}{\eta'} \left\{ \left[\left(\frac{\Delta\omega_1}{\omega_R} \right) + 1 \right]^2 - 1 \right\} \qquad (5.21b)$$

$$\frac{r}{\omega_R^2} = \frac{1}{2\eta'} \left\{ \left[\left(\frac{\Delta\omega_2}{\omega_R} \right) + 1 \right]^2 - \left[\left(\frac{\Delta\omega_3}{\omega_R} \right) + 1 \right]^2 \right\} \qquad (5.21c)$$

For each experiment, the longitudinal stress was determined through impedance matching calculations as described in Section 4.2. As discussed earlier, the $D - u_p$ relationship for diamond is not known. For this work, it was calculated from the finite strain expressions in Eq. (2.90) and the Rankine-Hugoniot jump conditions given by Eq. (2.64). For a given density compression, the strain may be determined by Eq. (2.67) and the stresses from Eq. (2.90). From the calculated stress value and the density compression, the shock velocity and the particle velocity may be calculated from Eqs. (2.92) and (2.93), respectively. It is convenient to express results in terms of the density compression $\mu = (\rho/\rho_0) - 1$.

The {pqr} values determined from the experimentally observed frequency shifts and the relations in Eqs. (5.21) are presented in Table 5.1. In this table, the longitudinal stress has been defined by Eq. (2.91) to have a positive value. The uniaxial strain and density compression are indicated in columns 2 and 3, respectively. The values for {pqr} have been determined for each experiment and the mean value is indicated at the bottom of each column along with the 1-sigma standard deviation. The error in the {pqr} values cited for each experiment result from the error in the measured frequency shifts given in Table 4.4. The corresponding values determined from the uniaxial stress study of Grimsditch et al.[8] are also shown in Table 5.1.

Table 5.1 Anharmonicity Constants For [110] Data.

Exp.. #	$P_{11} (kbar)$	η	$\left(\dfrac{\rho}{\rho_0}\right)-1$	$\dfrac{p}{\omega_R^2}$	$\dfrac{q}{\omega_R^2}$	$\dfrac{r}{\omega_R^2}$
1 (91-006)	122	-0.0100	0.0100	$-2.94 \pm .26$	$-1.82 \pm .13$	$-2.14 \pm .16$
2 (92-044)	152	-0.0122	0.0124	$-2.50 \pm .24$	$-2.13 \pm .13$	$-2.16 \pm .17$
3 (92-015)	167	-0.0133	0.0136	*	$-1.85 \pm .12$	*
4 (91-052)	203	-0.0160	0.0164	$-3.06 \pm .15$	$-1.94 \pm .08$	$-2.32 \pm .07$
5 (92-038)	268	-0.0208	0.0215	$-3.23 \pm .16$	$-1.81 \pm .09$	$-2.32 \pm .07$
6 (92-003)	318	-0.0244	0.0253	$-2.97 \pm .10$	$-2.04 \pm .06$	$-2.27 \pm .05$
7 (92-030)	372	-0.0281	0.0293	*	$-1.98 \pm .04$	*
8 (92-062)	429	-0.0318	0.0334	$-2.83 \pm .09$	$-2.15 \pm .05$	$-2.35 \pm .04$
9 (92-032)	452	-0.0333	0.0351	$-3.20 \pm .09$	$-1.98 \pm .05$	$-2.36 \pm .04$
Mean Values From This Study				$-2.96 \pm .23$	$-1.96 \pm .12$	$-2.27 \pm .08$
Uniaxial Stress Study of Grimsditch et al.[8]				$-2.81 \pm .19$	$-1.77 \pm .16$	$-1.9 \pm .2$

*   Insufficient data to determine value.

Comparing the mean values from the present study to those of Grimsditch et al.,[8] it is clear that the present values are larger. The values given here for $|p|, |q|,$ *and* $|r|$ are respectively 5%, 10%, and 19% larger than those of the previous study of Grimsditch et al.[8]

Figures 5.2-5.4 present the results of this analysis. The frequency shift from the ambient value of 1332.5 cm^{-1} is plotted as a function of the percent density compression. For reference purposes, the top axis in these figures reflects the longitudinal stress P_{11}, defined by Eq. (2.91).

Figure 5.2 is a plot of $\Delta \omega_1$ versus density compression. The experimental values are shown as solid triangles with vertical error bars reflecting the uncertainty in the measured frequency shift. The open triangles to the left of each data point correspond to the top horizontal axis. They represent the same frequency shift (and associated frequency error), but are shown for stress calculated from the linear elastic model. Thus, the open triangle data points may be considered as a lower bound to the uncertainty in the longitudinal stress for this work. The solid line in Figure 5.2 is the predicted frequency shift for $\Delta \omega_1$ from Eq. (5.14) using the mean {q} value from this work. The fit appears to very good over the range of compression considered in this study. This result is not too surprising, since the {q} value was determined from the mean values provided by the data. In contrast, the dotted line in Figure 5.2 represents the fit to Eq. (5.14) using the {q} value reported by Grimsditch et al.[8] It is easily seen that the experimental values for the $\Delta \omega_1$ frequency shift observed in the present study, are not correctly described by the predictions based on the {q} reported by Grimsditch et al.[8] At density compression approaching 4% the two predictions differ by $\approx 10\%$. The {q} value of Grimsditch et al.[8] was determined over a much smaller compression range, on the order of a single interval of the top horizontal axis (≈ 10 kbar) in this figure.

Figure 5.3 is a plot of the $\Delta \omega_2$ frequency shift versus density compression. In this figure the experimental values are shown as solid squares. The measured frequency error
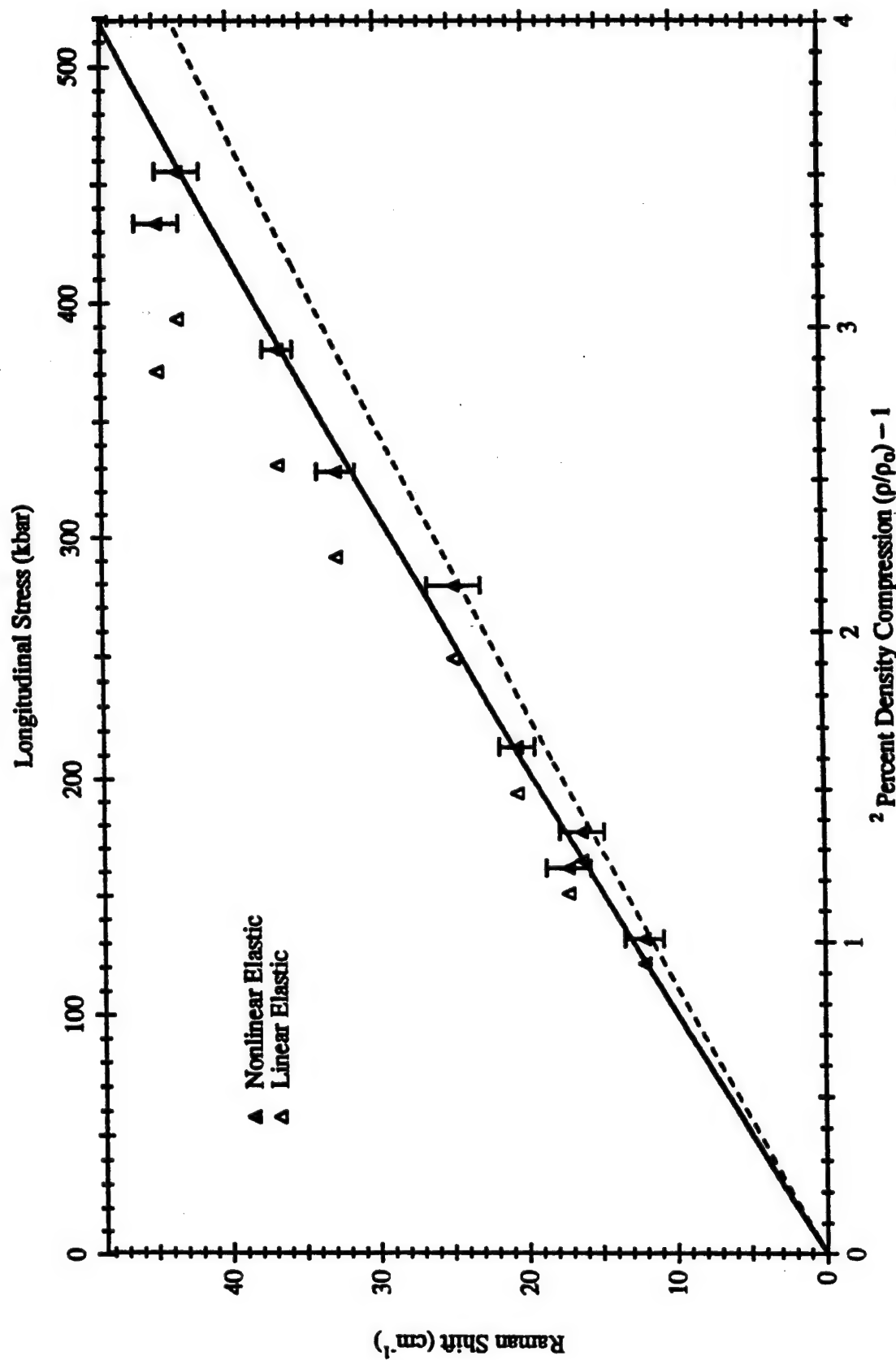
Fig. 5.2 $\Delta\omega_1$ Versus Density Compression. The solid triangles are the frequency shifts for stress values determined using the finite strain theory. The open triangles represent the same frequency shifts for stress determined from the linear elastic constants. The solid line is the fit to Eq. (5.14) using the {q} of the present study, and the dotted line is the fit to Eq. (5.14) using the previous values of Grimsditch et al.[14]
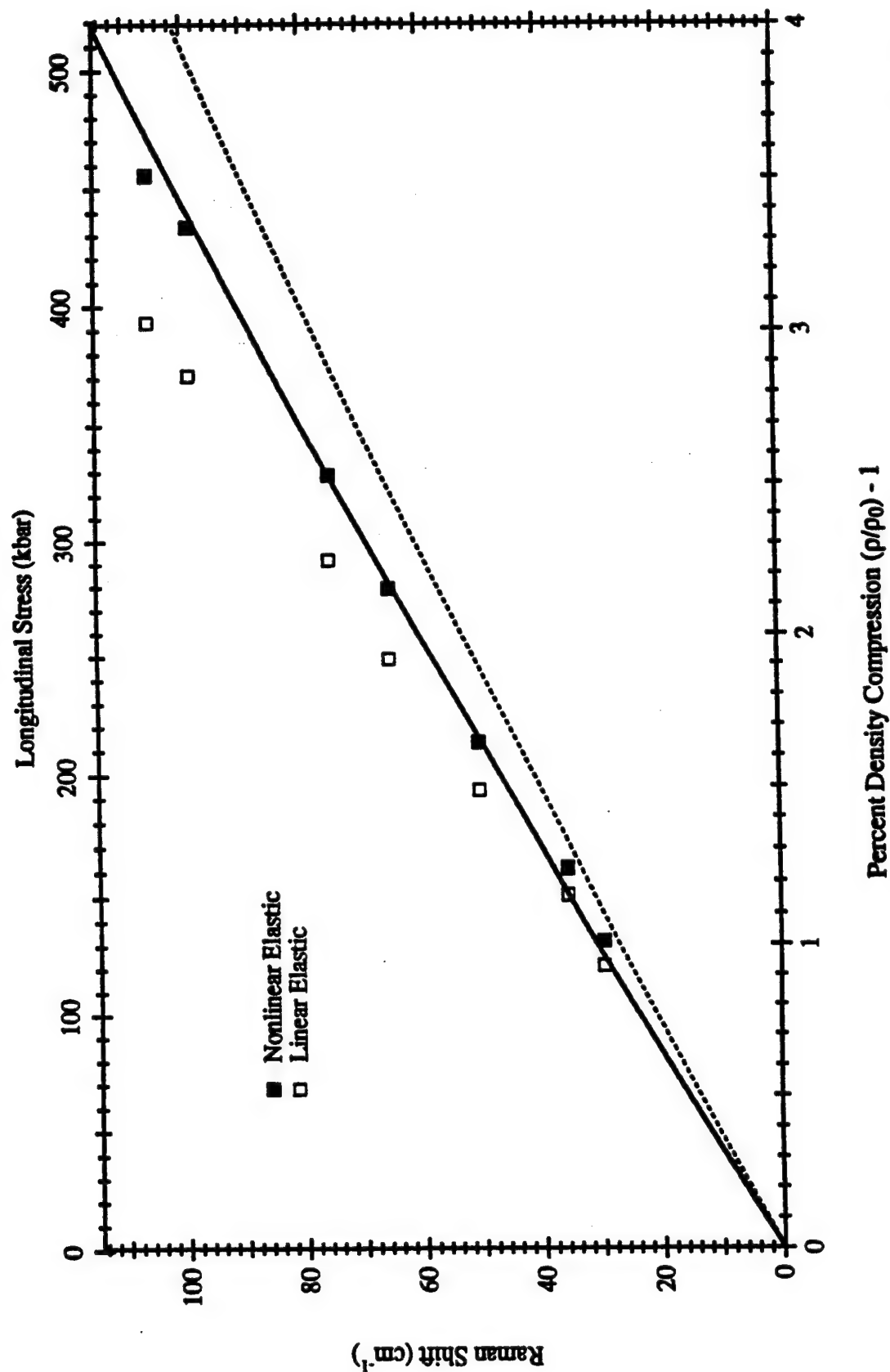
Fig. 5.3 $\Delta\omega_2$ Versus Density Compression. The solid squares are the frequency shifts for stress values determined using the finite strain theory. The open squares represent the same frequency shifts for stress determined from the linear elastic constants. The solid line is the fit to Eq. (5.14) using the (pqr) of the present study, and the dotted line is the fit to Eq. (5.14) using the previous values of Grimsditch et al.[14] Frequency shift error is less than the symbol size.

Fig. 5.4 $\Delta\omega_3$ Versus Density Compression. The solid circles are the frequency shifts for stress values determined using the nonlinear elastic finite strain theory. The open circles represent the same frequency shifts for stress determined from the linear elastic constants. The solid line is the fit to Eq. (5.14) using the (pqr) of the present study, and the dotted line is the fit to Eq. (5.14) using the previous values of Grimsditch et al.[14]
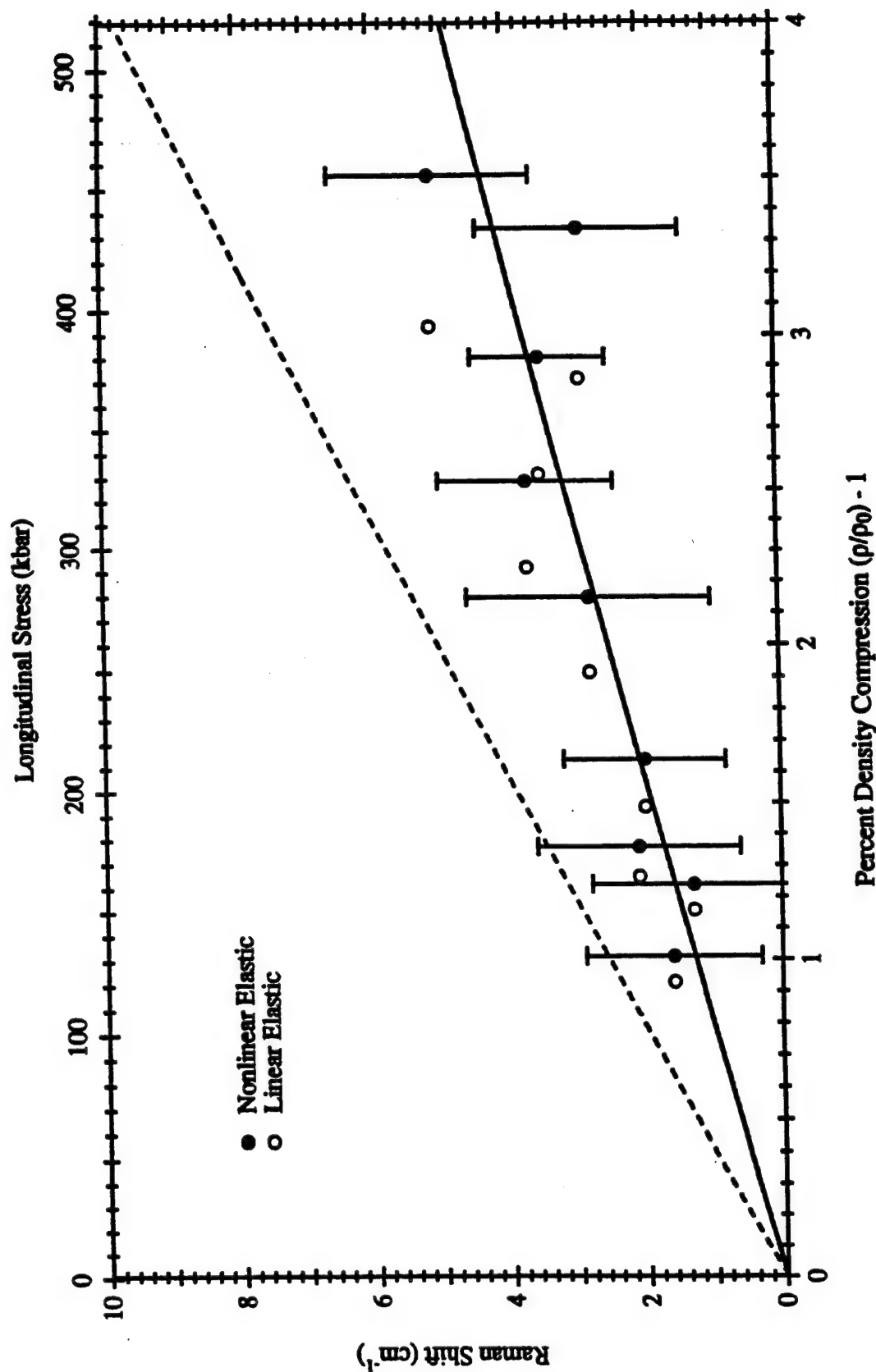
is less than the size of the symbol. As in the previous figure, the linear elastic stress value for the same frequency shift, is indicated by the open square to the left of each experimental value. The solid line in Figure 5.3 is the predicted frequency shift for $\Delta\omega_2$ from Eq. (5.14), using the mean {pqr} value from this work. Again, the predicted frequency shift is seen to be in very good agreement with the experimental values. The dotted line, representing the predicted behavior of Eq. (5.14) based on the {pqr} reported by Grimsditch et al.,[8] is $\approx 20\%$ lower than the present prediction (solid line). This is consistent with the larger value for {r} reported in this study.

Figure 5.4 is a plot of the $\Delta\omega_3$ frequency shift versus density compression. The experimental values are shown as solid circles and the corresponding points for linear elastic stress are shown as open circles to the left of each experimental value. Note that the seemingly large error bars in this figure are a consequence of the very small frequency shift that is being measured. This is also reflected by the vertical axis, which is only 10 cm^{-1} full-scale. The frequency shift of $\Delta\omega_3$ predicted by Eq. (5.14) is shown as a solid line for the {pqr} determined from the present work and a dotted line for the {pqr} values reported by Grimsditch et al.[8] The larger shifts predicted with the Grimsditch et al.[8] {pqr}, is primarily due to the difference in {r} values, since $\Delta\omega_3 \propto (p+q-2r)$.

It may be concluded that the experimental values measured in the present study are not well-described by predictions based on the {pqr} of Grimsditch et al.[8] A very good fit is found by using Eq. (5.14) and the mean {pqr}, determined from individual experiments in the present study. It was remarked earlier that this result is not to surprising because the mean {pqr} are determined from the experimental data. It is reassuring to note that the predictions, based on the microscopic theory presented in Chapter 2, behave so well over such a large compression range. In the following section the mean {pqr} of the present study will be used with the microscopic theory, to predict the frequency shift behavior for the [100] experiments.

A-184

5.2.2 Analysis of the [100] Data

As stated earlier, the experiments performed along the [100] crystallographic orientation can provide an independent check of the {pq} values determined from the [110] experimental data. The mean {pq} values are used in Eq. (5.6) to predict the behavior of the singlet and doublet frequency shifts.

Figure 5.5 presents the results of this analysis. In this figure, the solid symbols represent the experimental values measured in this study. Triangles are used to represent the singlet, and squares are used to represent the doublet. The error in the measurement of the shifted frequency is indicated by the vertical error bar. The open symbols to the left of the singlet and doublet results, represent the frequency shift for the linear elastic case. The solid lines in this figure are fits to the singlet and doublet frequency shifts, predicted by Eq. (5.6) and using the mean {pq} from the [110] experiments. The predictions are seen to be in excellent agreement with the observed frequency shifts. The dotted lines in this figure represent the predicted results using Eq. (5.6) and the {pq} values reported by Grimsditch et al.[8] The fits to the experimental values based on these predictions, are clearly inferior to the solid lines, representing the present predictions. These results lend credence to the mean {pqr} reported in the present study.

For completeness, the {pq} are now calculated from the [100] experimental values. Eq. (5.6), which describes the singlet and doublet frequency shift, may be inverted to yield the following expressions

$$\frac{p}{\omega_R^2} = \frac{1}{\eta}\left\{\left[\left(\frac{\Delta\omega_S}{\omega_R}\right)+1\right]^2 - 1\right\} \tag{5.22}$$

$$\frac{q}{\omega_R^2} = \frac{1}{\eta}\left\{\left[\left(\frac{\Delta\omega_D}{\omega_R}\right)+1\right]^2 - 1\right\} \tag{5.23}$$
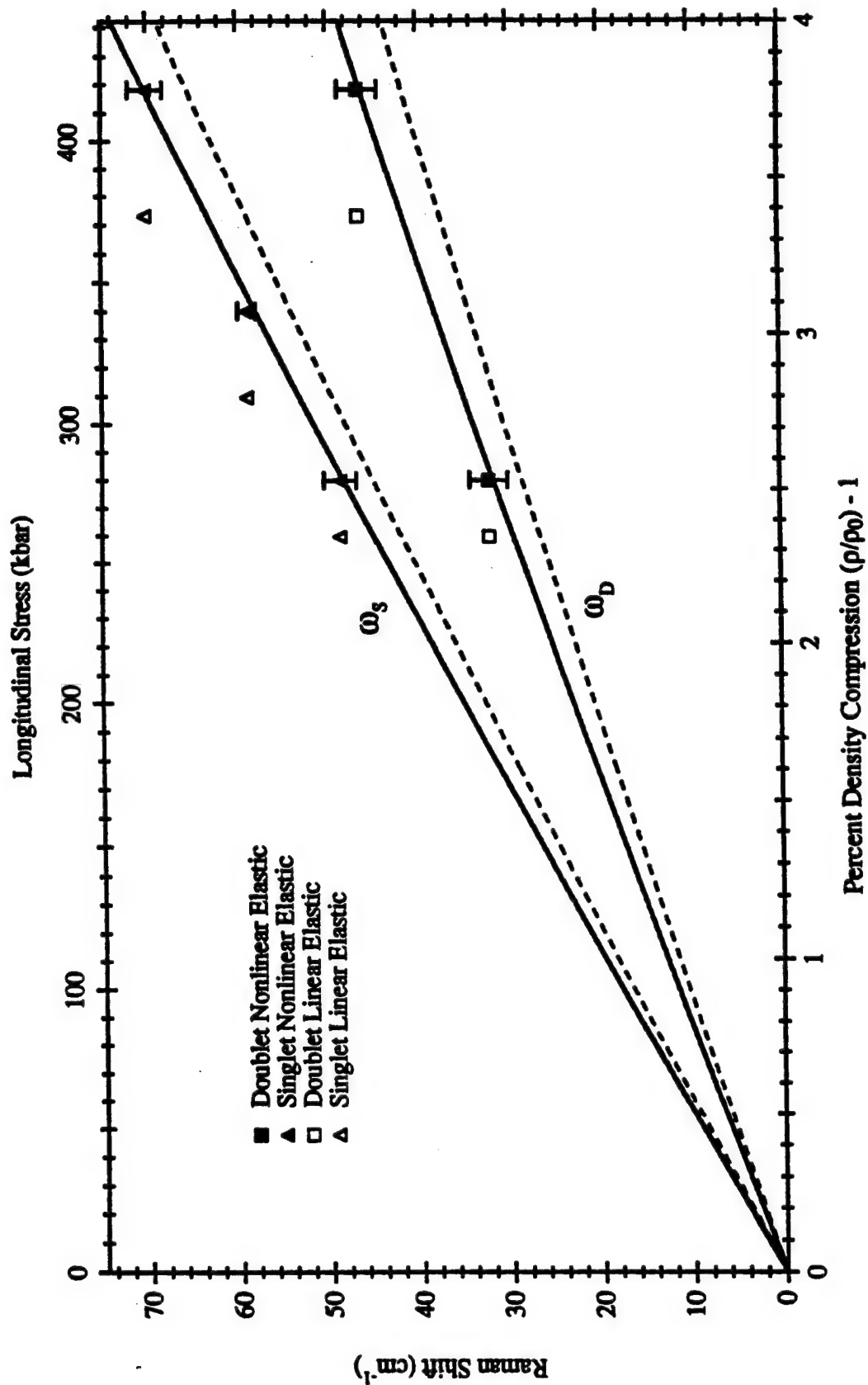
Fig. 5.5 $\Delta\omega_s$ and $\Delta\omega_D$ versus Density Compression. The solid triangles(squares) are the frequency shifts for the singlet(doublet) at stress values determined using the finite strain theory. The open triangles(squares) represent the same frequency shifts for stress determined from the linear elastic constants. The solid line is the fit to Eq. (5.14) using the {pq} of the present study, and the dotted line is the fit to Eq. (5.14) using the previous values of Grimsditch et al.[14]

A-186

The results from Chapter 4 for the shifted singlet and doublet may be substituted into Eqs. (5.22) and (5.23) to determine the {pq} values for the [100] experiments. Table 5.2 presents the results. As for Table 5.1, the longitudinal stress, strain, and density compression are also given. The excellent agreement of the [100] experimental values with the predictions based on the [110] mean {pqr}, indicate that inclusion of the {pq} values calculated from the [100] data will have little effect on {pqr}. This is evident in the final mean values for {pq}, which have changed by only 0.5%.

It is interesting to note, that for other cubic semiconducting materials such as Si, Ge, and GaAs with the same octahedral symmetry, the doublet lies higher in frequency than the singlet,[24] in contrast to the case for diamond. This of course indicates that $|q| \rangle |p|$ for these materials. The three parameter Valence-Force-Field model used by Grimsditch et al.,[8] indicates that {p} and {q} are proportional to a anharmonic bond-bending (directional force) parameter $\overline{\delta}$ that is opposite in sign for the two cases. This suggests that the higher frequency-shifted mode is dictated, at least in part, by the strength of the constant $\overline{\delta}$ which is roughly three times larger in diamond.

5.3 COMPARISON WITH PREVIOUS STRESS MEASUREMENTS

The values determined in the previous section for the anharmonic parameters {pqr} are used in the following discussion to assess the predictive capability of the quasiharmonic model developed by Ganesan et al.[13] The secular matrix given by Eq. (2.46) permits determination of the frequency-shift behavior for any arbitrary deformation of the crystal lattice once the anharmonic parameters have been determined.

It is important to reiterate that the results of Section 2.4.2 are based on the quasi-harmonic approximation to the vibrational Hamiltonian. In this approximation the crystal potential is expanded in a Taylor series as a function of 'new' atomic positions that result from the application of an external strain. The sub-lattices vibrate about new equilibrium

Table 5.2 Anharmonicity Constants for [100] Data.

Exp.. #	$P_{11}(kbar)$	η	$\left(\dfrac{\rho}{\rho_0}\right)-1$	$\dfrac{p}{\omega_R^2}$	$\dfrac{q}{\omega_R^2}$	$\dfrac{r}{\omega_R^2}$
10 (92-042)	278	-0.0245	0.0254	-3.03 ± .08	-1.99±.09	**
11 (92-061)	339	-0.0293	0.0306	-3.07 ± .04	*	**
12 (92-060)	418	-0.0358	0.0378	-3.01 ± .06	-1.98 ± .07	**
Final Mean Values From This Study Exps. #1-12				-2.98 ± .20	-1.97 ± .11	-2.27 ± .08
Uniaxial Stress Study of Grimsditch et al.[8]				-2.81 ± .19	-1.77 ± .16	-1.9 ± .2

*   Insufficient data to determine value.

**   Not applicable for this orientation

positions with frequencies that are shifted from the unstrained (ambient) frequency. The Taylor series is truncated to terms quadratic in the strained atomic positions and thus some information is lost.

5.3.1 Calculation of Hydrostatic Shift

In this section the predictions based on the present study and the hydrostatic results discussed in Section 2.2.1, are compared. For the purposes of this discussion the mean compressive stress determined from uniaxial strain loading is defined by,

$$\langle P_U \rangle = -\frac{1}{3}(\sigma_{11} + \sigma_{22} + \sigma_{33}) \tag{5.24}$$

where σ_{ij} are the nonvanishing stresses given in Eqs. (2.83) and (2.90) for the [100] and [110] orientations, respectively. Similarly, the mean frequency shift may be defined as the centroid of the splittings. The centroid is determined by the weighted average of the frequency shifts.[86] The weight factor is specified by the mode degeneracy, so that a doublet is counted twice, etc. Hence,

$$\text{For [110]}: \quad \langle \Delta\omega \rangle = \frac{\Delta\omega_1 + \Delta\omega_2 + \Delta\omega_3}{3} \tag{5.25a}$$

$$\text{For [100]}: \quad \langle \Delta\omega \rangle = \frac{\Delta\omega_S + 2\Delta\omega_D}{3} \tag{5.25b}$$

The nonvanishing stress values, the mean compressive stress $\langle P_U \rangle$, and the mean frequency shift $\langle \Delta\omega \rangle$ for all experiments performed in this study, are presented in Table 5.3. The nonzero stresses were calculated from the finite strain expressions given in Chapter 2. For each experiment, the density compression associated with the uniaxial

Table 5.3 Mean Stress and Splitting Centroids.

Exp. # (Shot #)	σ_{11} (kbar)	σ_{22} (kbar)	σ_{33} (kbar)	$\langle P_U \rangle$ (kbar)	$\left(\dfrac{\rho}{\rho_0}\right)-1$	$\langle \Delta\omega \rangle$ (cm^{-1})
1 (91-006)	122	2.3	12.9	45.7	0.0100	14.5 ± 0.8
2 (92-044)	152	2.8	15.9	56.9	0.0124	18.13 ± 0.9
3 (92-015)	167	3.0	17.4	62.5	0.0136	*
4 (91-052)	203	3.64	21.2	75.9	0.0164	24.37 ± 0.8
5 (92-038)	268	4.65	27.9	100.2	0.0215	31.0 ± 1.0
6 (92-003)	318.5	5.4	33	118.9	0.0253	37.3 ± 0.8
7 (92-030)	372	6.1	38.6	138.9	0.0293	*
8 (92-062)	428.5	6.9	44.4	159.9	0.0334	48.8 ± 0.9
9 (92-032)	452	7.2	46.8	168.7	0.0351	51.4 ± 0.9
10 (92-042)	278	37.5	37.5	117.6	0.0254	37.6 ± 1.1
11 (92-061)	338.5	47	47	144.2	0.0306	*
12 (92-060)	417.5	60.2	60.2	179.3	0.0378	54.4 ± 1.2

strain is also indicated. The asterisks denote averages that could not be computed due to insufficient data.

In order to compare the results from this study with those of other workers, a common variable must be found to make the comparison meaningful. Density compression provides a useful variable to contrast the results for stress loading. For a given density compression, experimental data for uniaxial stress, uniaxial strain, or hydrostatic loading can be compared in a consistent manner.

For hydrostatic pressure, P_H, all stress components are equal: $\sigma_{11} = \sigma_{22} = \sigma_{33}$. Thus, the hydrostatic pressure is given by

$$P_H = -\sigma_{11} \tag{5.26}$$

For hydrostatic stress, it can be shown[87] that the nonlinear elastic expression is given by

$$P_H = -\left(\frac{\rho}{\rho_0}\right)^{\frac{1}{3}}\left\{(C_{11}+2C_{12})\frac{1}{2}\left[\left(\frac{\rho_0}{\rho}\right)^{\frac{2}{3}}-1\right] + \frac{1}{2}(C_{111}+6C_{112}+2C_{123})\left[\frac{1}{2}\left[\left(\frac{\rho_0}{\rho}\right)^{\frac{2}{3}}-1\right]\right]^2\right\} \tag{5.27}$$

For a particular density compression $\mu = (\rho/\rho_0)-1$, the hydrostatic pressure is described by Eq. (5.27) using the same second and third order elastic constants given in Tables 2.5 and 2.6. The hydrostatic data that describe the frequency shift of the triply degenerate Raman frequency as a function of applied pressure may be written as

$$\Delta\omega_H = \left(\frac{d\omega_H}{dP_H}\right) \times P_H \tag{5.28}$$

where the $(d\omega/dP_H)$ have been provided in Table 2.1 for various values given in the literature.

To reiterate, for each density compression listed in Table 5.3, we have a datum given by the mean frequency shift (splitting centroid) determined from the present study. For the same density compression, a hydrostatic pressure P_H is defined by Eq. (5.27) and is used in Eq. (5.28) to yield the corresponding frequency shift.

To compare the results of the present study with the available "hydrostatic" values, the results of Parsons[14], Tardieu et al.,[6] and Goncharov et al.[15] were chosen. These particular studies were selected from Table 2.1 because:

1) They spanned the breadth of the available static high pressure data.

2) Because the values given by Mitra et al.,[16] Hanfland et al.,[17] Boppart et al.,[5] and Goncharov et al.[15] were close to one another, the latter value was selected to be representative of these four studies.

3) The value given by Grimsditch et al.[8] was excluded because it is the subject of the next section.

Figure 5.6 presents the results of the comparison. In this figure the solid triangles represent the mean frequency shift at the density compression values given in Table 5.3. These values are compared to the hydrostatic stress studies represented by the dotted and dashed lines indicated in the figure. To determine the frequency shifts due to hydrostatic stress, Eq. (5.27) was first evaluated for density compression of 1% to 4% and then substituted into Eq. (5.28). The top axis corresponds to the hydrostatic pressure (in kbar) given by Eq. (5.27) for the corresponding density compression on the bottom axis. It is seen in the figure that the experimental values from the present work agree reasonably well with the hydrostatic data, falling closest to the mid-range values of Goncharov et al.[15] The solid line in this figure represents the predicted frequency shifts using Eq. (2.59) and the mean {pqr} from the present study. These results suggest that the centroid of the
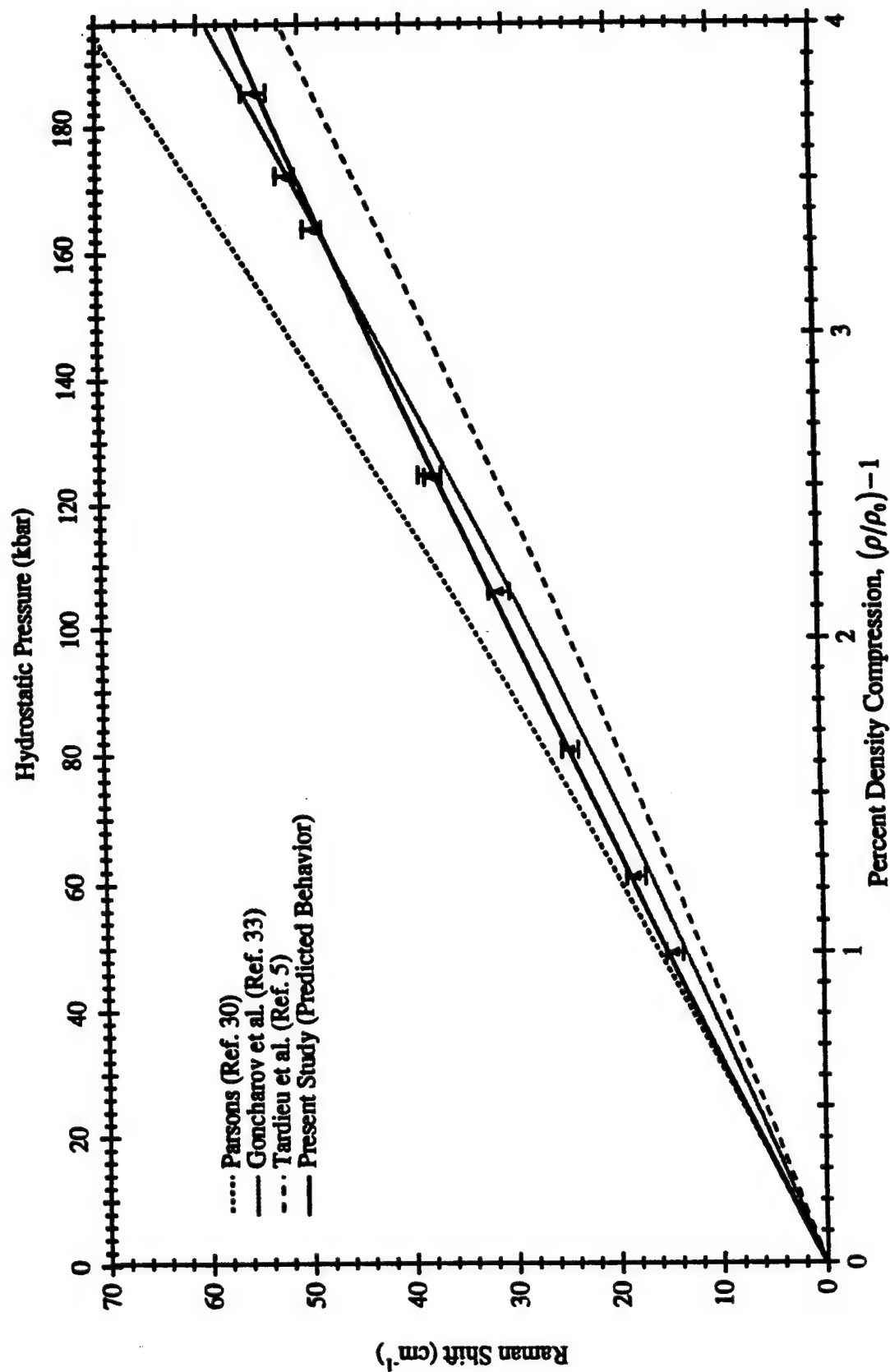
Fig. 5.6 Mean Frequency Shift versus Density Compression. Solid triangles are the mean frequency shifts determined from experimental values. Hydrostatic measurements are indicated in the legend (see Table 2.1). The solid line is the prediction of Eq.(2.59) using the {pqr} from the present study. The hydrostatic pressure has been calculated using the nonlinear elastic expression given by Eq.(2.23) and is indicated on the top horizontal axis.

splittings observed for uniaxial strain loading is not strongly influenced by the nonhydrostatic stresses. In other words the splitting centroid behaves just as the degenerate frequency subjected to hydrostatic stress. The predicted behavior (solid line) is observed to be in good agreement with the experimental results of this study as well as the hydrostatic stress results.

One last comparison may be made with the hydrostatic data provided in Table 2.1 by calculating a value for the mode Grüneisen constant γ. It may be calculated from[8]

$$\gamma = -\left(\frac{p+2q}{6\omega_R^2}\right) \tag{5.29}$$

Using the experimental values for {pqr} listed in Tables 5.1, it is found that the mean value for this parameter is: $\gamma = +1.15 \pm 0.03$, where the error is one standard deviation from the mean. This value compares favorably with the values cited in Table 2.1. It is approximately 15% larger than the mean of the hydrostatic values ($\overline{\gamma} = 1.00 \pm 0.17$) but within the margin of error.

5.3.2   Uniaxial Stress and Uniaxial Strain Induced Frequency Shifts

The only uniaxial stress study on diamond reported in the literature is that of Grimsditch et al.[8] They performed uniaxial stress experiments up to 10 kbar on [100] and [111] oriented samples. Their results for the {pqr} values have already been presented for comparison in Tables 5.1 and 5.2.

For uniaxial stress applied along either [100] or [111], the normal modes are split into a singlet (ω_S) and a doublet (ω_D) with eigenvectors parallel and perpendicular to the applied stress similar to the uniaxial strain case considered in Chapter 2. The only experimentally determined frequency shifts from the present work that may be compared to the uniaxial stress measurements is for uniaxial strain along [100]. This has been

illustrated in Figure 5.5 where the Raman frequency shift from the ambient location has been plotted as a function of density compression. As already discussed, the present results are not well described by the {pqr} determined from the uniaxial stress data.

It is useful to compare the present results to the uniaxial stress work for density compression for the range 0-0.1% corresponding to the stress considered in the Grimsditch et al.[8] study. At such small density compression the agreement is expected to be very good. Figure 5.7 presents this comparison. The error bars in this figure reflect the uncertainty in the best fit of Grimsditch et al.[8] for three values of density compression. The error in the present predictions are of the same order of magnitude. In Figure 5.7 (a), the [100] comparison reflect the slightly larger values for {pq} found in this study (see Table 5.1). Note, from Eq. (2.49), that the singlet is proportional to {p} only and the doublet is proportional to {q} only. In the [111] comparison of Figure 5.7 (b) however, the singlet is a function of {p+2q+4r}, whereas, the doublet is a function of {p+2q-2r}. Thus, the difference between the values given for the anharmonic parameters determined from the uniaxial stress and uniaxial strain data are enhanced for the singlet and, interestingly, counteract each other for the [111] doublet frequency shift. For both orientations the differences between the present predictions, and that of Grimsditch et al.,[8] is small, as expected.

To conclude this section, the study of Gupta et al.[11] will be briefly discussed. Their work represents the only other uniaxial strain study of the Raman spectrum of diamond. As mentioned earlier, the paper by Gupta et al.[11] was designed to demonstrate the feasibility of time-resolved Raman measurements under shock loading. In their study, they considered the application of uniaxial strain along [110] in diamond under conditions very similar to those of Experiment #1, of the present study. One notable difference was the angle of the incident light, which they estimated to be 20° from the normal. From the analysis presented in Section 5.1 of the present chapter, $\theta_r \approx 8°$, and
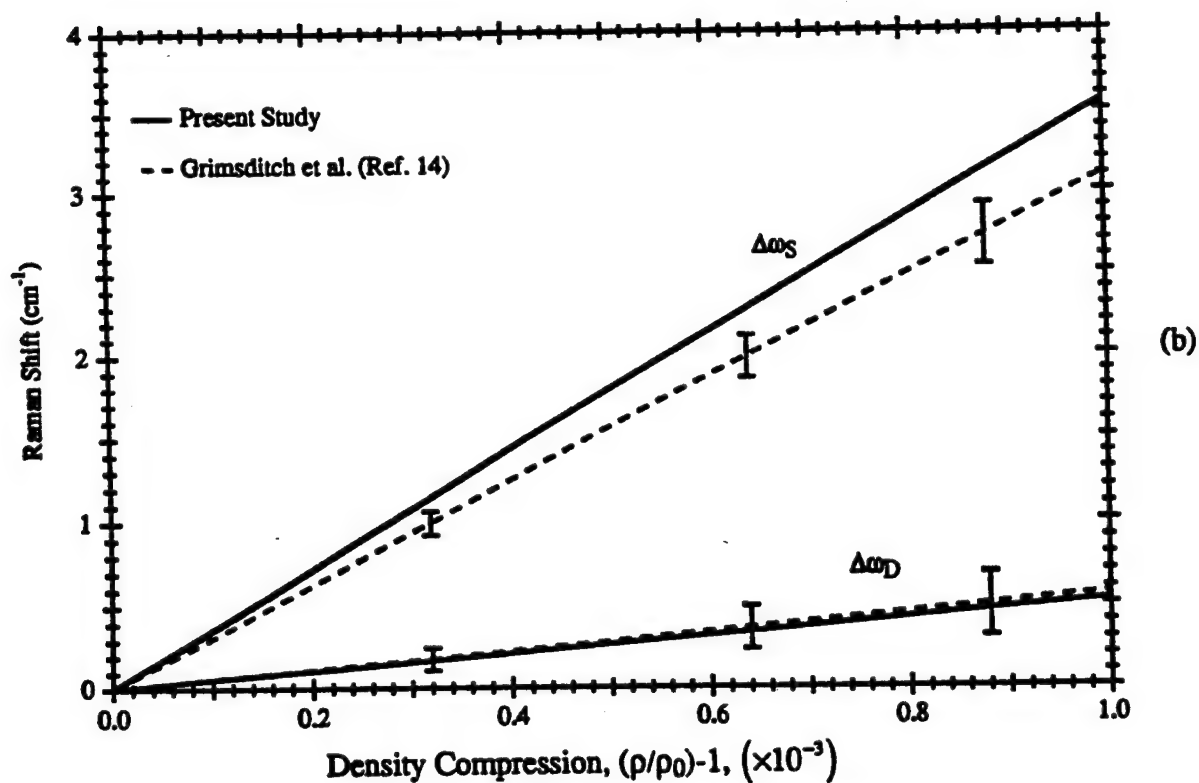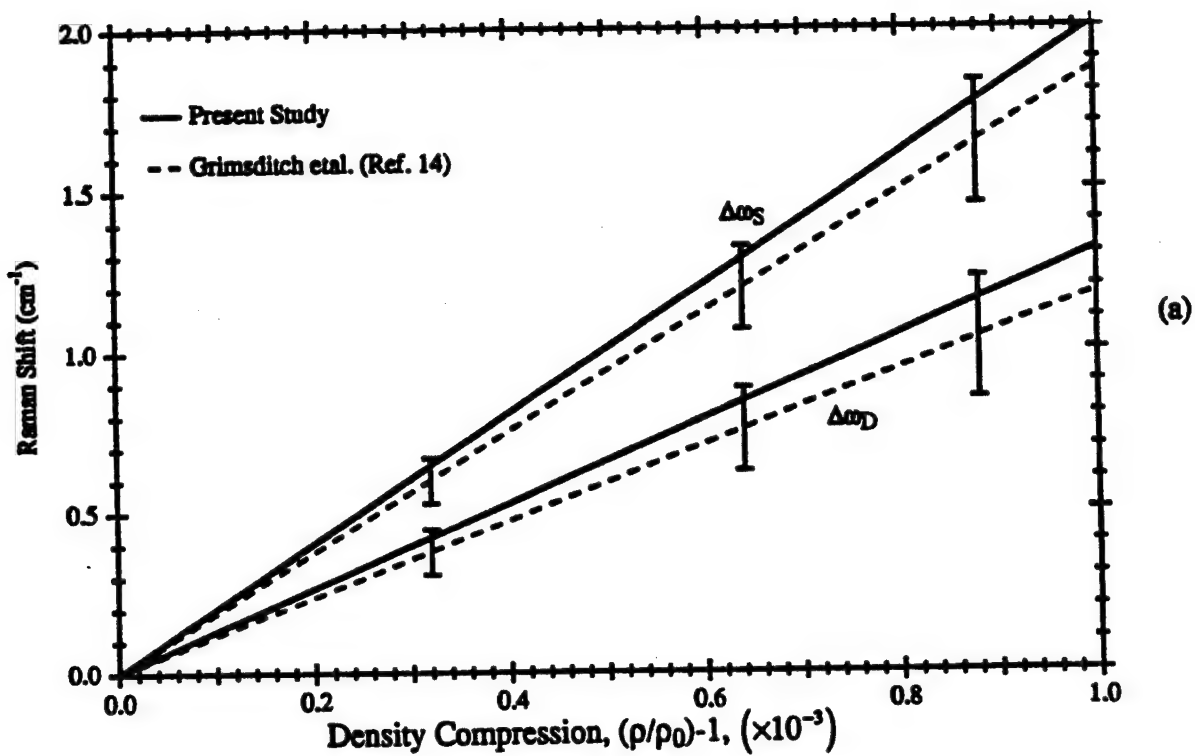
Fig. 5.7 [100] and [111] Uniaxial Stress and Uniaxial Strain Comparisons. (a) for
uniaxial stress conditionalong [100], and (b) for uniaxial stress along [111]. The
error bars denote mean error from the best fit to data of Grimsditch.

Eq. (5.20) indicates that the intensity of the highest frequency mode $\Delta\omega_2$ is at least 50 times smaller than $\Delta\omega_1$ and 100 times smaller than $\Delta\omega_3$. Given the limitations of their experimental arrangement, this mode would have been impossible to observe. Indeed, even with the experimental improvements made for the present study it still would have escaped detection. Even though a shifted frequency may be predicted by the quasi-harmonic model, it is the polarization selection rules for the specific experimental geometry that dictate whether the shifted frequency may be observed.

It has also become clear through private communication with Gupta, that the values used in Ref. 11 for {pqr} were the 'best fit' values given in the paper by Grimsditch et al.[8] It is unclear what the cited 'best fit' values in Table 1 of the Grimsditch et al.[8] paper represent, because the results from their own work are given in a separate column under the heading 'Present Study' . To the author's knowledge, there have been no other published results for the experimentally determined anharmonic {pqr} values for diamond. For completeness, the 'best fit' {pqr} presented by Grimsditch et al.[8] are:

$$
\left.
\begin{array}{l}
p = -2.92 \ \omega_R^2 \\
q = -1.90 \ \omega_R^2 \\
r = -1.20 \ \omega_R^2
\end{array}
\right\}
\qquad (5.30)
$$

These values are inconsistent with their own results and, due to the 50% difference from the {r} value cited for the present work, the predicted splittings using Eq. (5.30) were not even considered. However, they were used in the study of Gupta et al.,[11] but the spectral resolution was not sufficient to resolve the splittings, and only one line was reported shifted to $8.9 \pm 1.0 \ cm^{-1}$. This is in fairly good agreement with the mean shifted line of $\overline{\Delta\omega_{1,3}} = 6.9 \pm 1.8 \ cm^{-1}$ taken from the average of $\Delta\omega_1$ and $\Delta\omega_3$ in Experiment #1 of the present study, indicating that, perhaps, they were observing the superposition of these two modes.

5.3.3 Discussion of the Grüneisen Parameter

The mode Grüneisen parameter (γ_i), is expected to be a constant within the limit of the quasiharmonic approximation. In terms of the anharmonic parameters {pq}, it is defined by Eq. (5.29). Goncharov et al.[15] have reported that the mode Grüneisen parameter increases with pressure, in contrast to other isomorphic cubic semiconductors such as Si and Ge. Thus, it is of some interest to examine the present results for any such dependency.

In Tables 5.1 and 5.2 the mean fits to the {pqr} were determined from the individual experimental values. To examine the individual results more closely, they have been plotted as a function of density compression in Figure 5.8. Also shown in this figure is the linear fits for {p}, {q}, and {r} as functions of density compression. This plot suggests that there is a dependency on density compression. The linear fits to the {pqr} are found to be:

$$\left.\begin{aligned}
\left(\frac{p(\mu)}{\omega_R^2}\right) &= -2.75(\pm.24) - 9.5(\pm10)\mu \\
\left(\frac{q(\mu)}{\omega_R^2}\right) &= -1.84(\pm.11) - 5.5(\pm4.5)\mu
\end{aligned}\right\} \tag{5.31}$$

and

$$\left(\frac{r(\mu)}{\omega_R^2}\right) = -2.10(\pm.05) - 7.7(\pm2.2)\mu \Big\} \tag{5.32}$$

where $\mu = \left[(\rho/\rho_0) - 1\right]$ is the density compression. Thus, the error in the slopes is of the same magnitude of the slope values. It might be argued that {r} displays some dependence on density compression, however {r} does not contribute to the mode Grüneisen parameter as defined by Eq. (5.29). The previously determined mean values for {pqr} fit the experimental values displayed in Figure 5.8 just as well as the linear fits.
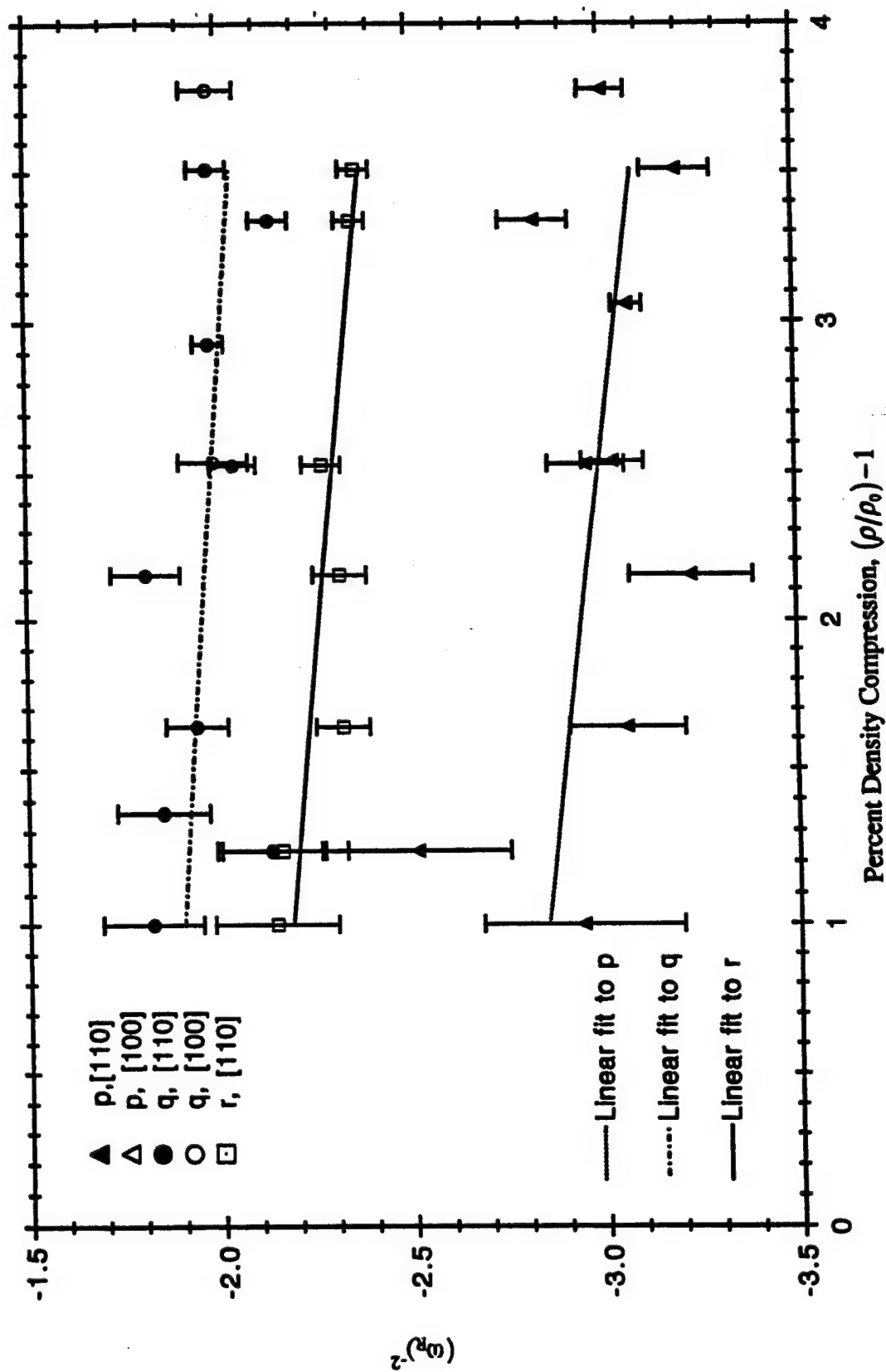
Fig. 5.8 Individual Anharmonic Parameters (pqr) vs Density Compression. Symbols represent experimentally determined values from Table 5.1 (solid symbols) and Table 5.2 (open symbols). Solid and dashed lines are the linear fits.

This was to be expected, given that the results presented in this study have been well described by the mean {pqr} values and the quasi-harmonic model for frequency shift behavior. Substituting the values of Eq. (5.31) into Eq. (5.29) yields

$$\gamma(\mu) = 1.07(\pm.05) + 3.4(\pm1.9)\mu \qquad (5.33)$$

To rewrite Eq. (5.33) in terms of hydrostatic pressure, it was plotted and fit as a function of Eq. (5.27) for density compression to 4%. The pressure dependency is given by

$$\left(\frac{\partial\gamma}{\partial P_H}\right)_0 = +0.0007(\pm.0004) \; kbar^{-1} \qquad (5.34)$$

Thus, if the Grüneisen parameter depends linearly on hydrostatic pressure, Eq. (5.34) indicates that the slope is positive. This result is in rough agreement with that of Goncharov et al.[15] who calculated the pressure dependent mode Grüneisen parameter to be: $(\partial\gamma/\partial P_H) = +0.0022(\pm.0016)(GPa)^{-1}$. Although the result given by Eq. (5.34) is three times as large as that of that of Goncharov et al.,[15] the two values agree within the experimental error cited.

Goncharov et al.[15] point out that, the positive pressure dependence for $\gamma(P_H)$ is in contrast to the results for the isomorphic cubic semiconducting materials Si and Ge. Figure 5.9 shows the behavior of the mode Grüneisen parameter for diamond, silicon, and germanium as a function of density compression, using the values given by Goncharov et al.[15] and Eq. (5.34) of the present study. Goncharov et al.[15] suggest that the positive slope of $\gamma(P_H)$ for diamond might indicate that its tetrahedral coordination stabilizes under compression, in contrast to Si and Ge that undergo a phase transformation from cubic to body-centered tetragonal. The asterisk in this figure denotes the first-order semiconductor-to-metal phase transition observed for the Si and Ge materials.[27]
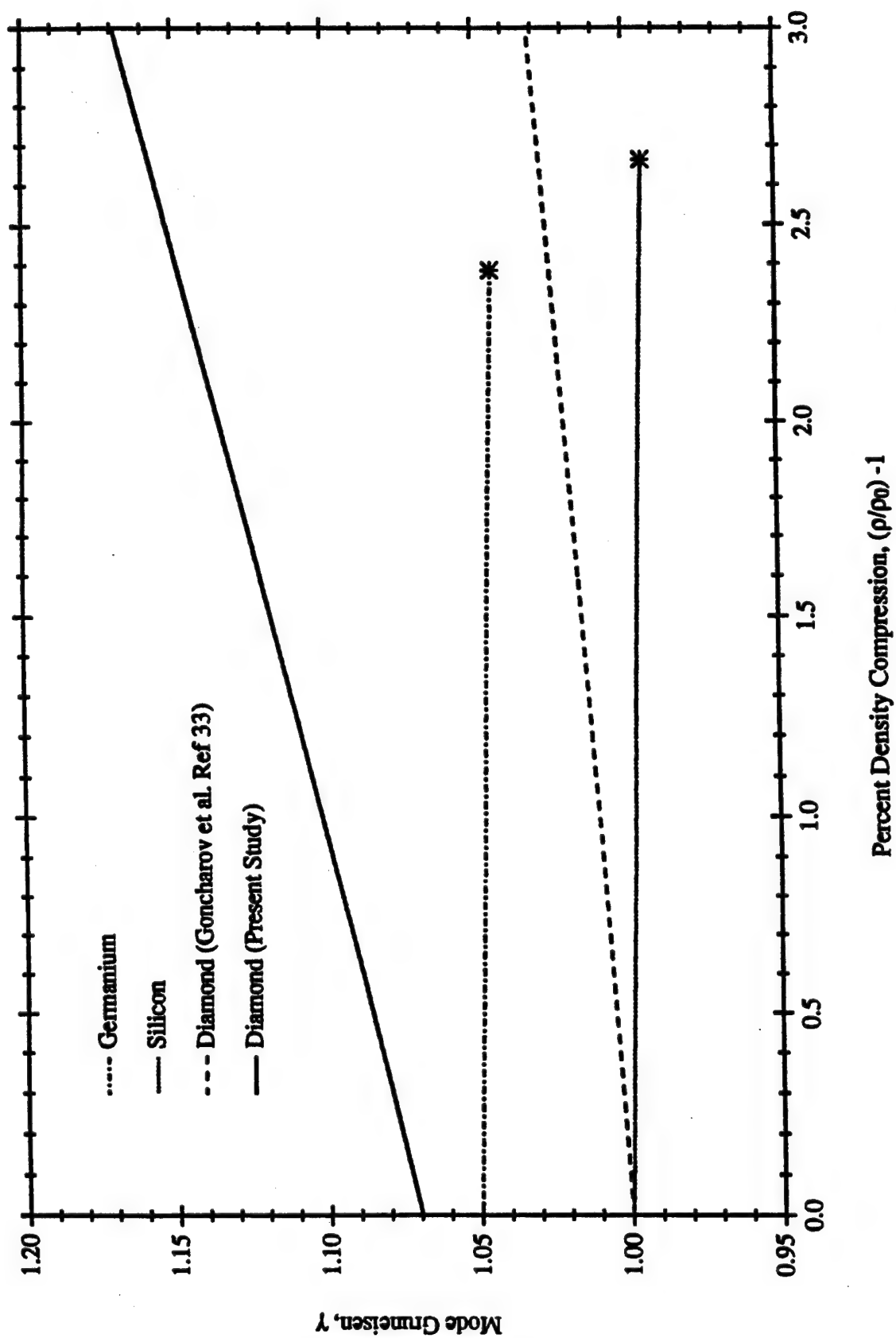
Figure 5.9 Grüneisen Parameter as a Function of Density Compression. The germanium and silicon data have been truncated where they go through a phase transition.

In the Valence Force Field (VFF) model it is shown that the shear wave mode for the tetrahedrally coordinated cubic semiconductors is directly proportional to the VFF parameter β that represents the degree of bond-bending, or directional force, present in the system. This is usually contrasted to α, which represents the degree of bond-stretching, or central force, present. In this model, the second-order elastic constants for cubic materials are written

$$
\left.
\begin{aligned}
C_{11} &= \frac{(\alpha + 3\beta)}{4a} \\[2mm]
C_{12} &= \frac{(\alpha - \beta)}{4a} \\[2mm]
C_{44} &= \frac{\alpha\beta}{a(\alpha + \beta)}
\end{aligned}
\right\} \tag{5.35}
$$

where a is the lattice constant. For central forces $\beta = 0$ and $C_{12} = C_{44}$, which is the Cauchy relation for cubic materials. This does not hold for diamond, because each atom is tetrahedrally coordinated, that is, it does not sit on a center of inversion. In view of the phase transformations of Si and Ge it might be of interest to look at the shear wave modes for cubic materials, using Eq. (5.35). From Eqs. (2.61)-(2.63) it may be seen that three shear modes are possible

$$
\left.
\begin{aligned}
C_{44} &= \frac{\beta}{a}\left(\frac{\alpha}{\alpha + \beta}\right) \\[3mm]
\frac{C_{11} - C_{12}}{2} &= \frac{\beta}{2a} \\[3mm]
\frac{C_{11} - C_{12} + C_{44}}{3} &= \frac{\beta}{3a}\left[1 + \left(\frac{\alpha}{\alpha + \beta}\right)\right]
\end{aligned}
\right\} \tag{5.36}
$$

Using the values of Anastassakis et al.[61] and Bell[88] for α and β (given in Appendix E), the shear waves represented by Eq. (5.36) may be tabulated for C, Si, and Ge. Table 5.4 gives the values for these shear waves.

Table 5.4 Shear Wave Values For C, Si, and Ge.

Material	$\dfrac{\beta}{a}\left(\dfrac{\alpha}{\alpha+\beta}\right)$ (kbar)	$\left(\dfrac{\beta}{2a}\right)$ (kbar)	$\dfrac{\beta}{3a}\left[1+\left(\dfrac{\alpha}{\alpha+\beta}\right)\right]$ (kbar)
Diamond	1301	1151	1201
Silicon	200	129	153
Germanium	156	101	119

For silicon and germanium the values given for $\beta/2a$ in Table 5.4 are very close to the reported values of 125 kbar and 110 kbar cited by Goncharov et al.[15] for the semiconductor-to-metal phase transition in these materials. For diamond $\beta/2a \approx 115\ GPa$, however no such phase transition has been observed. Bell et al.[53] subjected a diamond sample to a reported 280 GPa in a Diamond Anvil Cell. They reported no observed symmetry change or plastic flow in the sample studied. Post-experiment X-ray analysis of the sample confirmed that the symmetry remained cubic.

Lastly, it is worth pointing out that, in comparing the present results to the hydrostatic results it has been tacitly assumed that $\langle P_U \rangle \cong \langle P_H \rangle$. Figure 5.10 shows the mean stress resulting from uniaxial strain along [110] and [100] in diamond and the hydrostatic stress given by Eq. (5.27). All three functions have been plotted for a maximum density compression to 4%. It is seen that $\langle P_U \rangle \cong \langle P_H \rangle$ is a reasonable assumption.
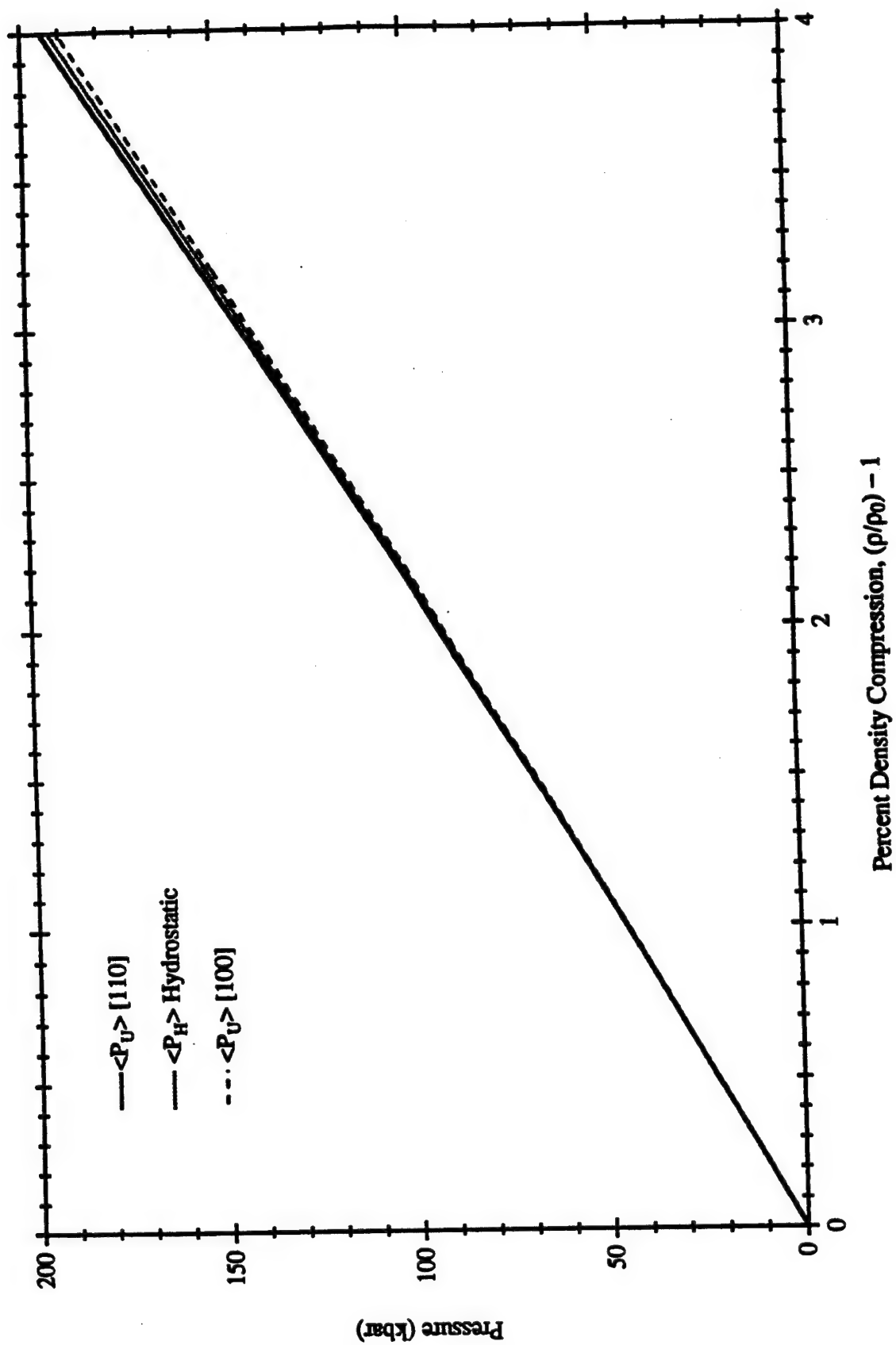
Figure 5.10   Mean Stress and Hydrostatic Pressure versus Density Compression.

Chapter 6

SUMMARY AND CONCLUSIONS

The work reported in this dissertation was motivated by the need to better understand the symmetry changes in the Raman spectrum of diamond single crystals subjected to large nonhydrostatic stresses. Information pertaining to the lattice dynamical response may be extracted from the optical data in the form of three anharmonic parameters {pqr}. These parameters are related to the microscopic forces acting at the atomic level.

It is hoped that the observation of strain-induced symmetry changes in a simple crystal, such as diamond, will encourage similar studies involving more complex structures.

6.1 SUMMARY

Application of stress or strain to the diamond crystal alters the Raman spectrum by shifting and/or splitting the degenerate Raman line. The response of the Raman spectrum in diamond was investigated in a series of shock compression experiments performed along the [100] and [110] crystallographic orientations. Behind the shock front, a uniform but strongly nonhydrostatic stress state is achieved

The experimental design was guided by detailed calculations that predicted the changes in the degeneracy, frequency shift, and intensity of the strained Raman spectrum for the present experiments. These calculations also provided the basis for the data analysis.

Experimental Method

The experimental methods used in this work built upon previous developments by other workers.[12] Modifications were made to the target cell to accommodate the small

sample size, and to the optical system to enhance time-resolution. The target cell was redesigned to allow for a precise alignment of the incident and scattered light. The quasi-backscatter geometry of the target cell permitted observation of a shifted Raman line, forbidden in the selection rules for pure backscatter geometry. OFHC copper was used to mount the diamonds and to serve as a heat sink for dissipation of the laser heating. A 1μm optical surface on the copper buffer enhanced signal collection and reflected the bulk of the elastically scattered light.

The impact materials used in this study were OFHC copper, tantalum, and platinum. The shock Hugoniot for these materials is well documented. The choice of impactor material was determined by the desired stress in the diamond. To accurately predict the longitudinal stress in the diamond, impedance matching calculations were performed using the Rankine-Hugoniot jump conditions. For the purpose of this work the shock/particle velocity in diamond was determined using finite strain theory and the Rankine-Hugoniot jump conditions. However, it should be noted that the finite strain theory utilized third-order isentropic constants that were calculated rather than measured.

To aid the experimental design, calculations were performed to determine strain-induced changes in the degeneracy, relative intensity, and frequency of the spectrum. A quasi-harmonic model[13] was used to correlate the observed spectral behavior to the directional forces acting at the atomic level. The quasi-harmonic model provides a first-order perturbation correction to the Raman frequency subjected to uniaxial strain. Two approximations are assumed in this formulation: first, it is assumed that the adiabatic approximation is valid, and second, the crystal potential is limited to the quasi-harmonic approximation. The perturbed dynamical matrix was expressed as a fourth rank tensor that reduces to three components {pqr} for cubic crystals. Solutions to the resulting secular equation revealed the predicted frequency shifts as functions of {pqr} and the applied strain. For uniaxial strain along [100], two perturbed eigenfrequencies were

predicted, a singlet and a doublet. Strain applied along [110] resulted in three distinct frequencies.

Because the Raman signal is polarization sensitive, it was necessary to determine the selection rules applicable for the quasi-backscatter geometry used in this study. These rules also permitted a rough determination of the expected relative intensities.

Experimental Results

Twelve shock experiments were performed on diamond. A total of nine experiments were performed with uniaxial strain along the [110] crystal direction and three with uniaxial strain along the [100] direction. The fastest time-resolution obtained in these experiments was 10 nanoseconds.

The [110] diamond experiments were performed for peak longitudinal stresses ranging from 122 kbar ($\approx$1% density compression) to 450 kbar ($\approx$3.5 % density compression). Two shifted Raman lines were observed in all nine of these experiments and a third, much less intense line, was determined in seven of the nine experiments. All frequency shifts were observed to increase with longitudinal stress, although at different rates. In each case the shifted peak location was determined by a Gaussian fit to the data.

For experiments performed on the [100] diamond orientation only two peaks were observed, corresponding to the predicted singlet and doublet locations. The singlet was shifted to higher frequency than the doublet and exhibited a relative intensity 3-9 times larger that of the doublet. The longitudinal stress ranged from 278 kbar ($\approx$2.5 % compression) to 417 kbar ($\approx$3.8 % compression) indicating that the diamond lattice is more compressible along the [100] direction.

Analysis

For each experiment, the fitted values for the observed peak locations were used to determine the values of the {pqr} parameters. The least squares, best fit, for {pqr} values

determined from the [110] data was then used to predict the behavior for the [100] applied strain. The experimental data for the [100] orientation was found to be in good agreement with the predicted locations, thus providing an independent check of the parameter values. For comparison purposes, the frequency predictions based on the previous values given by Grimsditch et al.[8] were also examined and found to yield less satisfactory fits to the experimental data.

The theory developed to describe the experimental results of this work may be applied to any arbitrary stress, or strain state, which is uniform and well defined. For uniaxial strain, application of the theory is particularly straightforward. It is also easily adapted to give predictions for uniaxial stress and hydrostatic stress environments. To compare the present results to the static high pressure data, the mean spherical stress for each experiment was calculated from the nonvanishing principal stress values determined from finite strain theory. The weighted centroid of the observed Raman line shifts was compared to the shift of the degenerate Raman spectrum examined under static high-pressure loading. Good agreement was obtained in these comparisons.

The {pqr} values determined in this study were also examined for any dependence on density compression. Any observed dependence of the {pqr} values on density compression implies that the mode Grüneisen parameter also depends on density compression. Comparison was made to the previous work of Goncharov et al.[15] for the pressure dependence of the mode Grüneisen parameter in diamond. The present results suggest a positive slope in agreement with Goncharov et al.,[15] although, the uncertainty in the slope is quite large. Also, the magnitude of the slope is three times as large as that given by Goncharov et al.[15]

6.2 CONCLUSIONS

Based on the experimental data and analysis presented in this work the following conclusions are stated:

(1) A time-resolution of 10 nanoseconds has been achieved in the Raman spectrum of diamond during shock-loading experiments. The time-resolution demonstrated for the experimental results reported here is the fastest reported to date.

(2) The degenerate Raman line was observed to split during shock compression experiments on diamond. This is the first reported observation of such splittings during shock experiments. Data for the [110] orientation indicate that the observed spectrum is accurately described by three singlets, suggesting a complete lifting of the degeneracy. Raman spectra for the [100] orientation were consistent with singlet and doublet lines, suggesting a partial removal of the degeneracy at ambient conditions. All frequency-shifts were observed to increase with density compression.

(3) Theoretical developments based on the quasi-harmonic model provide excellent agreement with the experimentally observed frequency shifts for the [110] and [100] crystallographic orientations of diamond.

(4) For the very large nonhydrostatic stresses considered in this study, the nonlinear elastic expressions for the stress-strain response provided a good fit to the experimental results.

(5) Expressions are given for the shock/particle velocity relationship along the [100] and [110] directions in diamond. These expressions were determined by combining the finite strain analysis and the Rankine-Hugoniot jump conditions. The lack of experimental data on the diamond Hugoniot represents the largest uncertainty in the present work.

(6) Using the anharmonic parameters {pqr} from the present study, the predictive capability of the quasi-harmonic model[13] is demonstrated to be very good for diamond.

(7) The present work shows that time-resolved Raman spectroscopy during shock loading is a useful technique for exploring strain-induced symmetry changes. The

very large nonhydrostatic stress, characteristic of uniaxial strain experiments, permits determination of anharmonic frequency contributions that may not be obtained from hydrostatic loading.

6.3 RECOMMENDATIONS

Experimentally it would be desirable to corroborate the present data (particularly the value for {r}) with additional uniaxial strain experiments along the [111] crystallographic orientation. For the [111] orientation, the theory presented in this work predicts a doublet and singlet that depend upon all three anharmonic parameters. At 1% compression the singlet-doublet separation should be approximately 30 cm^{-1}, which is easily resolved experimentally.

In light of the possible dependence of the {pqr} values on density compression, it is recommended that the theoretical framework be extended to second order in the strain to include the sixth rank tensors describing strain-induced frequency shifts. Experimental measurement of the higher order expansion coefficients might prove to be difficult. However, the theoretical development might shed some light on fundamental differences between uniaxial strain experiments and hydrostatic experiments. For example, it can be shown that for uniaxial strain the modified dynamical matrix $G_{\alpha\beta}(\eta)$ varies as,

$$\left[\frac{\partial G_{\alpha\beta}(\eta)}{\partial \eta_{11}}\right]_{uniaxial} = (p+2q) + \frac{1}{2}(G_{111} + 2G_{112})\eta_{11}$$

whereas, for hydrostatic stress

$$\left[\frac{\partial G_{\alpha\beta}(\eta)}{\partial \eta_{11}}\right]_{hydrostatic} = (p+2q) + \frac{1}{2}(G_{111} + 6G_{112} + 2G_{123})\eta_{11}$$

Finally, it is recommended that stress or particle velocity measurements be performed on diamonds with well known crystallographic orientations to better characterize the diamond Hugoniot. The largest uncertainty in the present work is due to the lack of these experimental data. Continuum measurements may also be used to evaluate some of the third-order elastic constants in diamond for which no experimental values are known. In addition, extending the measurements to much higher stress might also improve the {pqr} values determined from the present work.

REFERENCES

1   Seal, M. and W.J.P. Enckevort, "Applications of diamond in optics", *SPIE, Diamond Optics*, **969**, 144, (1988).

2   Berman, R., "Physical Properties of Diamond", Clarendon Press, (1965).

3   Solin, S.A. and A.K. Ramdas, "Raman Spectrum of Diamond", *Phys. Rev. B*, **1**(4), 1687, (1970).

4   Cardona, M., "Resonance Phenomena", *Light Scattering in Solids II*, ch. 2, Springer-Verlag, (1982).

5   Boppart, H., J. van Straaten, and I.F. Silvera, "Raman spectra of diamond at high pressures", *Phys. Rev. B*, **32**(2), 1423, (1985).

6   Tardieu, A., F. Cansell, J.P. Petitet, "Pressure and temperature dependence of the first-order Raman mode of diamond", *J. Appl. Phys.*, **68**(7), 3243, (1990).

7   Anastassakis, E. M., "Morphic Effects in Lattice Dynamics", Dynamical Properties of Solids Vol.4, 157, (1980), North-Holland Publishing, Horton and Maradudin Eds.

8   Grimsditch, M.H., E. Anastassakis, and M. Cardona, "Effect of uniaxial stress on the zone-center optical phonon of diamond", *Phys Rev. B.*, **18**(2), 901, (1978).

9   Schmidt, S.C., D.S. Moore, and J. W. Shaner, "Raman Spectroscopies in Shock-Compressed Materials", *Shock Waves in Condensed Matter*, J. R. Asay, R.A. Graham, and G. Straub (editors), 293, (1983).

10 Gupta, Y., "Progress in Understanding Shock Deformation in Condensed Materials at the Atomic/Molecular Level: Recent Experimental Developments", Plenary Paper , Seventh APS Topical Conference on Shock Waves in Condensed Matter, 1991.

11 Gupta, Y.M., P.D. Horn, and C.S. Yoo," Time-resolved Raman spectrum of shock-compressed diamond", *Appl. Phys. Lett.*, **55**(1), 33, (1989).

12 Gustavsen, R and Y.M. Gupta, "Time-resolved Raman measurements in α-quartz shocked to 60 kbar along the z axis", To Be Published.

13   Ganesan, S., A.A. Maradudin, and J. Oitmaa, "A Lattice Theory of Morphic Effects in Crystals of the Diamond Structure", *Ann. of Physics*, **56**, 556, (1970).

14   Parsons, B.J., "Spectroscopic mode Grüneisen parameters for diamond", *Proc. Roy. Soc. Lond. A.*, **352**, 397, (1977).

15   Goncharov, A.F., I.N. Makarenko, and S.M. Stishov, "Raman scattering from a diamond at pressures up to 72GPa", *JETP Lett.*, Vol41(4), 184, (1985).

16   Mitra, S.S., O. Brafman, W.B. Daniels, and R.K. Crawford, "Pressure-Induced Phonon Frequency Shifts Measured by Raman Scattering", *Phys. Rev.*, **186**(3), 942, (1969).

17   Hanfland, M., K. Syassen, S. Fahy, S.G. Louie, and M. L. Cohen, "Pressure dependence of the first-order Raman mode in diamond", *Phys. Rev. B.*, **31**(10), 6896, (1985).

18   Adapted from "Introduction to Solid State Physics", by C. Kittel Fig. 30.

19   Smith, H.M.J., "The Theory of the Vibrations and the Raman Spectrum of the Diamond Lattice", *Phil. Trans. Roy. Soc.* **A241**, 105, (1948).

20   Raman, C. V., *Proc. Roy. Soc.*,**122A**, 23, (1928).

21   Ramaswamy, C., *Indian J. Phys.*, **5**, 97, (1930).

22   Gilson, T.R. and P.J. Hendra, "LASER RAMAN SPECTROSCOPY", Wiley-Interscience

23   Wells, A.F., "STRUCTURAL INORGANIC CHEMISTRY", Clarendon Press, 4th Ed., 1975.

24   Cerdeira, F., C.J. Buchenauer, F.H. Pallak, and M. Cardona, "Stress-Induced Shifts of First-Order Raman Frequencies of Diamond and Zinc-Blend Type Semiconductors", *Phys. Rev. B*, **5**(2), 580, (1972).

25   Born, M. and K. Huang, "Dynamical Theory of Crystal Lattices", Clarendon Press, (1954).

26   Jayaraman, A., *Rev. Mod. Phys.*, **55**, 65, (1983).

27   Weinstein, B. A. and G.J. Piermarini, "Raman scattering and phonon dispersion in
℈   ⸱⸱℈P at very high pressure", *Phys. Rev. B*, **12**(4), 1172, (1975).

28   Ferraro, J.R., "Vibrational Spectroscopy At High Pressures", Academic Press,
(1984).

29   Davies, H. W., *J. Res. Nat. Bur. Stand. Sect. A.*, **72**, 149, (1968).

30   Forman, R.A., G.J. Piermarini, J.D. Barnett, and S. Block, *Science*, **176**, 284, (1972).

31   Grüneisen, E., In *Handbook der Physik*, Vol. 10, ed by Geiger and Scheels, Ch. 1,
(1926).

32   Rodriguez, S. and A.K. Ramdas, "Inelastic Light Scattering in Crystals", in
Highlights of Condensed-Matter Theory, ed. by F. Bassani, F. Fumi, and M. Tosi, pg 369,
(1985).

33   Loudon, R., "The Raman Effect in Crystals", *Adv. in Phys.*, **13**, 423, (1964).

34   Herzberg, G. "Molecular Spectra and Molecular Structure", V2, Van Nostrand
Reinhold, pg260, (1945).

35   Born, M. and R. Oppenheimer, *Ann. Physik* , **87**, 457, (1927).

36   Loudon, R., "Theory of the first-order Raman effect in crystals", *Proc. Roy. Soc.*,
A275, 218, (1963).

37   For example see reference 33, Eq. (23)

38   Herzberg, G. "Molecular Spectra and Molecular Structure", V2, Van Nostrand
Reinhold, pg260, (1945).

39   Poulet, H. and J.P. Mathieu, "Vibration Spectra and Symmetry of Crystals", *Gordon
and Breach*, pg 326, (1976).

40   Reference 39 pg. 332

41   Reference 39 pg. 406

42   Anastassakis, E., E. Burstein, "Morphic Effects I - Effects of External Forces On Photon-Optical Phonon Interactions", *J. Phys. Chem. Solids*, Vol.32, 313, (1971).

43   Anastassakis, E and E. Burstein, "Electric-Field-Induced Infrared Absorption and Raman Scattering in Diamond", *Phys. Rev. B.*, 2(6), 1952, (1970).

44   Nye, J.F., "Physical Properties of Crystals", Oxford Science Pubs., (1985)

45   Peiser, H.S., J.B. Wachtman, and R.W. Dickson, "Reduction of Space Groups to Subgroups by Homogeneous Strain", *J. Research NBS*, Vol. 67A(5), 395, (1963).

46   Tinkham, M., "Group Theory And Quantum Mechanics", McGraw-Hill, (1964), pg25.

47   Colthup, N.B., L.H. Daly, and S.E. Wiberley, "Introduction to Infrared and Raman Spectroscopy", Academic Press, 3rd edition, (1990).

48   Fateley, W.G., F.R. Dollish, N. T. McDevitt, and F.F. Bentley, "Infrared and Raman Selection Rules for Molecular and Lattice Vibrations: The Correlation Method", *Wiley-Interscience*, (1972).

49   Leibfried, G. and W. Ludwig, "Theory of Anharmonic Effects in Crystals", *Solid State Physics*, **V12**, 276, Academic Press (1961), Seitz and Turnbull eds.

50   Anastassakis, E. and E. Burnstein, "Morphic Effects II - Effects of External Force on the Frequencies of the $q \approx 0$ Optical Phonons", *J. Phys. Chem. Solids*, **32**, 563, (1971).

51   Thurston, R.N., and Brugger, K., "Third-Order Elastic Constants and the Velocity of Small Amplitude Elastic Waves in Homogeneously Stressed Media", *Phys. Rev.*, **133**(6A), A1604, (1964).

52   Thurston, R,N., "Wave Propagation in Fluids and Normal Solids", *Physical Acoustics*, **Vol I-A**, Academic Press, (1964), W. Mason Ed.

53   Bell, P.M., Mao, H.K., and K. Goettel, "Ultrahigh Pressure: Beyond 2 Megabars and the Ruby Fluorescence Scale", *Science*, **226(4674)**, 542, (1984).

54   Pavlovskii, M.N., "Shock Compression of Diamond", *Soviet Physics-Solid State*, Vol. **13**(3), 741, (1971).

55   McSkimin, H.J. and P. Andreatch, "Elastic Moduli of Diamond as a Function of Pressure and Temperature", *J. Appl. Phys.*, **43**(7), 2944, (1972).

56   Kondo, K. and T.J. Ahrens, "Shock Compression of Diamond Crystal", *Geophys. Res. Lett.*, Vol. **10**(4), 281, (1983).

57   Brugger, K., "Pure Modes for Elastic Waves in Crystals", *J. Appl. Phys*, **36**(3), 759, (1965).

58   Auld, B.A., "Acoustic Fields and Waves in Solids", **Vol.1**, Wiley Interscience, (1973).

59   see for example G. E. Duvall and G. R. Fowles,"Shock Waves", in High Pressure Physics and Chemistry, **Ch.9**, 209, Academic Press, Ed. R.S. Bradley, (1963).

60   Horn, P.D. and Y.M. Gupta,"Wavelength shift of the ruby luminescence R lines under shock compression",*Appl. Phys. Lett.*, **49**(14), 856 (1986).

61   Anastassakis, E., A. Cantarero, and M. Cardona, "Piezo-Raman measurements and anharmonic parameters in silicon and diamond", *Phys. Rev.*, **41**(11), 7529, (1990).

62   Keating, P.N., "Effect of Invariance Requirements on the Elastic Strain Energy of Crystals with Application to the Diamond Structure",*Phys. Rev.*, **145**(2), 637, (1966).

63   Keating, P.N., "Theory of the Third-Order Elastic Constants of Diamond-Like Crystals", *Phys. Rev.*, **149**(2), 674, (1966).

64   Horn, P.D., "Time-Resolved Recording Of Low Intensity Optical Spectra In Dynamic Experiments", *Shock Dynamics Center*, Internal Report **SDL-86-02**, (1986).

65   Gustavsen, R.,"Characterization of the WSU Shock Dynamics Laboratory Time-Resolved Raman Spectroscopy System", *Shock Dynamics Center*, Internal Report **SDL-90-00**, (1990).

66   Edwards, D.F., and H.R. Philipp, "Cubic carbon (diamond)", *Handbook of Optical Properties of Solids*, Academic Press, (1985).

67   Properties of Diamond, Dubbeldee Harris Diamond Corp.

68   Mitchell, A.C., & W.J. Nellis, 'Shock compression of aluminum, copper, and tantalum', *J. Appl. Phys.*, **52**(5), 3363, (1981).

69   Holmes, N.C. et al., 'The equation of state of platinum to 660 GPa (6.6 Mbar), *J. Appl. Phys.*, **66**(7), 2962, (1989).

70   CRC Handbook of Physics and Chemistry

71   Metadi Diamond paste is a pronduct of Buehler Ltd., Lake Bluff, Illinois.

72   Fowles, G.R., G.E. Duvall, J. Asay, P. Bellamy, F. Feistmann, D. Grady, T. Michaels, and R. Mitchell, "Gas Gun for Impact Studies", *Rev. of Scientific Inst.*,**41**(7), 984, (1970).

73   Siegman, A. E., "Lasers", pg. 1021, University Science Books, (1986).

74   Cynosure, Inc., Bedford Mass.

75   Hutley, M.C., "Diffraction Gratings", Academic Press, (1982).

76   Demtroder, W., "Laser Spectroscopy", Springer Series in Chemical Physics #5, Springer-Verlag, (1982).

77   Lerner, J.M., and A. Thevenon, "The Optics of Spectroscopy", A Tutorial by J. Y. Optical Systems, Inc.

78   Rich, C. and D. Cook, "Lippmann Volume Holographic Filters For Rayleigh Line Rejection In Raman Spectroscopy", *SPIE* **V 1461**, 1-7, (1991).

79   "Holographic Interference Notch Filters", Kaiser Optical Systems, Inc., Ann Arbor Mi.

80   Figure adapted from Hadland Photonics Ltd., Imacon 790 series Image Converter Camera Brochure.

81   Campillo, A.J. and S.L. Shapiro, "Picosecond Streak Camera Fluorometry-A Review", *IEEE J. of Quantum Electronics*, **QE19**(4), 585, (1983).

82   Lampton, M., "The Microchannel Image Intensifier", *Scientific American*, Nov., 62, (1981).

83   IGOR by Wavemetrics, Lake Oswego, Or., 97035

84   Barker, L.M. and R.E. Hollenbach, *J. Appl. Phys.*, **41**, 4208, (1970).

85   See for example: (a)Anastassakis, E., S. Iwasa, and E. Burstein,"Electric-Field-Induced Infrared Absorption in Diamond", *Phys. Rev. Lett.*, **17**(20), 1051, (1966). (b) Grimsditch, M., M. Cardona, J. Calleja, and F. Meseguer, "Resonance in the Raman Scattering of CaF$_2$, SrF$_2$, BaF$_2$, and Diamond", *J. of Raman Spectroscopy*, **10**, 77, (1981).

86   Onari, O., M. Cardona, E. Schonherr, and W. Stetter,"Effect of Stress on the Raman Spectra of Mg$_2$Si and Mg$_2$Sn.",*Phys. Stat. Sol.*,**b79**, 269, (1977).

87   Conner, M.K., "Shear Wave Measurements to Determine the Nonlinear Elastic Response of Fused Silica Under Shock Loading", M. S. Thesis, 129pp, Washington State University, Pullman Wa. (1988).

88   Bell, M. I., "Stress-Dependence of the Raman Frequencies and Elastic Constants of Cubic Semiconductors", *Phys. Stat. Sol.(b)*, **53**, 675, (1972).

DISTRIBUTION LIST

DEPARTMENT OF DEFENSE

DEFENSE INTELLIGENCE AGENCY
ATTN: DIW-4

DEFENSE NUCLEAR AGENCY
ATTN: SPSD D PYLE
ATTN: SPSD P SENSENY
ATTN: SPSP K KIM
ATTN: SPWE
ATTN: SPWE E TREMBA
ATTN: SPWE G ULLRICH
2 CY ATTN: SSTL
ATTN: TDTR

DEFENSE TECHNICAL INFORMATION CENTER
2 CY ATTN: DTIC/OCP

FIELD COMMAND DEFENSE NUCLEAR AGENCY
ATTN: FCTI G S LU
ATTN: FCTO
ATTN: FCTT-T E RINEHART
ATTN: FCTT DR BALADI
ATTN: FCTTS G GOODFELLOW
ATTN: FCTTS P RANDLES

DEPARTMENT OF THE ARMY

U S ARMY COLD REGION RES & ENG LAB
ATTN: CECRL-MAILROOM

U S ARMY ENGR WATERWAYS EXPER STATION
ATTN: C WELCH CEWES-SD-R
5 CY ATTN: CEWES-SD-R HOWARD WHITE
ATTN: RESEARCH LIBRARY

U S ARMY NUCLEAR & CHEMICAL AGENCY
ATTN: MONA-NU DR D BASH

U S ARMY RESEARCH LAB
ATTN: SLCBR-SS-T

DEPARTMENT OF THE NAVY

DAVID TAYLOR RESEARCH CENTER
ATTN: CODE 1770

DEPARTMENT OF THE AIR FORCE

AIR FORCE ARMAMENT LABORATORY
ATTN: A BRINSON
ATTN: D WATTS

AIR UNIVERSITY LIBRARY
ATTN: AUL-LSE

HQ 497 IG/INOT
ATTN: INT

PHILLIPS LABORATORY
ATTN: EDWARD TAYLOR

DEPARTMENT OF ENERGY

LAWRENCE LIVERMORE NATIONAL LAB
ATTN: ALLEN KUHL

LOS ALAMOS NATIONAL LABORATORY
ATTN: J OGLE

SANDIA NATIONAL LABORATORIES
ATTN: DIV 9333 DR PAUL COOPER
ATTN: TECH LIB 3141

OTHER GOVERNMENT

CENTRAL INTELLIGENCE AGENCY
ATTN: OSWR/NED 5S09 NHB

DEPARTMENT OF DEFENSE CONTRACTORS

AEROSPACE CORP
ATTN: LIBRARY ACQUISITION

AEROTHERM CORP
ATTN: J SAPERSTEIN

APPLIED RESEARCH ASSOCIATES
ATTN: R FLORY

APPLIED RESEARCH ASSOCIATES, INC
ATTN: J KEEFER
ATTN: N ETHRIDGE

APPLIED RESEARCH ASSOCIATES, INC
ATTN: C J HIGGINS
ATTN: F E SEUSY
ATTN: N BAUM

APPLIED RESEARCH ASSOCIATES, INC
ATTN: J SHINN

APPLIED RESEARCH ASSOCIATES, INC
ATTN: R FRANK

APPLIED RESEARCH ASSOCIATES, INC
ATTN: J L DRAKE

BDM FEDERAL INC
ATTN: E DORCHAK

CARPENTER RESEARCH CORP
ATTN: H J CARPENTER

FLUID PHYSICS IND
ATTN: R TRACI

GEO CENTERS, INC
ATTN: B NELSON

IIT RESEARCH INSTITUTE
ATTN: DOCUMENTS LIBRARY

JAYCOR
ATTN: J STUHMILLER

JAYCOR
ATTN: CYRUS P KNOWLES

KAMAN SCIENCES CORP
ATTN: D BRYCE
ATTN: J CHANG

KAMAN SCIENCES CORP
ATTN: DASIAC

KAMAN SCIENCES CORPORATION
ATTN: DASIAC

LOGICON R & D ASSOCIATES
ATTN: C K B LEE
ATTN: D SIMONS
ATTN: LIBRARY

LOGICON R & D ASSOCIATES
ATTN: D CARLSON

LOGICON R & D ASSOCIATES
ATTN: G GANONG
ATTN: J RENICK

MAXWELL LABORATORIES INC
ATTN: C PETERSEN
ATTN: K D PYATT JR
ATTN: P COLEMAN
ATTN: S PEYTON

MAXWELL LABORATORIES INC
ATTN: S HIKIDA

PACIFIC-SIERRA RESEARCH CORP
ATTN: H BRODE

SCIENCE APPLICATIONS INTL CORP
ATTN: C HSIAO
ATTN: G EGGUM
ATTN: H WILSON
ATTN: TECHNICAL REPORT SYSTEM

SCIENCE APPLICATIONS INTL CORP
ATTN: W LAYSON

SCIENCE APPLICATIONS INTL CORP
ATTN: G BINNINGER

SRI INTERNATIONAL
ATTN: A FLORENCE
ATTN: DR JIM GRAN
ATTN: J GIOVANOLA
ATTN: J SIMONS
ATTN: M SANAI
ATTN: MARK GROETHE
ATTN: P DE CARLI

SUNBURST RECOVERY INC
ATTN: C YOUNG

TECH REPS, INC
ATTN: F MCMULLAN

TITAN CORPORATION
ATTN: J ROCCO
ATTN: J THOMSEN
ATTN: S BABCOCK

TITAN CORPORATION (THE)
ATTN: R ENGLAND

TRW INC
ATTN: TIC

WASHINGTON STATE UNIVERSITY
2 CY ATTN: PROF Y GUPTA

WEIDLINGER ASSOC, INC
ATTN: H LEVINE

WEIDLINGER ASSOCIATES, INC
ATTN: T DEEVY

WEIDLINGER ASSOCIATES, INC
ATTN: M BARON